Modelling of Dynamic Friction Across Solid Material Interfaces Using Molecular Dynamics Techniques

Nicholas Epiphaniou

Submitted for the Degree of Ph.D.

Department of Aerospace Sciences
Cranfield University
Cranfield, UK

2010

Cranfield University

School of Engineering

Ph.D.

Nicholas Epiphaniou

Modelling of Dynamic Friction Across Solid Material Interfaces Using Molecular Dynamics Techniques

Supervisor: Prof. Dimitris Drikakis

October 1, 2009

Abstract

The topic of this PhD is to investigate materials interfaces under the application of compressive forces and dynamic friction. Friction studies are important in applications for high-speed machining and ballistic penetration modelling, two areas where it is important to understand the behaviour of rapidly moving interfaces. Gaining insight into the velocity dependence of the effective tangential force, and its time-evolution, under various external loads is also of particular interest. It is important to understand on an atomic and/or molecular level the fundamentals of tribological processes. Some of the processes investigated in this thesis include plastic deformation due to high compression, the response of materials when sliding occurs in terms of temperature variation across the interface and its relationship with atomic diffusion. Moreover, the materials dependence on operating conditions of temperature, loading and dynamic friction are factors that ultimately determine the design of tribological systems.

In the last few years it has been shown that materials properties depend on the size, as smaller specimens are relatively stronger than larger ones. This thesis is aiming to employ state of the art numerical and theoretical methods, which are vital to give a significant insight and understanding of the fundamental issues concerning dynamic friction of tribological processes at the atomic scale. The mechanical behaviour is investigated in detail to reveal an accurate theoretical description of the frictional force at metallic surfaces. Special consideration is taken into account for the mechanism that causes dissipation in the form of heat. The strong deformation when materials undergo dynamic friction causes energy to dissipate away from the interface at a high rate.

Additionally, investigation of the plastic deformation and its variation under conditions prevalent at high speed sliding is carried out. Knowledge of the yield point under these conditions is important to obtain accurate constitutive models for the shear stresses. Investigating how the material strength varies under sliding friction and obtaining accurate evaluation of the stresses involved has proved difficult and time consuming. This is primarily attributed to the fact that experiments are difficult to conduct and expensive facilities are required. This thesis focuses on aspects of this complex process with the aid of molecular dynamic simulations.

Acknowledgements

Writing these few words was probably the easiest part of this thesis. Looking back at the time and effort required to complete this PhD gives me nightmares at night. I would like to say many thanks to my supervisor Prof. Dimitris Drikakis for providing the opportunity to undertake this PhD, his regular supervision and advice proved vital for completing this work successfully. Special thanks go to Dr. Marco Kalweit who supported me throughout these years and provided useful input, information, and stimulating discussions about molecular dynamics. I would like to express my appreciation to EPSRC and AWE for the financial support throughout this project. The regular meetings with Graham Ball and Nigel Park from AWE have been very constructive. Special thanks to the team at Sandia, Steve Plimpton and Paul Crozier, for their support throughout these years.

I would like to say many thanks to the people from the volleyball club that every year support the team. Especially to those who participated in the finals of the BUSA championship in 2008, namely Pier, Greg, Laurent, Michael, Alberto, Ludovic and Dominique. Also thanks to the members of the FMaCS group, in particular, Antonis, Marco, Ben, Giannis, Nikos and Javier for all the fruitful discussions. I couldn't, of course, forget Cynthia, Hara, Giota and Nafsika. Special thanks to my colleague Kevin at BHR Group for his constructive comments on this thesis and his support during the writing up process.

Finally, and most importantly I would like to give a special thank you to my family, my mother Maria, father Michael, brothers Gregory and John, and my girlfriend Kali for their continuous support throughout the past years. Without them I don't think I could have achieved half of what I have done today. I am very grateful for all that you have done for me and I would like to dedicate this work to you.

Contents

List of Figures

Nomenclature

Latin Symbols

A	area
$\boldsymbol{a}$	acceleration
a	lattice parameter
C_e	electronic specific heat
C_p	specific heat capacity
c	speed of sound
$\boldsymbol{c}_c$	cooling coefficient
c_i	centro-symmetric parameter
c_l	longitudinal speed of sound
c_t	transverse speed of sound
C_s	heat flux coefficient
$\mathcal{D}$	diffusion coefficient
d	grain diameter
dt	integration timestep
E_{tot}	total energy of embedded atom method (EAM) potential
$E(t)$	internal energy
$E_{xc}[\rho(r)]$	exchange correlation energy
$e(\tau)$	energy per atom
E	modulus of elasticity
E_k	kinetic energy
$E_{k,int}$	internal kinetic energy
ΔE_k	change in kinetic energy
Fb	three component force due to pairwise interaction
F_n	normal force
Fp	three component force due to bonded interaction
F_t	tangential force

$\tilde{F}_t$	stochastic force
$F_{tang}(\tau)$	average frictional force
f	friction factor of the reflective plane
f	scaling factor for energy transfer scheme
f_{tang}	tangential frictional force
f_{ij}^{tang}	tangential force acting on atoms *i* and *j*
f_i	atomic force on atom *i*
f_h	fraction of the frictional heating
f_{rp}	external force imposed by the reflective plane
G	shear modulus
GB	grain boundary
G_T	Gibbs free energy
G_l	Gibbs free energy of liquids
G_s	Gibbs free energy of solids
g_p	coupling constant due to electron phonon interaction
g_s	coupling constant due to energy loss because of electronic stopping
g	gravitational constant
$\mathcal{H}$	Hamiltonian of the system
H	enthalpy of the system
$h(\tau)$	enthalpy per atom
$\Delta(H_m)$	heat of fusion
Q	heat
J	mechanical equivalent of heat
J_y	heat flux in y-direction
k	thermal conductivity
k_{exp}	experimental thermal conductivity
k_{MD}	thermal conductivity estimated by molecular dynamics (MD) simulations
k_B	Boltzman's constant
k_e	electron's thermal conductivity
k_s	spring stiffness
l	length of the simulation box
L_x	length of the simulation box in x direction
L_y	length of the simulation box in y direction
L_z	length of the simulation box in z direction
l_o	initial length of the simulation box

m_i	atomic mass
m_e	electron mass
m_{Cu}	atomic weight of copper
m_{rp}	mass of reflective plane
N	number of atoms
N_R	number of atoms belonging to the reservoir
N_f	number of degrees of freedom
N_t	timestep
P	pressure
P_n	normal pressure
p	pressure per atom
$\boldsymbol{p}$	momentum
$\boldsymbol{p_l}$	linear momentum
$\Delta\vec{\boldsymbol{p}}$	change in momentum vector
$\mathcal{R}$	amount of rescaled velocity
$\mathcal{R}_m$	rotation matrix
r_c	potential cut-off distance
r_i	atomic position
r_g	radius of the grain
r_0	interatomic bond length
$\boldsymbol{R}_j$	vector position
$\boldsymbol{R}_{j+6}$	vector position of the six pairs of nearest neighbours in face centred cubic (FCC) crystallographic structure
$\mathcal{S}$	predefined group of atoms for velocity transfer scheme
$S_e(E)$	electronic stopping if ions in solids
S_{ab}	per atom stress tensor
$(S_{ab})_{local}$	local per atom stress tensor
$(S_{ab})_{global}$	global per atom stress tensor
$T(t)$	instantaneous temperature
T	temperature
T_o	temperature of the surroundings
T_a	atomic temperature
$\acute{T}_a$	temperature evaluated by energy balance transfer
T_e	electron’s temperature
T_m	melting temperature
T_{ss}	temperature of superheating solid

T_{sl}	temperature of supercooling liquid
t	time
U_u	unknown potential of interest
U_e	shear wave
$u_o(r)$	external potential
$u_{s,o}(r)$	local potential (Kohn-Sham)
$u(i\,j)$	core-core pair interaction between two atoms i and j
$u(\tau)$	volume per atom
V	volume
V_g	volume of grain
$\mathcal{V}$	interatomic potential
v	local instantaneous velocity of N atoms
v_i	atomic velocity
v_c	critical point of velocity
v_u	velocity of the upper reservoir
v_u^*	corrected velocity of the upper reservoir
v_l	velocity of the lower reservoir
v_r	relative sliding velocity
v_{th}	thermal velocity
v_0	cut-off velocity
v_{rp}	velocity of reflective plane
W	hamiltonian of the reference system
v_{sub}	subtracted velocity

Greek Symbols

α_e	thermal expansion coefficient
α_l	thermal expansion coefficient of the liquid phase
α_s	thermal expansion coefficient of the solid phase
β	nucleation barrier parameter
γ	surface energy
γ_{sl}	surface tension for solid-liquid
γ_i	friction coefficient due to energy loss
γ_s	friction coefficient due to electronic stopping
γ_p	friction coefficient due to electron phonon interaction
γ_ϵ	strain

Δ_ϵ	energy per timestep
$\dot{\gamma}_\epsilon$	strain rate
λ_I	coupling parameter for integration method
λ_e	mean free path of electron
λ_m	mass enhancement parameter
λ_p	mean free path of phonon
μ	coefficient of friction
ρ_i	electron density contributed by atom *i*
$\rho_0\,(r)$	density of interacting system
σ	stress
σ_c	cohesive strength
σ_y	yield stress
σ_{yt}	yield strength
σ_{max}	maximum stress
σ_{xx}	internal local stress in x direction
σ_{yy}	internal local stress in y direction
σ_{zz}	internal local stress in z direction
τ	frictional shear stress
τ_{sc}	electron scattering time
$\boldsymbol{v}_i$	velocity vector
Ω	atomic volume

List of Abbreviations

AFM	atomic force microscopy
BMG	bulk metalic glass
BC	boundary conditions
CFM	chemical force microscopy
CoF	coefficient of friction
CPU	central processing unit
DFT	density functional theory
DSMCM	direct simulation Monte Carlo methods
EAM	embedded atom method
EMT	effective-medium theory
FCC	face centred cubic
FMACS	fluid mechanics and computational science

FEM	finite element method
FP-LMTO	full-potential linear muffin-tin orbital
FPLAPW	full potential of linearized augmented plane waves
GGA	generalized-gradient approximation
GPT	generalized pseudopotentials theory
HAGBs	high-angle grain boundaries
LAMMPS	large-scale atomic/molecular massively parallel simulator
LDA	local density approximation
LAPW	linearised augmented plane wave
LSDA	local spin density approximation
MEAM	modified embedded atom method
MEMS	micro-electro-mechanical systems
NEMS	nano-electro-mechanical systems
MD	molecular dynamics
MGPT	model generalized pseudopotential theory
MSD	mean square displacement
μVT	grand canonical ensemble
NEMD	non-equilibrium molecular dynamics
NGP	nearest-grid-point
NVE	micro-canonical ensemble
NVT	canonical ensemble
NPT	isothermal isobaric ensemble
PP	pseudopotential
PDF	pair distribution function
RNEMD	reverse non-equilibrium molecular dynamics
SPaSM	scalable parallel short-scale MD
TKC	thermal conductivity correction scheme
VASP	vienna ab initio package
QM	quantum mechanics

CHAPTER 1

Introduction

Materials science of experimental and theoretical techniques has focused attention on the properties of materials ranging from macro- to nano- scale. The outstanding possibilities of nanocrystalline materials have been the subject of in depth research over the past few years as discussed by Meyers et al. [179]. Nanocrystalline materials are characterised by large volume fraction of grain boundaries affecting the mechanical, physical and chemical properties when compared with coarse-grained polycrystalline. They are obtained by introducing high density interfacial grain boundaries, which is achieved if the crystal size is typically of 10 nm. There are several names in the literature for nanocrystalline materials such as ultra-fine grained materials, nanophase materials, nanometer-sized crystalline or nanostructured materials. The enormous amount of research in this area is enabled by developing and applying new methods such as transmission electron microscopy and tunneling microscopy and preparing structures with novel features and properties. Amongst other technological developments are the advances of high temperature superconductors, quasicrystals and metallic glasses as illustrated by Gleiter [77]. Research on nanocrystalline materials is categorised under the field of nanotechnology in which processes are investigated at dimensions ranging from 0.1 to 100 nm [67, 59]. Feynman [59] known for many insights and famous phrase ‘There’s plenty of room at the bottom’, is considered by many to be a pioneer in the field of nanotechnology. Applications of the field of nanotechnology include the properties of nanocrystalline materials, the nano-electromechanical systems, high hardness cutting tools and bottom up fabrication techniques, materials reinforced with nanoparticle, protein engineering and many more.

Modelling the material behaviour is an essential step for progress in materials science and engineering, since they help to explain the physics and/or dynamics of physical pro-

cesses. Obtaining numerical simulations either at the micro-scale using continuum theories or at the nano-scale using atomistic theories is essential because of the difficulties of conducting experiments at extreme conditions. Although, conducting experiments at the nanoscale is highly cost effective, the lack of analysis tools and the limitations of measuring properties of interest is more critical for these systems. Atomistic techniques enable scientists to visualise the material's behaviour in dynamic processes; they can act as input to micro-scale systems by supplying missing experimental variables and possibly act as a validating tool. Undoubtedly, the numerical simulations are of great importance in the engineering and scientific community.

1.1 Nanotribology: Techniques and applications

Nanotribology studies the science of adhesion, friction, lubrication and wear of surfaces in which relative motion takes place at the nanoscale. The word tribology comes from Greek: "'$\tau\rho\iota\beta\omega$"' which means rub and "'$\lambda o\gamma o\varsigma$"' meaning principle or logic. Friction has been studied for several years via experimental and theoretical work in which advances have been made revealing diverse phenomena and enormous complexity confirming the non-linear nature even for the simplest tribological processes. Scientists and engineers are working on the development of low friction surfaces and thin lubricating films, which is important in the miniaturization of moving components in devices such as micro-elecro-mechanical systems (MEMS), computer systems, micro-machines, bio-systems and many more as highlighted by Lyshevski [168]. The empirical friction laws that are described in the following sections are not sufficient to analyse the tribological issues associated with these devices. This is due to the great importance of surface chemistry.

Within the new area of nanotribology the frictional contact behaviour and wear is studied at the nanoscale. Friction is closely associated with lubrication, adhesion and wear; investigation of non-equilibrium processes occurring at the atomistic scale are essential to explain friction phenomena at the micro-scale. Thus, the following sections address the issues related to tribological processes from macro to nano-scales.

1.2 Historical and modern views of friction, lubrication and wear

Understanding of the friction, lubrication and wear mechanisms is highly important to the development of nanotribology and its applications. The range of industrial applications includes aerospace, automotive, biomedical, textile, optical, military, metallurgical, power generation and many more. Friction uses up a substantial amount of energy generated, while a large amount of financial resources is required to replace worn components. Tribology is a very old science going back to the prehistoric epoch in which tribological tools have been used to generate fire or griding flint tools. Several achievements have been obtained to make people's life easier such as the stone socket for the potter's wheel, the blow drill, lubricated wooden sledge to transport huge monolithic stones and many more applications. In Egypt, around 2400 BC, in order to facilitate the transportation of big statues, people would pour water in front of a sledge eliminating thus the effect of friction. Years later Greeks and Romans were the first to develop machine components, rolling bearings and gears. Even though information on tribology has grown over the years the existing knowledge of most scientists, engineers and designers in this important area is not sufficient to overcome fundamental tribological problems.

The review by Dowson [52] shows that modern approaches and theories started when Leonardo Da Vinci developed the first friction laws 500 years ago, claiming that the frictional force is directly proportional to the applied load and also independent of the contact area. During the industrial revolution of the 16th century and the development of machines, the investigation of sliding friction phenomena upon the application of lubricants was necessary to reveal their beneficial effects, amongst them the reduction in friction. The importance of rolling friction was firstly perceived by Robert Hook (1680) in which he conducted frictional studies of sliding bearings. Hook pointed out that elastic and plastic deformation plays an important role in the rolling friction. In 1699 Amontons investigated the phenomenon of sliding friction and published the macroscopic laws of friction, which had been formulated by Leonardo da Vinci approximately one hundred years earlier. Experimental observations were made by Philippe de la Hire on friction in which Amonton's results were confirmed. Many of frictional studies are recorded and many remarkable contributions on the phenomenon were achieved by Leibnitz (1646-1716), Desaguliers (1683-1744), Leonhard Euler (1707-1783) and Isaac Newton (1642-1727). An enormous experimental work was also achieved by Charles Augustin de Coulomb (1736-1806), who was

one of the biggest contributors on friction. He actually confirmed Da Vinci and Amontons laws, adding that the frictional force is also independent of the sliding velocity. These laws are known today as the Amonton-Coulomb laws.

Frictional applications are closely associated with the use of lubricants in order to reduce the friction forces and decrease the damages due to rubbing surfaces. Lubricants such as animal fat, vegetable oil and solid lubricant have been available since the 18th century, however in the middle of the 19th century mineral oils gradually started to replace them. Nikolai Pavlovich Petrov and Beauchamp Tower made remarkable discoveries on the behaviour of journal bearings lubricated with oil, proving that the friction in bearings depends on the viscosity of the oils. They also developed a formulae that calculate the friction of moment bearings.

Osborn Reynolds used some of the results of Towers and developed the basic equations of hydrodynamic lubrication (Reynolds equation), which is a mathematical formula describing the pressure distribution in the clearance of a journal bearing. The development of hydrodynamic lubrication theory was studied by various other researchers like Richard Sribeck, Johannes Wilhelm Sommerfeld, Anthony George Malden Michell and others. Along with hydrodynamic lubrication, boundary lubrication appeared in the scientific community in which the initial steps were made by William Bate Hardy in 1916. He showed that the coefficient of friction for different materials can be influenced by the molecular weight of the lubricants [52, 8].

When solids are sliding against each other there is a removal of materials from the solid surfaces due to the mechanical action. Wear is a complex nonlinear process and is influenced by many factors such as adhesion, abrasion, corrosion, fatigue and many more mechanical properties. In many applications these factors are dominant, however they are beyond the scope of this PhD work.

1.2.1 Temperature evaluation during friction experiments

Theories of friction were developed during the eighteenth and ninetheenth centuries and attempt to give insight into frictional behaviour in particular to the surface roughness and the material interlocking of the surface asperities. In 1936 two significant contributors have appeared in the scientific community studying the physical properties of surfaces under dy-

namic loading, Bowden and Tabor [233]. Bowden and Tabor [24] continued the frictional work during and after World War II. There are several aspects of friction that have been raised over the years, some of which are still unsolved. If metallic surfaces are brought in contact then strong adhesion is observed especially if the surfaces are very clean. This contributes to plastic deformation when sliding is initiated, in which wear and friction will be excessive. In real life this is difficult because surface contamination reduces the adhesion. Low levels of adhesion are also observed on metals which have d-bonding and show reduced interfacial strength. Bowden and Tabor [233] frictional model showed that frictional energy is dissipated by plastic deformation of the atomic slip along certain crystalline planes.

The experimental work by Bowden and Ridler [23] showed that when surfaces are sliding against each other the frictional force will be converted to heat and the temperature of the interfacial region will be raised. The local surface temperature can be very high and in some tribopairs exceeds 1000 °C, whilst the temperature of the rest of the material remains quite low. Several factors affect the temperature near the interfacial region; the load, the sliding speed, the coefficient of friction and the thermal conductivity of the material. This phenomenon is also observed even on surfaces in which lubrication was present. Bowden and Ridler [23] calculated the surface temperature on several tribopairs assuming that the area of contact is the end of a cylinder via the following relation:

$$T - T_o = \frac{\boldsymbol{f}_h \mu F_n g v}{J \pi r} \sqrt{\left(\frac{1}{2 \boldsymbol{c}_c k R_c}\right)} \tag{1.2.1}$$

where T is the temperature of the surface, T_o is the temperature of the surroundings, $\boldsymbol{f}_h$ is the fraction of the frictional heating that will go into either the upper or the lower body (typically 0.5 for materials with comparable values of thermal conductivity), F_n is the load applied to the sliding body, g is the gravitational constant, v is the sliding velocity, μ is the coefficient of friction, J is the mechanical equivalent of heat, $\boldsymbol{c}_c$ is the cooling coefficient, k is the thermal conductivity and R_c is the radius of the cylinder.

The early experimental work that was carried out by Bowden and Thomas [25] and Bowden and Ridler [23] was on Cu-steel, Ga-steel, Pb-steel and Constantan(Cu-Ni alloy)-steel tribopairs. The work showed that the local surface temperature was very high, recording values of 1273 K at low sliding speeds of up to 50 m/s, although the mass of the metal was quite cool as mentioned above. They also showed that the frictional heat on metals that are poor thermal conductors is not conducted away from the surface very rapidly, thus,

the surface temperature is high. He mathematically proved that the interfacial temperature should vary inversely with the square root of thermal conductivity.

Bowden and Freitag [21] also conducted friction experiments at very high speeds on balls spinning in a vacuum reaching velocities from around 200 to 800 m/s. The results of this investigation showed that the frictional resistance decreases as the speed increases and low values of frictional force are achieved. At sliding speed of 600 m/s the coefficient of friction falls to a value of 0.2. There is direct evidence that high surface temperatures are achieved by melting or softening the area of contact; these temperatures are measured using a thermo-electric method. This area of contact depends on the velocity at which the plastic strains are propagated in the metal. The results of the steel ball sliding on Cu was obtained by varying the load from 10 to 20g and using different surface roughness which both show no significant deviation from Amonton's law. Bowden and Freitag [21] finally showed that because of the high shear imposed on the material complete plastic yielding is not possible under this load conditions.

1.2.2 Frictional models

Several models have been proposed to give the origin of friction as described by Robbins and Muser [207]. Frictional models that take into account the surface roughness and adhesion when surfaces are brought into contact are discussed by Bowden and Tabor [24]. At the atomic scale, Tomlinson [238] was the first to show the existence of a mechanism associated with the energy loss during friction, with the assumption that there is a non-adiabatic change in the atomic position. Tomlinson [238] proposed an independent oscillator to explain the energy dissipation during friction phenomena. This model replaces the bottom surface of atoms with a periodic potential. This potential fluctuates due to the relative motion of the interfacial atoms during sliding, as shown in Figure 1.1(a). When the potential reaches the local minima, atoms are sliding. However, when an atom moves slowly reaching a position where the barrier between two local minima vanishes, the potential reaches the local maxima. As a result the atom rapidly jumps to the next location of the minimum potential. This process causes vibration to the entire system due to instability caused by the jumping of the interfacial atoms. The same energy dissipation mechanism was used in the Frenkel-Kontorova model [208, 136, 243] and Frenkel-Kontorova-Tomlinson as described by Weiss and Elmer [253] and by Weiss and Elmer [253], shown in Figure 1.1(b), with the exception that there is a more in-depth consideration of the interaction between the sur-

face atoms. In both cases the independent oscillator model uses the simple spring stiffness, k_s, to describe the interaction between the interfacial atoms and the bulk. Additionally, it is difficult to link the simplified models directly to complete tribological systems because both the elastic and thermal oscillations of the interfacial atoms are required.

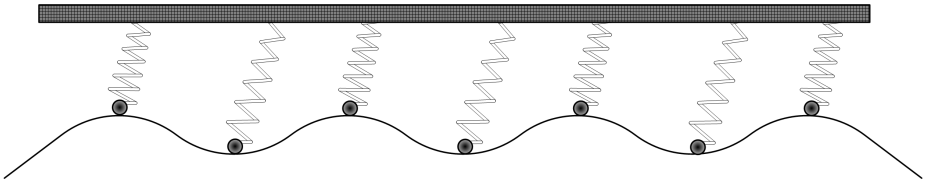

(a) Independent oscillator model of Tomlinson

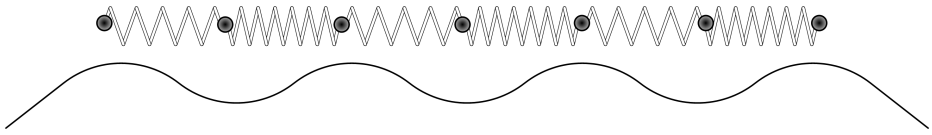

(b) Independent oscillator model of Frenkel and Kontorova

Figure 1.1: Tomlinson and Frenkel-Kontorova models for interfacial slip

The work by Xu and Huang [259] proposed a different frictional model based on the composite oscillator model for investigating the energy dissipation mechanism of wearless atomic scale friction. The composite model is based on a macroscopic oscillator that captures the characteristics of the equilibrium stage during friction and a micro oscillator of interfacial atoms that captures the non-equilibrium and the energy dissipation process. Xu and Huang [259] showed that the interfacial exciting force frequency plays a vital role during frictional phenomena. The results of Xu's study show that the calculated frictional force derived from the composite oscillator model is in a very good agreement with experimental values conducted using an ultra high vacuum atomic force microscope (AFM). The AFM tip was covered by Cu coating which was sliding on a Cu surface. Hence, the model was proven to describe the energy dissipation mechanism in a frictional process more accurately than the Tomlinson or Frenkel and Kontorova models.

Hirano and Shinjo [102] studied the origin of the frictional force by investigating the interaction of two clean surfaces. Atoms of the two contacting surfaces were interacting via an interatomic potential and he identified that there were two origins; the atomic and the dynamic locking. In atomistic locking atoms at the proximity of the interface are exposed to constant changes when sliding distance changes, while the potential has arbitrary strength. On the other hand, dynamic locking takes place when atoms discontinuously

change; this is because the interatomic potential increases in strength. In this study Hirano and Shinjo [102] showed that dynamic locking should not occur in realistic systems. In a later study [103] were first investigated the Frenkel–Kontorova model and apply it to dynamical simulations of sliding. They found out that when the corrugation of the substrate is small, see Figure 1.1(b), and the sliding distance is increasing with time, the kinetic friction approaches zero. [103] called this phenomenon as "superlubric", which was dependent on the corrugation threshold and the orientation of the surfaces. The superlubricity appears in both high and low sliding velocities; it occurs because the kinetic energy repeatedly increases and decreases with time. Additional work on low sliding friction is reviewed by Robbins and Muser [207] but this is beyond the scope of this thesis.

1.2.3 Lubrication and low speed sliding friction at the nanoscale

When lubricants are confined between two similar or dissimilar solid surfaces, they influence properties like the coefficient of friction μ, depending upon the load, speed and lubricant viscosity. They have various applications predominantly in mechanical components where reduction in friction and control of the interfacial heating and plastic deformation is required. Computer simulation studies attempted to give an understanding of tribological processes and insights into lubrication mechanism. Amongst those the review of Robbins and Muser [207] presents the work that has been undertaken in lubricated surfaces from hydrodynamic studies to molecular dynamics (MD) simulations from 1979 up to 2000. They showed that MD coupled with density functional theory (DFT) can be used to derive information about the atomic and electronic microstructure of the interface.

Continuum theories on hydrodynamics and elasto-hydrodynamics do not capture the physics as the structure approaches the atomic scale. The no-slip boundary condition for the fluid velocity and the solid surface assumes that the fluid velocity is equal to the velocity of the solid at the surface. MD simulations showed that the slip boundary condition was not dependent on the wall velocity. Therefore, both the fluid and the region near the interface responded linearly validating the fluctuation-dissipation theorem as discussed by Robbins and Muser [207].

An MD study done by Kong et al. [142] on bilayers of dioctadecyldimethylammonium chloride adsorbed between two solid surfaces showed that the friction coefficient, μ, was calculated as a function of density of the particular lubricant, the relative shearing velocity

and the applied normal force. The main observation of this work was that the μ decreases with decreasing amphiphile density and increases with increasing shear velocity. Other boundary lubrication studies are published in [16, 150, 261, 236, 237].

In slow speed sliding, in which velocity is kept constant, there is a distinct phenomenon in which a combination of periods of rest and sliding is observed, associated with squeaking noises. This unsteady motion consists of a stick in which the two sliding surfaces are stuck to each other followed by a sudden slip which is known as a stick-slip oscillation. The nature of the transitions between stick and slip as well as the steady sliding in models for boundary lubrication was studied numerically by Batista and Carlson [11].

Moreover, MD simulations carried out by Landman et al. [146] can be applied to get properties of interfacial junctions and to examine the nano-elastohydrodynamics in sheared lubricated surfaces. Elastohydrodynamics have been extensively studied by Olver and Spikes [194]. Lubricants such as hexadecane and tetracosane have been studied by Gao et al. [72]. These lubricants form high ordered layers with parallel in plane of surfaces. They appear to increase in their viscosities at various stages of the sliding motion. According to Landman et al. [146] when lubricant is squeezed into tight spaces between two surfaces, then the molecules act more like 'soft solids'. Then ordered layers are formed, which significantly influence the motion of sliding surfaces. How the molecules of a lubricant need to be arranged to obtain low friction and wear under sliding conditions is a question that needs thorough investigation. Novel simulation methods are possible to achieve this according to Hu's work [112] and the recent work by Jabbarzadeh et al. [122, 123]. Nevertheless, MD studies of Atomic Force Microscopy (AFM) have been conducted to clarify connections between order of lubricants and friction as shown by Mikulski et al. [180], which describes an amorphous carbon tip sliding against a monolayer of n-alkane chains.

There are methods to control and reduce the friction in thin-film boundary lubricated surfaces according to Gao et al. [71]. This study describes an extensive MD simulation which revealed the dynamics of molecular films, their structural characteristics, and the mechanism of transition under shear simulations. Moreover, chemical effects at the interface are of particular interest. A work done by Patrick et al. [196] describes the chemical force microscopy (CFM) using MD simulation. Study on fluid transport near/or in contact with walls are also feasible as shown by Hu et al. [113],[113, 114] that simulated the behaviour of Poiseuille and Couette flows. Simulations were performed for a fluid with spherical molecules to investigate successfully the rheological properties in thin film lubri-

cation.

A study by Mikulski et al. [180] describes the amorphous carbon tip sliding against a monolayer of n-alkane chains. In this study a tightly packed pure monolayer of 14 carbon atoms was compared to mixed monolayers of 12 and 16 carbon atoms chains. Sliding in the direction of a chain under the application of repulsive forces (positive) showed that pure monolayers have lower friction than mixed. The distribution of forces indicated that both pure and mixed monolayers resist tip motion, and that both layers exhibit friction anisotropy. Also, the contact distribution of forces changes dramatically with change in direction and therefore increase in friction is obtained. Ohzono and Fujihira [191] examine the frictional properties in terms of protuberance, length of molecules and conditions such as temperature and applied loads. Finally, frictional anisotropy is observed at 50 K according to Ohzono and Fujihira [192].

1.3 Material interfaces and high speed sliding friction at the atomic scale

The problem of high sliding friction has been extensively studied by various researchers [84, 85, 141]. Generally a good understanding of the science behind the sliding of material interfaces at the atomistic level requires the generation of frictional interactions of materials at a larger scale. There are various structural changes, which are accompanied by composition changes as well as materials mixing near the interface of these systems as discussed by Rigney et al. [206]. Theoretically, the systems considered in this report are dissipative and understanding of this mechanism is important. The purpose of this section is to discuss the state of the art and to address several points regarding materials simulations and modelling processes involved in sliding friction. Knowledge of mechanical, chemical and thermal properties of materials is important. In non-equilibrium molecular dynamics (NEMD) models where strongly driven interfaces exist, there is a connection between the velocity weakening and structural transformations at high velocities. This is closely associated with plastic deformation. Thus, large-scale simulations (10^6) atoms are important to analyse this structural behaviour at velocities greater than 10 m/s, and these are considered.

1.3.1 Applications of non-equilibrium molecular dynamics (NEMD)

One of the most difficult problems studied by NEMD is the propagation of shockwaves in solids. In explosions shock waves are caused by collisions of objects. When they are applied to solids, even perfect crystals, defects can be produced because of uniaxial compression. In the case of solids the sudden generation of dislocation changes the microstructure of the materials according to Holian et al. [106]. Additionally, stacking faults are nucleated by pre-existing defects within the microstructure also described by Holian and Lomdahl [104]. When simulating a shock wave the time needed to establish realistic results is long, thus NEMD is expensive in proportion to the length of time needed for a simulation of a propagating wave to the number of particles needed. However, strong shockwaves can be successfully studied by NEMD methods because strong shocks are quite thin (on the order of few lattice spacings) and propagate fast. Moreover, when the strength of the shock wave decreases (impact velocity) limitations start to appear due to the increase in shock thickness, and defects become very important.

Processes such as annealing or solidification from melting do not undergo steady state propagation like shockwaves because the timescales are significantly large, and beyond the capabilities of MD. This creates the need to investigate phenomena at increasing timescales as discussed by Streitz et al. [226]. Interesting phenomena involving dry friction between metals can be derived and plenty of examinations at both the atomistic and continuum level were completed, showing that plastic deformation produces extremely complex microstructures [255, 104, 105].

The speed and reliability of computers nowadays have increased dramatically and therefore allow investigators to initiate large-scale parallel computer simulations with a large number of atoms. A good example of this is the simulation of tantalum (Ta) BCC metal and uranium actinide by Streitz et al. [226]. In this study, simulations of 8 and 16 million atoms were used to investigate the solidification from melting of pure tantalum and uranium metal. The system used is the BlueGene/L and is a massively parallel scientific computing facility. The high density cellular design provides very high performance with low cost, power, and cooling requirements. This system is considered to be the one of the five faster computers in the world and is owned by Lawrence Livermore National Laboratory (LLNL). The complex microstructure and phases occurring during the solidification improved knowledge and understanding of metals with high atomic number. Moreover, the system size played an important role to determine not only the process of nucleation and

growth but the resulting microstructure.

1.3.2 Dynamic friction simulations and velocity dependent frictional force

This study investigates dynamic friction at high speeds and at this point a short literature review is undertaken to reveal the state of the art. In general, the science of sliding friction for thin films is more complex than those of bulk-elastic flow, which is due to many associated factors, such as surface roughness, chemistry and electronic structure of the material. Thus, understanding the non-equilibrium non-linear physics of this evolution of substructure forms the basis of the understanding and modelling of dry friction. From a theoretical point of view dry friction is an example of non-equilibrium material flow phenomenon. The work by Hammerberg et al. [91] studies the atomistic simulation of sliding friction that has been carried out in a velocity range of 10 to 1000 m/s in the high pressure regime of 5 to 15 GPa for Ta/Ag and Cu/Ag tribopairs. Hammerberg et al. [91] showed that practical simulation times require the sliding velocity to be greater than 10 m/s so that sliding can be initiated.

At critical speed v_c of approximately 500 m/s the structure of the interface changes and greatly disordered regions appear in the weaker Al. On the other hand, Ta is only weakly deformed at pressure of 15 GPa. A highly localized region of strong deformations is formed in the Al and the tangential velocity within it is zero as a result of strong bonding between the Al and Ta. Ta is deformed elastically at this point. All these happen at relative velocity of 732 m/s.

The second example given in this work of dissimilar interface is Cu(001) sliding in the [001] direction at a velocity of 376 m/s on Ag(001) at a pressure of 5 GPa. It has been observed that vertical lines are created on both materials showing the idea of strain development. In the Ag, which is the weaker, there is a modification near the interface consisting of a complex pattern of dislocation and stacking faults. At this velocity the Cu retains its original structure but develops a number of dislocation loops. This is also shown at sliding velocity of 758 m/s. Thus, the structures in Cu show planar stacking faults and dislocation loops are created at the interface. The pressure decreases for high velocities from 1 GPa at 200 m/s to 0.4 GPa at 750 m/s. The number of atoms used is $55 \cdot 10^6$ atoms interacting with EAM potentials. The deformation properties of the weaker

material dominate the sliding behaviour and the generation of substructure in the weaker material at high velocities results in a decrease of the frictional force.

Similar work has been performed in Cu/Ag also by Hammerberg et al. [90]. In this work the same configuration has been used as shown by Hammerberg et al. [91] but the simulation domain contained 2.8 million atoms, and the velocity ranged from 0 to 1000 m/s at a pressure of 5.1 GPa. Specifically, three velocities have been considered here and these are 25 , 300 and 500 m/s. Also the densities of Cu and Ag are appropriate for such a high pressure. The blocks first were equilibrated for a period equal to $10t_o$ at the appropriate pressure, where t_o is the characteristic time scale approximately an optical phonon period. The integration timestep is $0.01t_o$. When the system reached equilibrium at this pressure it was then subjected to initial conditions (forces and velocities) at $t_i = 10t_o$. The system ($t > t_i$) reached a steady state at $500t_o$. The tangential force is $F_t = N_r \cdot f_{tang}(t)$, where N_r is the number of atoms in the reservoir. Here Newton's equation of motion is integrated subject only to the reservoir's boundary conditions[1], the periodic boundary conditions (PBC) (only applied in the directions x and z) and the interatomic potentials. Rough surfaces were tested at speeds greater that 400 m/s. Additionally, the $f_{tang}(t)$ is a fluctuating force and the average value is given by the following formula:

$$f_{tang}(t) = \frac{1}{\Delta t} \int_{t-\Delta t}^{t} F_{tang}(\tau) \cdot d\tau \tag{1.3.1}$$

The value of F_{tang} introduces the same averages for upper and lower reservoirs. In this study results are similar to Hammerberg et al. [91] in terms of dislocations and stacking faults appearing in Cu and Ag, as well as the velocity weakening of frictional force at high velocities. Finally, in this study it has been observed that the velocity dependence of the frictional force is presented by the power law, $f_{tang} \approx v^{-\beta}$ where $\beta = 3/4$, shown in figure 1.2.

Another work by Hammerberg et al. [87] describes the physics of high-speed sliding friction by showing the importance of velocity dependence of the effective tangential force under various external loadings. Investigating the physics of sliding friction, parallel computers allow relative velocities of the order of 1000 m/s. This paper refers to a 2-D simulation interacting with Embedded-Atom-Method potentials and Lennard-Jones. The long time average over the microscopic localized stick-slip events is the average tangential force which enters Amonton's law defining the coefficient of friction. Amonton's law first stated

[1]Boundary conditions include the normal, tangential forces and the thermosetting conditions.

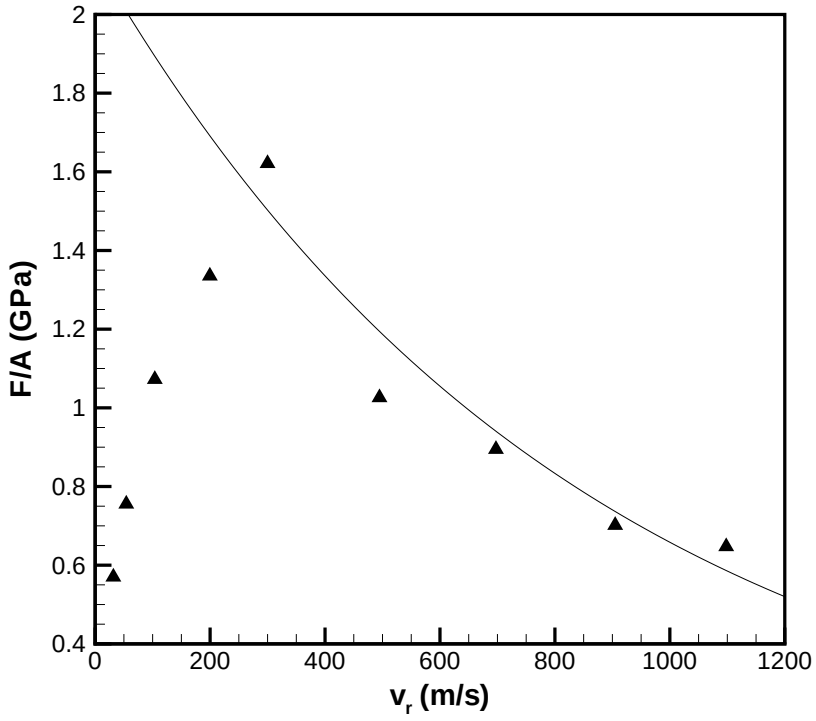

Figure 1.2: Velocity weakening of frictional force [90].

that frictional force is directly proportional to the normal force. Deviations exist when the normal force is applied in cases where adhesion between two surfaces contribute to an extra force.

The simulation discussed by Hammerberg et al. [87] is the homogeneous Cu-Cu interface. The outcome of this work summarizes the following:

1. At sliding velocities beyond the critical point $v_c \sim 0.1c_l$ (c_l is the longitudinal speed of sound) the coefficient of friction is a decreasing function of velocity.

2. The sliding is characterized by dynamic formation of microstructure from an initial defect-free crystalline interface. This microstructure is fine near the interface and coarsens away from it. The grains are elongated in the direction of the plastic flow.

3. In the fine scale region it is observed the mechanical material mixing. For interfaces with atomic scale roughness cold weld interface is observed when $v < v_c$. If the roughness is above about ten atomic spacings and microasperities are introduced the interface retains its sliding character.

The dislocation along the interface initially is associated with kink-antikink dynamics in nonlinear systems found by Hammerberg [87]. A description of this is the Frenkel-Kontorova model as described by Röder et al. [209]. The 2-D simulations for the same material interfaces are dominated at early times by dislocation dynamics, these large atomistic simulations discussed in this section provide very useful information regarding the physical mechanism of dissipation at interfaces sliding to each other. The microstructure of the material under strong shear forces, large plastic strains and materials mixing were observed.

A good example of 2-D simulation of amorphous systems is presented interacting via Lennard-Jones potentials by Yong [70, 69]. The coefficient of friction undergoes a transient behaviour prior to steady state response. The coefficient of friction at steady state is observed to decrease with an increase in sliding velocity. Material mixing is also observed in the interface. The mixed layer grew at a rate that scaled with the square root of time. The density is decreasing in the region nearby to the sliding interface. Fu et al. [69] conducted experimental investigation on the tribological properties of $Zr_{41.2}Ti_{13.8}Cu_{12.5}Ni_{10.0}Be_{22.5}$ bulk metallic glass alloy (BMG). Because of the amorphous structure some experimental techniques are not applicable to BMG. Therefore an alternative approach is to use molecular dynamics simulations. In some cases MD simulations provide useful information which is difficult to obtain experimentally. The issue discussed by Fu et al. [69] was to precisely form the interatomic potentials of the alloy system simply because potentials of specific atoms are not available. The computational effort to produce a large scale 3-D simulation would be enormous; therefore 2-D simulation has been conducted using Lennard-Jones potentials. Although, embedded atom method (EAM) potentials could be used, L-J potentials describes the major features of the metallic interactions neglecting many-body interactions.

Another two-dimensional MD simulation was conducted using embedded atom methods potentials at relative sliding velocity of $0.01 < v_r/c_t < 0.3$ for Cu also by Hammerberg et al. [88]. The phenomena observed associated with high velocity sliding include dislocations parallel and normal to sliding frictions. Nucleation of the microstructure, large plastic deformation, diffusive coarsening and materials mixing has been observed. The specimen was treated in two dimensions which were large enough to accommodate dislocation deformation and dynamics. Also micro-structural generations which are small enough can be achieved on reasonable simulation timescales. The relative velocity must be significantly large, necessary for creating a dynamic state. Molecular dynamics for sliding interfaces have minimum relative velocity below which computational time become very

long. Hammerberg et al. [88] used velocity of $0.03c_t$. For Cu this velocity is of order $100m/s\,(=0.03c_t)$. Due to the fact that Cu is a ductile material, the interfaces that form are described on the atomic scale by main-body density dependent interaction potentials. This behaviour has a result that the tangential force decreases at high velocities while the microstucture coarsens away from the interface.

The simulation set up of Hammerberg et al. [88] is similar to Hammerberg et al. [91]; the c_l and c_t (longitudinal and transverse speed of sound) are 5.6 and 3.0 respectively. The reservoir regions consist of 20 atomic layers and the whole computational volume consists of 65,256 atoms. The interfaces discussed here are smooth and a continuous wave perturbation with single wavelength is imposed. The coefficient of friction is given by

$$\mu = \frac{F_{tang}}{F_n} \Rightarrow \mu = \frac{\langle g\,(t)\rangle}{g_{normal}} \Rightarrow \mu = \frac{\left(-\sum_{i\in Res}\sum_j f_{ij}^{tang} / \sum_{i\in Res}\cdot m_i\right)}{g_{normal}} \tag{1.3.2}$$

where f_{ij}^{tang} is the force acting on reservoir atom. The initial Cu density is $\rho = 1.27$ which corresponds to a pressure of 30GPa. Above the critical velocity v_c of order $v_r/c_t = 1/10$ there is a decrease in coefficient of friction. For $v_r < u_c$ the interface has welded together and the two pieces have formed a single work-hardened object where sliding occurs against the upper and lower reservoirs. The behaviour of welded interfaces of Cu/Cu tribopair have also been verified by simulations that have been obtained initially. For $v_r > u_c$ slip occurs at the interface. The $v_r = 0.49$ at time $500t_o$. The interface has become dynamically unstable due to the formation of fine grained polycrystalline structure near the interface that coarsen with distance from the interface as a function of time. Plastic deformation is occurring at the interface. The microscopic granularity produced in sliding the original interface results in mechanical mixing of the material. Finally the interface, which initially has a uniform velocity, undergoes a series of stick-slip events and finally results in a wave structure in the transverse velocity field.

Another work by Hammerberg et al. [92] describes the sliding friction at compressed Ta/Al interfaces; the pressure applied is of order of 15GPa showing similar results in terms of the velocity weakening of the frictional force. In this paper an investigation of the minimum energy interface structures was done by annealing Al/Ta blocks containing up to 200,000 atoms. This large scale non-equilibrium molecular dynamics was carried out to investigate the microstructure progression and dissipation mechanism for dry sliding friction along two interfacial orientations of Al/Ta which are Al(100)/Ta(100) and Al(110)/Ta(110) configurations. The simulations were performed in scalable parallel short-scale MD code

(SPaSM) [251, 12].The simulation methodology here is the same as used in various papers described above. It consists of two metallic blocks of equal size. The interface located at the position y=0 and periodic boundary conditions used in the x and z directions. Finally the dimensions of the computational box are (x,y,z) =(142x523x132) Å containing 600,000 atoms. The sliding was between Al (FCC) and Ta (BCC) for Al (111)/Ta (110) with sliding direction at the $\left[0\bar{1}0\right]_{FCC} / [001]_{BCC}$ orientation. The frictional force versus relative velocity for the two interfaces indicates a linear region at low velocities and highly localized plastic deformation region at high velocities, where the frictional force decreases with velocities $v_r^{-3/4}$, as in Figure 1.2. When high velocities occur the structure exhibits strong disorder in the tangential direction and density correlations in the normal direction are analogous to a restricted fluid of amorphous solid. Some theoretical arguments for the velocity dependence have been also discussed by Hammerberg et al. [86].

1.4 Aim and Objectives

Tribology is a multidisciplinary area that requires background knowledge in many topics such as fluid mechanics, elasticity, plasticity, materials science, heat transfer and dynamics. The tribological development of formulae and accurate experimental methods for engineering design is still insufficient. This is due to the fact that the material properties measured using a test apparatus are system dependent, meaning that they are valid only for a particular device. Problems of friction have been studied for a long time through classical laws such as Coulomb's and Amonton's laws. The understanding of the complex response at contact is affected by factors beyond those considered in classical laws [49, 174]. It has been observed that atomic excitation modes such as vibrations, bending and/or rotation, electron-hole excitation and shear waves are present during friction. Consequently, the theories that exist in continuum mechanics are not always applicable to analyse a system's response to high loading conditions. The material near the interface experiences microcracking within the microstructure and this subsequently leads to fractures at micro scale. For that reason, interfaces need to be treated at atomic level via computational materials science methods.

With the advances of molecular dynamics methods scientists have discovered for the first time the processes involved at the sliding interface. Yet still the major aspect of dynamic friction is not completely understood, namely energy dissipation. The dissipation

mechanism is rather complex involving non-equilibrium phonon, electron-hole formation, structural transformation, bond breaking, and electron emission. This energy is dissipating by both electronic and phononic processes. The phononic mechanism contributes to friction since vibrations are produced when the interfacial atoms are imposed to mechanical energy. As shown by Tomlinson [239] the mechanical energy is converted to sound energy and then into heat, which is primarily carried by electrons within the metallic lattice. Since MD are simulating the thermal vibration of atoms, the physics are not fully captured via this method, hence the energy dissipation is still not well understood. This PhD work aims to give an explanation and ultimately the solution of this issue.

Additionally, the aim of this work is to develop a frictional model in which accurate constitutive models for shear stresses can be obtained. Considering the aim given above the objectives of this PhD are given in more detail:

1. Molecular Dynamics Methods

   a) Implementing into the MD code tools for pressure and constant velocity boundary conditions.

   b) Validating the interatomic potentials for Cu and Ag metals by measuring thermodynamic and mechanical properties.

   c) Simulating the dynamic friction of perfect crystal Cu/Ag tribopair to analyse: The structural transformation, velocity weakening of the frictional force, temperature variation across the interface and yield point variation under certain conditions.

   d) Simulating and compare results of nanocrystalline Cu/Ag tribopair. Examine the grain boundary formation and differences with the properties obtained in (c).

   e) Discuss the diffusion bonding of Cu/Ag interfaces at pressure of 5.1 GPa.

2. Continuum Methods

   f) Dynamic friction simulation of Cu/Ag tribopairs using 1-D hydrocode.

   g) Coupling the MD with two temperature model (TTM) diffusion equation to resolve issues of energy dissipation.

There is a considerable amount of research in dynamic dry friction and thin film lubrication according to Robbins and Muser [207]; however, there are many unanswered questions since the physics that control the forces acting across a material's interface under high compression is not yet clearly understood. Thus, by fulfilling the above objectives this PhD programme aims to provide insight and understanding into physics of dynamics friction under dry sliding conditions.

1.5 Publications

During the writing up process of the thesis the following papers have been submitted:

- N. Epiphaniou, M. Kalweit, D. Drikakis, G. Ball and N. Park, *Molecular Dynamics Simulations of Dynamic Friction and Mixing at Rapidly Moving Material Interfaces*, Journal of Computational and Theoretical Nanoscience, 2008 (published).
- N. Epiphaniou, M. Kalweit and D. Drikakis, *Mechanical Behaviour of Nanocrystalline Metals under High Speed Sliding Friction and Compression Forces using Atomistic Techniques*, 2008 (in preparation).

Additionally, past conference presentations have been presented:

- N. Epiphaniou, M. Kalweit and D. Drikakis, *"Molecular Dynamics Simulations of Dynamic Friction and Mixing at Rapidly Moving Material Interfaces"*, Conference/-workshop in Numerical Methods for Multi-material Fluid Flows, Czech Technical University in Prague, September 10-14, 2007.
- N. Epiphaniou, M. Kalweit and D. Drikakis, *"Mechanical Behaviour of Nanocrystalline Metals under High Speed Sliding Friction and Compression Forces using Atomistic Techniques"*, World Tribology Congress, Kyoto, Japan, September 6-11, 2009.

1.6 Outline of this study

The thesis is organised in seven chapters and this section provides an overview along with a brief description of the content of the individual chapters. Chapter 1 and 7 are the introduction and conclusion to the thesis. The second chapter, ”Molecular dynamics”, describes the numerical methods and models at the atomistic level used within this work. An overview of the MD methods and the equilibrium and non-equilibrium approaches are presented. Chapter 3 focuses on the materials behaviour of crystalline solids and is divided into two parts, covering thermodynamic and mechanical properties. A description of the validation cases is given along with tests to ensure that the molecular dynamics code is giving valid results. Chapter 4 deals with the simulation tools that have been developed and implemented on the molecular dynamics code. In particular, implementation of pressure and sliding desired conditions. Chapter 5 presents the results of the dynamic friction simulations of metallic interfaces. Finally, chapter 6 gives an insight on the yield point of perfect and nanocrystalline materials under high strain rates and pressure conditions.

CHAPTER 2

Molecular dynamics

"I've encountered a lot of people who sound like critics but very few who have substantive criticism. There is a lot of skepticism, but it seems to be more matter of inertia than it is of people having some real reason for thinking something else."

Eric Drexler

This chapter provides an overview of the Molecular Dynamics (MD) techniques employed as part of this research. Over the past few years computational techniques have offered an excellent way of exploring the structures and properties of engineering materials at an atomic level [31, 101, 80, 1, 254, 202]. The scope of material modelling is to bridge the mathematical theory with experimental observation on various complex systems and conditions. Various computer simulation studies have provided reliable models that can help the interpretation of data taken from the experiments. Additionally, they can offer an understanding of the system that is simulated and make possible the investigation of material properties in cases where experiment cannot be conducted. A good example of the latter is found in the field of high shock compression and dynamic friction.

2.1 Modelling at different length-scales

The current trends in computational materials science have been investigated by scientists in the past, and observations regarding the force that is linking models at various lengths

and timescales are considered in [76, 189, 158]. When dealing with materials simulations there are four different characteristic length scales. These are the atomic scale (10^{-10} m) in which electrons dominate and the quantum state determines the interaction amongst other atoms. At the nanoscale (10^{-9} m) atoms are the key players and their behaviour is described by classical interatomic potentials, the effects of bonding between atoms are arbitrated by electrons so quantum mechanical theories govern the material's response. According to these theories, Schrodinger and/or relativistic Dirac equations are not sufficient to fully give a quantum mechanical solution. The Born-Oppenheimer approximation, based on the decoupling of the wave-function for the nucleus and electrons, significant reduces the problem. Also the introduction of the DFT represents an advance toward the calculation of electronics structure of materials as discussed by Finnis [60].

According to DFT the quantum mechanical state determines the electronic density function $\rho(r)$ of a single atom rather than the atomic wave-functions. If the electronic density function is known, the properties of the system can be easily defined. Density functional methods are capable of high precision first principles calculations of properties such as the ground state, lattice parameter, cohesive, surface, stacking-fault energies. At the nanoscale simulations can be conducted through molecular dynamics. This method enables the simulation of atoms ranging from several thousand to billions. Additionally, the electronic degrees of freedom are condensed leading to a reduced problem to the classical equations of the motion for the atoms. The interatomic potential provides the quantum mechanical nature of the system. Typical length scales of the MD method are of the order of 10^{-7} to 10^{-10}m and the timescale is in pico-seconds, as shown in Figure 2.1.

The next stage of coarse graining is the mesoscopic scale, which has a range of 10^{-4}m and in this case lattice defects like dislocation and grain boundaries play an important role. The interactions between them are derived from atomic theories so that molecular dynamics are also capable of investigating these defects. Finally the last scale is the macroscopic 10^{-2}m where constitutive equations and laws can describe various phenomena and effects since the system is considered as a continuous medium. Finite element method (FEM) can be used to describe the elastic and plastic medium since it captures the response caused by the difference in material properties and microstructural elements. As can be seen by the Figure 2.1 the first region is quantum mechanics. These kind of calculations are called quantum mechanical (*abinitio*) predicting interactions between atoms or molecules and model chemical reactions on a atomic-microscopic scale revealing properties such as distribution of atoms in space, chemical bonding, and energy of defects. Electronic structures

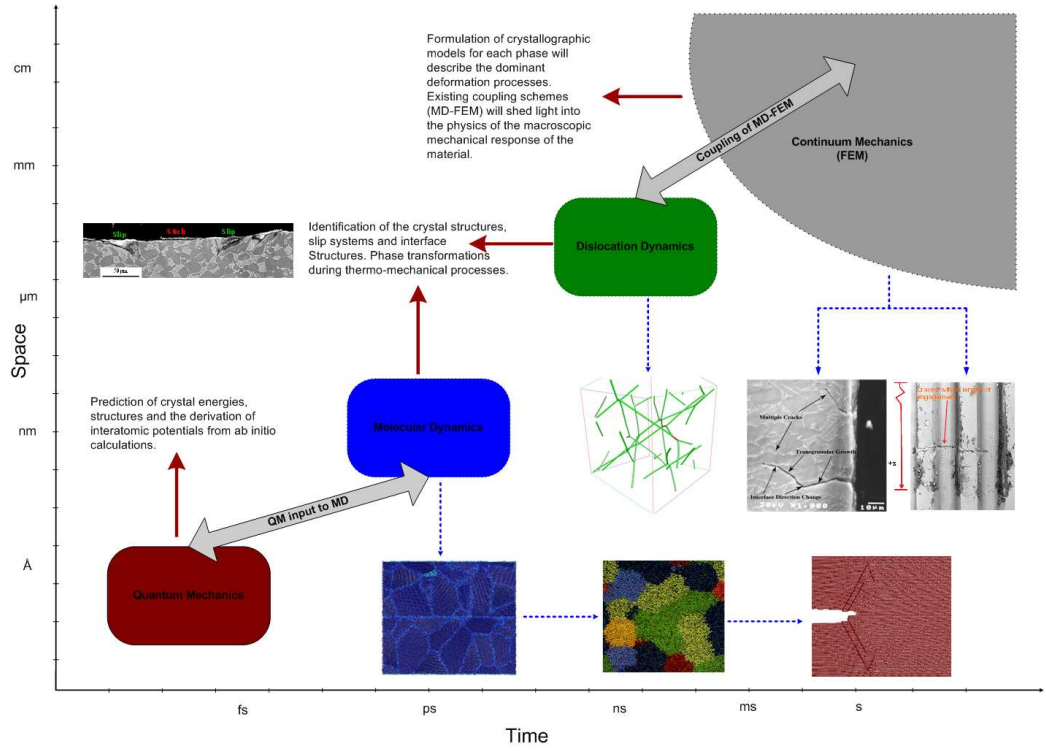

Figure 2.1: Modelling and different scales and limitations of various computational techniques.

are considered vital because they include the band structure and density of electronic states as shown by Dronskowski [54] and Hafner [80]. Thus, in order to understand and improve the properties of mesoscopic materials, it is crucial to comprehend the atomistic aspects of these materials. Methods based on statistical and continuum mechanics can use the above information in order to investigate the mesoscopic and macroscopic behaviour of the materials.

One of the strongest quantum mechanical methods to study the ground state properties of solid states with correlated atoms and electrons on atomic scale is the DFT. DFT is based on the theorem by Hafner [80], who showed that the total energy of a many-electron system in an external potential is a unique function of the electron density. This function has its minimum at the ground-state density. The main assumption in the Kohn-Sham (KS) method is that for each interacting electron system with external potential $u_0(r)$, a local potential $u_{s,0}(r)$ (Kohn-Sham potential) exists such that the density $\rho(r)$ of the non-interacting system equals the density $\rho_0(r)$ of the interacting system. The interaction between the electrons is described by an electrostatic term and the exchange correlation energy $E_{xc}[\rho(r)]$. The latter can be obtained using the local density approximation (LDA) or the generalized-gradient approximation (GGA). GGA is more accurate because it accounts for the depen-

dency of the exchange-correlation function on the gradient of the electron density.

Another method is the tight binding approach [137, 31], which integrates electronic structure calculation into molecular dynamics through an empirical tight-binding Hamiltonian. This bridges the gap between ab initio molecular dynamics and simulations using empirical classical potentials. Also, tight binding has been used for producing interatomic potentials for transition metals. This method will not, however, work for uranium (f-orbital) because it only includes spd orbitals. These techniques are highly efficient and accurate, however, they restrict the simulation domain to few atoms, and the computing time required for the calculations is high.

2.2 The methodology of molecular dynamics

Molecular dynamics were first introduced in thermodynamics and physical chemistry to calculate the collective or average thermochemical properties of various physical systems including gases, liquids, and solids as stated by various authors [2, 207, 203]. The MD method is based on the classical molecular model that corresponds to the physical view of the late nineteenth century [200, 2, 82, 53]. Rieth [203] showed that atoms in this case are considered to be point masses whose interactions can be approximated by analytical potential functions, so called interatomic potentials. The intramolecular interactions, by which a group of atoms is combined to a molecule, can be accurately modelled. Initially it is determined between which atoms chemical bonds exist and usually bonds cannot break or fuse during the simulation. The different types of bond moving, i.e. stretch, bend, torsion, etc., are governed by potential functions that are adapted to each combination of atoms by different parameters of the function. In many cases, small molecules like water can be approximated to be rigid so that no bond motion occurs. Likewise the intermolecular interactions, such as electrostatic or London dispersion interactions are modelled by a potential function. Therefore, having the classical molecular model as a starting point, MD simulations turned up recently as an approach to study interfacial phenomena.

Over the last few years several MD algorithms have been developed and the analysis can give an insight on the physical phenomena such as dynamic friction, via simulation of instantaneous atomic behaviour. In MD the system is modeled at the atomic scale and simulation of motion of atoms is followed by integration of Newton's Second Law. In general, the electrostatic forces trigger the interaction between atoms; this gives the conception of

metallic, covalent, and Van Der Waals bonds and forces. The motion of the ions, which are the atomic nuclei together with their core electrons, is generally slower than the motion of the electrons; this is because the nucleus is much heavier (typically 10^4 orders of magnitude) than the electron. The electron system has relaxed to equilibrium at each point of motion of the ions. This is an assumption known as the Born Oppenheimer approximation which is the basis for removing the electrons from the model and creating effective interatomic potential energies as given functions of the relative positions of the atoms.

Simulations can be performed using a few hours of central processing unit (CPU) time depending on the size and timescale of the system on desktop workstations. Modern parallel computers allow investigators to use MD programs for simulations involving up to several millions or billions of atoms [226, 75, 247]. This method has some advantages compared to alternative approaches, such as quantum mechanical or direct simulation Monte Carlo methods (DSMCM), when investigating phenomena such as dislocations, stick-slip etc. This is because quantum mechanical methods (ab initio) are restricted to a few atoms and DSMCM can not capture many molecular phenomena because of their statistical approach.

2.2.1 Equation of motion

The main objective of molecular dynamics is to simulate the thermal vibration of atoms in a classical way by solving Newton's equation of motion, $f_i = m_i \boldsymbol{a}_i$ [2, 53, 200, 68]. The force on each particle is given as a function of the interatomic potential energy $\mathcal{V}$, which depends on the positions of the atoms, by $f_i = -\nabla_{r_i}\mathcal{V}$, hence for each atom in the system the following equation describes the dynamics of the entire system:

$$m_i \frac{\mathrm{d}^2 r_i}{\mathrm{d}t^2} = -\nabla_{r_i}\mathcal{V} \tag{2.2.1}$$

where m_i and $\boldsymbol{r}_i$ are the mass and position of atom i and t is the time. The system's partial differential equations have no exact solution for a system with N-body problem (if N¿2), thus, integration of the equation 2.2.1 gives the changes of the atomic momenta and positions in time. The solution is achieved by discretizing the equations in time. For atomistic simulations there is no need for spatial discretization because this is given by the atomic distances, which is a form of spatial discretization. In MD simulations each atom/particle cannot be divided further. The accuracy of the simulation depends strongly on the poten-

tial function and the simulation domain size of the timescale during the study. The next section describes a brief overview of interatomic potentials available, methods, techniques, and applications. The information provided in this section is part of the feasibility study of the uranium-niobium alloy that was conducted to investigate the resource requirements for modelling the particular alloy.

2.2.2 Interatomic potentials for metals

There is a variety of potentials widely used in MD simulations: Morse developed by Morse [188], Lennard-Jones [2, 199], Buckingham developed by Ogorodnikov and Rogovoi [190], Schommers developed by Schommers [218], Finnis-Sinclair [61, 227], Tersoff developed by Tersoff [235], Stillinger-Webber developed by Stillinger and Weber [224] and finally potentials using EAM. The most accurate potential for describing a metallic structure is the EAM as described by Daw et al. [45]. EAM has been extensively used in MD studies and provides an excellent tool for modelling metallic bonding of closed-shell metals, which is one of the reasons used for Cu and Ag in this thesis. Alloys have also been studied with success by Foiles et al. [66].

Most EAM potentials produce forces that are almost radially symmetric on the atoms. This is satisfactory when modelling materials with closed shell configuration like most of the transition and noble metals. These types have a spherically symmetric bonding. The situation becomes more complicated for elements with partially filled d-orbital (tantalum) and/or f-orbital (uranium and most actinides). Metals with this kind of atomic configuration generate angular forces on the atoms, which are important for the structural and mechanical properties of metals.

Finnis and Sinclair [61] developed the Finnis-Sinclair potential, similar in principle to the EAM potentials, that do not take into account the s, p, d, and f symmetries, which are required for calculating accurately the properties of actinides and some transition metals with semi-filled d bands. As an alternative the modified embedded atom method potential (MEAM), that include the s, p, d, and f symmetries shown by Baskes [9] and the model generalized pseudopotential theory (MGPT) potentials could be used. The latter are derived from the first-principles generalized pseudopotentials theory (GPT) using density functional theory as shown by Harison [95].

The existing molecular dynamics code is distributed by [197] with the interatomic potential for the metal of interest and models an ensemble of particles in a liquid, solid, or gaseous state. Interatomic potentials such as MEAM based on the combination of experimental data and data derived from first-principles (ab initio) can also be constructed. Interatomic potentials describe the atomic interactions by several analytical functions. To reduce the number of parameters produced by EAM equations several assumptions have to be made within this analytical framework. These parameters are usually determined by fitting experimental data at 0K with most data taken for perfect crystals; such as lattice constants, cohesive energy and elastic constants.

When constructing an empirical potential first principles force data are usually included along with experimental data. To obtain interatomic potentials the Force Matching method developed by Ercolessi and Adams [56], could be used to derive realistic empirical potentials using the ab initio such as VASP (Vienna Ab Initio Package), this tool uses an accurate force calculation. This method reproduces the first principles forces and the experimental data with those calculated by empirical potentials. Generally, potentials derived by force matching methods successfully predict the material properties. One possibility for obtaining interatomic potential files in appropriate format to be used by molecular dynamics code is to use a fitting program in conjunction with the MEAM potential.

Baskes [10] used MEAM potentials to reproduce the extreme and anomalous behaviour of Plutonium (Pu), which undergoes six allotropic transformations. These anomalous properties are due to the rapid spatial variation of f-electron density. A similar behaviour is exhibited by uranium as shown by simulations obtained by Streitz et al. [226], who used the BlueGene/L high-performance parallel facility at Lawrence Livermore National Laboratory. The interatomic potentials used by Streitz et al. [226] are MGPT potentials and are derived from the first-principles GPT using density functional theory. Additionally, the ab initio electronics structure methods including both full-Potential linear muffin-Tin Orbital (FP-LMTO) and Pseudopotential (PP) techniques were employed. The MGPT potential bridges ab initio electronic calculations and large-scale static and dynamic atomistic simulations, which proved to be an extremely accurate tool for calculating properties occurring during rapid solidification at the short time scale of 10^{-12} to 10^{-6} s.

In Streitz et al. [226] work the simulations for the transition metal tantalum and actinide uranium were performed using atomic systems comprising of 64,000 to 525,828,000 atoms. They used the FP-LMTO method for treating broad nearly-free-electron sp bands, narrower and more tightly bound d bands, as well as very tightly bound outer core states all on the

same footing. The FP-LMTO method can be used to study the basic structural, vibrational, elastic, and ideal-strength properties in Ta to 1000 GPa pressure. The ab initio PP approach allows greater flexibility in treating relaxed defect structures. Both the FP-LMTO and PP methods was employed to study vacancy and self-interstitial formation and migration in Ta, as well as high-symmetry features of generalized stacking-fault (γ) energy surfaces. These results have been used to develop and validate the Ta MGPT potentials.

An alternative to FP-LMTO and PP methods is the full potential of linearized augmented plane waves (FPLAPW) [20, 260]. Linearised augmented plane waves (LAPWs) is an effective basis for the solution of the Kohn-Sham equation where the major task is in the local spin density approximation (LSDA) to density functional theory. This method accurately calculates the electronic structure and magnetic properties of polyatomic systems from first principles. One successful program available in the scientific community is WIEN2k developed by Blaha et al. [20]. Electronic structure calculations can also provide useful information regarding the energetic properties of chemical systems, including molecular structures and spectroscopic features.

2.2.3 Molecular dynamics integrator

Generally, there is no analytical solution of the equation of motion and this generates the requirement of a numerical time integrator. The MD code used for the current investigation is LAMMPS (Large-scale Atomic/Molecular Massively Parallel Simulator), which has been developed at Sandia Laboratories. LAMMPS proved to be superior compared to any other MD code because of its capabilities and ease of modifying or extending with new functionalities. Plimpton [197] showed that for time integration, LAMMPS employs the velocity/position Verlet scheme. This integrator is the engine of the MD code which generates the motion on the particles and calculates their trajectories. So knowing the velocities, position and other dynamic properties at a certain time t, the algorithm generates the velocities, positions at later times i.e. $t + \Delta t$; the timestep Δt of the integrator is usually kept constant. The time step of a molecular dynamics simulation must be adapted to the fastest variation of potential energy, which is normally caused by bond stretching. The frequencies of bond stretching vibration are in the 10^{-10} fs range, in general the timestep is the $1/10$ of the highest-frequency vibration. There are three main criteria the molecular dynamics integrator should fulfil and these are summarised here:

Efficiency: Key for efficient algorithm lies in a low ratio of force calculations per simulation time. This is achievable if the number of force calculations per time step are minimised and to enable at the same time the application of a large time step Δt.

Stability: The algorithm has to be stable so that energy is conserved, therefore small perturbations do not cause instabilities. Several methods exist and stability in each case is a function of several parameters such as step size and steepness of the potential gradients.

Accuracy: The algorithm has to create trajectories that resemble realistic ones; this can be assessed on models where analytical solution is easily obtainable.

MD simulations in general are computationally very demanding, taking into account that realistic systems involve non-uniform geometries and periodic boundary conditions. Simulations can be performed using a few hours of CPU time depending on the size and timescale of the system on desktop workstations. Modern parallel computers have allowed investigators to use MD programs for simulations involving many million of atoms as shown in as described by Streitz et al. [226].

2.2.4 The velocity Verlet scheme

Amongst the most widely used algorithms implemented in molecular dynamics codes is the velocity Verlet algorithm which is invoked for time integration and is based on the Verlet algorithm scheme shown by Verlet [249]. This variant of the pure Verlet method uses positions $r_i(t)$, velocities $v_i(t)$ and accelerations $\boldsymbol{a}_i(t)$ that are defined at the same time, minimising the round-off-error according to Swope and coworkers [228]. The scheme has the form of the following formula:

$$r(t+\delta t) = r(t) + \delta t \cdot v(t) + \frac{1}{2} \cdot \delta t^2 \cdot \boldsymbol{a}(t) \tag{2.2.2}$$

$$v(t+\delta t) = v(t) + \frac{1}{2} \cdot \delta t \, |\boldsymbol{a}(t) + \boldsymbol{a}(t+\delta t)| \tag{2.2.3}$$

Efficient implementation of the scheme is obtained through two stages implemented in the following steps:

1. First the velocity is advanced by a half step using the equation:

$$v(t + \frac{1}{2}\delta t) = v(t) + \frac{1}{2}\delta t \cdot \boldsymbol{a}(t) \tag{2.2.4}$$

2. Then the position is advanced to $r(t + \delta t)$ using equation 2.2.2 and

3. Calculating the acceleration $\boldsymbol{a}(t + \delta t)$.

4. Completion of the velocity calculation is obtained by another half step:

$$v(t + \delta t) = v(t + \frac{1}{2}\delta t) + \frac{1}{2}\delta t \cdot \boldsymbol{a}(t + \delta t) \tag{2.2.5}$$

5. Finally the kinetic energy is calculated based on the $v(t + \delta t)$.

The velocity Verlet algorithm therefore propagates velocities in two stages and splits the calculation process into the applied acceleration term.

2.2.5 Periodic boundary conditions

The boundary conditions in MD simulations aim to mimic the material response of the surrounding volume and allow incorporation of the dynamic response of non-equilibrium processes. A good example of this is could be energy dissipating boundary conditions that reproduce the heat conduction of solid materials. The attempt to achieve this is highlighted in later chapters, and this section aims to emphasise the build in capabilities of LAMMPS.

In periodic boundary conditions (BC), the simulation box is replicated throughout space to form an infinite lattice, see Figure 2.2. Usually, the computational demands are high if simulating a large piece of metal or crystal is required. Therefore boundary conditions are often used to help predict the properties of the material in bulk, as well as to eliminate surface effects from the computation.

In particular the role of BC is to prevent boundary reflection and maintain the external loading, therefore reducing the effect of finite system size. One approach would be to fix the atoms at the boundary to certain positions. It has been proved through several atomistic simulations that the boundary reflection resulting from this BC is considerable, and the results deteriorate severely. A fairly recent review on various boundary conditions

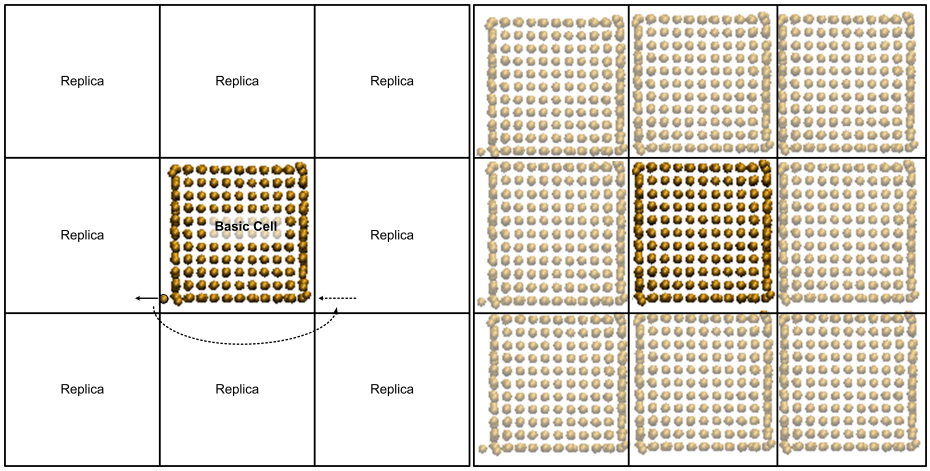

Figure 2.2: Left: Periodic boundary condition in 2-D, simulation box in the middle (basic cell). Atoms can leave the basic cell and enter it at any time from the opposite site. Right: images of replica boxes to illustrate periodic boundary conditions in x and y directions.

for molecular dynamics simulations is given by Li and Weinan [154] for crystalline solids at low temperature. In general, BCs of solids are considered with the objective of eliminating the reflection of phonons. This work presents a variational formalism in order to construct boundary conditions that minimize this total phonon reflection.

From Figure 2.2 it can be seen that when a molecule moves in the central box, its periodic image, or the so called ghost atom, moves in all the other boxes having the same orientation. Thus, as the particular molecule leaves the central box, one of its ghost atoms will enter the central box through the opposite face. The central box does not contain any walls and the system has no surface.

2.2.6 Molecular dynamics ensembles

Macroscopic properties such as temperature T, volume V, pressure P, energy E, number of particles N, and chemical potential μ , are used to describe a large system of particles. This system and all its thermodynamic properties is called an ensemble. There are several ensembles that can be used, but most of the simulations used in this work are NVE; this is called micro-canonical and prescribes that constant number of particles, volume and energy are satisfied. Similarly there are other ensembles such as the Canonical (NVT), Grand Canonical (μVT) and finally the Isothermal-isobaric (NPT).

Most of the MD simulations of sliding friction, including this study, have been carried

out in the microcanonical ensemble along with the appropriate integration algorithm described in Section 2.2.4. The advantage of these schemes is that they give good long-term stability of the total energy even with quite large time steps. The NVE strictly specifies that the energy is conserved meaning that no heat can flow through the walls of the domain size. This study deals with the dynamic behaviour of metals, therefore non-equilibrium conditions, thus a mechanism is required to remove energy through heat transfer, which will be discussed in later chapters.

2.2.7 Equilibrium and non-equilibrium molecular dynamics

In order to investigate the microscopic properties of a system, it is necessary to bring the system to equilibrium to ensure more realistic results. By using the term equilibrium it is meant that the thermodynamic properties of the system, such as temperature, volume and pressure will not change when the system is left alone. In all the simulations conducted equilibrium was an important step before the application of any force. In addition, when a system is at equilibrium the potential energy is at a minimum for a given set of thermodynamic properties.

Molecular dynamics simulations resemble real experiments in which the same approaches are used. Initially there is a sample preparation in which careful selection of the model containing N number of particles is considered following the solution using Newton's equation of motion for the system so that certain thermodynamic properties such as internal energy, pressure and kinetic energy do not change over time. This is a way of bringing a system to its equilibrium state.

In NEMD improvement on the efficiency of the transport coefficients is calculated via a linear response theory and time correlation functions. This however induces a significant amount of statistical error. In NEMD the system's response is considered to be highly non-linear, thus perturbations are examined in this regime. The calculated correlation functions during a molecular dynamic step represent the actual fluctuations occurring in the system properties. For long simulation times the signal-to-noise ratio is undesirable due to possible contribution to the transport coefficients. In non-equilibrium states much larger fluctuations are possible, which are induced artificially, thus the signal-to-noise ratio of the response could be greatly improved.

The measurements obtained from NEMD simulations are in principle the same as those obtained in simple equilibrium averages for monitoring the pressure and temperature over time. The idea behind the molecular dynamic method is to be used as a tool of validating experimental results or even trust it in cases where experiment cannot easily be obtained. Thus, the procedure used in molecular dynamics simulations corresponds closely to the experimental set-up. A good example is the calculation of the thermal conductivity, analysed in chapter 3.2, in which a flow of momentum or energy flux is created for the desired material. The following section aims to give an introduction of the procedure and initialisation of a typical molecular dynamics simulation.

2.2.8 Initialisation of molecular dynamics

Prior to any molecular dynamics simulation, atoms or molecules are generated, meaning that they are each allocated memory in which positions and velocities are assigned. Molecules and complex structures require the introduction of bonds between the individual atoms. The system needs to be in equilibrium state prior to any dynamic conditions, therefore the initial configuration must not be influenced by the outcome of the simulation. A typical LAMMPS' input script contains four crucial parts for setting up a realistic simulation to study certain phenomena.

The first stage is the initialization in which various parameters such as the units, the boundary conditions and the atomic style need to be defined given the appropriate force field parameters. The second stage consists of the atom definition in which the simulation domain size containing the atoms needs to be defined. This is obtained via a separate file that could be invoked by LAMMPS, which includes the molecular topology or using the already existing commands that generate the simulation domain and apply the appropriate crystallographic orientation.

The third stage is then to set the appropriate force field coefficients, simulation parameters and output options once the molecular topology is defined. At this stage initial velocities are also assigned to atoms and special commands are applied for a variety of boundary conditions. Various methods of time integration as well as diagnostic tools to measure simulation domain data and materials response are also implemented. Temperature alteration via velocity rescaling, adjusts the system to the required average temperature. In thermal

equilibrium velocities are given in equation 2.2.6:

$$\left\langle v_i^2 \right\rangle = \frac{k_B T}{m_i} \tag{2.2.6}$$

where $\left\langle v_i^2 \right\rangle$ is the atomic velocity averages and m_i is the atom mass. Equation 2.2.6 is used to define the the instantaneous temperature at time t, $T(t)$ given by:

$$k_B T(t) \equiv \sum_{i=0}^{N} \frac{m_i v_i^2}{N_f} \tag{2.2.7}$$

The instantaneous temperature $T(t)$ needs to be adjusted so that it matches the temperature T required for the system of interest, this is done by scaling the velocities by a factor of $(T/T(t))^{1/2}$. The final stage is the simulation run by specifying the timestep needed for the study. Molecular dynamics can be used for a variety of equilibrium phenomena in which statistical mechanics are capable to cope with limitations as shown by [200]. Shifting from and equilibrium state to study phenomena of non-equilibrium nature like dynamic friction allows MD to take the role of an experimental tool.

CHAPTER 3

Face centered cubic crystals and their properties

"Employ your time in improving yourself by other men's writings, so that you shall gain easily what others have labored hard for."

Socrates

This chapter presents the thermodynamic and the mechanical properties of nanocrystalline FCC materials. The first part of this chapter discusses the molecular dynamics procedures to obtain the thermodynamic properties and validate the interatomic potentials used throughout this work against experimental studies. Amongst those are the melting point T_m, the heat capacity C_p, the thermal expansion α_e, and the thermal conductivity k of both Ag and Cu metals. Considering the importance of the structural integrity in many mechanical components, section two is concerned with processes to calculate intrinsic mechanical properties direct from the atomistic behaviour. Amongst those are the modulus of elasticity E, shear modulus G and the yield stress σ_y of Cu metal and Cu nanowire.

3.1 Simulations of melting point

This section presents a review of several methods available for the calculation of thermodynamic properties for copper (Cu) and silver (Ag) metals. These metals were used for frictional studies under high speeds and compression as discussed in chapter 5, therefore, the validation of the interatomic potentials was necessary. Calculation of the thermodynamic melting point is not trivial for bulk metal, as has been shown by various study groups

[167, 176, 187, 185, 125, 127], in which several methods have been published. Generally, evaluating the melting point is not a straightforward approach because it requires the calculation of Gibbs free energies, which is a multi-stage process that needs several different molecular dynamics simulations. By definition the melting point is where solid and liquid phases coexist, and there are several ways of doing this via molecular dynamics combined with the thermodynamics integration method as described by Frenkel and Smit [68]. Therefore, this section briefly reviews the available methods for computing the melting points, as well as the results achieved in this study at standard and non-standard atmospheric conditions.

3.1.1 Thermodynamic integration

Thermodynamic integration is a widely known method for computing the melting point of solid materials by evaluating the Gibbs free energy of solid and liquid phases as obtained by Frenkel and Smit [68]. By definition, at constant pressure, usually atmospheric conditions, where $P = 0$ bar, the thermodynamic melting point T_m is at the point at which the free energy of the solid must be equal to that of the liquid, $G_s(T) = G_l(T)$. Additionally, by definition the Gibbs free energy at certain conditions of temperature and pressure (usually at P = 0 bar) is related to internal energy U and the entropy S by $G_T = U_T - T \cdot S_T$. Using molecular dynamics the energy of the system and other thermodynamics properties can be determined. However, the entropy of the system cannot be evaluated directly in terms of ensemble average. One approach is to obtain the Gibbs free energies G_T, at temperature T, of a system (I) via thermodynamic integration between the system (I) and a convenient reference system (II) with a known value of G_{T_o} at temperature T_o. The thermodynamic integration will be obtained using the fundamental equation known as Gibbs-Helmholtz below:

$$\frac{G_T}{T} = \frac{G_{T_o}}{T_o} - \int_{T_o}^{T} \frac{E(\tau) + P \cdot V(\tau)}{\tau^2} d\tau \quad \overset{P=0}{\Longrightarrow} \quad \frac{g(T)}{T} = \frac{g(T_o)}{T_o} - \int_{T_o}^{T} \frac{e(\tau)}{\tau^2} d\tau \qquad (3.1.1)$$

where $E(\tau)$ is the internal energy of the system (I), V is the volume, P is the pressure (kept at zero bars), which can be obtained via molecular dynamics simulations for a range of temperatures. Symbols in lowercase denote thermodynamic properties per atom. The thermodynamics definition of enthalpy given by $h(\tau) = e(\tau) + pv(\tau)$ is evaluated and fitted to a polynomial with respect to T so that an analytical integration is obtained via Equation 3.1.1. A coupling integration method is used to calculate G_{T_o} using the system with the

Hamiltonian as in Equation 3.1.2:

$$\mathcal{H} = (1 - \lambda) \cdot W + \lambda \cdot U_u \tag{3.1.2}$$

where according to Ciccotti and Hoover [39] λ is a coupling parameter taking values between 0 and 1, U_u is the potential of interest (described with EAM) and W is the Hamiltonian of the reference system, with known free energy such as a perfect solid as seen by Lutsko et al. [166]. Equation 3.1.2 provides the total energy between the two potentials W and U_u, assuming that reversible work is required to switch from one system to another. Finally, the unknown free energy of the potential U_u, G_{T_o}, can be obtained using the Equation 3.1.3, where G_{WT_o} is the free energy of the reference system at temperature T_o.

$$G_T - G_{WT_o} = \int_0^1 \left\langle \frac{\partial \mathcal{H}}{\partial \lambda} \right\rangle d\lambda \Rightarrow G_T - G_{WT_o} = \int_0^1 \langle U - W \rangle_\lambda \cdot d\lambda \tag{3.1.3}$$

This approach has been used for calculating the melting point of copper (Cu) on the (001) crystallographic plane by Lutsko et al. [166]. In this work Lusko calculated the free energy in the solid state. A harmonic reference system of perfect solid was used and for the liquid phase the convenient reference system was an ideal gas the potential for which the free energy needed was EAM [43, 44]. Once the free energy per atom for both solid and liquid phase was plotted, the melting point for the material of interest was estimated to be at 1171 ± 30 K. The calculated melting point for Cu in this case is significantly lower than in experimental studies due to the fact that the potential was parameterised for compound copper-nickel (Cu-Ni) alloy and not for elemental Cu. Also, the pair potential functions were shifted smoothly to zero at the cut-off point r_c. Using the above procedure to calculate the Gibbs free energy Jeong [126] estimated the copper melting point to be at 1246 K. A similar approach was used by Foiles and Adams [64] for the calculation of the Gibbs free energies of Cu, Ag, Au, Ni, Pd and Pt metals. In this study the free energy was obtained at an arbitrary temperature by integrating over a range of temperatures using the following expression:

$$\frac{d}{dT}\left(\frac{G}{T}\right)_{N,P} = -\frac{H}{T^2} \tag{3.1.4}$$

The enthalpy H of the system was calculated via a series of Monte Carlo simulations for the desired range of temperatures. The thermodynamic melting points predicted for Ag and Cu are 1170K K and 1340 K respectively, which proved to be in good agreement with experiments giving relatively low error (within 5%). Table 3.1 by Foiles and Adams [64] gives a comparison against the experimental values of various metals. Mei et al. [177] stud-

ies thermodynamic properties of density change in melting, heat fusion, thermal expansion and heat capacities for Cu using an analytic EAM model which is valid for any choice of cut-off distance. Melting of pure metals using coupling constant integration has been also reported for other metals such as Al shown by Mei and Davenport [176]. Lopasso et al. [157] studied alloy compound such as Fe-Cu showing that the melting point of Cu is 1017 K, which is $(3/4)T_m$. Additionally, Cu-Ni was investigated by Lutsko et al. [166], Au-Cu by Han et al. [93] and Au-Ni by Arregui et al. [3].

Element	MC (K)	Experiments
Ag	1170	1230
Au	1090	1338
Cu	1340	1358
Ni	1740	1726
Pd	1390	1825
Pt	1480	2045

Table 3.1: Comparison of Monte Carlo (MC) simulations and Experimental melting points [64].

3.1.2 Direct simulation of melting point

A different approach is to simulate a fully periodic system of solid material by heating it above the melting point, or cooling a periodic liquid below the melting point. This approach determines the temperature at which the lattice collapses, because T_m can be considerably lower than the temperature at which the crystal spontaneously melts. In this study a crystalline bulk material was used to simulate the homogeneous melting process at temperatures significantly higher than the equilibrium melting point. The melting point will be overestimated in the case of a heated solid and underestimated when a liquid is cooled below the melting point of the material. This is mainly due to the free energy barrier that causes superheating of a solid, reflecting the lack of a nucleation site for the liquid phase, and supercooling of a liquid. As a result a hysteresis effect is observed on constant-pressure molecular dynamics simulations as shown in Figures 3.1(a) and 3.1(b) for Cu and Ag respectively. According to the theory of the homogeneous nucleation and previous molecular dynamics studies the highest or lowest temperature at which superheating or supercooling occurs depends on the nucleation barrier parameter β [162, 161, 163] given by:

$$\beta = \frac{16 \cdot \pi \cdot \gamma_{sl}^3}{3 \cdot k_B \cdot T_m \cdot \Delta H_m^2} \tag{3.1.5}$$

where γ_{sl} is the surface tension of solid-liquid, ΔH_m is the heat of fusion, T_m is the melting temperature, and k_B is the Boltzmann's constant. The outcome of these studies shows that it is possible to estimate the thermodynamic melting point by only using the values of superheating a solid and supercooling a liquid with temperatures of $T(ss)$ and $T(sl)$ respectively by this relation:

$$T_m = T_{ss} + T_{sl} - \sqrt{T_{ss} \cdot T_{sl}} \tag{3.1.6}$$

3.1.3 Molecular dynamics methodology for direct melting approach

This section discusses the methodology of the direct melting approach for evaluating the melting point of Cu and Ag metals. To that means molecular dynamics simulations were conducted using a cubic cell with dimensions of (x, y, z)=(5, 5, 5) Å consisting of 500 atoms with periodic boundary conditions applied in all directions for bulk geometry. For time integration the velocity Verlet scheme as shown by Drikakis and Kalweit [53] was employed with integration timestep of $dt = 2 \cdot 10^{-15}$sec. The atoms interact with interatomic potentials developed by Daw et al. [45] within the EAM framework. The simulations were performed within the NPT thermodynamic ensemble, and thermodynamic properties, such as internal energy, pressure, enthalpy volume and lattice parameters were closely monitored.

The solid phase simulations began from a perfect FCC lattice at temperature of 300 K. Equilibrium was achieved at this temperature by maintaining it for 800 ps, which is long enough to measure the thermodynamic averages with minimal error. The system's configuration of the equilibration run was used by increasing the system's temperature every 100 K at high heating rates, rescaling the temperature every 100 timesteps. The subsequent step was to maintain the resulting temperature for an additional 800 ps in which thermodynamic values were recorded. This approach was continued until the temperature reached 1900 K. The same approach was used for the liquid phase is which an FCC lattice of the desired metal was constructed at temperatures of 1900 K and temperature was decreased every 100 K at high cooling rates in a stepwise manner as for the solid phase.

The analytical EAM potential developed by Mei et al. [177] predicted that when copper is superheated melting occurs at 1650K, which is the same as that calculated by the molecular dynamics simulations in this study. The internal energy per atom as a function of the temperature is shown in Figure 3.1(a), which gives the values of direct superheating of the

solid and supercooling of the liquid copper, indicating values of 1650 K and 950 K respectively. With regard to the Ag block, values of 1350 K and 850 K have been estimated for superheating and supercooling a bulk lattice respectively, as shown in Figure 3.1(b). Using Equation 3.1.6 shown in the previous section, the melting point of Cu and Ag were evaluated to be around 1327 K and 1128 K respectively. This is very close to values obtained by Foiles and Adams [64] in Table 3.1.

The molecular dynamics results in this study compared favourably agaisnt the work by Mei et al. [177], Belonoshko et al. [14] and experimental data from Gear [73], Hahn [81] and Harrison [97]. Figures 3.2(a) and 3.2(b) show the energy per atom and lattice parameter against temperature compared with Mei et al. [177] study.

The lattice parameter was calculated from the atomic volume, which was recorded from the MD simulations along with other thermodynamic properties. The formula for the lattice parameter is given by $a = (4 \cdot \Omega)^{\frac{1}{3}}$ where Ω is the atomic volume given by $\Omega = V/N$, where V is the volume of the simulatin box and N is the number of atoms. The solid phase data in this case was fitted to a third order polynomial giving the following equations for energy and lattice parameter:

$$E_s(T) = 0.0339\left(\frac{T}{T_m}\right)^3 - 0.0052\left(\frac{T}{T_m}\right)^2 - 3.5403 \tag{3.1.7}$$

$$a_s(T) = 0.0252\left(\frac{T}{T_m}\right)^3 - 0.0117\left(\frac{T}{T_m}\right)^2 + 0.086\left(\frac{T}{T_m}\right) + 3.6139 \tag{3.1.8}$$

The liquid phase was fitted to a first order polynomial giving the equations $E_l(T) = E_o + C_p T$ for energy and $a_l(T) = a_o(1 + \alpha_l \cdot T)$ for lattice parameter, where E_o is the energy in eV, C_p is the specific heat, a_o is the initial lattice parameter in Å, and α_l is the thermal expansion for the liquid phase in K^{-1}. Table 3.2 shows the results from the simulations conducted in this study and compares them against results from Mei. The values were obtained by the fitting of the liquid phase to a linear function as shown above. The linear coefficient of thermal expansion for the liquid phase shows the biggest difference of around 19%, with other properties, i.e. heat capacity C_p, energy E_o and lattice parameter a_o, showing similar results.

The linear coefficient of thermal expansion for the liquid phase α_l was obtained from the equation fitted to data (see Figure 3.2(b)), and that for the solid phase was calculated

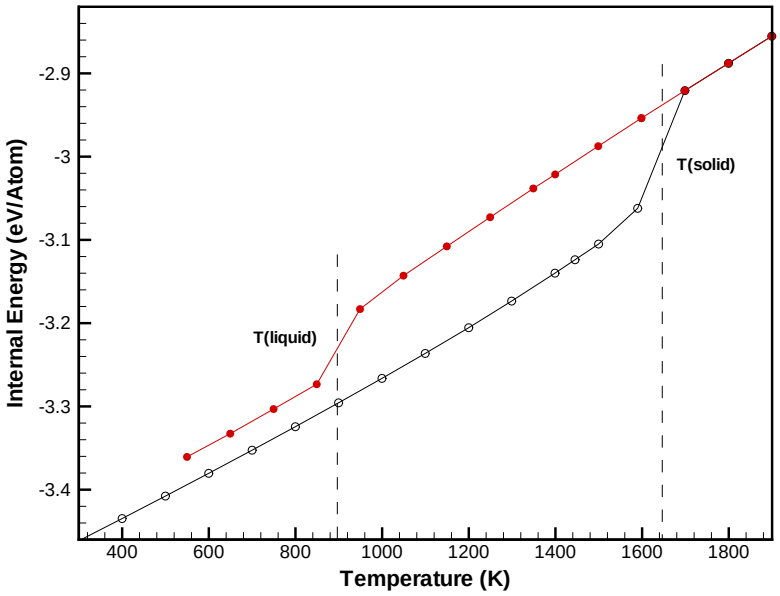

(a) Superheating (T(solid)) and supercooling (T(liquid)) of Cu solid (open circles) and liquid (closed circles) phase.

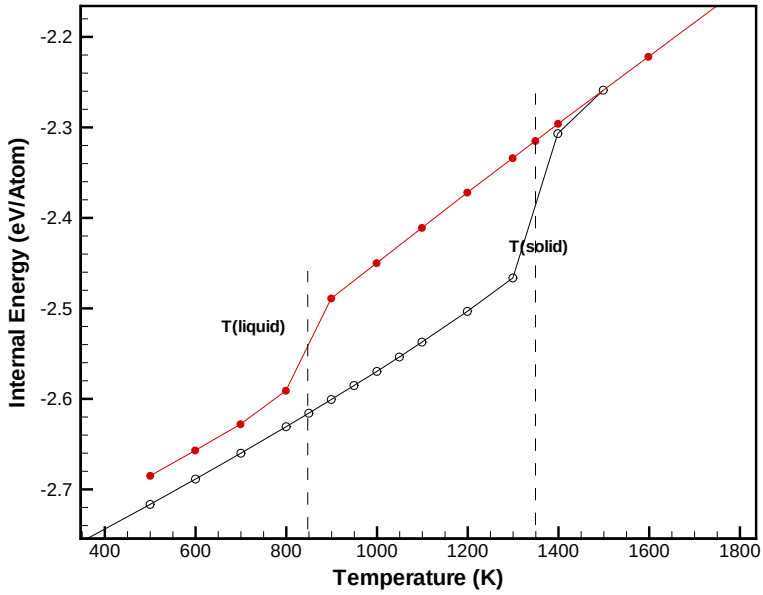

(b) Superheating (T(solid)) and supercooling (T(liquid)) of Ag solid (open circles) and liquid (closed circles) phase.

Figure 3.1: MD simulations of the hysteresis loop because of the superheating of the solid and supercooling of the liquid phases. T(solid) and T(liquid) corresponds to superheating and supercooling respectively.

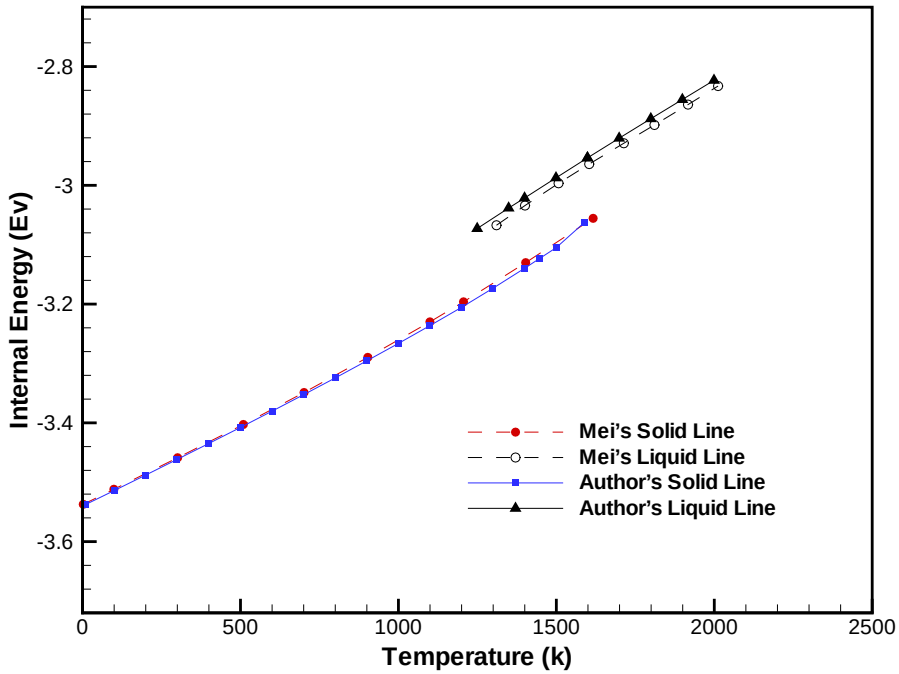

(a) Internal energy per atom against temperarure

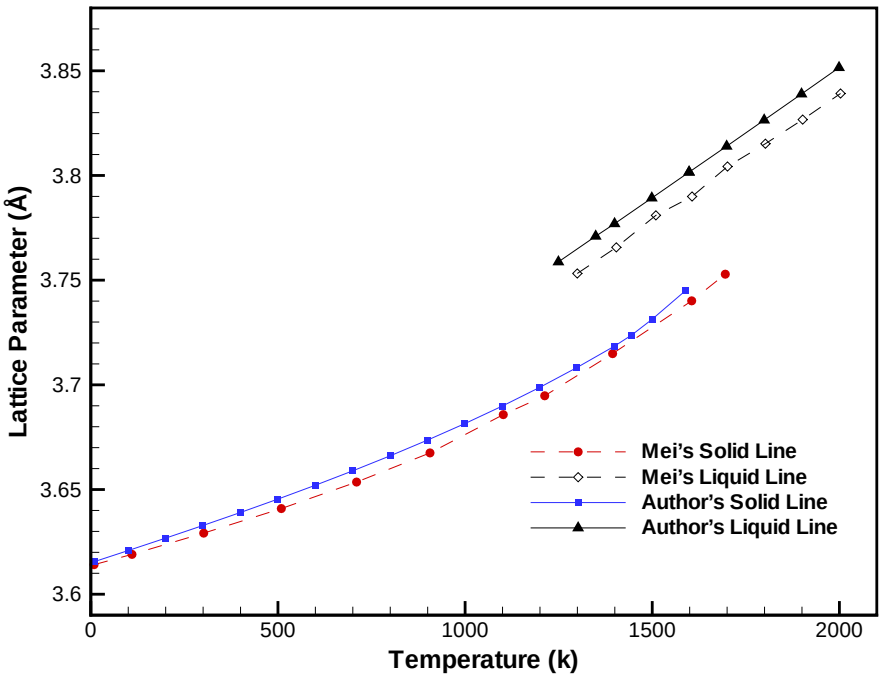

(b) Lattice parameter against temperature

Figure 3.2: Comparison of Epiphaniou model against data taken from Mei et al. [177] for Cu metal.

Property	Epiphaniou	Mei et al. [177]
E_o (eV)	-3.4838	-3.4973
a_o (Å)	3.6038	3.5938
C_p (J/K)	$3.48k_B$	$3.87k_B$
α_l (K^{-1})	2.774E-5	3.414E-5

Table 3.2: Molecular dynamics results of Cu liquid phase: Comparison.

via Equation 3.1.9:

$$\alpha_s = \frac{1}{a} \cdot \frac{da}{dT} \tag{3.1.9}$$

where the derivative of da/dT was calculated numerically with a temperature step of 100K. Table 3.3 summarises the results from this study and compared against others in [177, 14, 65, 83, 81, 97, 17]. The Table compares the linear coefficient of thermal expansion at room temperature and the results show good agreement with other molecular dynamics studies as well as experimental work. The calculated values of the thermal expansion for a temperature range of 200 K to 1400 K can be observed with the aid of Figures 3.3(a) and 3.3(b). Figure 3.3(a) shows the results from this study plotted against other molecular dynamic simulations and figure 3.3(b) gives very good agreement of this data with Gear [73], Hahn [81] and Harrison [97] experimental work. Additionally, the heat capacity C_p per atom was also evaluated by taking the first derivative of the Equation 3.1.7. The value of C_p was obtained for a temperature range of 200 K to 1400 K and the results show very good agreement with experimental and MD studies, as shown in Figure 3.4.

	MD					Experiments	
Material	Epiphaniou	Mei	Foiles	Hakkinen	Belonoshko	Han and Harrison	Billings
Cu	16.97	15.00	16.40	18.10	20.28	16.55	16.70

Table 3.3: Linear coefficient of thermal expansion α_s for copper: comparison against MD and experiments.

3.1.4 Solid-liquid interfacial method

Heating a solid system directly gives larger values of the melting point due to solid-liquid interfacial energy. The nucleation barrier can be overcome if a free surface is generated, however, in molecular dynamics testing a solid with a configuration like this would not deliver the properties of bulk material. In this section, alternative approaches that can be used for the determination of melting are reviewed along with the selected method investigated in this study. There are three methods for calculating the melting point by generating

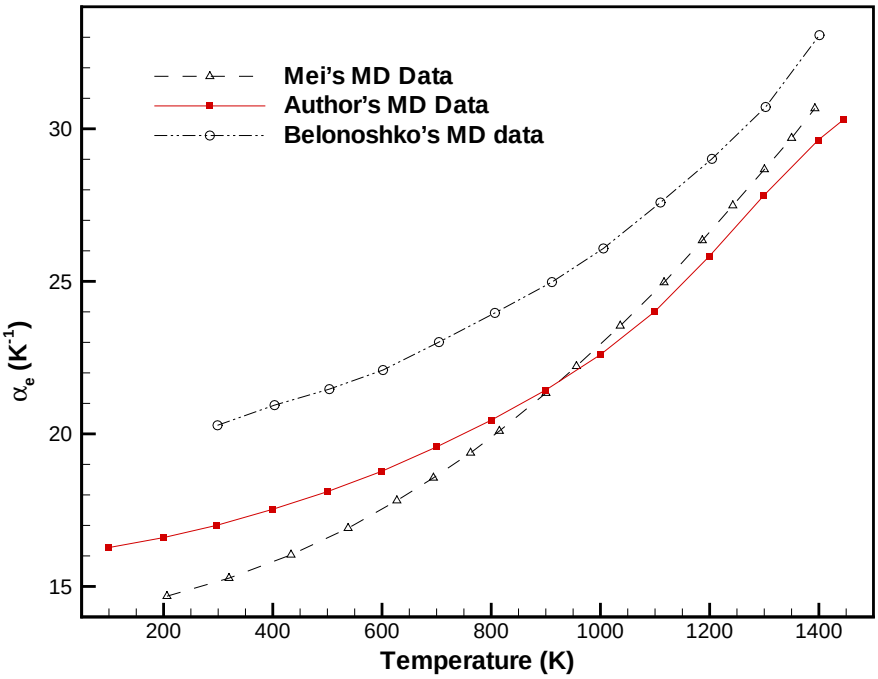

(a) Molecular dynamics studies

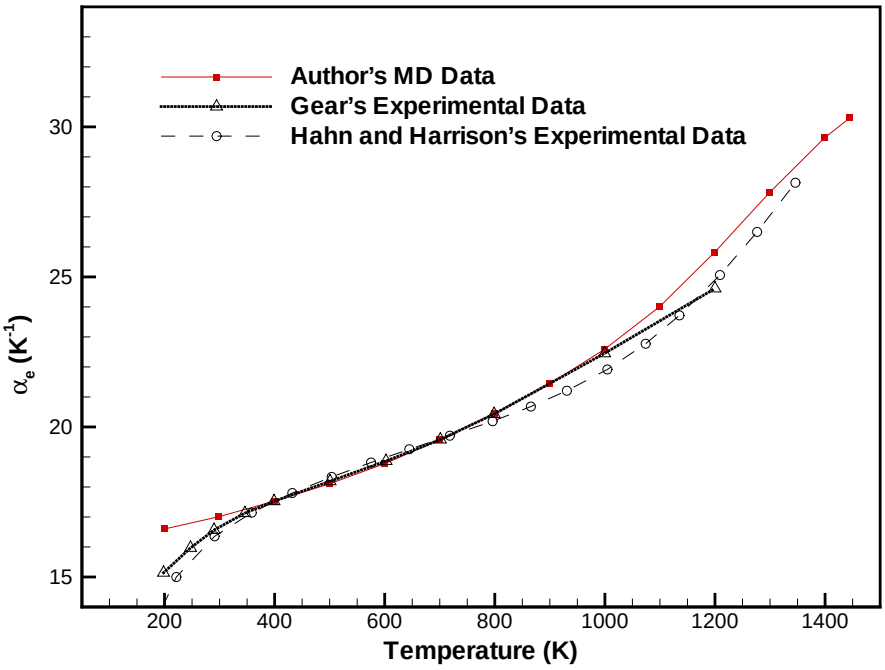

(b) Author's MD simulations against experiments

Figure 3.3: Evaluation of linear coefficient of thermal expansion ($10^{-6}K^{-1}$) for Cu: Comparison against data taken from Mei et al. [177], Belonoshko et al. [14], Gear [73], Hahn [81] and Harrison [97].

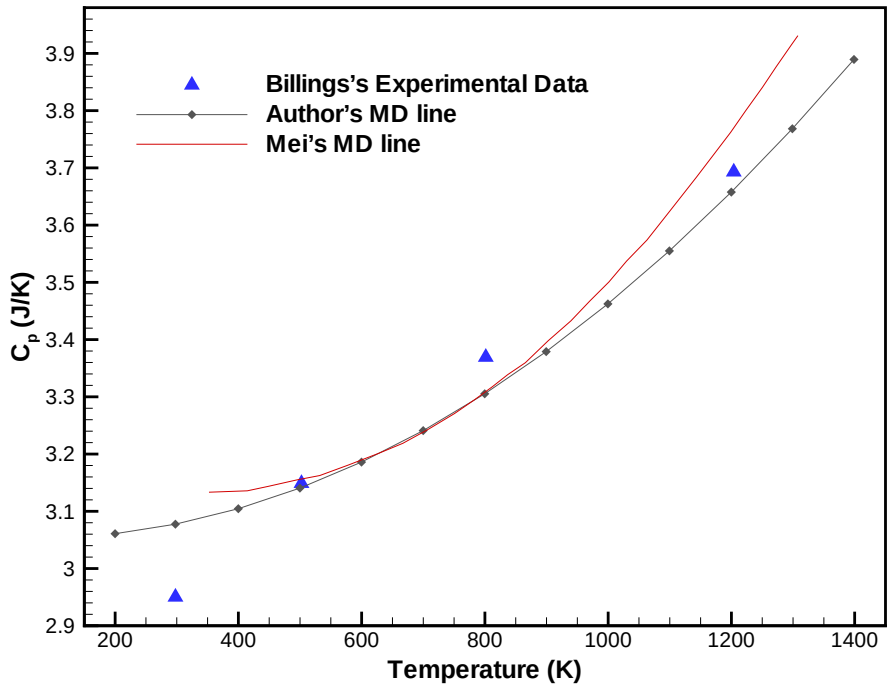

Figure 3.4: Heat capacity C_p given in units of Boltzman's constant k_B against temperature for Cu.

two different phases on the same materials, solid and liquid. The first approach is called the "sandwich" method, in which a set-up of solid-liquid-solid phase is achieved and its progress is observed during annealing. This method was adapted by Hong et al. [107] to study the melting point of Ni_3Al alloy. If upon annealing the structure develops into a liquid state then the current temperature is above the melting point: on the other hand, if at a certain temperature the structure turns into a solid state, then this temperature is below the melting point of the material. The second approach is to construct a solid-liquid interface and measure the moving velocity of the interface at different temperatures [107, 165]. By plotting the moving velocity against temperatures and extrapolating it at room temperature, the melting temperature of the material can be obtained.

Finally, the third method is based on solid-liquid construction arranged geometrically, such that the interface remains constant in volume using an NVE ensemble as obtained for binary alloys by Hong et al. [107], Morris et al. [187] for aluminum and Landman et al. [145] for Si. In these studies the molecular dynamics simulation consists of two stages. First is the preparation, where the two MD simulations obtained separately for solid and liquid are brought to equilibrium in the NVE ensemble. In the second stage the two systems are brought together and the total system progresses towards a thermodynamic equilibrium at constant volume energy ensemble. However, the drawback of this procedure is that the

simulation is biased through an anisotropic stress tensor. Hence, the components of the stresses in the x, y, and z-directions can be quite different, as seen in Morris and Song [186]. You et al. [264] has overcome this problem by having as a first stage pure solid with a certain value for the lattice parameter in the NPT ensemble, at a temperature lower than the melting point. When the solid phase is brought to equilibrium the liquid phase is generated by raising the temperature at values above the melting temperature, followed by a cooling to the original temperature. Using this approach, You et al. [264] showed that the internal local stresses σ_{xx}, σ_{yy}, and σ_{zz} for the liquid phase should have the same values and the next stage of the coexisting phases could start in the NVE ensemble.

According to Foiles and Adams [64] the use of the constant energy ensemble causes the motion of the interface to slow down due to the lack of source or sink for the energy linked to the latent heat that forces the transition between solid and liquid phases. Thus, the use of NVE thermodynamic ensemble may not be as accurate as the constant temperature (NVT) thermodynamics ensemble. In this study the solid-liquid construction was employed as shown by [64] for verification of the melting point of both Cu and Ag. Simulation of solid and liquid phase containing the same material using the NVT thermodynamic ensemble was conducted in two stages. This method has the liquid and the solid phases geometrically arranged so that the interface volume remains constant as melting or freezing occurs. The simulation boxes were (x, y, z)=$(60, 250, 60)$ Å containing approximately 69000 Cu atoms and (x, y, z)=$(80, 250, 80)$ Å containing approximately 86000 Ag atoms. Simulation box was chosen to ensure enough atoms are present with minimum thermal noise. The integration timestep and algorithm is the same as discussed in Section 3.1.3.

The first stage is the preparation, and is similar to other approaches as mentioned above, where the two phases were brought to equilibrium for 27 ps. The solid was equilibriated at room temperature while the liquid was equilibrated at a temperature of 1900K under the NPT thermodynamic ensemble where pressure was set up at P=0 bar. The second stage was to run both solid and liquid phases at a particular temperature, for which the appropriate lattice parameter of the material was pre-calculated via the NPT simulation discussed in Section 3.1.3 and used in the first stage. The temperatures ranged from 1000 K to 1400 K for Cu and 800 K to 1200 K for Ag. Both phases were kept at the desired temperature constant for 270 ps within the NVT thermodynamic ensemble where the volume of the simulation was also kept constant.

Figures 3.5(a), 3.5(b), 3.5(c), 3.5(d) and 3.5(e) show the final configuration for Cu, in which the solid phase is coloured blue and the liquid phase in red. Because of the difficulty

of finding the exact melting point via this approach, it was estimated that the melting point of Cu is between 1250 K and 1300 K, similar to the previous EAM results of 1246 K in [126] and 1340 K shown by Foiles and Adams [64]. It was observed that at temperatures $T \leq 1250$ K the solid phase gradually grows, solidifying the liquid phase. At a temperature of T=1250 K in figure 3.5(b) solidification of the liquid is observed, but very close to the interfacial region, which indicates that the temperature is below the melting point of the material. Simulation at temperature of 1300 K shows that the stagnation state is reached as shown in figure 3.5(c). At temperatures of T≥ 1350 K the liquid phase grows liquefying the solid phase indicating that the particular temperature is above the melting point, thus continuous melting of the solid phase is observed. Simulations were run for a long time to ensure that either the solidification of the liquid or the melting of the solid phase reach equilibrium positions and stop growing. Figure 3.5 shows the snapshot of the final state of the simulations at temperature ranging from 1100 K to 1400 K for copper metal.

Simulation of the Ag two phase system was obtained using the same method as for Cu. Figure 3.6(a) shows the materials' response at a temperature of 1100K indicating that the solid phase grows, solidifying the liquid phase. When the temperature is set to 1200K as seen in Figure 3.6(b), the liquid phase is growing and the solid phase is starting to melt. This is also the case for a temperature of 1300K, shown in Figure 3.6(c). Therefore the melting point of Ag is between temperatures of 1100K and 1200K which is in good agreement with Foiles and Adams [64] and the value calculated via Equation 3.1.6 (Section 3.1.2).

3.1.5 Melting point at non-standard atmospheric conditions

In subsequent chapters sliding friction simulations will be discussed for the pressure of 5.1GPa, therefore for the purpose of the analysis it is useful to measure the melting point at this pressure condition. The simulation method described in section 3.1.4 was used for Cu and Ag with the same EAM potential. Results show that the melting point is dramatically increased; the melting point of copper at 5.1 GPa lies between 1500 K and 1600 K. This is in a good agreement with experimental results measured at pressure conditions of 5 GPa giving melting point of the material equal to 1547 K. On the other hand, MD simulations of Ag show a melting point between 1550 K and 1650 K, which is a small deviation to the experimental value of 1523 K.

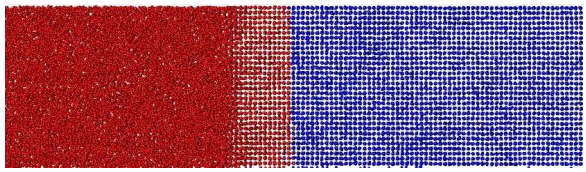

(a) Temperature at 1100K

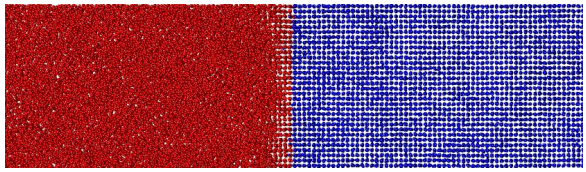

(b) Temperature at 1250K

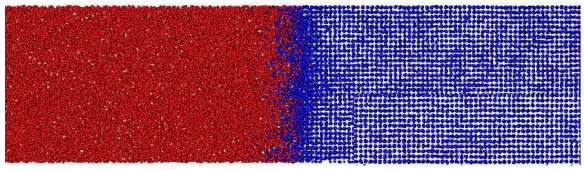

(c) Temperature at 1300K (stagnated state)

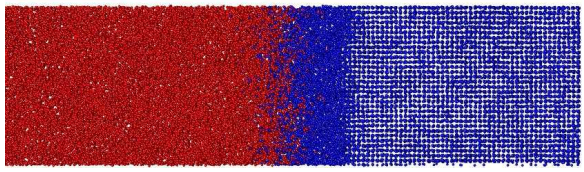

(d) Temperature at 1350K (continuous melting)

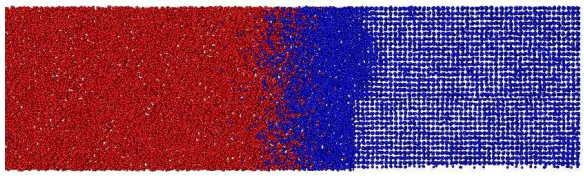

(e) Temperature at 1400K

Figure 3.5: Simulations of Cu two phase system at a range of temperatures. The liquid phase is shown in red and the solid phase of copper atoms are coloured in blue.

3.2 Various approaches to thermal conductivity

Understanding of energy transport phenomena of thin films has been the centre of attention for several years, generating a new field of study called microscale heat transfer highlighted

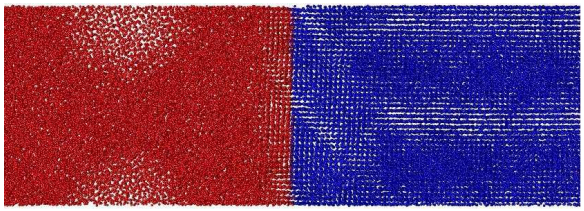

(a) Temperature at 1100K

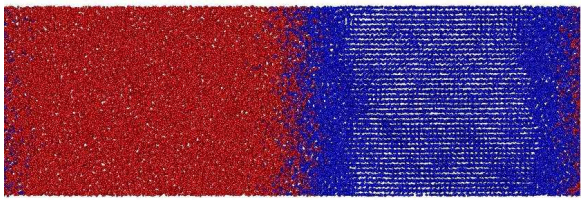

(b) Temperature at 1200K (stagnated state)

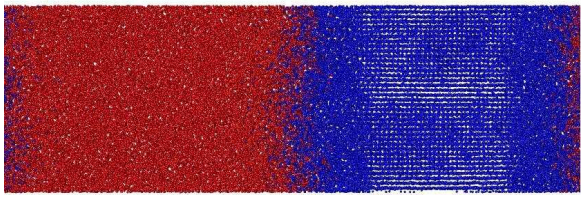

(c) Temperature at 1300K (continuous melting)

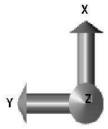

Figure 3.6: Simulations of Ag solid-liquid phase system at a range of temperatures. The liquid phase is shown in red and the solid phase of copper atoms are coloured in blue.

by Bejan and Kraus [13]. Studying the heat transfer at the microscale is simply to investigate the thermal energy tranfer in which the continuum model is sometimes insufficient to explain certain phenomena. When the continuum model fails then the computationally expensive molecular dynamics approach is usually adopted. When considering metallic materials thermal and electrical conduction occurs via the electrons in which molecular dynamics cannot describe their role. Electrons are so fast and much lighter than the nucleus that their effect is treated as a single potential energy representing the ground state. This is a siginificant limitation when physical problems such as friction are considered in which thermal conduction plays a vital role. Additionally, molecular dynamics methods account for the contribution of phonons (atomic vibration) to the thermal conductivity but do not account for the free electrons or elecron-phonon interaction.

Molecular dynamics techniques derived from first principles (ab initio) also known as

quantum mechanics (QM), can capture the movement of electrons as shown in the Car-Parinello method by Car and Parrinello [29], however they are limited by the number of atoms, because they are computationally more expensive than MD. At the submicron scale, classical heat transfer is restricted by QM techniques because the specific heat, C_p, of the structures should approach zero according to Prevenslik [198]. Additionally, atoms interacting in thin films are under electromagnetic confinement and QM cannot cease small levels of thermal energy. As a result the C_p in thin films tends to zero, thus any heat gained cannot be conserved by increasing the system's temperature. In particular, when rubbing of crystals is initiated at the submicron level temperatures reach high values, as discussed in later chapters. This is due to the fact that the heat capacity predicted via MD simulations in Section 3.1.3 is in a good agreement with experimental data. Other means of conservation are required such as the quantum induced radiation (QED) as proposed by Prevenslik [198]. Therefore, this section reviews the MD methods related to thermal conductivity issues and investigates the possibility of using state-of-the-art techniques to overcome the limitations associated with dynamic friction. Additionally, the author aims to show how these techniques could be used in conjunction with the sliding friction simulations in Chapter 5.

Macroscopic investigation allows modelling of the heat transfer and temperature fields, but in simulation of the atomic scale using MD is difficult to achieve. An important point is that the free electrons contribute primarily to thermal conductivity in metals, while lattice vibration (phonons) contribute to thermal transport in semiconductors and insulators. There are several studies describing ways of calculating the thermal conductivity in semiconductors [148, 214, 100, 240, 115, 98, 266, 138, 131] using Lennard-Jones or Morse potentials. Tretiakov and Scandolo [240] estimates the thermal conductivity of solid argon using Lennard-Jones interatomic potential and shows that the computed values are in a good agreement with experiments. The results also confirm that the Green-Kubo method described by Allen and Tildesley [2] proved to be very powerful in calculating the thermal conductivity of crystals at high temperature, provided that advanced interatomic potentials are used. This approach could predict the thermal conductivity of more complex materials in cases where experimental data are difficult to obtain. Additionally, Tsuji et al. [241] proposes using virtual free electrons imposed between copper atoms to adjust the thermal diffusivity and electrical resistivity for copper simulated using Morse potentials.

Thermal conduction in solid materials takes place by the contribution of both the vibrational energy within the lattice (phonons) and the free electrons. Free electrons have generally short wavelengths in the order of a few Å (0.1nm), which makes them major con-

tributors to thermal conductivity, especially at low temperatures. Their scattering mechanism is important in microscale heat transfer. Figure 3.7 shows the electon-electron and electron-phonon scattering mechanisms of free electrons in metallic materials. The mean

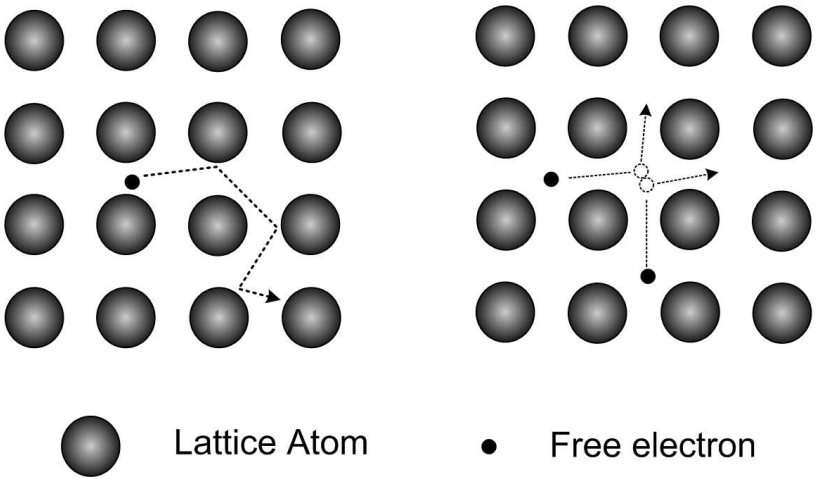

Figure 3.7: Free electron scattering mechanisms in metals. Left: Electron-phonon scattering. Right: Electron-electron scattering.

free path of an electron λ_e is given by the thermal velocity v_{th} ($v_{th} = \sqrt{\frac{3k_BT}{m_e}}$) times the scattering time τ_{sc} and for bulk metals is typically on the order of 10 to 30 nm where electron lattice scattering dominates. The transport properties are influenced by the thin film size and if the thickness is approaching the order of the mean free path of electron λ_e, boundary scattering takes a crucial role. When the thin film is heated electron system becomes so hot that the electon-electron scattering can become significant. This size dependency was observed by Heino and Ristolainen [100] who showed that for small domain systems typically less than 40 times the phonon mean free path λ_p, the contribution by phonons to thermal conductivity is reduced. Hence, when considering mircroscale heat transfer it is wise to consider the microscopic energy carriers (electrons) and the full range of possible scattering mechanisms as shown in figure 3.7.

In this work molecular dynamics simulations were conducted to evaluate mechanical and thermodynamic properties such as bulk modulus, thermal expansion, melting points T_m and heat capacities C_p on Cu and Ag metals and results show good agreement compared to experiments. Although the mechanical and most thermodynamical properties are consistent with experiments, however, molecular dynamics simulations underestimate the values of thermal conductivities for these metals according to Heino and Ristolainen [100]. Heino and Ristolainen [100] studies the thermal conductivity of metals by phonons using EAM interatomic potentials developed by [177]. Heino proved that there is a size dependency

of the thermal conductivity k. Considering their curves of thermal conductivity against domain size the obtained values are 4.6 W/mK and 2.3 W/mK for Cu and Ag respectively, for the selected domain size of 16 nm. These values are unrealistically small compared to experimental values which are 397 W/mK and 420 W/mK for Cu and Ag respectively.

3.2.1 Thermal conductivity simulations of Cu and Ag interatomic potentials

Schelling et al. [214] show that there are several methods of obtaining the thermal conductivity of metals by phonons. This section discusses the molecular dynamics simulations that were conducted on Cu and Ag metals to obtain the values of thermal conductivities for the domain size with distance in y dimension equal to 16 nm. This value was taken because the friction numerical simulations have domain size of y=16 nm for each material slab. Thermal conductivity is size and temperature dependent as discussed by Heino and Ristolainen [100] and Jund and Jullien [131]. Size effects are present when the simulation domain is very close to or smaller than the mean free path of the phonons; this is because at these sizes the electron contribution to the thermal conductivity dominates fully. In this work the direct method was used for evaluating the thermal conductivity of the system using Fourier's law of heat flow as shown in Equation 3.2.1:

$$k = -\frac{J_y}{\partial T/\partial y} \tag{3.2.1}$$

where $\partial T/\partial y$ is the temperature gradient and J_y is the heat flux, which is equal to $\Delta\epsilon/(2\cdot A^2\cdot \Delta t)$. $\Delta\epsilon$ is the energy per time step Δt and A is the area of the sample perpendicular to the heat flow. The usual approach is to impose a temperature gradient and record the resulting heat flux as shown by Oligschleger and Schön [193], as in experiments where the thermal conductivity is determined by measuring the required heat flux to maintain a constant temperature gradient. The reverse non-equilibrium molecular dynamics (RNEMD) approach was employed for this study, in which a known heat flux by exchanging kinetic energy between two particles is applied to the simulation domain. The RNEMD was developed by Mller-Plathe and Reith [184] in which a heat flux was imposed and the system response was the generation of a temperature gradient along the desired direction. The algorithm is part of LAMMMPS tools and provide several features such as conservation of the total energy and the total linear momentum to avoid an artificial drift of the kinetic energy at certain conditions.

The RNEMD divides the simulation box into layers in the desired direction of which heat flux will be imposed. In this study the y direction was taken as the direction of the flux and the simulation is divided into layers along this direction. The cold layer is at y = 0 and the hot layer is at the middle, $L_y/2$, where L_y is the entire length of the simulation domain. The algorithm identifies the atom with the highest kinetic energy in the cold layer, and the atom with the lowest kinetic energy in the hot layer. Once these atoms are identified their velocity vectors are exchanged if the hottest atom in the cold layer holds a higher value of kinetic energy than the coldest atom in the hot layer. The total kinetic energy per timestep, $\Delta\epsilon$, transfered by these swaps is recorded and the heat flux evolution can be calculated. When the system is imposed to this procedure over time a temperature gradient evolves and the temperature profile can be analysed.

Applying the Muller-Plathe algorithm developed by Mller-Plathe and Reith [184] a simulation domain was constructed with $(x, y, z) = (4a, 45a, 4a)$ Å containing approximately 2000 atoms. The values of a for Cu and Ag are 3.587 and 4.0422 Å respectively, with periodic boundary conditions imposed in all directions. In experiments the heat loss to the surroundings is an issue but molecular dynamics overcomes this by the use of boundary conditions. The sizes in x and z directions were four times the lattice parameters, approximately three times the cut-off radii, which ensures that all atoms are used once in the force calculation so that no image atoms are required from the periodic boundaries. Initially the system is imposed to temperature rescaling to 300 K for 10,000 time steps until an equilibrium is reached, with integration timestep constant at 2 ns. The direction of applied heat flux is kept constant for both metals towards the y = [100] crystallographic plane. The simulation with constant heat flux was run for 200,000 time steps using NVE thermodynamic ensemble to evaluate the thermal conductivity at the average temperature of 300 K.

The temperature profiles were obtained by dividing the system into layers and calculating the average temperature of the atoms in each layer. Figure 3.8 shows the linear temperature gradient for copper block after the simulation had reached a steady state; similar temperature profiles obtained for Ag metal. A linear curve was fitted to the temperature profiles, highlighted in black, as seen in Figure 3.8, from which the temperature gradient dT/dy was calculated. The kinetic energy exchange was calculated and therefore the heat flux in the system was determined to be 96.96 GW/m^2 for Cu and 64.77 GW/m^2 for Ag. Hence, the system's thermal conductivities at these conditions for Cu and Ag were calculated to be 3.26 and 2.18 W/Km respectively, which is close to the values obtained by Heino and Ristolainen [100] and almost 10 times lower than the experimental values.

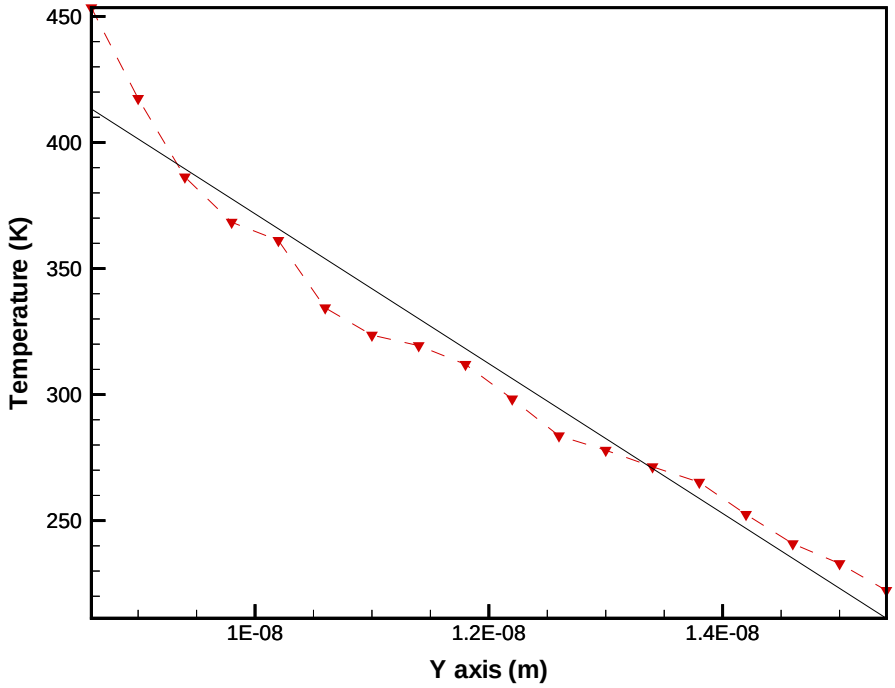

Figure 3.8: Dotted line: Temperature profile of Cu in the simulation cell (only one half is shown here). Solid line: linear fitting curve.

The thermal conductivity underestimation of pure MD simulations can be overcome by considering the electron motion within the medium. When electrons at low temperatures are traveling through a hot thermal region they can remove some of the energy introduced by the phonon vibration and result in decreasing the temperature. Stoneham [225] described that electrons have this interesting ability to act as either heat sink or heat bath, removing or adding energy to the atoms. The first MD study in which electron-ion interactions were taken into account by Flynn and Averback [63] on radiation damage in solids. In pure metals the conductivity is predominantly carried by electrons than phonons, thus, coupling between electron and phonons is required to solve the energy dissipation issue associated with processes like friction. The implementation of the strong coupling between electron-phonon can be obtained by implementing heat transfer equations to work along with the MD code as shown by Finnis et al. [62] in simulation of collision cascades in Cu and Ni. Additionally, as discussed in section 3.2 there are various scattering mechanisms that occur within the lattice. When atoms collide some of the kinetic energy is transformed into heat in inelastic collisions which results in excitations of bound electrons of the medium and in excitations of the electron cloud of the ion. When these collisions occur electrons slow down, known as electronic stopping. Caro and Victoria [30] not only considers the strong electron-phonon coupling but considers also the electronic stopping

by introducing a frictional term as will be discussed in section 3.2.2. Therefore, the following section briefly discusses the thermal conductivity correction by the implementation of continuum thermal diffusion equations coupled with MD.

3.2.2 Two temperature model for thermal conduction

Analysis of the heat propagation in metals is obtained by the two temperature model (TTM) equations developed by Ivanov and Zhigilei [120], in which temperatures corresponding to the electron and lattice system are described. Combining the classical MD methods with the continuum description of thermal diffusion via the TTM an accurate evolution of the temperature profiles is expected. This hybrid computational model, coupling of TTM-MD, was primarily used to study the kinetics and microscopic mechanisms of laser melting shown by Ivanov and Zhigilei [121], and the high excitation levels corresponding to laser ablation [38, 213].

The energy transfer between the electronic and atomic subsystems due to electron-phonon is coupled by the non-linear differential equation of heat diffusion as shown in Equation 3.2.2. Ivanov and Zhigilei [120] developed Equation 3.2.2 for strong electron-phonon non-equilibrium due to the fast electronic excitation. This model can be used for test cases where the electron and lattice temperatures are almost equal and in cases where materials have undergone shock wave heating.

$$C_e \frac{\partial T_e}{\partial t} = \nabla(k_e \nabla T_e) - g_p(T_e - T_a) + g_s T_a^{'} \tag{3.2.2}$$

where C_e is the electronic specific heat, T_e is the electron's temperature, k_e is the electron's thermal conductivity, g_p is the coupling constant for electron-phonon interaction, g_s is the coupling constant that corresponds to the energy lost by the atomic system because of the electronic stopping. Finally, the parameter T_a is the atomic temperature of the system and T'_a (which has units of temperature) is evaluated by the energy balance as described by Duffy and Rutherford [55] and Rutherford and Duffy [210].

The diffusion Equation 3.2.2 takes into account the electron temperature, which is solved by the finite difference method on a continuum grid. This occurs simultaneously with the MD integration of the equation of motion for the atoms of interest. The diffusion

equation was recently implemented in LAMMPS to model the electron temperature, which is coupled with the molecular dynamics to account for the energy exchange between the atomic and electronic subsystems. In this algorithm the heat transfer is conducted via an inhomogeneous Langevin thermostat given by Equation 3.2.3:

$$m_i \frac{\partial v_i}{\partial t} = F_i(t) - \gamma_i v_i + \widetilde{F}(t) \tag{3.2.3}$$

where v_i and m_i is the velocity and the mass of an atom i and F_i is the force acting on that atom at time t. The γ_i denotes the friction coefficient due to energy loss and $\widetilde{F_i}$ is a stochastic force term with random magnitude and orientation which includes the energy gain due to electron bombardment. According to Caro [30] the energy loss represented by the second term in the right hand side of Equation 3.2.3 depends on the velocity of the moving atom. As shown in the electron excitation theory, systems with high kinetic energy cause movement of the electrons to higher energy state. As a result the electronic gas of valence electrons decrease the speed of atoms due to inelastic collisions between the bound electrons in the bulk matrix of the material and the ion moving trough it. This is known as electronic stopping of ions in solids, $S_e(E) = \lambda_m \sqrt{E_k}$. This is also shown at low energy limits, which means lower projectile velocity than the relevant electronic velocity in the target, i.e. the Fermi velocity in metals, as described by Lindhard and Scharff [156]. Thus, at lower velocities the atoms movement is associated with the rate of energy loss (dE/dt) and this energy is proportional to the difference between the atomic and electronic temperature. As a result, the energy loss part in Equation 3.2.3 is subdivided into friction coefficients due to electronic stopping (γ_s), and due to electron-phonon interaction (γ_p). The evaluation of γ_i in Equation 3.2.3 was altered according to the cut-off velocity, u_0. For $v_i > u_0$ then $\gamma_i = \gamma_p + \gamma_s$ and for $v_i \leq u_0$ the $\gamma_i = \gamma_p$.

The implementation in LAMMPS is such that the MD substitutes the TTM equation for the lattice temperature, since the equation couples both electronic and phonon temperatures. The algorithm assumes that none of the user-supplied parameters will vary with temperature. This assumption can be relaxed by modifying the algorithm to include the desired temperature dependency and functional form for any of the parameters, if kept unchanged a linear temperature dependence is assumed which is correct for most metals. The Langevin framework is applied locally on the volumes that represent the continuum grid points and couples the temperature of the atoms to an infinite heat reservoirs representing the local electrons. Finally, the TTM scheme allows the incorporation of two independent coefficients of friction for electron stopping and electron-phonon interaction as mentioned

above; parameters used for MD simulations of metallic Cu and Ag are shown in table 3.4. The values of mass enhancement parameter (λ_m) for Cu and Ag are 0.14 and 0.15 eV/Å respectively, these were evaluated from the stopping range tables SRIM by Ziegler et al. [270]. Duffy and Rutherford [55], used the value of λ to evaluate the coefficient of friction due to electronic stopping for both metals using the Equation $\gamma_s = (\lambda_m \sqrt{m_e})/\sqrt{2}$.

Properties	Copper (Cu)	Silver (Ag)
C_e $(mJ/moleK^2)$	0.620[183]	0.641[183]
k_e (W/mK)	401 [250]	400 [250]
γ_s	1.4	1.12
γ_p	0.3	0.19
u_0 (Å/ps)	76.02	111.08
ρ_e 1/ Å^3	0.0845 [250]	0.0585 [250]

Table 3.4: Constants of selected metals at room temperature used for MD simulation of dynamic friction.

In section 3.2.1 the thermal conductivity of Cu and Ag metals was evaluated by using a domain size of $(x, y, z) = (4a, 45a, 4a)$ Å; the domain size is larger than the mean free path of both metals to avoid size effects in the value of k. This domain was used to perform simulations activating the TTM algorithm; material properties shown in Table 3.4 were used for re-evaluating the thermal conductivity of these metals. The results show slightly larger values compared to the values obtained in section 3.2.1, which are 8.74 and 8.81 W/Km for Cu and Ag respectively; however, this is still significantly smaller than the experimental results. This shows that even though a more sophisticated model is used to account for the electron contribution to thermal conductivity, TTM requires a significant number of experimental variables, which makes the algorithm a lot more complicated, hence the implementation is prone to bugs.

3.2.3 Thermal conductivity correction (TKC) scheme

Another way of tackling the under-prediction of the thermal conductivity is described in this section. In section 3.2.2 an attempt was made in order to correct the heat propagation by the two temperature model. This will lead to a temperature identical for both the phonons and electrons within the system. The combination of the thermal diffusion Equation 3.2.2 and the classical molecular dynamics methods does not provide an accurate value of the thermal conductivity of both Cu and Ag metals. A new algorithm was implemented by the author in the grid analysis module created by Kalweit [132]. This schemes solves the heat

conduction equation by correcting the thermal conductivity as shown in Equation 3.2.4:

$$\frac{1}{A}\frac{dT}{dt} = -k \cdot \frac{dT}{dx} \tag{3.2.4}$$

where k is the thermal conductivity given by $k_{exp} - k_{MD}$. The grid analysis module defines a virtual grid of cells or grid of nodes to the molecular dynamics domain system as shown in Figure 3.9. This is a three-dimensional Cartesian grid in which each node is defined by indices i, j, k and the node's coordinates by $x_{i,j,k}$. Generally, a macroscopic variable, $\mathcal{A}_{i,j,k}$ of the particular grid node, is calculated as an instantaneous average over N number of atoms via the Equation 3.2.5:

$$\mathcal{A}_{i,j,k} = \sum_{a=1}^{N} \mathcal{A}_w W(\boldsymbol{d}, \boldsymbol{l}) \tag{3.2.5}$$

where $\mathcal{A}_w$ is the property $\mathcal{A}$ of atom w, $\boldsymbol{d}$ is the distance of atom w to node given by $\boldsymbol{d} = \boldsymbol{r}_w - x_{i,j,k}$, and finally $\boldsymbol{l}$ is the grid cell width. The $W(\boldsymbol{d}, \boldsymbol{l})$ is the weighting function evaluated for each dimension x, y, and z via the Equation 3.2.6:

$$W(\boldsymbol{d}, \boldsymbol{l}) = W(d_x, l_x)W(d_y, l_y)W(d_z, l_z) \tag{3.2.6}$$

This function depends on the distance of the particle to the node, $d_{x,y,z}$, and the length of the size cell, $l_{x,y,z}$. The type of the weighting function considered in this work is the nearest-grid-point (NGP) in which the properties of the atoms are entirely dependent on the nearest node, which is defined as:

$$W_{NGP}(d_{(x,y,z)}, l_{(x,y,)}) = \begin{cases} 1 & d_{(x,y,z)} \leq \frac{l_{(x,y,z)}}{2} \\ 0 & \text{otherwise} \end{cases} \tag{3.2.7}$$

To that end, macroscopic variables like potential energy, kinetic energy, pressure, velocity and many more, are calculated and averaged in time on the centre of the grid node illustrated in Figure 3.9.

Additionally, an energy transfer scheme was used to apply velocity rescaling in each layer. Velocity rescaling in MD simulations is widely used; however, the disadvantage is that momentum transfers due to the change of the velocity vectors. In this application it is advantageous to eliminate momentum transfer when transferring energy. Thus, the energy transfer scheme was adapted by first scaling the velocity vectors of the atoms belonging to

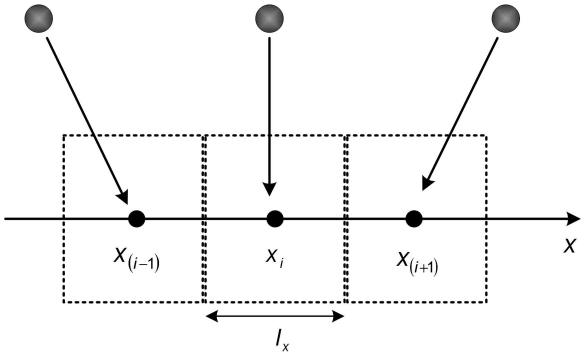

Figure 3.9: NGP scheme assigning atoms to grid points. Atoms are the shaded circles and grid points are shown in small black points.

a system $\mathcal{S}$, by Equation 3.2.8:

$$v_i^{current} = v_i^{previous} \cdot \mathtt{f} + \boldsymbol{c}, \tag{3.2.8}$$

where $\mathtt{f}$ is a scaling factor and $\boldsymbol{c}$ is the additional correction vector for conserving the overall momentum of the system. The scaling factor and correction vector are given by Equation 3.2.9 and 3.2.10 respectively, so that the energy transfered equals E_{trans}.

$$\mathtt{f} = \sqrt{1 + \frac{E_{trans}}{E_{k,int}}} \tag{3.2.9}$$

$$\boldsymbol{c} = v_{\mathcal{S}}(1 - \mathtt{f}) \tag{3.2.10}$$

The correction factor ($\mathtt{f}$) cannot be defined if the energy transfered is smaller than the internal kinetic energy ($E_{trans} < E_{k,int}$). This signifies that the energy transfer is not possible because one cannot remove more energy than what is available in the system.

The implementation of the algorithms is summarised as follows:

- The MD domain is discretised into grid nodes containing a large number of atoms so that temperature will be evaluated without excessive noise. The MD domain resolutions contains layers, which are parallel to the sliding interface.
- The temperature in each slice will be evaluated at regular intervals, dt.
- First the algorithm evaluates the heat flux coefficient, C_s, of each atomic species as shown in Equation 3.2.11:

$$C_s = t \cdot (k) \cdot A \tag{3.2.11}$$

- The kinetic energy added to each layer is then corrected by taking into account the realistic thermal conductivity of the materials. This includes layers in which material mixing occurs, hence, material concentration was taken into consideration during these calculations. Thus, the change in kinetic energy or heat flux that passes in and out of each layer is calculated by Equation 3.2.12, which is evaluated in each direction x, y and z:

$$J = \frac{1}{2} C_m C_s \tag{3.2.12}$$

- Finally the heat conduction Equation 3.2.4 is solved using the energy transfer scheme to rescale atomic velocities and as a result the temperature of each grid node without introducing momentum into the system.

- The algorithm was adapted so that it accounts for different species present in a grid cell by evaluating the concentration of each atom type.

The verification of the above algorithm was not possible on domain sizes with a very small number of atoms. It was found that discretising the system with grid resolution of less than 5 to 10 lattice spaces, the heat conduction equation was unstable and therefore the solution did not converge. The simulation domain chosen for the verification of the algorithm was $(x, y, z) = (144.6, 5.784, 5.784)$ nm containing 409600 atoms. Figure 3.10 is the plot of the temperature profile across the dimension of which the heat flux is imposed. Evaluation of the gradient from Figure 3.10 along with the calculation of the kinetic energy exchange over simulation time period, which is effectively the heat flux, gives the desired value of thermal conductivity for Cu. This value was estimated to be 400.79 W/Km and is in a good agreement with experimental values taken from Wang et al. [250].

The main limitations of the MD simulations are highlighted in this section and the author is aiming to give a solution to the under prediction of the thermal conductivity for Cu and Ag metals. An investigation was conducted to resolve the underestimation of, k, by using the TTM method however, the results are still not consistent with experimental values. In this study the author developed a new algorithm (TCK), in which the heat conduction equation is solved considering the experimental conductivity of the metals. Validation was successful resulting in values of k consistent with experiments. This is proved to be a major contribution for resolving the MD limitations and it will be used in subsequent chapters for dynamic friction numerical experiments.

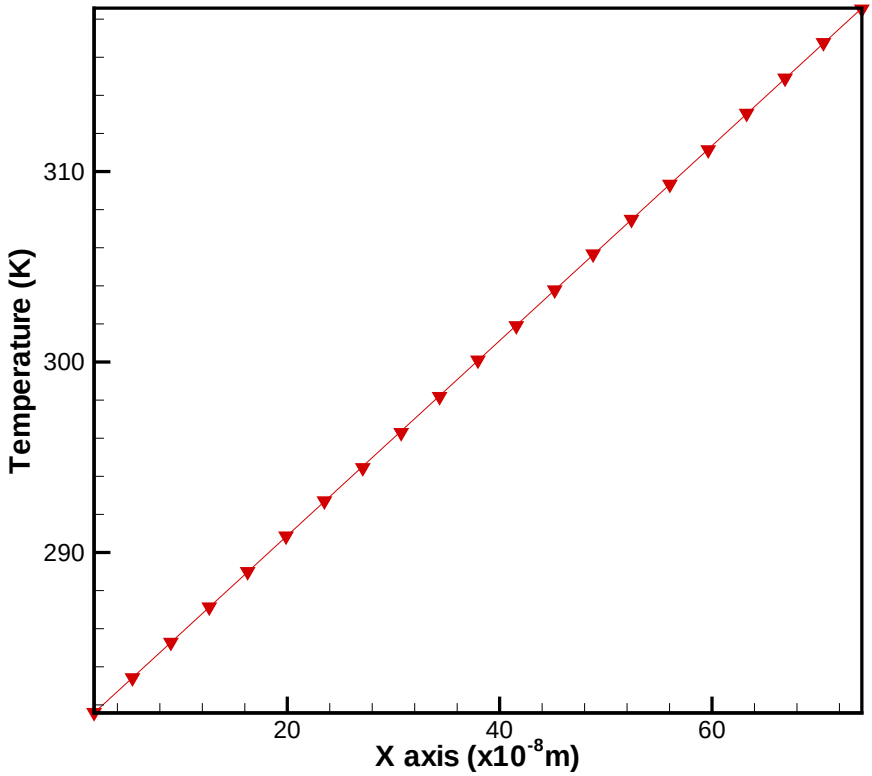

Figure 3.10: Temperature profile across x dimension for Cu domain size.

3.3 Mechanical Properties

With the rapid development of nanotechnology and nanoscience, the need to build nano-components is high for several applications such as memory circuits and improvements on CPUs. There is increasing progress towards nanotechnology devices which have enormous potential applications in the aerospace industry. Thus, MEMS have a major impact in applications such as computers, materials, sensors, actuators, avionics systems etc. They are mechanical systems at a micro-scale that combine mechanical, optical, and electromagnetic elements with electronics on semi-conductor substrate electronics. They could be used as sensors to identify physical parameters in their environment (pressure, acceleration, etc.) and/or actuators to act on this environment. Development of these devices is important for future exploration of space by improving the reliability of aerospace hardware and performance, while reducing the manufacturing costs. Additionally, embedding electromechanical components into earth-orbiting satellites or piloted vehicles and probes could reduce the overall cost of these missions.

Copper has received extensive mechanical testing due to its excellent electrical conductivity and other properties as shown by Heino and Ristolainen [99]. Copper can be used for electrical interconnections, which are structures that require metals to withstand thermal stresses when temperature changes. It can also be used in numerous applications as a heat conductor, electrical conductor, and as an alloying element of various metals for aerospace and automotive applications etc. The stresses involved in a high shear strained system have been often studied by the finite element method (FEM), in which elasticity and plasticity theories are taken into consideration. However, when the system becomes very small the atomistic effects from the nano-structure have to be evaluated and compared with results from the continuum. Therefore, Horstemeyer et al. [109] claims that a good link needs to be built between the continuum and atomic scale in order to determine the relations between the structure and properties for plasticity.

There is evidence that atomistic simulations obtained at extreme strain rates and size scales agree with the aspects of plasticity observed in macroscale experiments, according to Horstemeyer et al. [110]. The plastic behaviour of nanocrystalline metals has been extensively studied by means of molecular dynamics, thus the aim of this chapter is to give a brief literature review on the matter and outline the results of molecular dynamics simulations that were obtained on Cu for validating the interatomic potential developed by Foiles and Adams [64].

3.3.1 The response of Cu in dynamic tensile deformation

An important part of this development is the investigation of the mechanical properties of small scale systems, metal nanowires, typically at sizes that exceed 10^3 atoms to get reliable results. Copper has been the centre of attention for many studies under high strain rates with various atomistic potential models, such as EAM and effective-medium theory (EMT) discussed by Jacobsen et al. [124]. Research into the deformation mechanism of Cu nanowires has been extensively carried out by computer simulations via the molecular dynamics method. The work by Wu [258] demonstrates the results obtained on a Cu nanowire at imposed tensile loading across the [001] crystallographic direction and at strain rates ranging from 10^7 to $2 \cdot 10^9$/s. Amongst other properties Wu showed that at the above strain rates range the yield strength of the metal nanowire remains constant. The effect of the strain rate is determined by the reaction of the material to the external loading, and as discussed in the study by Wu [258] this reaction will be faster if the size of the specimen is

small.

Molecular dynamics simulations of single crystal Cu nanowire, also performed by Liang and Zhou [155], study the mechanical response under a range of strain rates and size scales. Liang and Zhou [155] showed that the modulus of elasticity is independent of strain rates and simulation box sizes. On the other hand, the yield stress increases with decreasing specimen size, by having higher values when thinner specimens were tested, and also increases with the loading rate. Chang and Fang [33] demonstrates the results on tensile and fatigue behaviour of nanoscale Cu at various temperatures, and the work by Chang [32] shows results on simulations of static and cyclic loading with increasing vacancies, also at different temperatures.

3.3.2 Molecular dynamics simulations of tensile loading on bulk Cu

The section describes the investigation of the deformation study on bulk Cu under uniaxial strain using MD method. The simulations were conducted on a three-dimensional system of FCC Cu and consisted of approximately 2000 atoms using periodic boundary conditions in all directions for bulk geometry. The simulation box was $(x, y, z) = (10, 16, 3)$ Å. The velocity verlet scheme was employed with integration timestep of dt=10^{-15} s. To perform the simulations two stages were used. The first stage was the equilibration in which after assigning the atomic positions and velocities, the system was brought to an equilibrium after 60 ps, time sufficiently long to relax the lattice. During equilibration, the entire system is evolved in the NPH thermodynamic ensemble based on the Nose/Hoover pressure barostat. This is effectively an isopressure/isostress and isoenthalpic ensemble, where number of atoms (N), pressure (P) and enthalpy (H) are kept constant. The purpose of applying this thermodynamic ensemble is to relax the lattice at atmospheric conditions of zero pressure and ultimately having zero stress affecting the system. The temperature was also controlled at 300 K by rescaling the velocities. Thermodynamic properties such as internal energy, pressure, enthalpy, and volume were closely monitored.

The second stage involved collecting all the data which was obtained by simulation at constant temperature and volume using the NVT thermodynamic ensemble. The NVT is based on the Nose/Hoover dynamics to appropriately control the temperature enabling the study of the system beyond the elastic limit. The NVT thermostat is suitable for a simulation box that is changing size and shape with time. At this stage the material is being

deformed by applying a strain rate of $1.8 \cdot 10^{-9}$/s in the y-direction. The velocity, v_i, was imposed at which the simulation box length changes; this is effectively the engineering strain rate given by $\dot{\epsilon} = V_o/l$. The system is allowed to deform until failure, which can be seen in Figure 3.11 and the microscopic stress tensor is calculated for each atom by the stress-volume equation:

$$(S_{ab})_{local} = -\left[m_i v_a v_b + \frac{1}{2}\sum_{j=1}^{N_p}(r_i - r_j)F_{p_{ij}} + \frac{1}{2}\sum_{j=1}^{N_b}(r_i - r_j)F_{b_{ij}}\right] \tag{3.3.1}$$

where $(S_{ab})_{local}$ is the local per-atom stress tensor, a and b take values of x,y,z for the 6 components of the stress tensor Sxx, Syy, Szz, Sxy, Sxz, Syz. The first term of Equation 3.3.1 is the kinetic energy contribution for an atom i. The second term is the pairwise energy, where atom j loops over the N_p neighbours of atom i, r is the position, and F_p is the three components of the force on atom i due to the pairwise interaction with atom j. Finally, the third term is the bond energy contribution, where atom j loops over the N_b bonds part of atom i, and F_b is also the three components of force on atom i due to the bonded interaction with atom j.

The stress on each atom was calculated using Equation 3.3.1, which is the negative of the pressure on each atom tensor. As previously mentioned, this is the stress-volume formulation, which means that the calculated value for per-atom stress is in units of pressure-volume. Therefore, dividing this value by per-atom volume, units of stress can be obtained. The individual atom's volume cannot be easily calculated, especially for solids. Hence, the stress of the entire system $(S_{ab})_{global}$ or global stress is calculated at every timestep by the equation:

$$(S_{ab})_{global} = \frac{1}{V} \cdot \sum_{i=1}^{N}(S_{ab})_{local} \tag{3.3.2}$$

where N is the number of atoms in the entire system and V is the volume of the simulation box. The strain of the simulation box is calculated at every timestep from the definition which states that strain is the change in length over the original: $\epsilon = (L_f - L_o)/L_o$, where L_f is the final box length at every timestep and L_o is the original length.

Calculating the exact values of the elastic modulus or the elastic constants without a degree of uncertainty is difficult. To obtain Young's modulus for small values of strains taken from a second degree polynomial fitted to the stress-strain curve, as shown in Figure

3.12. The constitutive relation is expressed in the form of the equation:

$$\sigma = -41.439\epsilon^2 + 55.179\epsilon + 0.5853 \tag{3.3.3}$$

Primarily, the yield stress of the material can be estimated by using the 0.2% proof stress by drawing a line as shown in Figure 3.12 and the intercept is the yield point. This value was estimated at $\sigma_y = 10.88GPa$. The modulus of elasticity or Young's modulus was also estimated as E=109.95 GPa as seen in Figure 3.12, which is very close to experimental values for pure Cu. In theory the ideal strength of a crystal should be 1/10th of its modulus according to Ju [130], which is also in good agreement with the estimated yield stress σ_y. Table 3.5 compares the values of Young's modulus of Cu against other experimental and molecular dynamics studies. By definition, the cohesive strength is the theoretical stress that causes fracture in tensile test experiments if material exhibits no plastic deformation. The cohesive strength is given by the formula shown by J.H. [128]:

$$\sigma_c = \sqrt{\frac{E\gamma}{4r_o}} \tag{3.3.4}$$

where E is Young's modulus, γ is the surface energy, and r_o is the interatomic bond length. For bulk Cu, with experimental values of E=$122.9 \cdot 10^9$ Pa, γ=1.79 J/m^2 taken by Barrigaa et al. [5] and interatomic distance r_o=3.615 Å the value of cohesive strength is calculated at σ_c=12.33 GPa. The theoretical cohesive strength given by the EAM potential is estimated at approximately 13 GPa, which is very close to the experimental value calculated via Equation 3.3.4.

Tested by:	Chang [32]	Lebedev [147]	Shen [220]	Read [201]	Epiphaniou
Material	Cu (Thin Film)	Cu (99.89% Purity)	Cu (Nanocrystalline)	Cu (Thin Film)	Cu (Bulk)
Experimental		122.9	100	107	
MD simulations	138.8				109.9

Table 3.5: Young's modulus comparison of MD simulations and experimental. Values are presented in GPa units.

3.3.3 MD simulations of tensile loading for Cu nanowire

As previously mentioned, Cu nanowires have been extensively studied via computer simulations for elastic properties, strength, and yield by many researchers [118, 50, 51, 133, 134, 155, 26]. This section presents the verification of the MD models against results obtained

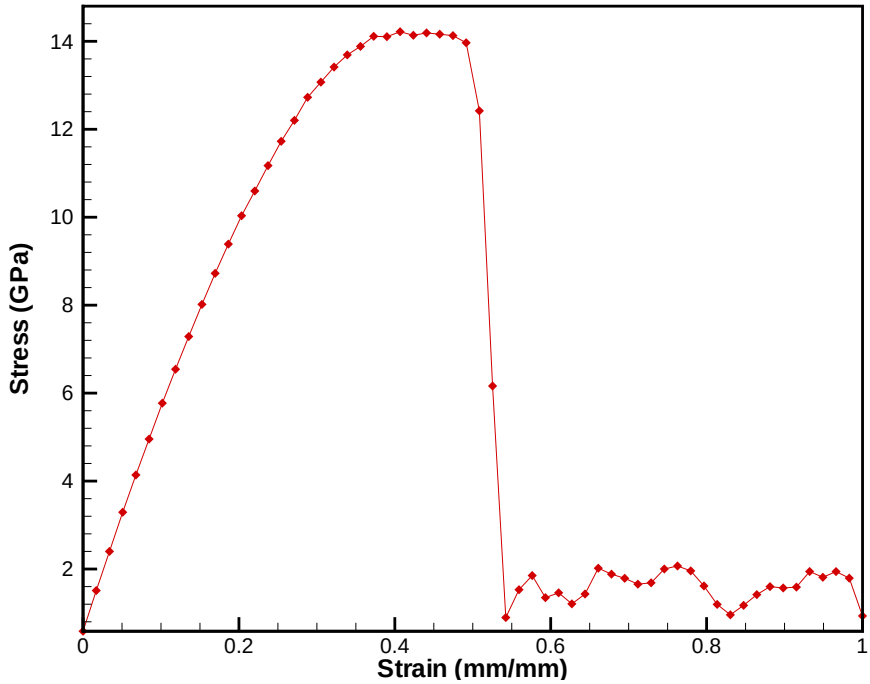

Figure 3.11: Stress response of bulk Cu under tensile loading.

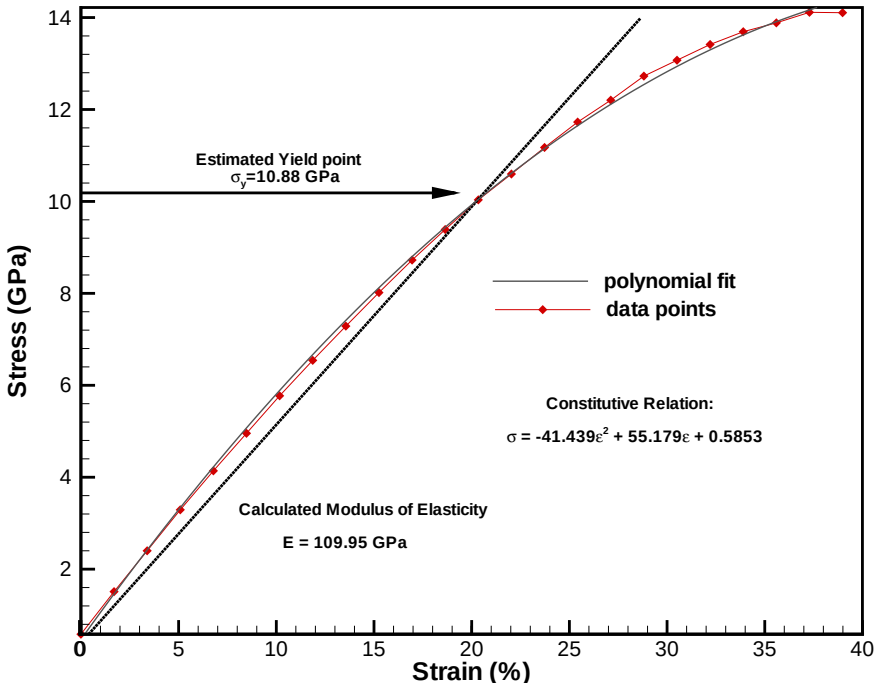

Figure 3.12: Second order polynomial fitting.

by Wu [258] for uniaxial loading of Cu nanowires. The molecular dynamics procedure includes the stages as mentioned in section 3.3.2, where first the lattice is relaxed using the

NPH thermodynamic ensemble at a control temperature of 298K, using periodic boundary conditions only in z-directions at which the extension loading was applied in the second phase of the simulation. Table 3.6 illustrates the conditions used in these simulations, compared to those of Wu [258].

	Epiphaniou (Nanowire)	Wu [258] (Nanowire)
Domain	(19.8,19.8,54.2)	(19.8,19.8,54.2)
Crystallographic Direction	[001]	[001]
Periodic	z-direction	z-direction
Strain Rate (/s)	1.8E+9	5.0E+7
Temperature (K)	300	300
Yield Strength (GPa)	7.06	7.11
Young's Modulus (GPa)	56	62

Table 3.6: MD conditions and comparison between Epiphaniou and Wu's model.

According to Wu the yield stress of Cu nanowire across the [001] crystallographic direction remains almost constant at strain rates ranging from 1E+7 to 2E+9/s. This was verified by the MD model in this study, which gives yield stress value of $\sigma_y = 7.06$ GPa, tested at strain rates of 1.8E+9/s, which is in good agreement with Wu. The calculated Young's modulus and the trend of the two lines shown in Figure 3.13 are also in good agreement.

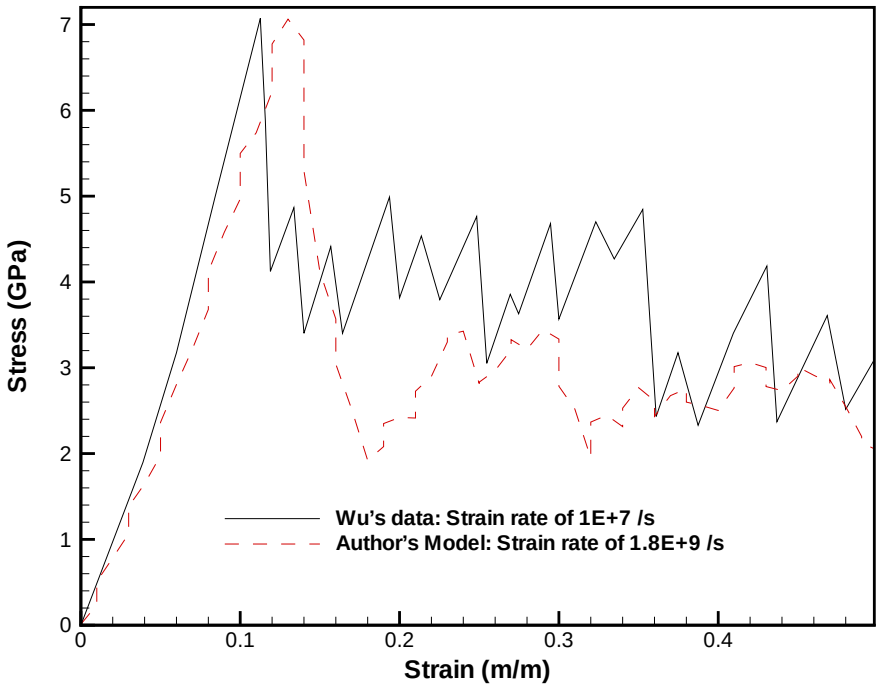

Figure 3.13: Comparison of tensile simulation on Cu nanowire. Wu's [258] against author's model.

3.3.4 Shear response in Cu thin films

There are several studies regarding the shear stress response of metallic materials, amongst those is the work done by Horstemeyer et al. [110],[57, 108], which was obtained using EAM potentials for Cu, Ni and Al. Horstemeyer et al. [110] studied the effects of stress response under several conditions by varying the crystallographic orientation, the temperature, the specimen size and the strain rates varying from 10^6 to 10^{12}/s. It also aims to bridge the scales from continuum to atomic and the major conclusion was that yield stress increases as the size of the simulation box decreases. The MD simulations carried out in Horstemeyer's study show a stress-strain response with several stress drop-off regions, which is very similar to experiments that have been conducted on Cu metal "whiskers" shown by Yoshida et al. [263].

These simulations identify three regions of mechanical response, as seen in Figure 3.14 for a nickel block containing 2,242 atoms. These are defined as "micro-yield 1", in which the stress-strain response reaches the end of the elastic region. The second region is defined as "micro-yield 2", which is adapted from macro-scale theory of a 0.2% proof stress at which yield occurs, and finally the third location defined as "macro-yield", which is the point of maximum stress. The three regions can also be seen in Figure 3.15 from Fang et al. [58] simulating with the same procedure on nickel metal containing 2000 atoms at strain rates of 1E+8/s.

Additionally, the effects of size and time-scale on the plastic deformation of Cu crystal under shear loading was also separately analysed also by Horstemeyer and Baskes [108]. As shown in Figure 3.16 for small samples, there is little dependence of the stress to failure with strain rate. The deformation in this case is primarily elastic because dislocation motion or slip cannot progress because of the size. On the other hand, in larger samples with domain systems containing larger than 10^3 atoms, dislocations are nucleated even at lower strains rates, and as a result, the yield stress decreases.

The work by Horstemeyer and others used a computational box in which free surfaces in the x,y-directions and periodic in z-direction were imposed. Also, the model is required to have a large cross-sectional area, therefore four unit cell thicknesses are used in the z-direction for their simulations. Two reservoirs were created in the top and bottom, containing a few lattice planes, and the remaining atoms were free to evolve throughout the simulation. The bottom reservoir was kept fixed by zeroing the x velocity, and the top

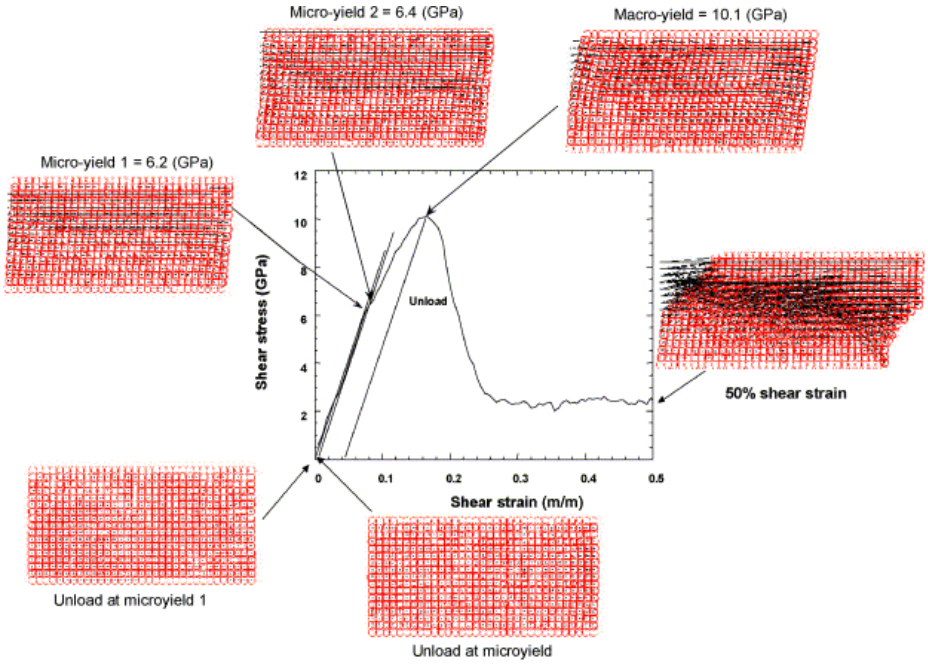

Figure 3.14: Shear deformation path for Ni, courtesy of Horstemeyer et al. [110].

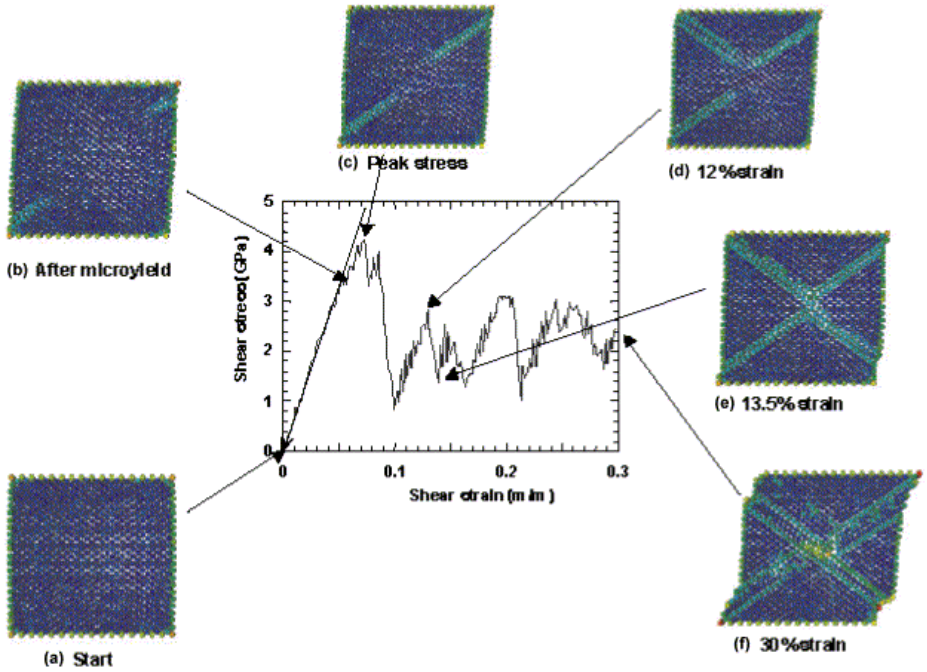

Figure 3.15: Shear test of nickel box, courtesy of Fang et al. [58].

reservoir atoms imposed at constant velocity to achieve the desired strain rates.

The MD simulations conducted in this chapter are for verification of the code and the EAM potential of Cu against previous MD studies. In these simulations, because of restric-

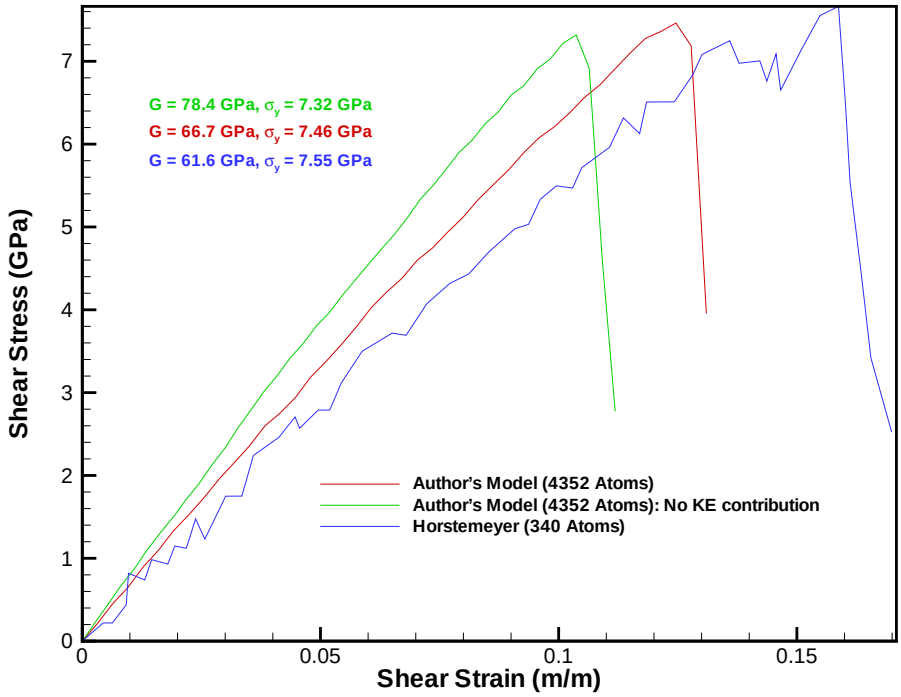

Figure 3.16: Comparison of shear simulation of Cu nanowire at strain rate of 1E+9/s: Horstemeyer's against author's model.

tions in the command used to simulate Cu, a slightly different approach was used to achieve the same effect. This means that a strain rate was applied onto the block of Cu by changing its shape and size. The only restriction is that periodic boundary condition had to be used in the direction of the shear strain. The shear strains were applied in the xy-direction and the conditions are compared against Horstemeyer et al. [110] work, as shown in Table 3.7. The results of this study are plotted in Figure 3.16, in which the shear modulus was evaluated giving valus of 66.7 GPa compared to 61.6 GPa, in a good agreement with results obtained by Horstemeyer.

	Horstemeyer (Thin Film)	Epiphaniou (Thin Film)
Domain (Atoms)	332	4352
Crystallographic Direction	[001],[011],[0-11]	[001],[011],[0-11]
Periodic	z-direction	x,y-direction
Strain Rate (/s)	1E+9	1E+9
Temperature (K)	298	298
Yield Strength (GPa)	7.55	7.46
Shear Modulus (GPa)	61.6	66.7

Table 3.7: MD conditions and comparison between Epiphaniou and Horstemeyer's shear model.

To conclude, the thermodynamic and mechanical properties of FCC metals were extensively studied to verify and validate the EAM potentials against computational and experimental studies. The potentials showed good agreement with experimental results; however, the thermal conductivity is greatly underestimated. This is due to the fundamental limitation of the MD method, which only accounts for the phonon contribution to the thermal conductivity and not for the free electrons or electron-phonon interaction. Investigation was carried out to resolve the underestimation of the thermal conductivity as discussed in Section 3.2.2 with the use of TTM; however, the results are still not consistent with experimental values. The development of a new algorithm, as discussed in Section 3.2.3 leads to a successful validation of the thermal conductivity k of Cu metal.

CHAPTER 4

Methodology for molecular dynamics simulations of sliding friction

"There is in my opinion great similarity between the problems provided by the mysterious behaviour of the atoms and those provided by the present economic paradoxes confronting the world."

Paul Dirac

This chapter is concerned with the algorithms required to apply the desired boundary conditions for friction simulations. These boundary conditions are imposed to predefined reservoirs located several hundred of lattice spacings away from the interfacial region. There are two different schemes of applying the desired pressure which are discussed within the text and distinct differences are highlighted. Additionally, an algorithm of implementing constant velocity also imposed on the reservoirs to maintain sliding at desired speeds. A number of test cases have been performed to verify that at specific boundary conditions the coefficient of friction μ is independent of the domain size of the simulation box. Finally, a brief discussion on atomistic visualisation is presented to describe the possibility of observing new structures, kinetic pathways and various micro-mechanism at the atomic scale.

4.1 Methodology, simulation setup and procedure

The MD simulations on high speed sliding have been performed with a normal pressure of 5.1 GPa and sliding speeds, $u_s = \{25, 50, 100, 150, 200, 300, \ldots, 1000\}$ m/s. The setup for the MD simulations of sliding is illustrated in Figure 4.1. The upper slab is made of copper and the lower slab of silver atoms. Both slabs are perfect FCC lattices with smooth surfaces in contact on the (001) crystallographic planes and sliding was initiated in the [001] crystallographic direction. The lattice parameters that were used for Cu and Ag are 3.5786 and 4.0422 Å respectively; these values were calculated from data taken by Marsh [170] and confirmed via molecular dynamics simulations using an NPT ensemble. The friction simulations have been performed for two domain sizes (L_x, L_y, L_z), which are given in Table 4.1. Both slabs are of identical dimension and their thickness (size in the y direction) is $L_y/2$.

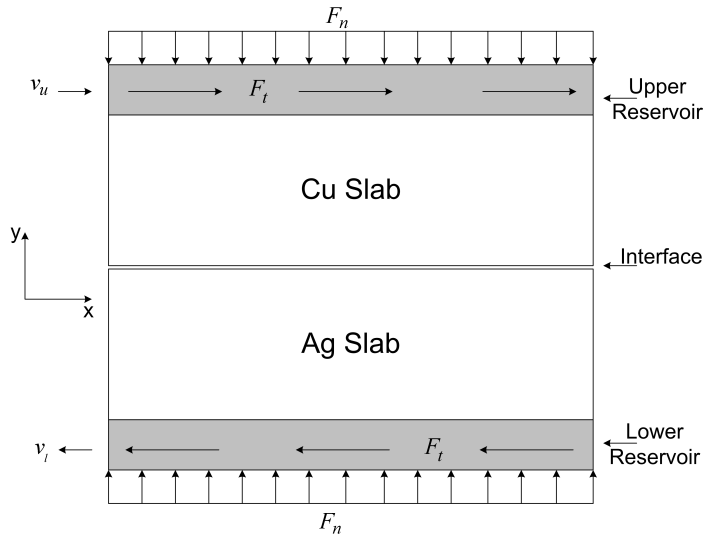

Figure 4.1: Setup configuration with two slabs. F_n is the normal force, F_t is the required frictional force and v_u, v_l are the velocities of the upper and lower reservoirs respectively.

Domain	L_x(nm)	L_y(nm)	L_z(nm)	N
(1)	410	320	330	3.1 million
(2)	300	300	100	1.3 million

Table 4.1: Sizes of the slabs for friction simulations.

Periodic boundary conditions are applied in the x and z directions. In the y direction, the boundary conditions are applied to the reservoirs on the upper side of the Cu slab and the lower side of the Ag slab (Figure 4.1). The reservoir regions (containing approximately 10^5 atoms) have a thickness of 10 Å (corresponding roughly to 6-7 lattice planes) in the y

direction. Simulations have also been conducted on reservoirs with thickness of 40 Å (20 lattice planes), which showed small differences in the frictional force per unit area. There are three constraints (boundary conditions) applied to the reservoirs:

1. A force, F_n, is applied to the reservoir atoms in order to press both blocks together with $P_n = 5.1\,\text{GPa}$. F_n is constant, acts normal to the interface (y direction) and is distributed equally to all N_R atoms in the reservoir. Thus, $F_n = P_n L_x L_z$ and the force on each reservoir atom is $f_y = F_n/N_R$. There are two algorithms developed to get the desired pressure, which are explained in Section 4.2.

2. To keep a constant relative sliding speed, the velocities v_u of the upper and v_l of the lower reservoir, are kept constant by applying the scheme described in Section 4.3.

3. The temperature inside the reservoirs is kept at 300 K by scaling the atomic velocity vectors, $\boldsymbol{v}_i$ in the z and y dimensions. The temperature rescaling is applied to only the translational degrees of freedom for the particles of consideration.

After the atomic positions have been assigned, the system is equilibrated at rest for 2.7 ps, which is sufficiently long to relax both blocks and the interface. During equilibration, the temperature of the entire system is kept at 300 K by scaling the atomic velocity vectors and the normal pressure of 5.1 GPa is applied, as described in boundary condition 1.

To start the actual friction simulation, the sliding speed, v_u, is added to the velocities of all atoms in the upper block and v_l to the velocities of all atoms in the lower block, respectively. The resulting velocity discontinuity establishes the sliding interface between the two material slabs that would otherwise be connected by cold welding. Once both material blocks move with a speed of v_r relative to each other, the MD simulation is performed for 270 ps with a time step $\delta t = 0.0027\,\text{ps}$. The time is long enough for the friction simulation to reach a quasi steady state, which is recognised by monitoring the tangential frictional force, f_{tang}. Beside the frictional force, the profiles of velocity, temperature and concentration are recorded. The measurements are taken every 100 timesteps and averaged over 100 values.

4.1.1 Selection of interatomic potentials for sliding friction

There is a variety of potentials commonly applied in MD simulations, which are derived from a range of models with different degrees of accuracy. First principles (ab initio) MD is the most accurate approach, because the calculation of the interatomic forces is obtained directly from electronic structures. However, this method involves extreme computational costs. Semi-empirical pair potentials such as Morse and Lennard-Jones potential as shown by Allen and Tildesley [2] are computationally much more efficient, but they fail to capture the physics of metallic bonding. To model interatomic interaction in metals efficiently and accurately, potentials based on the embedded atom method (EAM) have been developed by Daw et al. [45]. The EAM potential is defined as:

$$\mathcal{V}^{EAM} = \sum_{i=1}^{N} \left[F_i(\bar{\rho_i}) + \frac{1}{2} \sum_{j=1, j\neq i}^{N} U_{ij}\left(r_{ij}\right) \right] \tag{4.1.1}$$

where

$$\bar{\rho_i} = \sum_{j=1, j\neq i}^{N} \rho\left(r_{ij}\right). \tag{4.1.2}$$

The term $F_i(\bar{\rho_i})$ is the required energy to embed an atom i at site $\boldsymbol{r}_i$ with the electron density ρ_i contributed by atom i, and N is the number of atoms. The parameter $U_{ij}\left(r_{ij}\right)$ is the core-core pair interaction potential between the two atoms i and j separated by a distance r_{ij}. There are several parameters required by EAM potentials. These parameters are usually determined by fitting experimental data at a temperature of 0 K with data taken from perfect crystals, i.e. lattice constants, cohesive energy, elastic constants and vacancy formation energy, as described in [45, 66]. Most EAM potentials produce forces that are almost radially symmetric on the atoms. This is satisfactory when modelling materials with closed shell configuration (Cu and Ag) like most of the transition and noble metals that crystallise in an FCC lattice. These types have spherically symmetric bonding. The EAM potentials parameters for Cu and Ag used in the present study are the ones that are distributed along with LAMMPS. These have been developed and validated by Foiles et al. [66] and Daw et al. [45] using a range of thermodynamic quantities. They produce accurate properties and phase diagrams for pure Cu and Ag metals as well as for the Cu-Ag alloy.

Prior to performing friction simulations, the employed EAM potentials have been verified by calculating the melting points of Cu and Ag using the method proposed by [64]. At atmospheric pressure, the melting point of Cu was determined to be between 1250 K and

1290 K and that of Ag to be between 1100 K and 1200 K, which are in good agreement with Foiles and Adams [64]. For the pressure of 5.1GPa, which is used in the simulation, the simulated melting point was between 1500 K and 1600 K for Cu and 1550 K and 1650 K for Ag, which is in reasonable agreement with the experimental values of 1547 K and 1523 K for Cu and Ag respectively. It should be noted that these simulations were carried out under isotropic pressure and that for the friction simulations where stresses are highly anisotropic the material is expected to melt at lower temperatures.

4.2 Boundary conditions for compression

Molecular dynamics simulations, as opposed to experiments, are not limited by difficulties associated with obtaining high-velocity high-pressure regimes. Hence, modelling of the metal to metal deformation at high sliding and compression can be achieved as previously reported by the review of George [74]. Nevertheless, the difficulties lie more in the nature of having large system sizes and simulation times in order to obtain physically relevant results. Hammerberg et al. [86] showed that for a 2-D Cu/Cu system of lennard-jones particles with incommensurate interfaces a power law velocity dependence of the frictional force is present for three different uniaxial compressions, as shown in Figure 4.2. MD simulations show that as the uniaxial compression increases the frictional force also increases, which is generally true at both low and high speeds. As the velocity increases beyond the critical point approximately at 0.75 (Figure 4.2), the frictional force decreases as compression rises.

This section discusses and compares the implementation of the reflective plane and the pressure imposed via momentum flux for compressing metal slabs together.

4.2.1 Pressure application through reflective plane

The first attempt of applying the desired pressure was obtained by means of an artificially defined plane that holds as an obstacle to atoms passing across its surface. When atoms are approaching the plane their velocity vectors get reflected to the desired direction by $\boldsymbol{v}_i = -\boldsymbol{v}_i$. This is named the reflective plane and was given a mass, m_{rp}, velocity, v_{rp}, and external plane force, f_{rp}. Applying an external normal force onto the outermost atoms of the simulation domain as shown in Figure 4.1, introduces momentum and energy fluxes

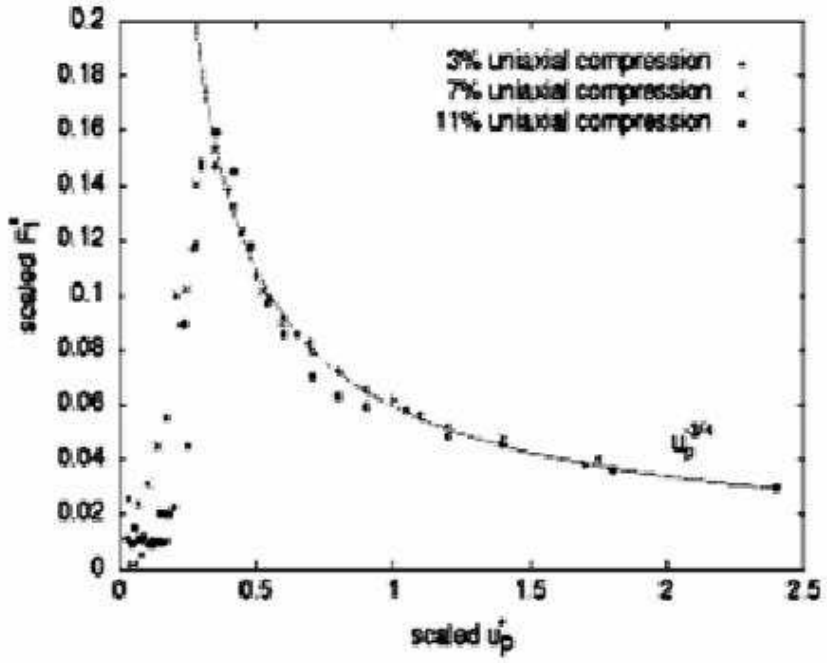

Figure 4.2: Scaled tangential force against scaled velocity of a 2-D LJ solid with an incommensurate interface. 3%, 7% and 11% uniaxial compressions are shown.

into the system. This is because the outermost atoms get accelerated by the plane to the desired direction. The implementation of this scheme leads to an uncontrollable energy transfer. The fluctuation of velocity leads to energy constantly fed to the system causing the oscillations shown in Figure 4.4. Figure 4.3 also shows the variation in system pressure over time indicating large fluctuations. Similar behaviour is observed if force is directly applied to the reservoir atoms by imposing a value of $f_i = (P_n A)/N_R$, where N_R is the number of atoms belong to the reservoir. The reflective plane scheme evaluates the overall plane force, F_{rp}, accelaration, $\boldsymbol{a}$, friction factor, $\boldsymbol{f}$, and updated reflective plane velocity, v^*_{rp}, by calculating every timestep these equations:

$$F_{rp} = f_{rp} + \sum_{i \in R} 2m_i v_i - v_{rp}\boldsymbol{f} \tag{4.2.1}$$

$$\boldsymbol{a} = F_{rp}\frac{1}{m_{rp}} \tag{4.2.2}$$

$$v^*_{rp} = v_{rp} + \boldsymbol{a}\Delta t \tag{4.2.3}$$

The first examination should be to verify that this plane imposes the correct pressure

of 5.1 GPa. In order to get quick results a small system had to be considered, in this case the domain was taken to be $(x, y, z) = (25, 100, 8)$ Å. Results show that the summation of the average force acting on each atom on the reservoir corresponds to the desired pressure. In other words, the actual pressure applied on the upper (Cu) and lower (Ag) reservoirs was indeed 5.1 and 5.0 GPa respectively. Consequently, the design of a new algorithm implemented into the molecular dynamics code is required to overcome the issue of imposing momentum by force, which was achieved by applying pressure via momentum flux as shown in Section 4.2.2.

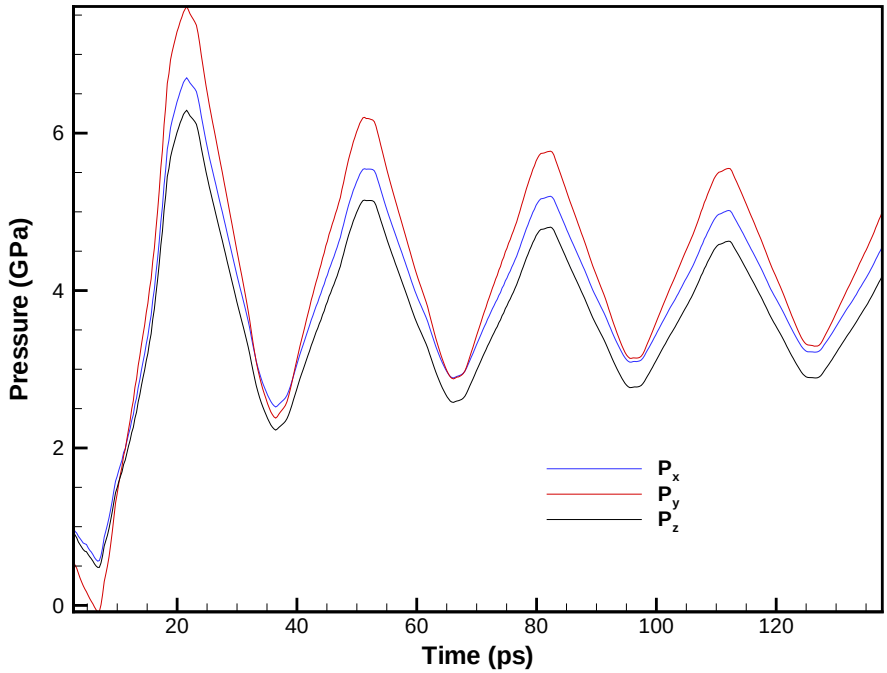

Figure 4.3: Pressure variation at 5.1 GPa: Simulation box containing 1.3 million atoms.

4.2.2 Pressure application through momentum flux

Identifying the issues associated with the reflective plane scheme the need to overcome the uncontrolled energy induced by atoms is required. The idea was taken by [132], which states that by separating the momentum transfer by stress from the transfer of energy flux by stress could give a solution to the uncontrollable oscillations within the system. To that mean a velocity reverse scheme was implemented in LAMMPS by the author. The idea implies that by reversing one component of the velocity vector $\boldsymbol{v}_i$ of an atom i introduces a momentum on the atom which is equal to $2m_i v_i$, however, its energy remains unchanged.

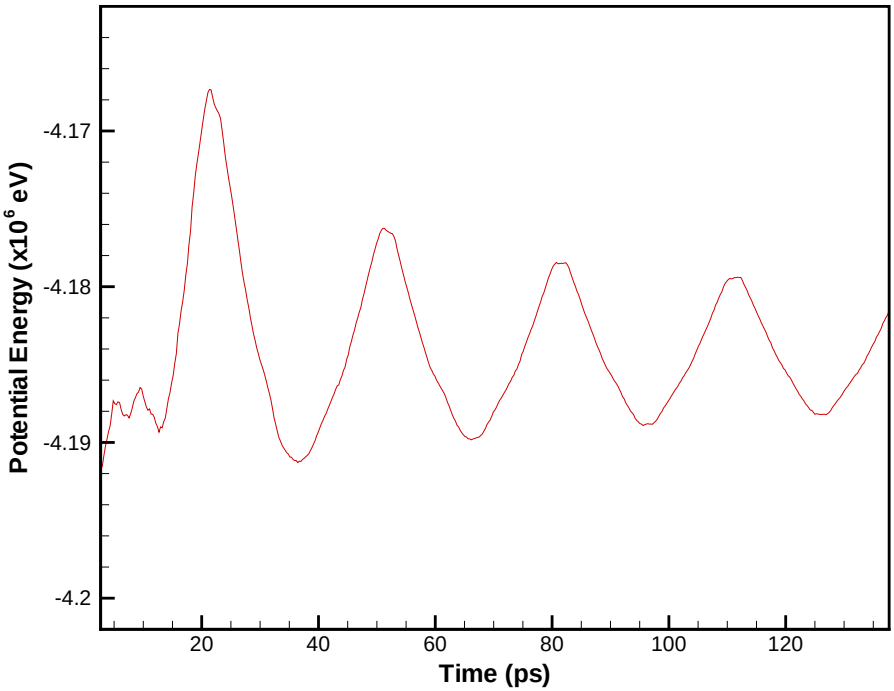

Figure 4.4: Potential energy variation: Simulation box containing 1.3 million atoms.

This idea implies that pressure should be applied in the form of momentum flux, hence starting from Newton's second law:

$$F_i = m_i \alpha_i \Rightarrow p_i \cdot A = m_i \cdot \frac{dv_i}{dt} \Rightarrow p_i = \frac{m_i}{A} \cdot \frac{dv_i}{dt} \tag{4.2.4}$$

By rearranging Equation 4.2.4 the momentum flux, $\boldsymbol{p}_i$, applied on each atom is obtained:

$$m_i \cdot dv_i = p_i \cdot A \cdot dt \tag{4.2.5}$$

where $m_i \cdot dv_i$ is the momentum $\boldsymbol{p}_i$ on each atom, thus Equation 4.2.5 becomes:

$$\boldsymbol{p}_i = p_i \cdot A \cdot dt \tag{4.2.6}$$

Figure 4.5 illustrates the idea behind the algorithm. The scheme implemented by the author uses the idea of searching for the atom with the highest position so when this atom is located momentum is applied corresponding to the desired pressure as shown in Equation 4.2.6. Additionally if the velocity sign was not the expected (for instance travelling toward the lower block in the positive direction), then this sign had to be reversed. By reversing the velocity an extra momentum is introduced to the system, and this had to be subtracted

from the overall momentum in each timestep. The amount of momentum to be subtracted is $\Delta\vec{p} = 2m_i\vec{v}_i$. As the simulation progresses the overall pressure applied was observed to be that desired with less oscillations of the total and potential energies of the overall system.

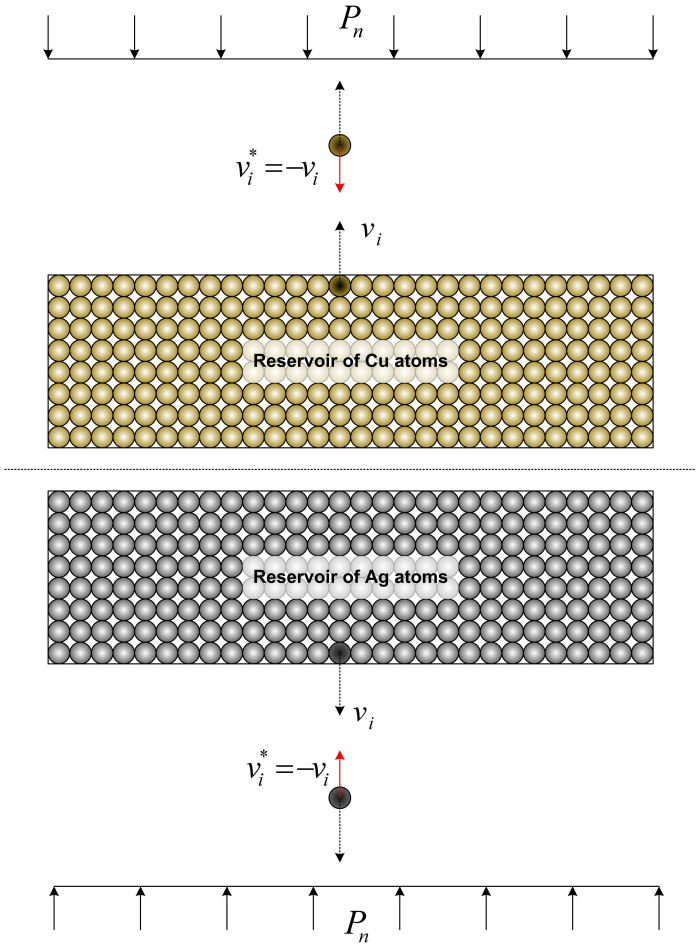

Figure 4.5: Schematic representation of pressure applied on reservoirs.

4.2.3 Results of small scale system

Compressing Cu/Ag materials at desired pressure of 5.1 GPa was obtained for domain size of $(x, y, z) = (25, 100, 8)$ Å containing 1278 atoms in total. The reason for choosing this small domain was to obtain results relatively quickly. As can be seen from Figures 4.6 and 4.7, the scheme shown in Section 4.2.2 achieves better thermodynamic equilibrium compared to the reflective plane method. Temperature variation also looks better compared to reflective plane in Figure 4.8. Nevertheless, in both cases the average force acting on the reservoir atoms corresponds to the desired pressure which is 5.1GPa. Table 4.2 illustrates

the results of each method.

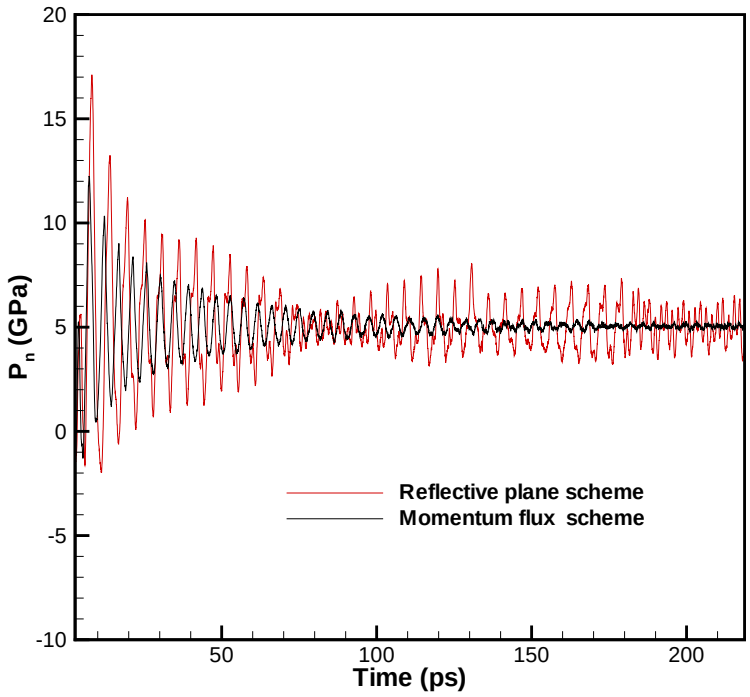

Figure 4.6: Pressure applied through momentum flux and reflective plane tool.

Cu Reservoir (GPa)	Ag Reservoir (GPa)	Scheme
5.1	-5.0	Reflective plane
5.0	-5.1	Momentum flux

Table 4.2: Pressure acting on the reservoirs using the two schemes.

Finally, an additional command was implemented into the MD code and this is to apply a tangential force acting on the reservoirs. The idea was to apply a force in the x direction so that the velocity of each atom is kept constant. In general the frictional force is defined as the force required keeping the relative motion between two blocks. The sliding direction took place in the ⟨100⟩ of Cu(010) on Ag(010) crystallographic planes.

4.3 Method of applying high sliding speeds

This section presents the method used to impose a constant velocity on all atoms on the reservoir region of the simulation box. The purpose of making this was to keep a constant sliding speed. The velocities v_u of the upper and v_l of the lower reservoir, are kept constant

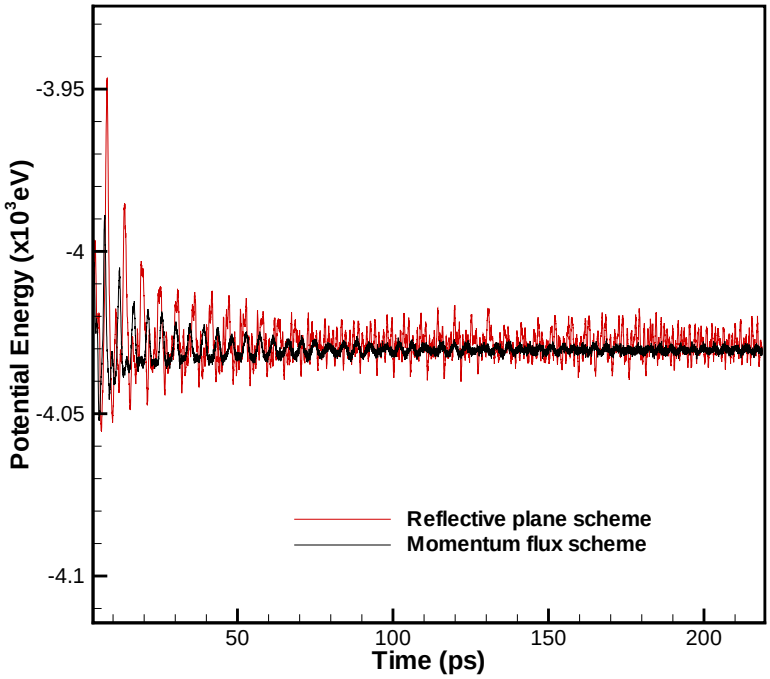

Figure 4.7: Comparison of potential energy between different tools.

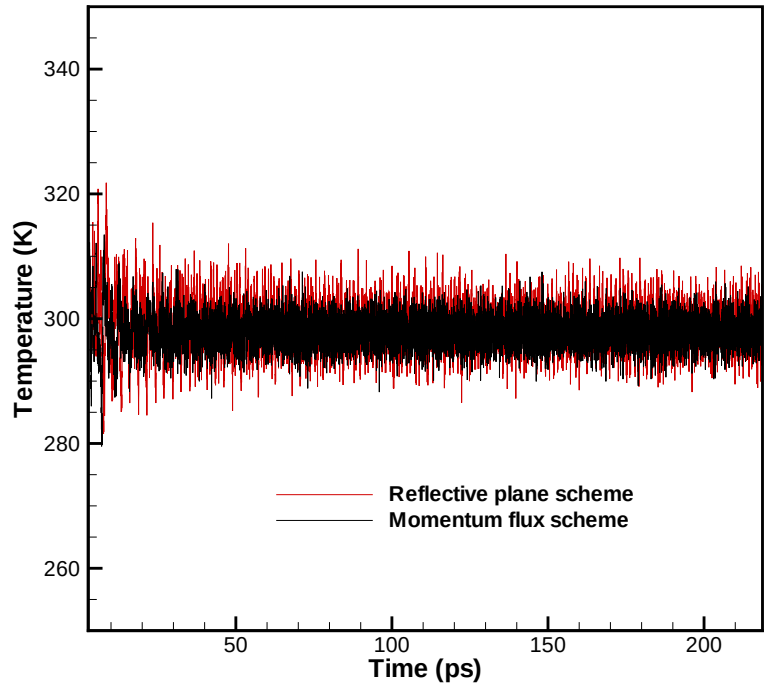

Figure 4.8: System's temperature variation. Momentum flux and reflective plane comparison.

so that the relative sliding speed v_r is given by $v_r = 2v_u = 2v_l$, the upper and lower velocities are equal in magnitude but different in direction ($v_u = -v_l$). This is achieved by correcting the velocities of each atom at each time step. The velocity vector $\boldsymbol{v}_{ix}$ of each atom i of the upper reservoir is corrected by:

$$\boldsymbol{v}_{ix} \rightarrow \boldsymbol{v}_{ix} + \left(\frac{v_r}{2} - v_u^*\right) \text{ with } v_u^* = \sum_{i=1}^{N_{RCu}} \boldsymbol{v}_{ix} \ , \tag{4.3.1}$$

where N_{RCu} is the number of atoms in the copper reservoir and v_u^* is the corrected velocity for the upper block. The tangential force F_t that is required to keep the constant speed can then be calculated by

$$F_t = \frac{m_{Cu} N_{RCu}}{\delta t}\left(\frac{1}{2}v_r - v_u^*\right) \tag{4.3.2}$$

where m_{Cu} is the atomic weight of copper and δt the time step of the MD simulation. The algorithm was created such that the desired constant velocity could be applied in any direction, however in this simulations constant velocity was applied only in the x-direction. The atoms in the Ag block were handled in the same way.

4.4 Evaluating sliding friction and interfacial thickness at several domain sizes

The algorithms described in the previous sections of this chapter for applying pressure in the reservoir regions as well as to keep the velocity constant, have been successfully implemented in the MD code and validated to ensure the desired conditions. The aim of this section is to analyse and validate the frictional model at conditions of high relative speed. This work was conducted for a Cu/Ag tribopair at relative sliding speeds of 200 m/s at different simulation domain sizes to evaluate the coefficient of friction (CoF), μ.

Table 4.3 presents the results obtained from six different domain sizes, starting from an initial domain of (x,y,z) =(70,380,60) Å and varying the x, y and z dimension appropriately. Initially, both materials were compressed to each other at pressure of 5.1 GPa with controlled temperature of the entire domain at 300 K. After equilibration, relative sliding speed of v_s=200 m/s was imposed for simulation time of 270 ps. The limited number of tests performed show the friction coefficient is independent of the simulation domain sizes. Nevertheless, to confirm the trend shown in this study, additional simulations are required

at different velocities and domain sizes. The frictional force per unit area (F/A) indicates an increase as the x and z dimensions increase. Nevertheless, the F/A remains constant when the y-dimension is doubled, which is also shown in results obtained by Hammerberg et al. [90].

Interfacial thickness (IT) is the region in which Cu and Ag atoms coexist during the above sliding conditions. It was shown that a small change in the x, z dimensions does not affect the interfacial thickness. However an increase in IT is observed if the x, z dimensions are tripled in size, which shows that the interfacial thickness changes by varying the simulation size.

Atoms	(x y z) Å	CoF (μ)	F/A (GPa)	IT (Å)
$120{\cdot}10^3$	70 380 60	0.263	1.335	19.8
$197{\cdot}10^3$	70 380 100	0.296	1.520	19.8
$589{\cdot}10^3$	70 380 300	0.270	1.367	27.0
$169{\cdot}10^3$	100 380 60	0.273	1.393	19.8
$512{\cdot}10^3$	300 380 60	0.294	1.521	25.2
$129{\cdot}10^3$	70 700 60	0.260	1.337	23.8

Table 4.3: X, Y and Z dependencies at relative sliding speeds of 200 m/s.

4.5 Atomistic visualisation

Atomistic visualisation plays a vital role in materials modeling when systems with an increasing number of atoms are involved. Important materials intrinsic and other properties such as Young's modulus, fracture, yield stress, shear stresses are associated with mechanical deformations, defects, dislocations and friction in solids and thin films. Materials become deformed or distorted upon the application of external forces, displaying a small region in which the deformation is reversible, the so-called elastic regime. If this external force is increasing the deformation then becomes irreversible and this deformation remains after the force or stress is removed, the so-called plastic regime. This area of research poses an interesting computational challenge for atomistic calculations and therefore the visualisation of large-scale models is necessary to observe related phenomena. As discussed by Li [152] visualisation is not a software engineering problem but also a physics and mechanics issue. The main function is to discover new structures, kinetic pathways and micro-mechanism with atomic resolution.

One of the main drawbacks of atomistic simulations are the large computational resources necessary to perform the simulations and the difficulty of analyzing the outcomes of these simulations. In other words post-processing the results, by accessing enormous files typically 1 to 3Gb size in simulation cases ranging from 1 to 3 million atoms, could be a relatively slow process depending on the computer specifications. There are several visualisation softwares for scientific research available by purchasing license such as Materials Studio, HyperChem, CAChe, ChemOffice, etc. and several others which are free and accessible to everyone such as VMD developed by Humphrey et al. [116], Rasmol by Sayle and Milner-White [212], Raster3D by Merritt and Bacon [178], AtomsViewer by Sharma et al. [219], and AtomEye by Li [153].

The purpose of this section is to show the results taken using VMD and AtomEye applications. These are the two applications primaraly used in this work. Visual molecular dynamics (VMD) was widely used for day-to-day research (a snapshot is given in Figure 4.9), however its capabilities were not enough to show how the microstructure changes under conditions of high pressure and sliding forces. As mentioned previously, the present work attempts to gain further insight into the atomic displacement processes taking place at sliding interfaces by employing molecular dynamics simulations along with the appropriate software for visualisation. There are several parameters for analysing defects, amongst which are the coordination number as shown by Callister [28] and the central symmetry parameter or centro-symmetric parameter.

To analyse how the microstructure evolves due to the high pressure and sliding speed conditions the centro-symmetric parameter was used. As a measure of the local lattice disorder, the centro-symmetric parameter as described by Kelchner et al. [140] is calculated for individual atoms and its value characterises whether the atom is part of a perfect lattice, a surface or a local defect, such as a stacking fault or a dislocation. For FCC materials, e.g. Cu and Ag, each atom is surrounded by 12 neighbour atoms which can be sorted into 6 pairs of opposite atoms. To calculate the centro-symmetric parameter for an atom i, the positions, $\boldsymbol{r}_j$, of its 12 nearest neighbour atoms ($1 \leq j \leq 12$) are sorted in such a way that $\boldsymbol{r}_j$ and $\boldsymbol{r}_{j+6}$ are opposite in respect to the position, $\boldsymbol{r}_i$, of the central atom. The centro-symmetric parameter is then given by:

$$c_i = \sum_{j=1}^{6} \left| \boldsymbol{R}_j + \boldsymbol{R}_{j+6} \right|^2 \ , \tag{4.5.1}$$

where $\boldsymbol{R}_j = \boldsymbol{r}_j - \boldsymbol{r}_i$ and $\boldsymbol{R}_{j+6} = \boldsymbol{r}_{j+6} - \boldsymbol{r}_i$ are the vectors from the central atom i to a pair

of opposing neighbour atoms j and $j+6$. If atom i is embedded within a perfect lattice, each of the 6 summands is equal to zero ($\boldsymbol{R}_j = -\boldsymbol{R}_{j+6}$) and, hence, the centro-symmetric parameter is also zero ($c_i = 0$). For imperfect lattices, the vectors $\boldsymbol{R}_j$ and $\boldsymbol{R}_{j+6}$ are not exactly opposite resulting in positive values of the centro-symmetric parameter that reflect the degree of material distortion.

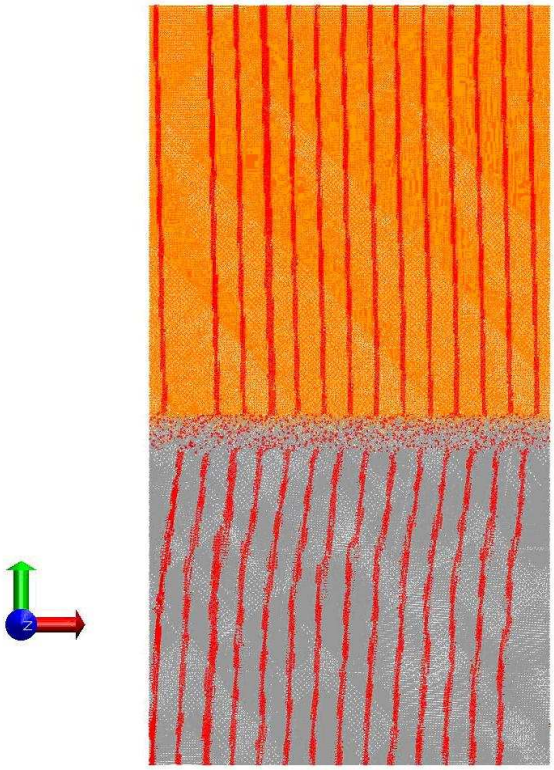

Figure 4.9: Snapshot of VMD at 400 m/s.

Therefore, it was necessary to find an application that has the capability of colouring the atoms according to a scalar value, i.e. centro-symmetry, coordination number. Figure 4.10 illustrates the final state under the application of 5.1 GPa pressure upon a domain size of (x,y,z) =(30,60,10) nm, which contains total 1.3 million atoms as shown in Table 4.1 (Domain (2)). Atoms were coloured according to the centro-symmetric parameter, c_i, and as can be seen no defects were recorded. The upper part is the Cu and the lower is the Ag, the interface is clearly shown were the colours of the atoms are slightly different. Additionally the results of the particular domain size are discribed in chapter 5. Figure 4.11 is a snapshot of the same system (Domain (2) of Table 4.1) taken as both slabs slide with relative velocity of 100m/s.

AtomEye developed by Li [153] was choosen to be the better option and this is because of the great functionalities offered. Amongst those are parallel and perspective projec-

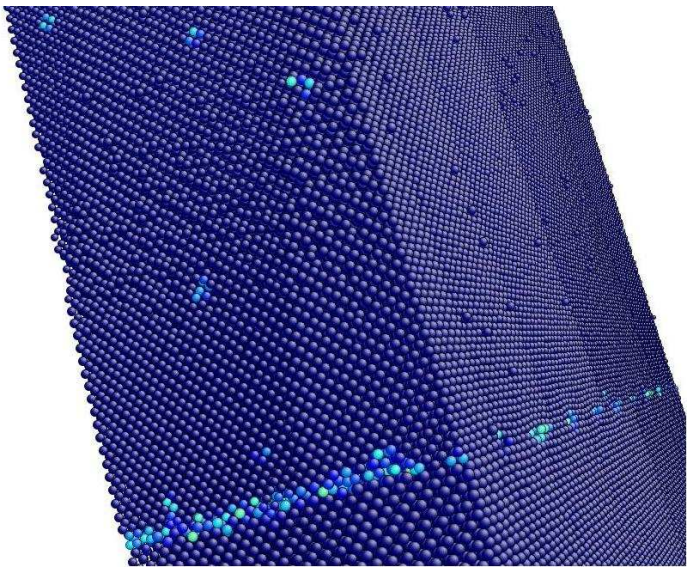

Figure 4.10: Visualisation of 1.3 million atoms with AtomEye software.

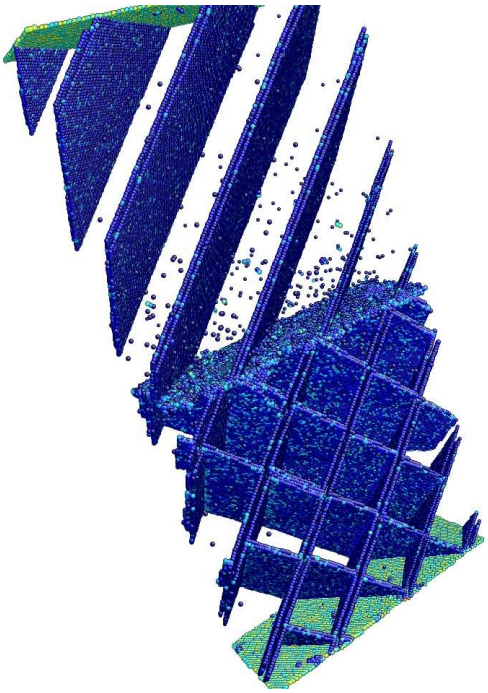

Figure 4.11: Sliding of Cu/Ag at 100m/s.

tions with full three-dimensional navigation; customizing bonds and coordination number calculation; colour-encoding of arbitrary user-defined quantities; calculation of the local atomic strain invariant; periodic boundary condition translations capability, high-quality JPEG, PNG and EPS screenshots; and animation scripting. The format of the files used by AtomEye was CFG (with file extension *.cfg), thus a file conversion tool was necessary to convert LAMMPS dump files with atomic trajectories appropriate CFG format.

CHAPTER 5

Molecular dynamics simulations of dynamic friction

"We build too many walls but not enough bridges."

Isaac Newton

Nanotribology studies are required to develop fundamental understanding of the interfacial phenomena taking place on a small scale. Frictional studies have applications on high-speed machining, ballistic penetration modelling, micro/nanomechanical systems (MEMS/NEMS) and many more due to the need for investigating the behaviour of rapidly moving interfaces. This chapter discusses the investigation of the velocity weakening of the frictional force and the structural transformation of nanocrystalline tribopairs. The heat dissipation in the proximity of the interface and its relation with the atomic diffusion and hence material mixing is also discussed.

5.1 Introduction

The phenomenon of friction at high speeds has been studied by various researchers [84, 85, 141]. Generally, modelling of sliding at material interfaces requires a thorough understanding of friction phenomena occurring at the atomistic level and at a nanoscale. Rigney et al. [206] showed that these include phase changes and various structural transformations

which are accompanied by composition changes due to material mixing that develops at the interface of these systems. Friction is a dissipative process that converts the kinetic energy of the sliding materials into heat, increasing the temperature in the proximity of the interface. For high sliding speeds, the temperature exceeds the melting point and a film of liquid material forms at the interface. Since the liquid film poses less restriction to sliding, the frictional force is significantly reduced. This is known as velocity weakening of the frictional force and has been demonstrated by the early experimental work of Bowden and Freitag [21] on friction of metal on metal at high sliding speeds. The earlier work by Bowden and Thomas [25] and [23] on various tribopairs showed that the frictional heating on the interface raised the local temperature to very high levels, although the temperature of the metal away from the sliding surfaces was quite low. Experimental studies of Bowden and Persson [22] and MD simulations by Hammerberg and Rigney [85] confirmed that for metals substantial velocity weakening occurs, which must be attributed to melting. Furthermore, experiments of Rigney et al. [205] have shown characteristic microstructural changes during ductile metal sliding, which indicate a highly strained plastic region near the interface.

Understanding of the mechanism of velocity weakening, structural changes, and diffusion at the interfaces is important in order to have a complete picture of the physics that control the forces acting across materials interfaces. There have been few attempts to model these phenomena. Continuum models are largely inadequate, since they are unable to model important complex physical phenomena at the interface and, thus, a microscopic analysis is required.

The following section present the results of large scale MD simulations of dynamic friction at Cu/Ag interface under high compression forces and high sliding speeds. The atomic information of the MD simulation allows a detailed analysis of the frictional force versus sliding speed, structural changes at the interface, diffusion in the proximity of the interface, the development of the heat dissipation and temperature profiles.

5.2 Results and discussion

This section analyses the results obtained by the MD dynamic friction simulations. If not stated otherwise the presented results refer to simulation domain (1) with the dimensions given in Table 4.1. As described in the previous section, the frictional force, F_t, approaches

a plateau value during the simulation around which it fluctuates. The level of the plateau can be obtained by averaging F_t in time, once the simulation has reached a steady state. This is shown in Figure 5.1 for the case of $v_r = 200\,\mathrm{m/s}$.

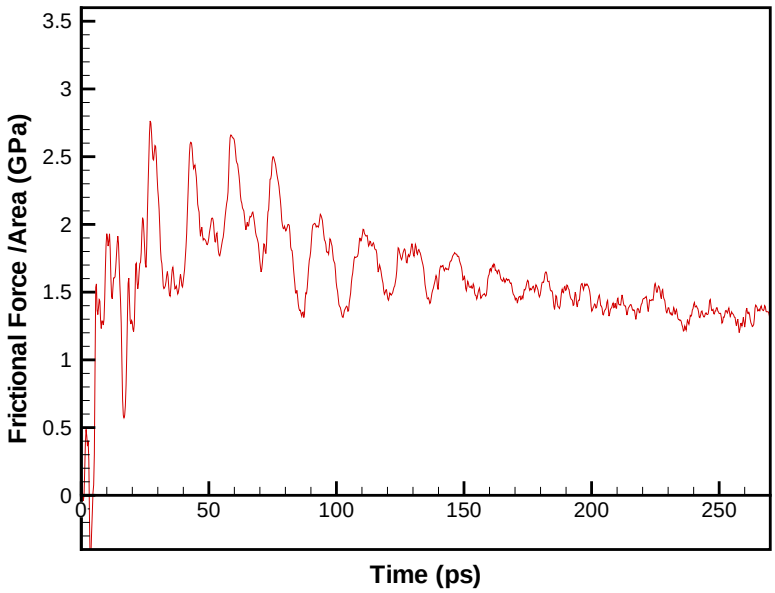

Figure 5.1: Frictional force per unit area at 200m/s relative speed.

In Figure 5.2, the averaged values of F_t (normalised to the surface area $L_x L_z$) are plotted against the relative sliding velocity v_r for both domain sizes. The graphs show that at low speeds ($v_r < 100$m/s), the frictional force is low and increases linearly. As the sliding speed increases further, the increase of the frictional force slows down and peaks at $200\,\mathrm{m/s}$ (critical speed). Increasing the sliding speed further leads to a decrease in the frictional force, approaching a plateau.

The curves are compared with the results obtained by Hammerberg et al. [89] for sliding friction of Cu/Ag, for the same geometrical dimensions as case (1) (Table 4.1). A smaller domain size is also presented in case (2) (Table 4.1) consisting of approximately 1.3 million atoms to confirm that in these simulations the domain size does not play an important role with regards to the critical speed. The trend in all three cases presented is consistent, although the point of maximum frictional force per unit area is higher in the results from Hammerberg. The difference can be accounted to contributions of the different interatomic potentials used [1] for the simulations. The interatomic potentials used in this study

[1] Email communication with James Hammerberg

were developed by Daw et al. [45] and Foiles et al. [66], whereas the potentials used by Hammerberg were developed by Johnson [129] and are described by Sprague et al. [221]. Another reason could be that Hammerberg used a simulation time of only 135 ps. This time was too short in some cases to reach a steady state and, therefore, the simulation time was doubled to 270 ps as seen in Figure 5.1. For the simulations with speeds greater that 400 m/s, Hammerberg used rough surfaces and reported that there is no difference to the results of simulations with smooth surfaces. This is logical if one considers that at higher speeds the interface liquifies so that surface features are destroyed almost instantly after commencing the sliding motion. All simulations in this study were conducted on smooth surfaces and the results proved to be consistent. It can be concluded that the original surface structure plays an unimportant role for the sliding process at speeds greater than 400 m/s.

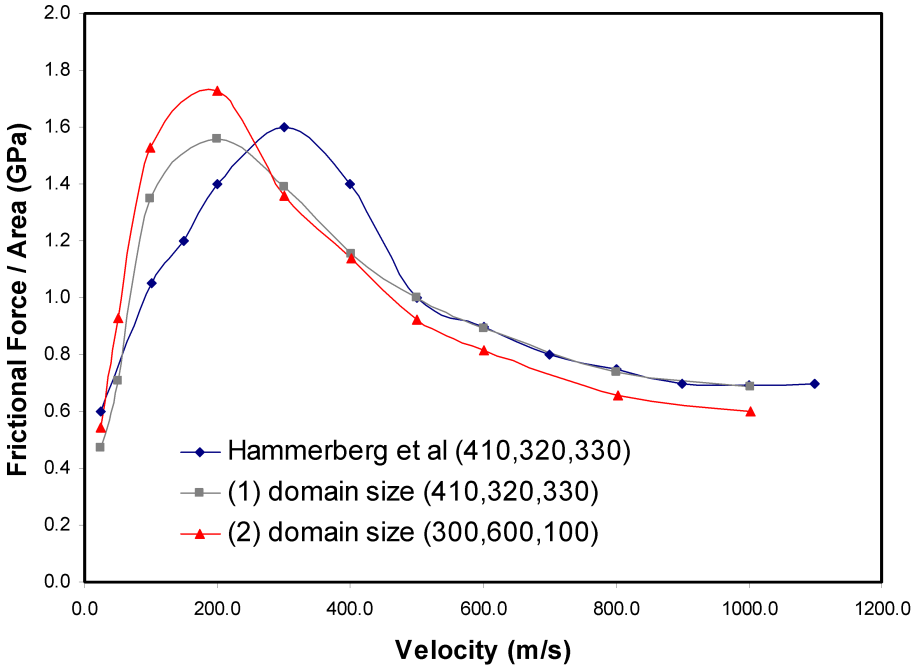

Figure 5.2: Velocity weakening phenomenon of the frictional force.

Figures 5.3 and 5.4 show the visualisation of the Cu/Ag system for relative sliding speed v_r of 200 m/s at initial (27 ps) and final stage (270 ps); the atoms are coloured according to the central symmetry parameter, c, using the AtomEye visualisation software developed by Li [153]. In these pictures only atoms with $0.03 \leq c \leq 0.05$ are visualised. This excludes atoms which are embedded in a perfect FCC crystal and visualises atoms that are part of stacking faults (intrinsic stacking faults are visible at centro-symmetry value of 0.042 in FCC crystals). Some of the isolated atoms visible do not belong to planar stacking faults, but represent local faults in the crystal structure. For low relative sliding velocities (25 m/s),

no indication of significant defects in either the Cu or the Ag slab could be found. For v_r above 50 m/s, a highly localised region of dislocations on both materials appear near the interface. Figure 5.3 shows dislocations for the case of $v_r = 200$ m/s shortly after sliding commences. Within the softer material (the lower block of Ag), dislocations that originate from the interface have progressed outwards. At the time shown, one stacking fault has already reached the reservoirs. The harder material (the upper block of Cu), shows no indication of deformation. At later times (Figure 5.4), both blocks are plastically deformed, and atoms near the interface show amorphous characteristics due to the high temperature, which is near the melting point of Ag.

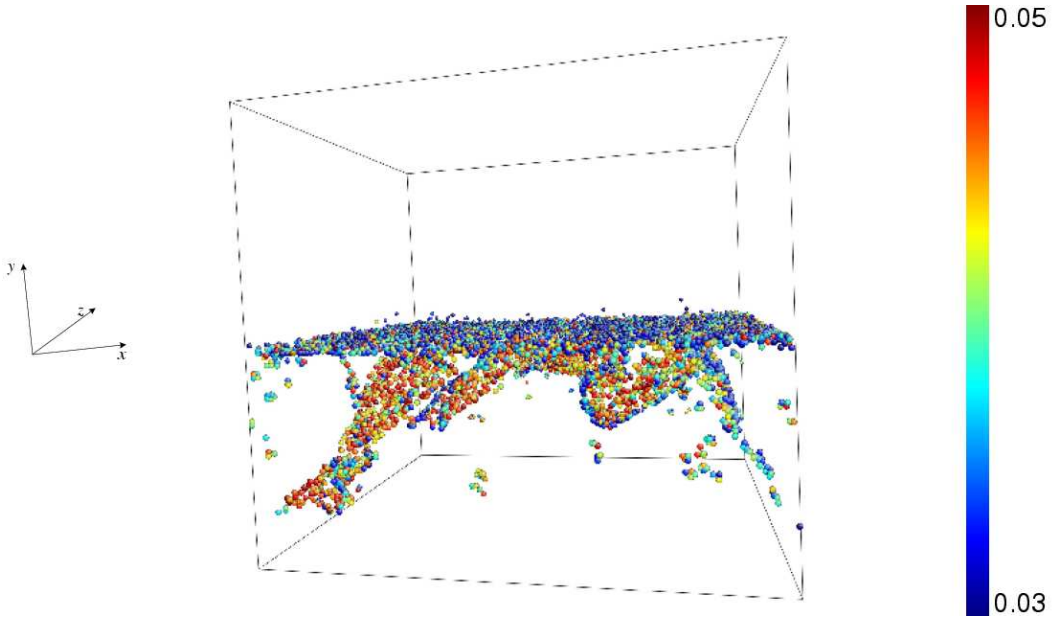

Figure 5.3: Visualisation of the central symmetry parameter for $\Delta V = 200$ m/s speed at 27 ps. The upper block is Cu and lower Ag.

5.2.1 Pressure equilibration and atomic diffusion

This section addresses the physical properties of solid interfaces. Interfacial issues in materials have been investigated by several researchers over the years. Wolf [256] distinguishes the difference between geometry and structure of an interface. This categorisation is due to the fact that lattice-parameter changes in the interfacial region (Cu/Ag) cause interfacial stresses that have an effect on the physical properties and chemical composition near the interface.

The understanding of the atomic diffusion across the interfaces of solid materials is

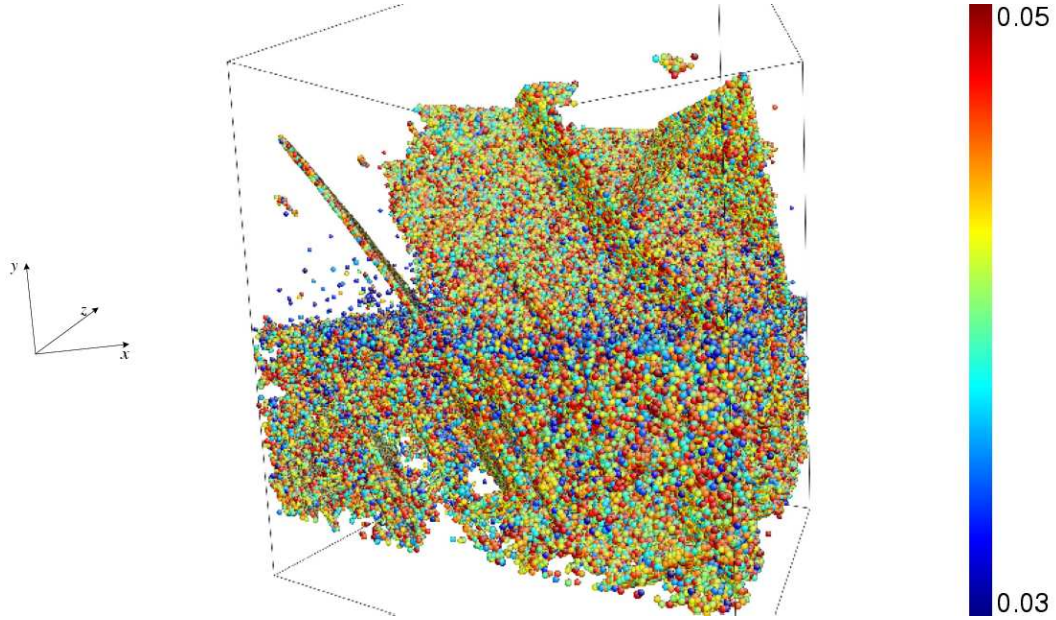

Figure 5.4: Visualisation of the central symmetry parameter for $\Delta V = 200\,\mathrm{m/s}$ speed at 270 ps. The upper block is Cu and lower Ag.

crucial for explaining the transformations of the material structure of metal surfaces that have been subject to high speed friction. Also, controlling the diffusion process is the key to several technologies such as welding [35, 34] and areas where dynamic friction dominates, i.e. friction stir welding [217, 27]. Welding using the friction stir technique influences both the material flow and the heat generation caused by the frictional force and the applied normal load. [171] showed that an interesting characteristic of the Cu-Ag system is the immiscibility at temperatures below 650 K due to the peculiarities of the eutectic point of the alloy. Indeed the mixing of Cu-Ag is only obtained at higher temperatures and formation of amorphous Cu-Ag is observed in this study. Molecular dynamic simulations provide the opportunity to calculate the atomic diffusion coefficient, $\mathcal{D}$, directly from the mean square displacement (MSD), which is a measure of the average distance a molecule travels. The definition of the one dimensional MSD is:

$$\mathrm{MSD} = \frac{1}{N}\sum_{i=1}^{N} |r_i(t) - r_i(0)|^2 \tag{5.2.1}$$

where $r_i(t)$ is the position component of atom i in the respective dimension x, y or z at time t. Using the Einstein expression [175] the diffusion coefficient, $\mathcal{D}$, is obtained from the one dimensional MSD by:

$$\mathcal{D} = \lim_{t\to\infty}\left(\frac{1}{2t}\mathrm{MSD}\right) \tag{5.2.2}$$

Prior to the investigation of the MSD under sliding condition, the diffusion across the interface was measured at rest while applying the normal pressure. Previous studies concerning atomic diffusion at certain pressures have been reported by Chen et al. [35]. This work studies the diffusion bonding of Cu-Ag slabs at pressures of 50, 100 and 150 MPa at three different cooling rates. The system is heated at a temperature of 1150 K and then cooled down, transforming the interface from amorphous to a crystalline structure. The stress applied plays an important role in diffusion showing that at lower pressure values, i.e. less than 100 MPa, there is no significant diffusion observed. The thickness of the interface is associated with pressure; higher normal pressure results in a higher thickness of the interface. In this study the interfacial thickness is considered as the region in which both materials (Cu/Ag) coexist. This work shows that there is little atomic diffusion between Cu and Ag blocks during pressure equilibration. The graph of percentage material concentration versus the y dimension indicates an interfacial region value of 4.5 Å, which is insignificant.

5.2.2 Mean square displacement (MSD) at various speeds

An example of the MSD results obtained at various speeds is discussed in this section. The MSD was calculated in the z-dimension, as x and y-dimensions are biased due to the simulation setup. As can be seen in Figure 5.5, the diffusion of Cu atoms increases for higher relative speeds. The same is observed for Ag (Figure 5.6), though the MSD values are slightly higher than those of the Cu atoms. This is expected since silver has a lower melting point T_m than copper and the transition of Ag from solid to liquid phase happens faster than that for Cu, especially near the interface.

Furthermore, three different groups of atoms were defined within the Cu block according to the geometrical regions in Table 5.1 to investigate the MSD at different distances from the interface and, in particularly, the state of the interfacial atoms. The lower region starts directly at the interface, which is located at y=210 Å and the upper region extends to the beginning of the reservoir at y=360 Å. Figure 5.7 shows that near the interface (lower group) the diffusion is much higher than in the middle or the upper groups. This is an indication of transition from solid to liquid phase in the interfacial region; the y-direction MSD results of the lower group also confirm this.

Although the calculation of the MSD is a good tool to analyse phase transition, it is not

Region	xlo,xhi (Å)	ylo,yhi (Å)	zlo,zhi (Å)
Lower	150, 180	210, 240	0, 330
Middle	150, 180	280, 320	0, 330
Upper	150, 180	330, 360	0, 330

Table 5.1: Regions of the Cu groups for calculating MSD.

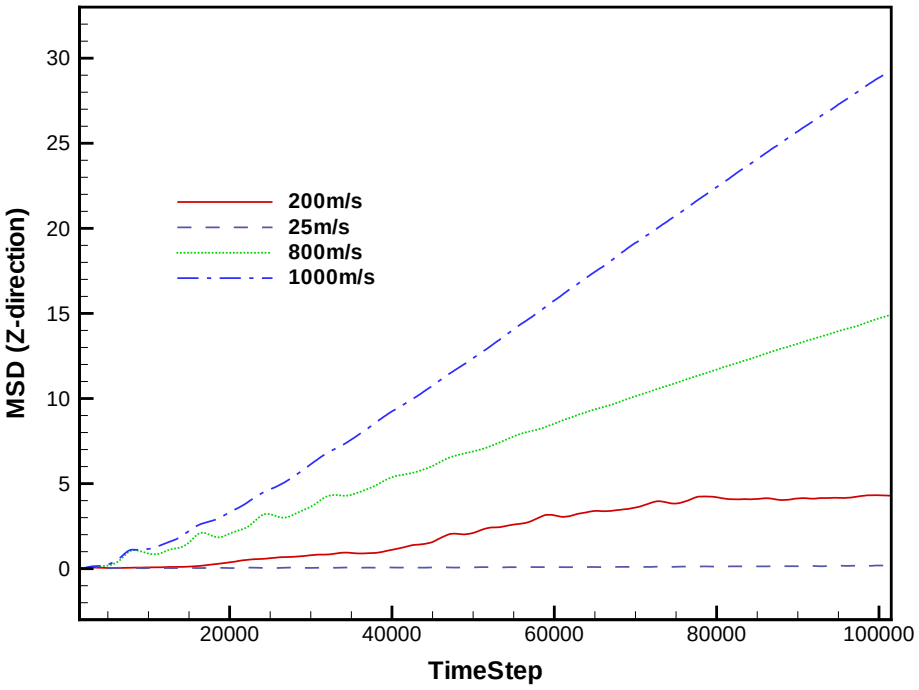

Figure 5.5: Z-direction MSD of Cu atoms at relative speeds of 25, 200, 800 and 1000m/s.

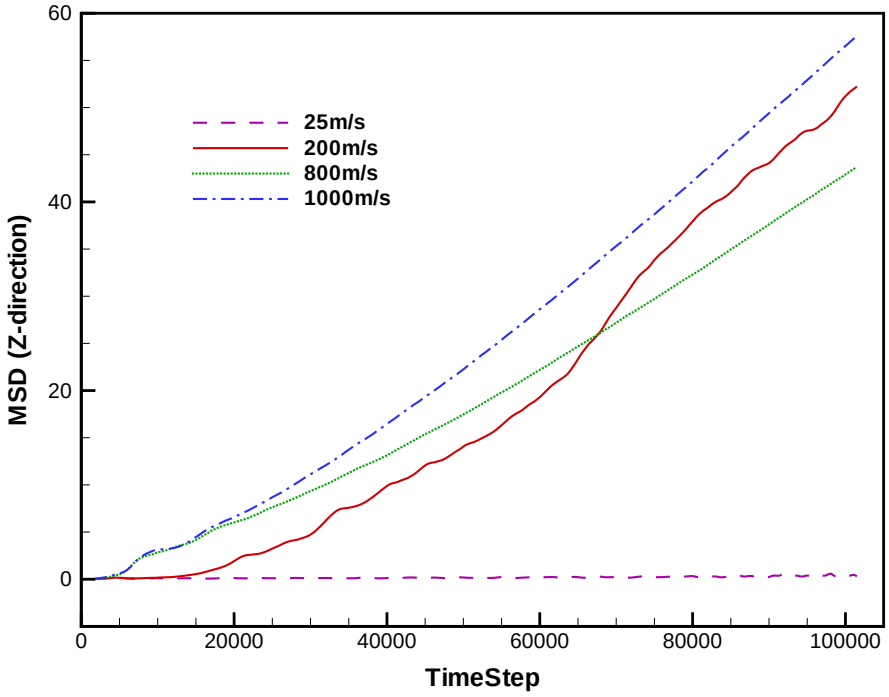

Figure 5.6: Z-direction MSD of Ag atoms at relative speeds of 25, 200, 800 and 1000m/s.

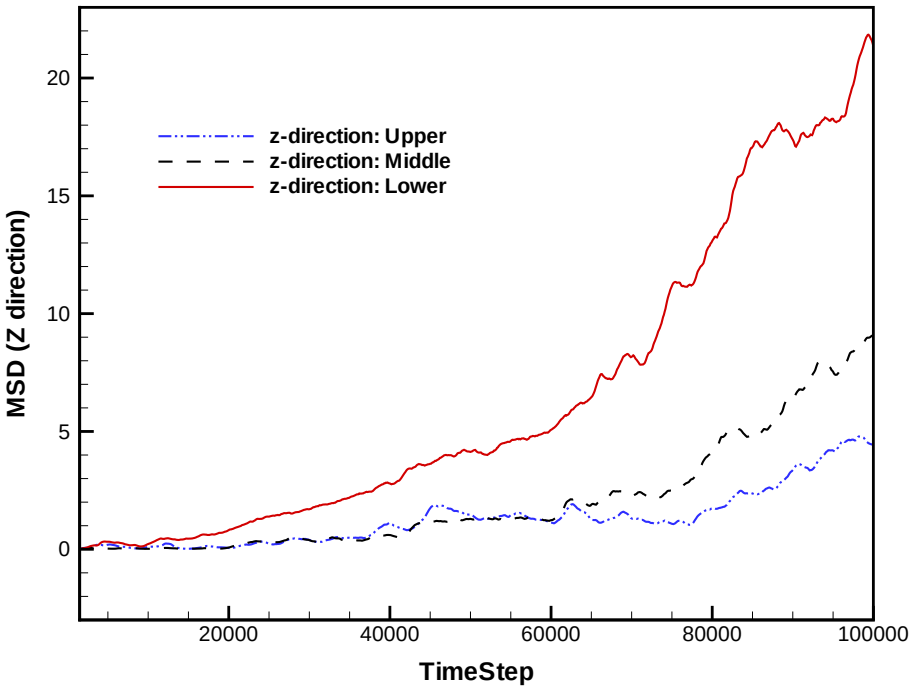

Figure 5.7: Z-direction MSD of Cu lower middle and upper groups; Obtained at relative speed of 200m/s.

accurate for measuring the mixing across the interface due to the varying rate of diffusion in time and space along the y-axis. The effects in the y-direction are more efficiently captured by evaluating material's concentration percentage. The study of the material's concentration percentage across the y-directions reveals the mixing of the interfacial region. The simulation box is initially set up so that the interface between Cu and Ag block is at the position of y= 210 Å. Nevertheless, the position is slightly shifted when applying the normal pressure because of the different compressibility of the two materials. The concentration of Cu and Ag atoms along the y-direction for different sliding speeds at 270ps simulation time are shown in Figures 5.8, 5.9 and 5.10. To measure the interfacial thickness, the same criteria as Chen et al. [35] were applied, who considered the interface (mixing region) to be limited by a concentration threshold of 5 %. Using this criteria, the interface thickness can be determined from the concentration plots. Figures 5.10 and 5.11 also show that the interfacial region consists of both Cu and Ag atoms. As can be seen, from 25 to 1000 m/s the interfacial thickness increases dramatically giving values of 19.32 Å, 27.37 Å and 83.72 Å. Carefully examining these figures one can observe that the interface stretches further into the Ag side than into the Cu side, which indicates that more Cu atoms diffuse into the Ag block than Ag atoms into the Cu block. That is consistent with Chen's study [35] and can be attributed to three causes: (1) the temperature in the Ag block is higher than in the Cu block; (2) together with the lower melting temperature of Ag this enables a faster diffusion within the Ag block (compare MSD for Cu and Ag in Figures 5.5 and 5.6); (3) the smaller size of Cu atoms may allow them to diffuse faster through Ag.

Finally, in Figure 5.12 the interfacial thickness is plotted against time (both axis are in logarithmic scale) for sliding speeds of 25, 400 and 1000 m/s. As expected, the interfacial thickness increases in time for all sliding speeds and it increases faster for higher sliding speeds. Hence, the diffusion is significantly higher for higher sliding speeds, resulting in thicker interfaces after the same simulation time. At a sliding speed of 25 m/s, the interfacial thickness reaches a maximum value. However, that does not happen for speeds greater than 25 m/s within the simulated time of 270 ps (compare the 400 m/s curve). Thus, the simulation time was doubled to 540 ps for the highest sliding speed of 1000 m/s to investigate the further development of the interface. One can see that the interfacial thickness flattens, but still does not reach a plateau within this time.

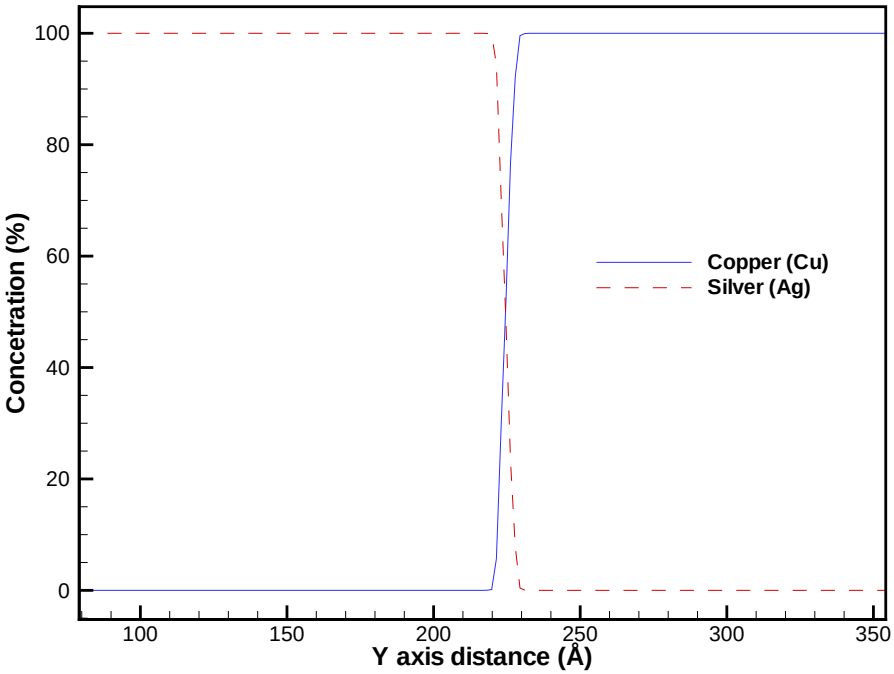

Figure 5.8: Material's concentration at 25m/s.

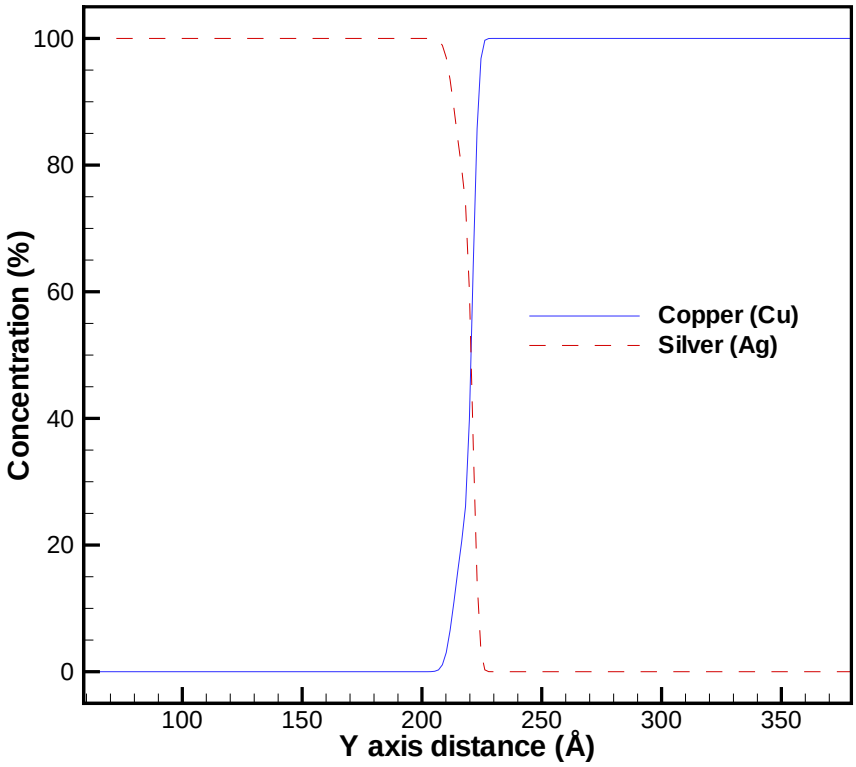

Figure 5.9: Material's concentration at 200m/s.

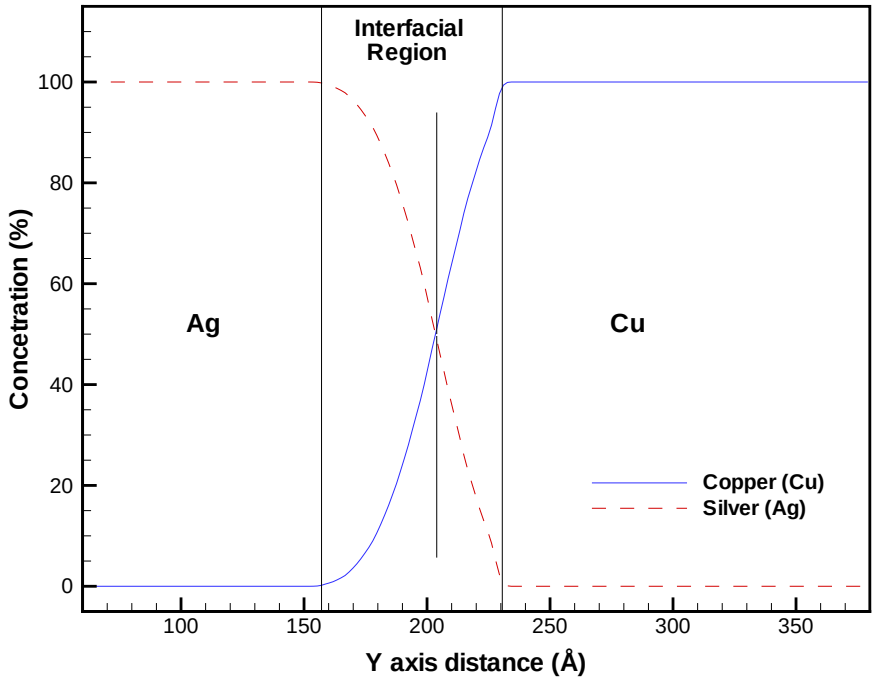

Figure 5.10: Material's concentration at 1000m/s.

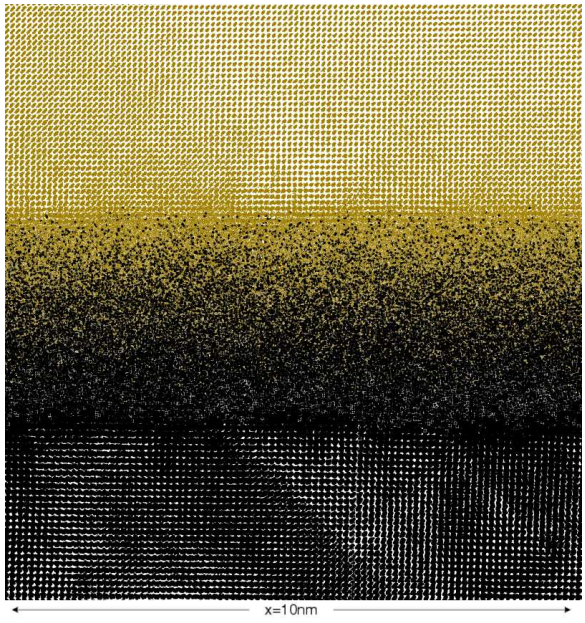

Figure 5.11: Snapshot close to the interfacial region at time 270ps. Sliding speed of 1000m/s, upper block is Cu and lower is Ag.

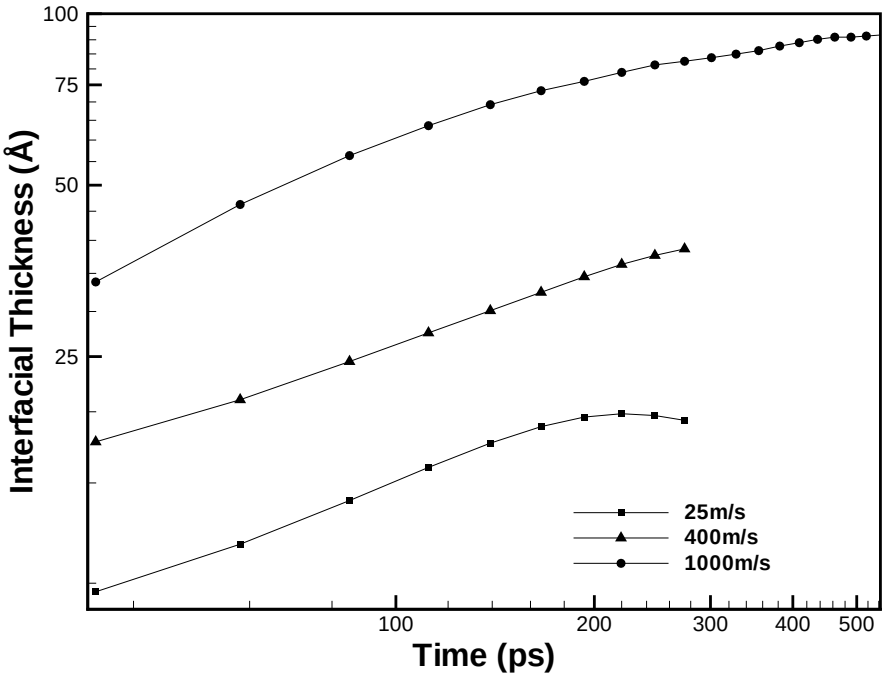

Figure 5.12: Variation of interfacial thickness over time at 25, 400 and 1000m/s.

5.2.3 Heat dissipation across material interface

When solid materials are in contact and slide at specific conditions, the frictional force dominates. This provides resistance to motion and heat is produced at the interface, raising the temperature of the system to very high values as shown in early experiments by Bowden and Thomas [25] and Bowden and Ridler [23] on Cu-steel, Ga-steel, Pb-steel and Constantan(Cu-Ni alloy)-steel tribopairs. This work proved that the local surface temperature was very high, exceeding values of 1273 K at sliding speeds of up to 50 m/s, although the mass of the metal was quite cool. The temperature distribution near the surface depends on several parameters such as normal load, sliding speed, coefficient of friction and thermal conductivity of the material, as shown by various macroscopic and atomistic studies [204, 15, 151, 96]. Plastic deformation during sliding also plays a key role in the temperature evolution of the material near the interface; it generally contributes most of the frictional heating, as observed by Li et al. [151] for Ni-Ni, Al-Al and Ni-Al tribopairs. In these simulations plastic deformation is not recorded at v_r of less than 50 m/s, and the temperature near the interfacial region remains low, below the materials' melting points.

To determine the temperature distribution across the material interface, the local instan-

taneous temperature T is calculated by:

$$T = \frac{2E_k}{3Nk_B} \quad \text{with} \quad E_k = \frac{1}{2} \cdot \sum_{i=1}^{N} (v_i - v)^2 \tag{5.2.3}$$

where E_k is the internal kinetic energy of N number of atoms, k_B is the Boltzman constant and v is the local instantaneous velocity of the N atoms. The simulation domain was divided along the y-axis into layers consisting of approximately $13,000$ and $18,000$ atoms for Ag and Cu respectively. The velocity and temperature profiles were computed every 100 time steps and averaged over 100 samples.

As previously discussed, the transition point of the frictional forces is at a speed of 200 m/s in this model. By investigating how the temperature evolves across the interface an interpretation is given on why the transition occurs earlier than that observed by Hammerberg et al. [89]. In Figure 5.13 the development of the temperature profile is plotted for a speed of 200 m/s. At 220 ps the temperature at the interface reaches approximately 950 K, which is close to the melting temperature of Ag. One can therefore expect the onset of melting and the formation of a liquid film at the interface due to thermal softening. Figure 5.13 also presents the (%) concentration of each material to show that the temperature rises first at the interface and not within the plastically deformed materials. Figure 5.14 shows the temperature profile for the sliding speed of 300 m/s. Here, the temperature at the interface reaches approximately 1250 K, which is already close to the melting temperature of Cu. Thus, a liquid film at the interface will be present, reducing the frictional force through lubrication.

At higher sliding speeds the temperature near the interface increases further; in the simulations obtained in this study at a sliding speed of 1000 m/s the interface temperature reaches values of approximately 2000 K. Undoubtedly, the influence of temperature on the mechanical behaviour (i.e. plastic deformation in close proximity of the interfacial region at times ranging from 2.7 – 5.4 ps) changes the friction force per unit area, this only applies to higher speeds usually greater than 400 m/s because of the severe high strain rates imposed on the interfacial region.

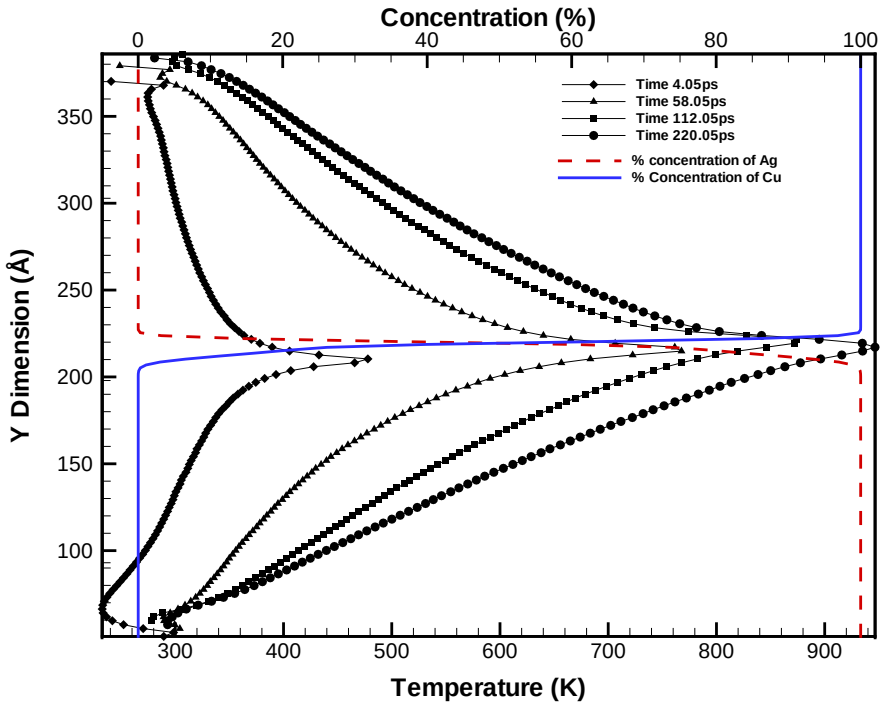

Figure 5.13: Relative speed of 200m/s.

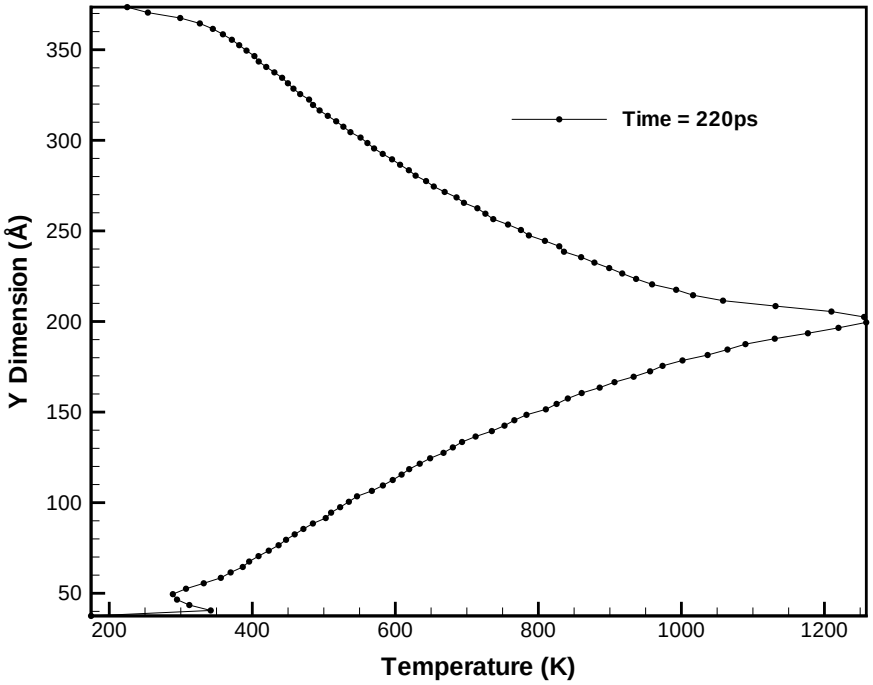

Figure 5.14: Relative speed of 300m/s.

5.3 Molecular dynamics limitations

The MD methodology used in this chapter provides physical insight into the mechanisms of dynamic friction at the scale of the atomic lattice. However, the quantitative behaviour of integral properties, such as the friction force per unit area, is subject to two sources of systematic error: under-prediction of thermal conductivity and artefacts arising from the reservoir boundary conditions. The nature of these errors and their impact on these simulations are discussed in this section.

An important approximation of classical MD is that only the motion of the atomic cores are simulated directly. The average contributions of the electrons are included in the empirical potential functions, such as the EAM potential. This simplification reduces the computational cost and allow one to perform MD simulations with several million atoms. However, it introduces a significant limitation when MD is used to simulate physical processes in which thermal conduction is important, such as dynamic friction at extreme conditions. In metals, the internal kinetic energy (heat) is conducted by two mechanisms, through phonons and through electrons. MD only accounts for the contribution of phonons (atomic vibration) to thermal conductivity, but does not account for the free electrons or elecron-phonon interactions, which provide the dominant mechanism for thermal conduction in metals (see for example the work by Heino and Ristolainen [100]). Therefore, in friction simulations, MD will tend to under-predict the rate of heat loss by conduction to the bulk metal, and hence over-predict the rate of temperature rise at the interface. However, other thermodynamic properties and mechanical properties are well represented by MD. MD simulations have been conducted in Chapter 3.1 to evaluate bulk modulus, thermal expansion α, melting points T_m, and heat capacities C_p, for Cu and Ag metals and results are in agreement with experiments. Nevertheless, the thermal conductivity k prediction of these metals using MD is very poor as explained in Chapter 3.2.1.

The imposition of time-invariant reservoir boundary conditions for temperature and velocity also presents sources of systematic error. It is necessary to provide a heat sink at the reservoir in order to mimic heat conduction into the bulk metal and hence limit the temperature rise in the domain. However, one-dimensional continuum calculations following the method of Winter et al. [255] show that the temperature at the reservoir location is not constant on the time scale of the MD simulations, but rises significantly with time, further details are discussed in the section 5.4. Neglecting this effect will tend to steepen the temperature gradients in the domain, leading to an increase in conductive heat

losses. The constant velocity boundary condition has the effect of trapping shear waves within the domain. When the relative sliding motion is initialized, elastic shear waves are produced at the interface that propagate into both materials. In reality, these will proceed unhindered into the bulk material, but in the MD simulations they are reflected back towards the interface, modifying the velocity distribution. Such reflections are the likely source of the oscillations observed in the calculated friction time-histories (see Figure 5.1). In order to address these issues, a new methodology is under development by Barton et al. [6] in which the MD domain is coupled to a continuum code developed by Barton et al. [7] in order to provide time dependent boundary conditions for the MD domain. The initial results shown by Barton et al. [6] are very promising because shear waves can travel away from the sliding interface and do not influence the sliding dynamics.

5.4 Continuum simulations of Cu/Ag interfaces

In order to verify the molecular dynamics limitations of the under prediction of the thermal conductivity and shear wave reverberation due to the boundary conditions, as described in Section 5.3, the author conducts a comparison of the MD simulations of Cu/Ag tribopair against continuum simulations of the dynamic friction. The continuum simulations were conducted at AWE's facilities using the algorithm developed by Winter et al. [255]. In this section, a description of the 1-dimensional hydrocode is given, which was used to simulate the Cu/Ag sliding as specified in Section 4.1 for a relative sliding velocity of Cu/Ag tribopair at 200 m/s.

The time dependent behaviour of sliding interfaces subject to dynamic friction was explored. The algorithm gives an insight into shear deformation processes work hardening, thermal softening, melting, and heat conduction when dynamic friction is initiated. Calculation of the shear strain is obtained as a function of position and time, which is used by the Steinberg-Guinan constitutive model developed by Steinberg et al. [222]. In this model the yield strength, σ_{yt} is given by Equation 5.4.1. The first term on the right hand side of Equation 5.4.1 represents the work hardening, the second term is the pressure hardening and thermal softening and the final term which is an exponential term gives the rapid decay in flow stress as the temperature approaches the melting point.

$$\sigma_{yt} = min\left[\sigma_{yto}\left(1+\beta\epsilon_p\right)^n, \sigma_{yt(max)}\right]\cdot\left[1+gP-h\left(T-300\right)\right]\cdot exp\left(-0.001\frac{T}{T_m-T}\right) \quad (5.4.1)$$

where σ_{yto} is the yield strength in the reference state, ϵ_p is the plastic strain, β, n, g, h are material dependent parameters, P is the pressure, and T, T_m are the temperature and melting temperature respectively.

The rest of the components of deviatoric shear stress are neglected and the pressure is kept constant throughout the simulation P=5.1 GPa. A staggered mesh is used, in which velocity and mass are node-centred, while the other variables are cell-centred. Two coincident nodes are placed at the material interface, one for each material, to capture the sliding velocity discontinuity, Δu. The code is using the predictor-corrector scheme to integrate the governing equations. The friction shear stress is assumed to be limited by the flow stress of the weaker material (which is Ag) as determined by the von Mises yield criterion in pure shear ($\tau_{max} = \sigma_{yt}/\sqrt{3}$). The heat flux supplied at the interface due to frictional heating is estimated from equation 5.4.2, and is partitioned between the materials to maintain temperature continuity at the interface.

$$\dot{Q} = \tau \Delta u \tag{5.4.2}$$

The mesh spacing at the interface was 0.625 nm increasing away from the interface at 3.65% per cell. A total of 750 cells were used, giving a total domain extent of ±1.16cm; this domain is much larger than the MD domain used in section 4.1, so that the hydrocode domain boundaries cannot influence the region corresponding to the MD domain. The simulations were initiated by applying uniform velocities of $\pm v/2$ to the bulk materials. As in the MD simulations the reservoir defined in the continuum domain was imposed in the same manner. The block of Cu and Ag metals have value of y dimension equal to 16 nm excluding the reservoir regions. Initial calculations produced a frictional stress that was much lower than the corresponding MD value. This was not unexpected, since this stress was assumed to be governed by the yield strength of the weaker material; the yield strength used in a continuum constitutive model is generally much lower than observed in MD simulations, which typically address small regions of perfect single crystals. Thus the values of the yield strengths used for the continuum simulations of Cu and Ag were scaled up by a factor of 17.5 so that similarity is achieved with the friction stress.

5.4.1 Thermal conductivity errors

Molecular dynamics has some limitations when applied to physical problems, such as friction where thermal conductivity plays an important role. As discussed in Chapter 3.2.1 thermal conduction in metals occurs via the free electrons, which are not explicitly modelled via MD. Therefore, the thermal conductivity values predicted via MD simulations are underestimated as shown in Chapter 3.2.1 as in MD studies by Heino and Ristolainen [100]. In order to demonstrate the effect of this error in the Cu/Ag friction problem, two comparative hydrocode simulations test cases were performed. The first one was conducted using the phonon-only thermal conductivities and the second one was performed using the experimental values.

Although there is a good agreement in the thermal conductivity between Heino's work and this study, his values were used because the continuum simulations were conducted prior to the study in Chapter 3.2.1. Heino and Ristolainen proved that the thermal conductivity is dependent on the domain size, therefore using their fits for Cu and Ag MD domains of 16 nm in the y direction, yield values of 4.6 and 2.3 W/mK respectively. For comparison, typical experimentally determined values are 397 and 420 W/mK for Ag and Cu respectively, suggesting that the MD values are unrealistically small by more than two orders of magnitude.

In both cases, simulated reservoir boundary conditions for temperature and velocity were applied. The resulting temperature distributions are plotted in 5.15, which is comparable with the MD results in Figure 5.13. Therefore, when the phonon conductivities are used, the hydrocode predicts reasonable agreeement with MD showing temperatures of 885 K compared to temperature of 960 K of the MD simulations. Finally, when the experimental values for thermal conductivity are used, the hydrocode temperature profiles are showing a temperature rise of 6.5 K after 220 ps, which indicates that at these conditions and timescales there is no significant change in the interfacial temperature.

5.4.2 Artefacts of the reservoir boundary conditions

The boundary conditions applied in the MD simulations impose a constant temperature and constant velocity in the lower and upper reservoirs equal to $v_u = -v_l = (1/2)v_r$ as discussed in section 4.1. The temperature was kept constant at 300 K at a distance of approximately

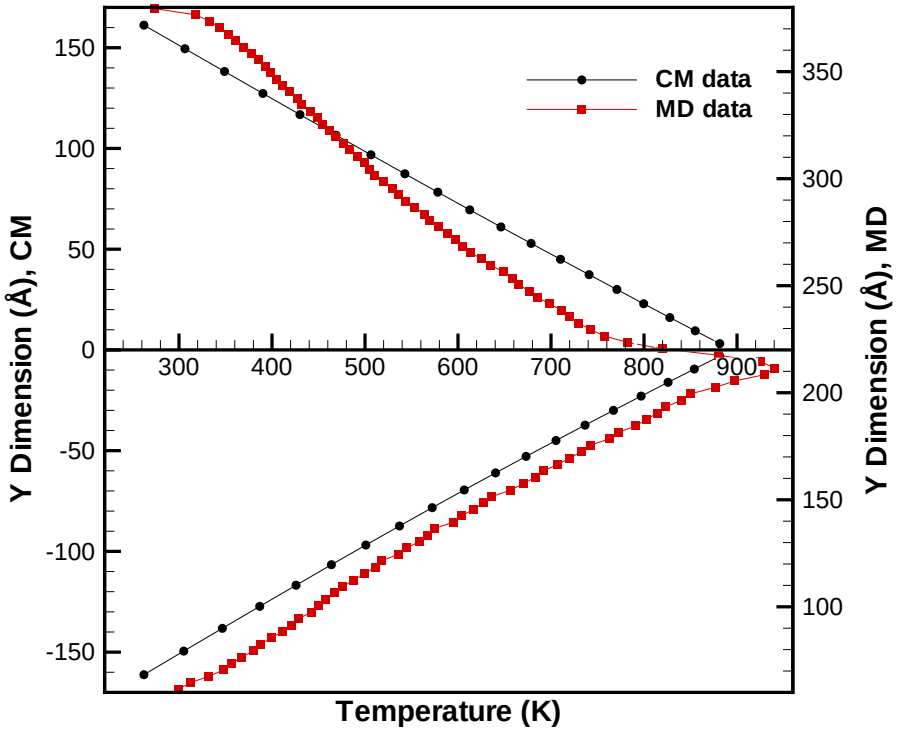

Figure 5.15: Comparison of the temperature distribution across continuum (CM) and MD domain at sliding speed of 200m/s and simulation time equal to 220ps.

±16 nm from the interfacial region. The boundary conditions effects were simulated for 220 ps via the hydrocode by applying the predicted thermal conductivity values taken of molecular dynamics simulations.

Due to the application of frictional stress elastic waves at the interface propagate at time t=0 into both materials at shear wave velocity of $U_E = \sqrt{G/\rho}$, where G is the shear modulus and ρ the density. The propagation time of the shear wave from the interface to the reservoirs should be smaller than the actual duration of the simulation; therefore, values of U_E for Cu and Ag were chosen to be 2300 and 1700 m/s respectively. The correlation of these waves and the tangential velocity as given by $\delta v = \pm\tau/\rho U_E$, causes a reduction of the interfacial velocity of around 120 m/s, which occurs initially. In the presence of the reservoirs and the boundary conditions of temperature and velocity applied within, the waves confined on this small domain are reflected and effectively undergo a multiple reverberations. The slip velocity at the interface is evaluated with and without the restriction of the boundary condition and is shown in the upper slab of Figure 5.16.

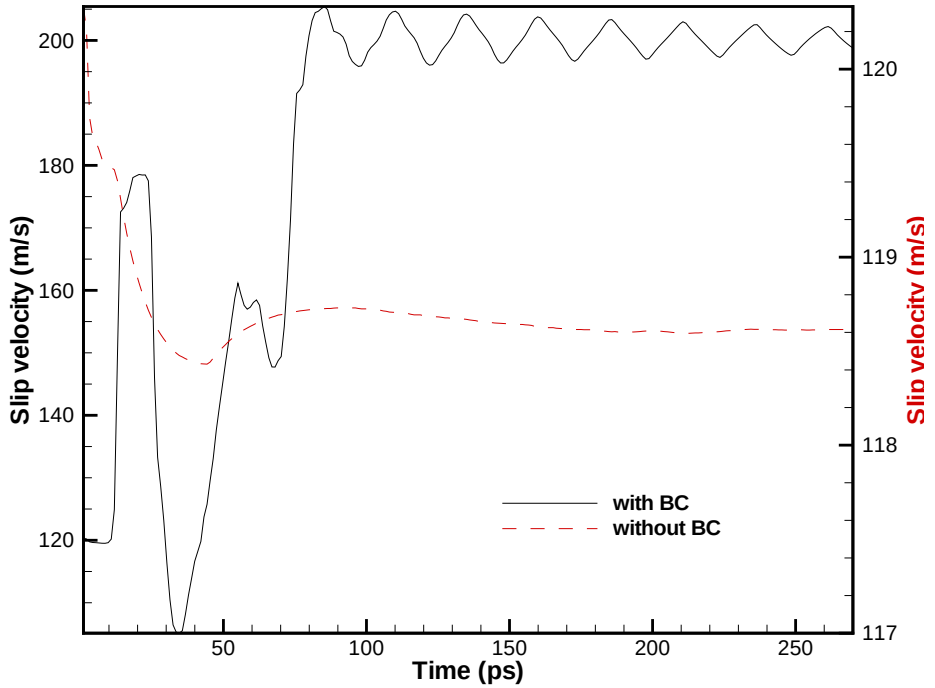

Figure 5.16: Hydrocode predictions of the evolution of the slip velocity at the interface. With (black line) and without (red line) the application of the reservoir velocity boundary condition. Result provided by Dr. Graham Ball.

The reflected shear waves considered in these simulations play an important role affecting the slip velocity, producing a late time slip velocity that is evaluated to be higher by about 40% in these simulations. When a boundary condition is not imposed as seen in Figure 5.16 the thermal softening and work hardening of the weaker material, in this case Ag, are in balance; hence, the friction shear stress is almost constant. When boundary conditions are applied (Figure 5.16) the shear stress reflected causes severe plastic deformation in the Ag which leads to an increase in work hardening and as a result an increase (almost double) of the shear stress. This increase in shear stress relaxes over time because of the thermal softening. The hydrocode predictions also show that these oscillations resemble those appearing in the hydrocode velocity history. As shown in equation 4.3.2, the MD predicts the frictional stress indirectly using velocity contributions and therefore part of that is the contribution of the shear wave reflections. A different approach used to calculate the frictional stresses on the Cu block is by using the the stress-volume relation formula used in Chapter 3.3.1. The work described in later Chapter (6.2) for one of the test cases of sliding friction at relative velocity of 200 m/s, the stress was obtained by excluding the kinetic energy contibution and the pairwise energy was taken into account. It is shown that the interatomic force term (pairwise contribution) is actually a valid way of measuring the

stress and can be identified with the Cauchy stress. The outcome of this investigation shows that results with and without the kinetic energy part have small variations in the stress-strain response.

As shown in Figure 5.1 the steady state comes after about 150 to 200 ps, however, the hydrocode's prediction shows that this could be simply a further artefact of the reservoir boundary conditions. Repeating the simulation time for 54 ns, disabling the reservoir boundary conditions and still keeping the thermal conductivities as predicted by MD simulations, the material's behaviour follows two phases as shown by Winter et al. [255]. During the first phase interfacial heating causes the stress to decrease due to thermal softening, which is also partly balanced by work hardening. The second phase is the so-called "asymptotic melting", in which the temperature approaches the melting point of the material. The frictional heating and conduction losses reach equilibrium. The one dimensional continuum study shows that the frictional stress should not attain steady state at the given time-scale defined by MD simulations. As previously mentioned in the case where the experimental conductivities are used, the stress evolution takes much longer to achieve steady state approximately by 2 to 3 orders of magnitude.

Summing up the work reported in this chapter, it has investigated the dynamic friction of Cu and Ag at a normal pressure of 5.1 GPa for sliding speeds ranging from 0.025 to 1 km/s. It confirms the velocity dependence of the frictional force as obtained by previous studies. Results indicate a direct connection between velocity weakening of the frictional force and structural transformation of nano-crystalline materials. In particular, plastic deformation occurs at sliding speeds greater than 50 m/s, firstly in the silver block. The measurements of temperature profiles across the interface shows that the melting point of silver is exceeded for sliding speeds above 200 m/s. The molten material forms a liquid layer that lowers the frictional force. Mixing of the interface is observed and the interface width (layer with mixed material) increases during the sliding process until it reaches a maximum. Higher sliding speeds result in thicker interfaces. It was observed that the copper atoms diffuse further into the sliver block than silver atoms into the copper block.

The following chapter focuses on how the yield point of these materials varies under conditions prevalent at high speed sliding. Knowledge of the yield point under these conditions is important to obtain accurate constitutive models for the shear stresses. Although MD provides insight into the structural transformation of material interfaces subjected to dynamic friction, modelling issues regarding thermal conductivity values obtained by MD and the effects of reservoir boundary conditions on the results were identified and drastic

measures to overcome these will be discussed.

CHAPTER 6

Yielding, deformation and failure of solid materials through sliding friction

"Measure what is measurable, and make measurable what is not so."

Galileo Galilei

The physical mechanisms that contribute to the frictional resistance to sliding were establish by Bowden and Tabor [24], as discussed in chapter 1.2.1. In reality material surfaces are inevitably rough and the real area of contact is actually a small fraction of the apparent area of contact. The areas of contact could effectively adhere and the sliding is divided into the adhesion term and the so called "ploughing" term, which is generated from the plastic deformation of the interfacial asperities. Frictional sliding is a very complex process involving large plastic strains, which give rise to complex dislocation generation within the material's microstructure. The purpose of this chapter is to investigate and focus on the aspects of this complex process with the aid of molecular dynamic simulations. Investigating the change of the yield point of the material under sliding friction and the accurate evaluation of the stresses involved has proved difficult and time consuming. This is primarily attributed to the fact that experiments are difficult to conduct and expensive facilities are required. Thus, Yu et al. [265] showed that exploring the fundamental rules prevailing the variation of materials strength is very complex process.

Understanding the mechanism underlining the nanoscale dynamic friction requires investigation of contact nanoidentation, experimental and analytical techniques. A novel sliding friction simulation set-up was constructed for nano-structured materials. Materials

in reality are not perfect containing numerous defects within the microstructure. The work in this chapter aims to shed light on to the complex frictional behaviour by comparing the stress strain response of nanostructured Cu/Ag tribopair against the simulation of perfect crystals, as well as investigation of the velocity weakening and structural transformation as described in chapter 5.

6.1 Evaluation of strain rate during sliding

Chapter 4 discusses the simulation set up and methodology for sliding friction, applied in the large scale MD simulations outlined in chapter 5. The deformation of the simulation box in this study cannot be easily obtained, because of the simulation set-up. The volume of the simulation box remains constant in the sliding direction due to NVE thermodynamic ensemble restriction. The x dimension will not change making it impossible to investigate deformation of the simulation box. Additionally, the strain will be local and thus different along the different dimensions. To overcome this issue and to be able to measure deformation a different approach was used by evaluating the strain rate from frictional velocity plots.

A typical frictional velocity plot against the y-direction of the simulation box is shown in the Figure 6.1, which is obtained at relative speeds of 200 m/s. There are three regions identified: the reservoir region in which all the forces, pressure and temperature rescaling are applied. The plastic deformation region in which the material is left to deform without any constraints and dislocations are present and finally the interfacial region, that melting and mixing at higher sliding speeds was also observed. A great interest lies on the plastic deformation region and the aim of this study is to evaluate the actual strain rate at each velocity. By definition strain rate is defined as the first derivative of the velocity in the x-direction over the y-dimension,

$$\dot{\gamma}_{\epsilon} = \frac{dv_x}{dy} \tag{6.1.1}$$

Equation 6.1.1 is calculated over the plastic deformation region, which is away from the reservoir and the interfacial region as shown in Figure 6.2.

The strain rate is evaluated using Equation 6.1.1 at each individual timestep shown in the isolated plastic deformation region for Cu, Equation 6.2, and averaged for the entire duration of the simulation. Another formulation of the strain rate $\dot{\gamma}_{\epsilon}$ is also given by Equation

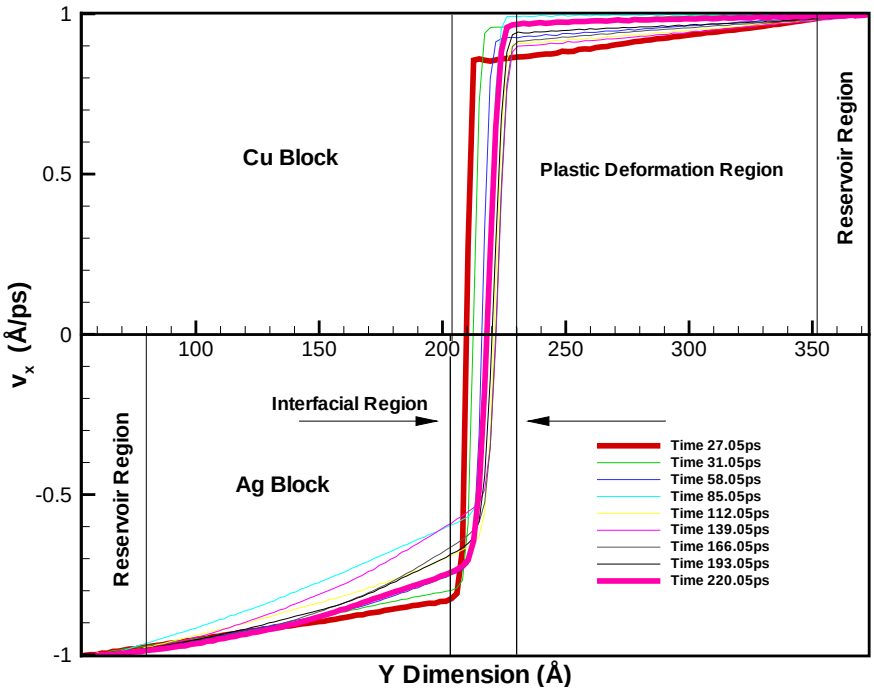

Figure 6.1: Frictional velocity against y direction of the simulation box at relative speed of 200 m/s.

6.1.2:

$$\dot{\gamma_\epsilon} = \frac{\gamma_\epsilon}{t} = \frac{\gamma_\epsilon}{N_t \cdot dt} \tag{6.1.2}$$

where γ_ϵ is the strain, N_t is the MD timestep, and dt is the integration timestep of the simulation. Using the Equation 6.1.2 the strain rates were calculated for two systems containing 7 and 20 lattice planes in the reservoir region. Table 6.1 tabulates the data and compares them against the theoretical strain rate.

The theoretical strain rate is effectively an engineering strain rate given by $\dot{\epsilon} = v/l_o$, where v is the velocity and l_o is the length of the simulation box. Since the reservoir's atoms have constant velocity the theoretical strain rate is evaluated by this equation, which is only valid on the reservoir and not on the entire block. Thus the need for calculating the strain rates from the plastic deformation region in Equation 6.2 is required to obtain a realistic deformation of the simulation box.

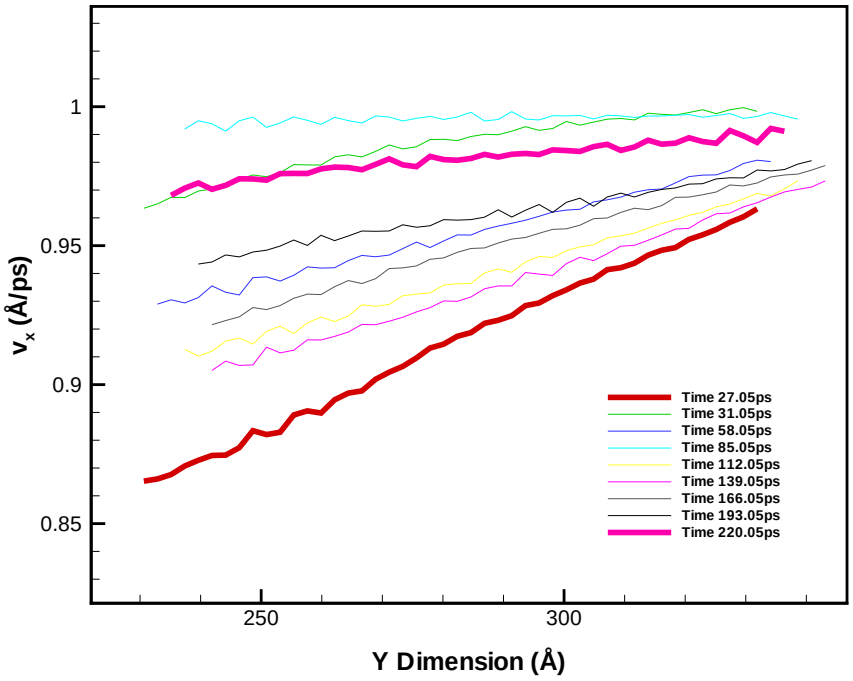

Figure 6.2: Plastic deformation region of Cu block extracted from Figure 6.1.

Velocity (m/s)	Strain Rate (/s)	Calculated Strain Rate (/s) (7 lattice Planes)	Calculated Strain Rate (/s) (20 lattice Planes)
25	7.81E+08	3.49E+07	1.83E+07
100	3.13E+09	1.72E+08	1.18E+08
200	6.25E+09	4.22E+08	1.14E+09
300	9.38E+09	3.07E+08	1.97E+08
400	1.25E+10	2.63E+08	1.28E+08
500	1.56E+10	9.67E+07	9.11E+07
600	1.88E+10	2.71E+08	-
800	2.50E+10	2.00E+08	8.50E+07
1000	3.13E+10	5.18E+07	1.01E+08

Table 6.1: Tabulated data for strain rates at different reservoir thicknesses of 7 and 20 lattice planes.

6.2 Evaluation of the stress during sliding

Although atomistic simulations have been a powerful tool for predicting the mechanical response as shown in chapter 3.3, computing the atomic stresses equivalent to Cauchy stress (true stress) is a controversial issue, because of the velocity related term in the virial stress Equation 3.3.2. Clausius [40], Maxwell [172] and Maxwell [173] were first to introduce the virial theorem to determine the stress field to a surface in which particles of constant volume were interacting. The calculation is based on time and spatial averaging to obtain a point-wise local virial stress, which results in an incorrect evaluation of stress. Cheung and Yip [37] used the formulation for a free surface and showed that the outer layer atoms possess non-zero values for the components of stress tensor normal to the surface.

The earliest formulation of virial theorem expressing mass, momentum and energy was reported by Irving and Kirkwood [119]. The proposed formula for virial stress contains several expressions which are not unique because of the ensemble averaging considered in region where inhomogeneity takes place. It is effectively a non local volume-average version of stress and similar expressions have been also adopted by Cormier et al. [41], and Lutsko [164]. According to Zhou [269] the virial stress violates the momentum balance, therefore giving a non-physical interpretation of the mechanical interactions at the atomic level. Zhou argues that the virial stress geometrically is a measure of momentum change in a fixed spatial region, and that the interatomic force calculation part of the equation is a sufficient measure of the Cauchy stress, thus the kinetic contributions should be excluded.

Zimmerman et al. [271] uses an alternative equation developed by Hardy et al. [94] to evaluate continuum stress in atomistic simulations, which is similar in discipline with virial theorem. The equation developed by Hardy et al. [94] relies in spatial averaging of the stress at fixed localized points. A normalisation function is used to feed information from neighboring atoms and their contribution to the stress field at the fixed point. When materials are deformed, at elevated temperatures, Hardy's stress which is expressed as a function of volume gives faster convergence to stress values expected from continuum methods as discussed by Zimmerman et al. [271]. The velocity and stress are defined so that they are consistent with the continuum balance of linear momentum. The stress in this equation is driven effectively by the interatomic potentials and the atomic velocity trajectories, therefore momentum is taken into account as opposed to the virial stress relation by Zhou [269]. These results proved better than the virial stress obtained by volume averaging at a fixed localised point.

Although, there is a controversy about the kinetic energy of the virial term, the simulations studied in chapter 3.3 showed that the stress corresponds to the Cauchy stress in continuum mechanics. The complete formula for stress (Equation 3.3.1) in chapter 3.3 was used meaning that the kinetic energy contribution was included in the calculations. Additionally, friction simulations obtained in this study show that a negligible variation of stress response occurs by enabling and disabling the kinetic part of the Equation 3.3.1. Figure 6.3 shows the stress strain response at relative sliding velocity remains almost unchanged. The green line data were calculated via Equation 6.2.1.

$$(S_{ab})_{global} = -\frac{N}{V} \cdot \left[\frac{1}{2} \sum_{j=1}^{N_p} (r_i - r_j) F_{p_{ij}} + \frac{1}{2} \sum_{j=1}^{N_b} (r_i - r_j) F_{b_{ij}} \right] \tag{6.2.1}$$

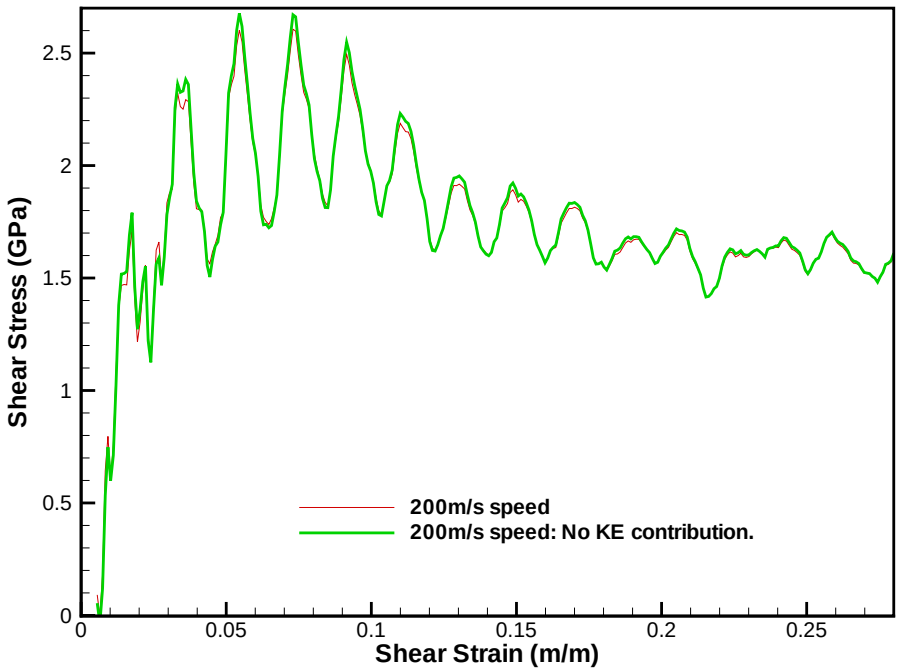

Figure 6.3: Stress strain relation at relative speed of 200 m/s. Solid line corresponds to the stress evaluated by using all the terms of the Equation 3.3.1. Dashed line is when the kinetic energy has been excluded.

Plots of the stress-strain curves also reveal the yield stress σ_y of the material during extreme sliding conditions. Taking this into account the simulation domain was separated into regions as shown in Figure 6.4.

Each region had box dimensions of (x,y,z)=(410,10,320) Å containing approximately 110,000 atoms. The stress-strain curves were plotted, and showed no significant change

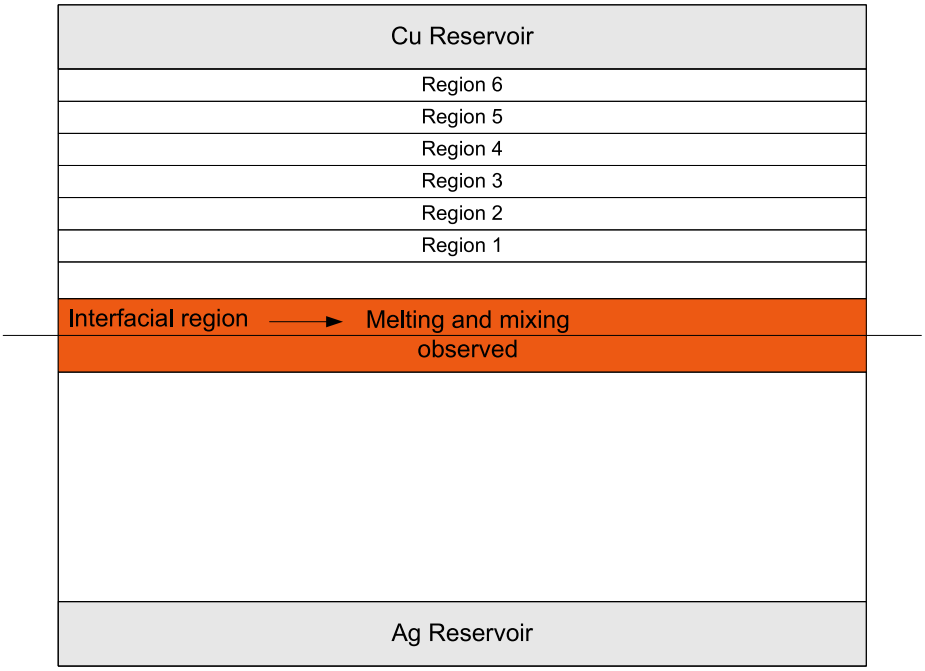

Figure 6.4: Schematic representation of plastic deformation region.

amongst the regions, thus values were averaged over the entire set of these regions. The results on relative speeds of 200 m/s is shown in Figure 6.5. Since little change is observed between the layers an average of all the layers is plotted as shown in Figure 6.6. Fitting a polynomial of 10th degree as shown in Figure 6.6, a trendline is drawn which is similar with a typical stress strain curve observed in experiments. Recalling the stress-strain curves from chapter 3.3.4 and the work done by Horstemeyer et al. [110] on nickel block shear simulations, regions of ”micro-yield 1”, ”micro-yield 2” and ”macro-yield” can be identified. In this study with the aid of Figure 6.6 for sliding at relative speeds of 200 m/s, these regions are shown giving a value of yield stress of $\sigma_y = 1.5GPa$ and the point of maximum stress is $\sigma_{max} = 2.1GPa$. As the stronger material slides on the weaker surface, the yield point of the material and subsequently the point of which maximum stress occurs increases up to relative speeds of 500 m/s according to Figure 6.7. It can be observed that at speeds higher than 500 m/s although the yield point continues to increase the adverse effect is observed at the point of which maximum stress occurs. Thus, for speeds of 800 m/s and 1000 m/s the yield point reaches the maximum value, $\sigma_y \approx 4$ GPa, indicating that beyond the speed of 800 m/s the σ_y remains constant.

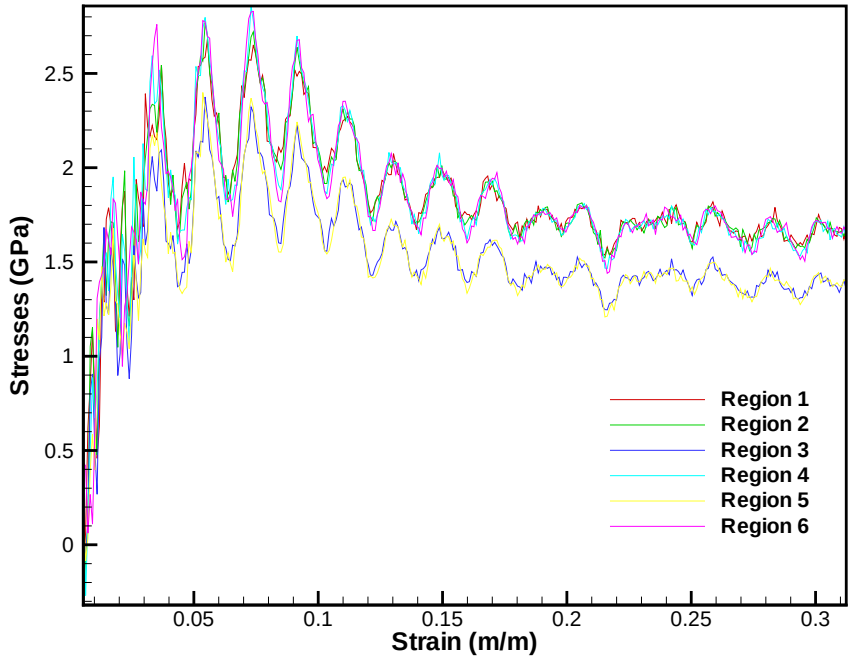

Figure 6.5: Stress-strain response of Cu at sliding of 200 m/s.

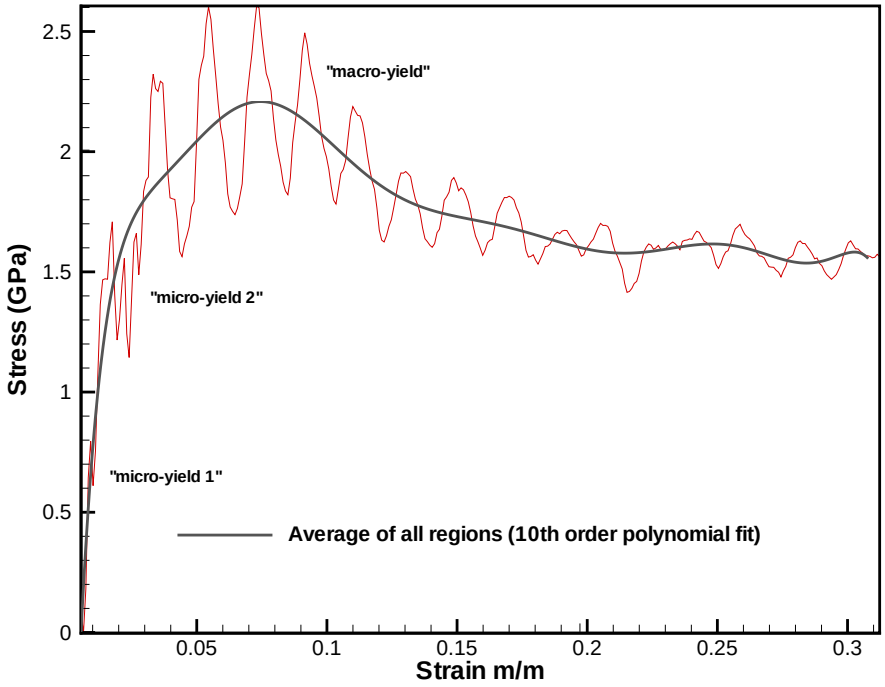

Figure 6.6: Stress-strain response of Cu block at relative speed of 200 m/s plotted by averaging the regions 1-6.

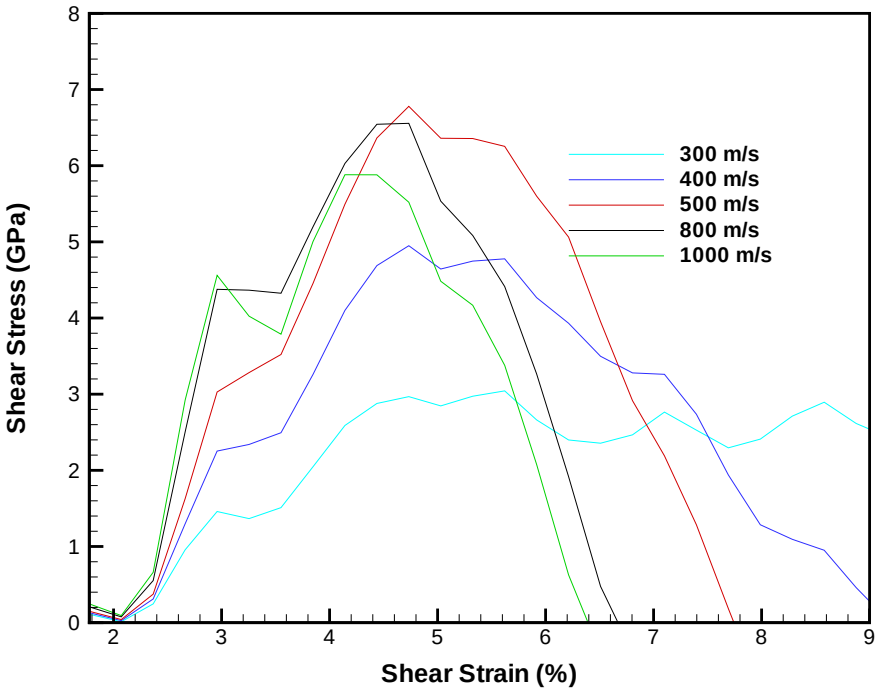

Figure 6.7: Average stress-strain (regions 1-6) response at relative sliding speeds ranging from 300 to 1000 m/s.

6.3 Evaluation of temperature and heat correction under dynamic friction

The results of the temperature profiles shown in chapter 5.2.3 show an increasing interfacial temperature, caused by the MD underestimation of the correct thermal conductivities for Cu and Ag metals. There is a continuous heat generation in the interfacial region due to friction, which raises the temperature to high values approaching and in some speeds exceeding the melting point of the materials. This section presents a way of correcting the MD underestimation by subtracting heat from a group of interfacial atoms so that their momentum is conserved.

Constant heat flux algorithm was implemented into LAMMPS; the description is reported by Aubry et al. [4]. The aim of this scheme is to scale the velocity per timestep by imposing constant kinetic energy (negative or positive) to a region of atoms without altering the total linear momentum of these set of atoms. Once a region of atoms is defined, $\mathcal{N}$, the

atomic velocity is scaled, v_i^*, per timestep by $\mathcal{R}$ and a constant velocity is then subtracted,

$$v_i \rightarrow v_i^* = \mathcal{R}v_i - v_{sub} \tag{6.3.1}$$

where $i \in \mathcal{N}$. Since the total linear momentum, $\boldsymbol{p_l} = \sum_{i\in\mathcal{N}} m_i v_i$, should remain unchanged this means so that $\boldsymbol{p_l} = \boldsymbol{p_l^*} = \sum_{i\in\mathcal{N}} m_i v_i^*$. Considering the momentum condition the v_{sub} is evaluated by Equation 6.3.2, the full derivation is shown by Aubry et al. [4]:

$$v_{sub} = \frac{(\mathcal{R}-1)\sum_{i\in\mathcal{N}} m_i v_i}{\sum_{i\in\mathcal{N}} m_i} \tag{6.3.2}$$

The total kinetic energy E_k, changes by ΔE_k, hence, $E_k^* = E_k + \Delta E_k$. Starting from the definition of the scaled kinetic energy, $E_k^* = 1/2 \cdot \sum_{i\in\mathcal{N}} m_i (v_i^*)^2$, and substituting for v_i^* in Equation 6.3.1 the value for $\mathcal{R}$ can be quantified by Equation 6.3.3:

$$\mathcal{R} = \sqrt{\frac{E_k + Q - \frac{1}{2}\frac{(\sum_{i\in\mathcal{N}} m_i v_i)^2}{\sum_{i\in\mathcal{N}} m_i}}{E_k - \frac{1}{2}\frac{(\sum_{i\in\mathcal{N}} m_i v_i)^2}{\sum_{i\in\mathcal{N}} m_i}}} \tag{6.3.3}$$

where Q is the added or subtracted value of the heat flux which is effectively the non-translational kinetic energy of a group of atoms. This implementation was first used by Lukes et al. [160] for a 3-D simulation domain in which thermal conductivity is evaluated by defining two different reservoirs hot and cold. Kinetic energy is added in the hot ($\Delta E_k > 0$) region and subtracted in the cold ($\Delta E_k < 0$) for long time until steady state is achieved then the 1-D heat flux J_y is determined as shown in Equation 3.2.1.

An analysis of the temperature variation was obtained by subtracting heat with the described methodology for a 3-D simulation domain of Cu sliding on Ag. The constant heat flux algorithm was imposed on the interfacial region containing approximately 5 lattice planes in each substrate. The two blocks containing approximately 1500 atoms which are compressed against each other prior to sliding. The boundary conditions used for this simulation are the same as in chapter 4.1, in which they are applied on reservoirs atoms occupying 7 lattice planes. Figure 6.8 presents the results at relative sliding speeds of 200 m/s. The red line in Figure 6.8 shows the temperature variation along the y-direction without the implementation of the heat flux alteration after 27 ps. The temperature generated in the interfacial region reaches approximately 630 K. Finally, the heat flux that should be subtracted, Q, was evaluated by using heat conduction Equation 3.2.1 (in section 3.2.1). This is shown in the blue line of Figure 6.8 by taking into account the experimental thermal conductivity values of both Cu and Ag. The interfacial temperature is sustained at 300 K

over the duration of the sliding simulation.

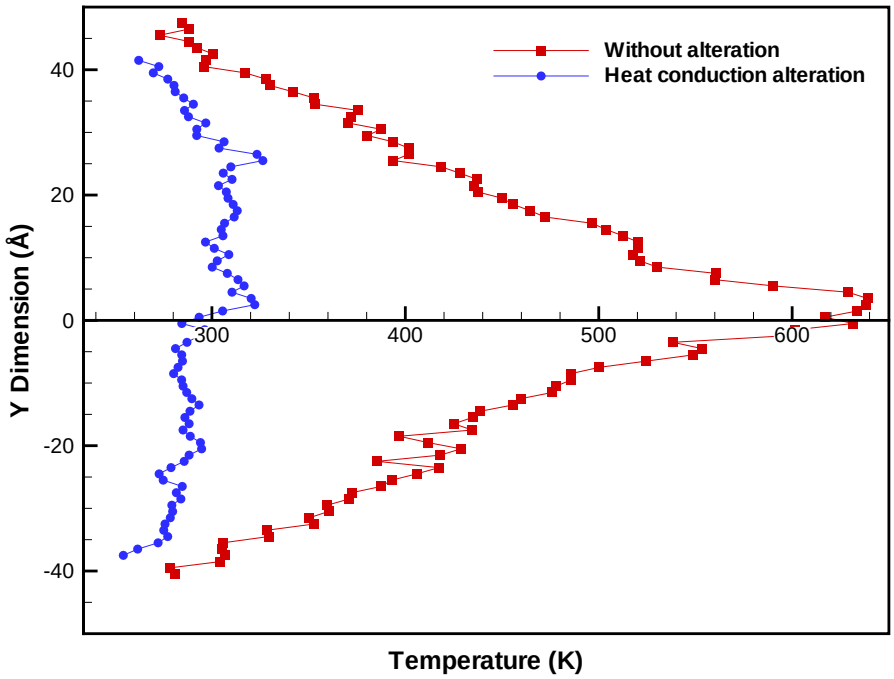

Figure 6.8: Small frictional domain to fix the temperature variation across the interface.

6.4 Mechanical behaviour and sliding of nanostructured materials

Investigation of the mechanical properties of materials at the nanoscale is receiving increasing attention in the field of nanotechnology. Pioneers in the field of materials science such as Gleiter [77], [78] identify the outstanding possibilities of nanoscrystalline materials and set the foundation of a global research work [18, 78, 159, 242, 79, 143, 248, 179]. Fundamental understanding of the nanoscale dynamic friction requires the knowledge of contact nanoidentation along with experimental and analytical techniques.

In polycrystalline metals the deformation involves two mechanisms the intragranular and the intergranular deformation as shown in Figure 6.9. Intragranular deformation is caused by the dislocation movement, while intergranular deformation by grain boundary sliding, migration, rotation and diffusion processes. The deformation mechanisms in nanostructured metals using experimental techniques proved to be highly difficult and challenging according to Weertman [252]. This is due to the complicated methods of obtaining

nanostructured materials free from defects. Nanostructure deformation is reported by various researchers, for example Milligan et al. [182] and Ke et al. [139]. They conducted in situ deformation studies on gold and films with grain sizes ranging from 8 to 25 nm. [182] showed deposition methods are applied to position nanostructured metals on top of electron-transparent aluminum films. The deformation was examined in situ, using transmission electron microscope (TEM) on material strained by typical bending mechanism. It was shown that the ultra-fine materials deform by grain boundary sliding and not by a dislocation mechanism nucleated within the grains. The mechanism of fracture was observed to be intergranular and deformation indicates that diffusion played an important role in these experiments.

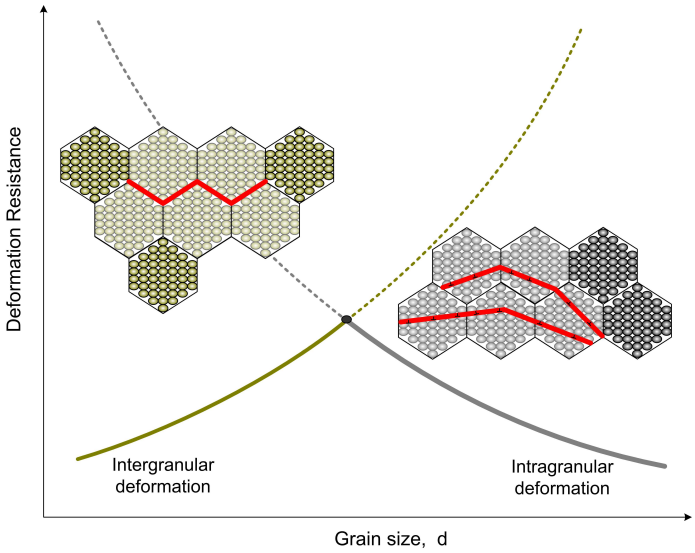

Figure 6.9: Illustration of inter- and intragranular deformation mechanisms.

Evidence of deformation due to dislocation was also observed on the experimental work obtained by Ke et al. [139] on silver blocks with grain sizes of 110 nm, but not on sizes ranging from 10 to 20 nm. The results indicate that grain rotation and boundary sliding are the main contributors to deformation. This was supported by Legros et al. [149] with grain sizes below 30 nm. Ichikawa et al. [117] conducted experiments on Ag and Ag/Fe alloy and identified that no dislocations were observed on fine grain sizes smaller than 100 nm under heavy cold rolling conditions. Dislocations have been observed in grains sizes larger than 200 nm.

Experimental studies on deformation of nanostructured metals have proved to be consistent according to the literature review undertaken by Cheng et al. [36]. The intragranular deformation is observed at metals with grain sizes above 30 nm, for FCC metals, however

this depends on the type of metal and its microstructure. Additionally, Cheng et al. [36] developed a model for strength on the grain size regime of 10 and 500-1000 nm, which predicts the strength as a function of grain size and the asymmetry of the yield strength under tension or compression conditions.

6.4.1 Molecular dynamics studies of ultra-fine metals under high deformation mechanisms

Fundamental understanding of deformation processes and mechanical response was gained by molecular dynamics simulations of nanocrystalline materials over the last decade [48, 267, 257, 179, 223, 195, 181, 169, 42, 19]. Swygenhoven and Caro [229], [231] conducted molecular dynamics simulation of nanostructured materials, which showed that metals with grain sizes below 10 nm proved that deformation occurs due to grain boundary sliding. The subsequent work by Schiotz et al. [215] for nanocrystalline Cu with grain sizes of up to 13 nm shows that both intergranular and intragranular mechanisms are active; however, one of them dominates and this is the intergranular. Schiotz also showed that from the stress-strain curves the materials softens as the grain size is increased which is actual a reverse Hall-Petch effect, also verified by Yip [262]. Additionally, MD simulation by Schiotz [216] verified the deformation mechanism at grain sizes of around 10-15 nm and proved that the flow stress varies with grain size and is consistent with the Hall-Petch relation given by

$$\sigma_y = \sigma_o + \frac{k}{\sqrt{d}} \tag{6.4.1}$$

where σ_y is the yield strength, σ_o and k are the material's dependent constants and finally d is the grain diameter. According to the Equation 6.4.1 the yield strength of polycrystalline metals shows an increase as the grain size decreases, hence metals with nanoscale grains are typically stronger than course grain metals. Thus, when the grain size is very small grain boundary processes increasingly dominate the plastic deformation.

The early studies of Swygenhoven et al. [231], [232, 229, 245] also show the grain size influences the deformation mechanism for FCC Ni. The simulations obtained on low and high angle of grain boundaries on grain sizes varying from 3 to 12 nm. He showed that partial dislocations appear within the grain boundaries in which the angle of boundary plays important role. Specifically, Swygenhoven et al. [231] showed that at low angle grain boundaries partial dislocations are efficiently nucleated. On the other hand, partial disloca-

tions do not produce dislocation movement even at grain size of 12 nm. More recent work from Van Swygenhoven and Derlet [244], [246] and Derlet and Swygenhoven [46] gives significant insights into grain boundary dislocation emissions. The work of Swygenhoven et al. [230] for nanostrucured Cu and Ni compares the two metal responses by showing that the stacking faults are observed at smaller grain sizes 8 nm in case of Cu and not in Ni with 12 nm grain sizes. This is observed due to the fact that Cu hold lower stacking fault energies compared to Ni. Additionally, the work done by Zheng and Zhang [268] on the mechanical response of nanostructured Cu at low and high angle grain boundary of average sizes ranging from 3.7 to 6.7 nm also proves that the grain boundary sliding dominates the deformation. In particular for low angle both dislocation motion and grain boundary sliding contribute during plastic deformation.

Chapter 5 discusses the various MD limitations, the domain size, the simulation times and the large number of calculations involved in sliding friction simulations, thus results should be interpreted carefully. Mechanisms such as creep, ordinary diffusion based deformation and microstructural changes due to grain nucleation and growth are difficult to study via these methods as shown by Weertman [252]. Since computer simulations produce samples free of impurities and defects is unlike the real experiments, caution should be taken on the interpretation of the results so that they used as guidelines for the experiments. One of the most important discovery of MD simulations is that dislocations are generated in the grain boundary, as will be seen in the sliding friction simulations of nanostructured Cu/Ag tribopair. Partial dislocations travel across grain boundaries.

Derlet and Swygenhoven [46] work on 2-D and 3-D nanostructured Ni and Al showed that there is a dependence of the strain rate with $1/d$. When dislocations nucleate, a slip plane will travel across the length of the grain. This will define the limiting scale of how far dislocation can travel, which is a distance comparable to grain size. The positional disorder of FCC nanocrystalline Ni as a function of grain size was also observed by Derlet and Swygenhoven [47]. They identified two different types of grain boundary (GB) atoms, the ones in which nearest neighbours are FCC so that GB atoms are in the lattice site of an FCC grain. If the nearest-neighbour atoms are non FCC then the GB atoms will be considered positionally disordered. This is also shown by analysing the pair distribution function (PDF). Positionally disordered GB atoms show an amorphous like behaviour of the PDF, whereas the GB atoms with FCC nearest-neighbours exhibit a second peak of the PDF plots. This effect is also shown in the simulations of the dynamic friction of Cu/Ag tribopair as shown in Figure 6.10. Atoms in this figure are coloured according to

the coordination number, which is a measure of the number of nearest neighbours available for a particular atom.

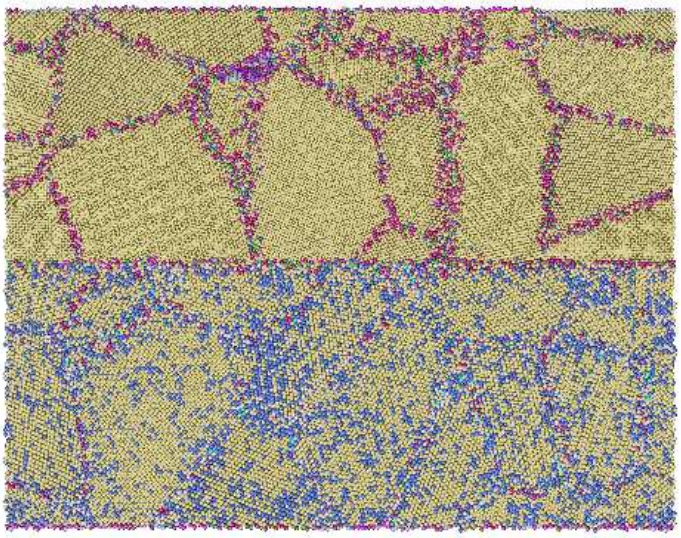

Figure 6.10: Relaxed grain boundaries of Cu/Ag tribopair showing the positionally disorder GB of the Ag slab (lower block). Grain boundary atoms are shown in purple dots whereas the atoms belonging to a grain are shown in gold for both upper and lower slabs. The positional disordered atoms are coloured in light blue.

The time scales involved with MD simulations are relevant to the simulations of plastic deformation. MD simulations of metals to observe the mechanical behaviour evolve at high strain rates typically greater than 10^7 /s as shown in chapter 3.3. This corresponds to 1% strain in 1 ns, which is many orders higher than experimental studies. The studies illustrated above reveal the technological importance of nanostructured materials by investigating in detail the dislocation activities and the grain boundary behaviour during deformation. Both experimental and MD simulation show that several deformation mechanisms maybe present depending on the grain size. In particular the grain size is divided into three categories. Firstly, from $1\,\mu\text{m} > d > 100\,\text{nm}$ the grains at this regime considered as ultrafine. The region of $100\,\text{nm} > d > 20\,\text{nm}$ in which the Hall-Petch slope is decreasing with decreasing grain size diameter, d. The dislocation generated in the grain boundaries can travel through the grains without significantly work hardening causing shear localization. Thirdly, Meyers et al. [179] showed that the region $20\,\text{nm} > d > 1\,\text{nm}$ in which most of the studies show that GB sliding dominate the deformation. These mechanism are dislocation slip, diffusion through dislocations, grain boundary sliding, void and growth nucleation. The complexities involved with the above mechanisms make the mechanical behaviour of bulk nanocrystalline materials a dark area still, which is not yet fully understood.

6.4.2 Voronoi construction for Cu/Ag tribopair sliding

Dynamic friction simulations of nanocrystaline materials were constructed for Cu and Ag to produce realistic systems with high-angle grain boundaries (HAGBs) with an average grain thickness of approximately 15 nm. The nanocrystalline atomic configurations were produced using the Voronoi construction as shown by Rapaport [200], in which a set of grains are chosen randomly rotated and filled with FCC lattice. Voronoi diagrams are constructed around a set of predefined sites and partition these sites into cells, in this case the desired grain boundaries (GB).

This procedure generates grain size that is very close to the log-normal distribution as shown by Kumar et al. [144]. In this procedure it is possible that atoms overlap or become very close to each other. As a result, unrealistically large forces between atoms and system energies are generated that force the system to an unrealistic state of infinitely increasing pressure, temperature and energy. An additional procedure was imposed to obtain more relaxed grain boundaries. The system is annealed for 50 ps by raising the temperature from 0 to 300 K followed by equilibration at 300 K for another 140 ps; unlike Schiotz et al. [215] energy minimisation was not required in this study, since the annealing and equilibration was sufficient to relax the grains of both materials. The thermodynamic properties after relaxation were closely monitored and are illustrated in Figures 6.11, 6.12, 6.13 and 6.14 for temperature and total energy of the system of Cu and Ag blocks. The annealing procedure is important to obtain a realistic system as shown by Schiotz et al. [215], in which the mechanical properties of nanocrystalline Cu showed that unannealed systems were softer, and the annealing conditions do not play an important role.

The procedure for generating grain boundaries on both Cu and Ag is as follows:

1. Two separate simulations were conducted on the materials of interests.
2. The LAMMPS dump files were unscaled using Python scripting to get the actual coordinates and sort the atomic indices for further post-processing.
3. The following step was to convert the LAMMPS dump file into CFG using the tool developed by the author. CFG is a configuration file formating appropriate for visualisation software like AtomEye.
4. Once the atomic topology is converted into CFG format the Voronoi utility developed by Li [153] was used to build the grains by the Voronoi construction method.

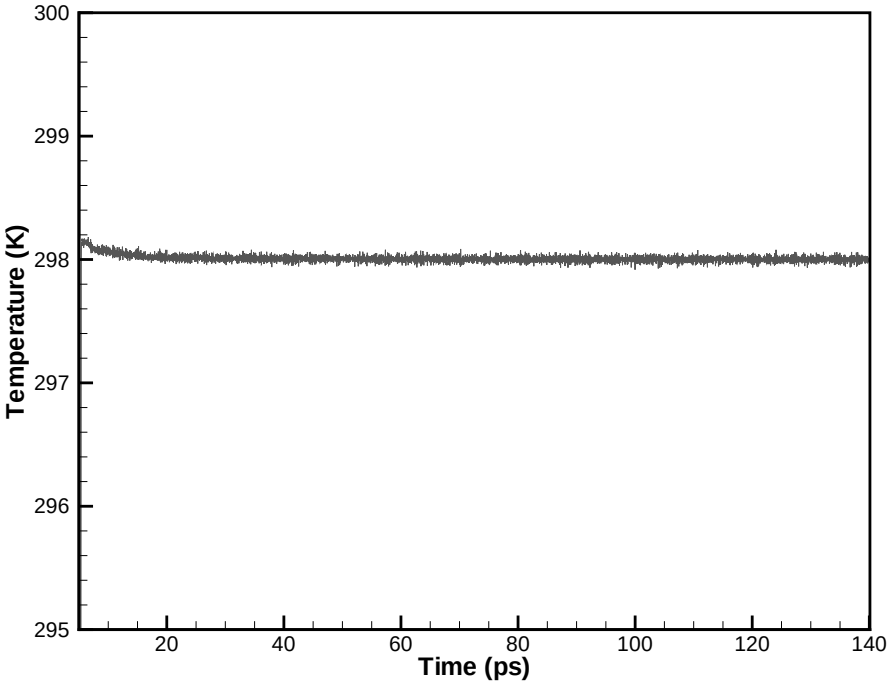

Figure 6.11: Temperature equilibration of Cu block prior to sliding.

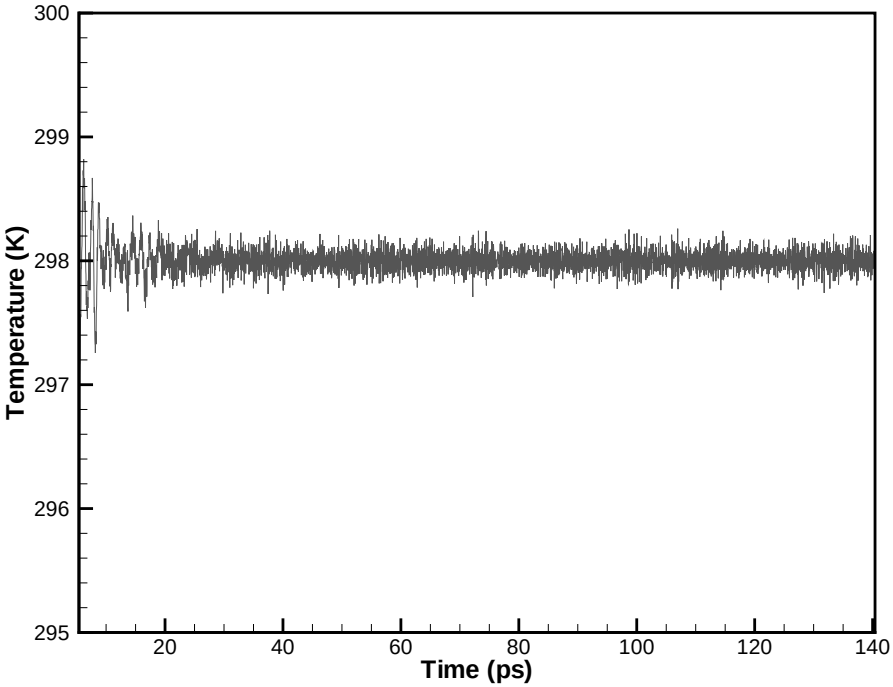

Figure 6.12: Temperature equilibration of Ag block prior to sliding.

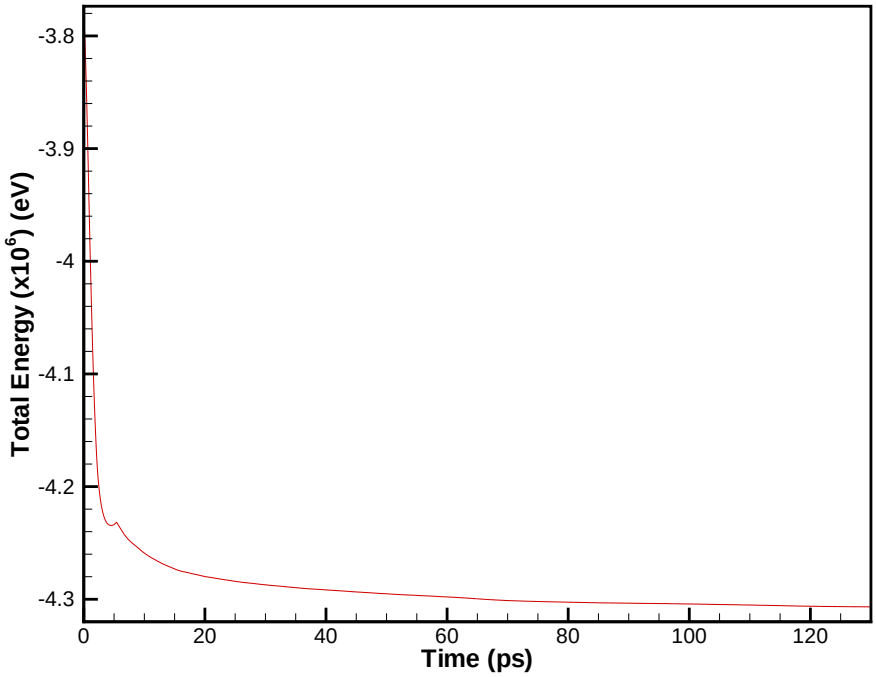

Figure 6.13: Total energy during equilibration of Cu block prior to sliding.

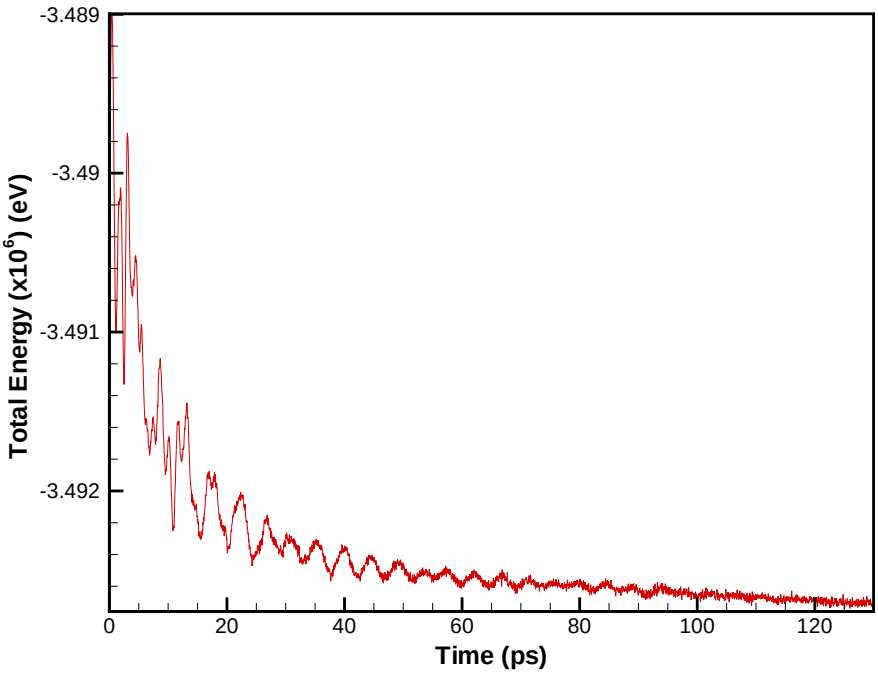

Figure 6.14: Total energy during equilibration of Ag block prior to sliding.

5. The coordinates of the nanocrystals are then unscaled since the ”voronoise” utility scales the coordinates of the atoms.

6. The newly created voronorised configurations of Cu and Ag elements are then placed into separate CFG files and are converted into data files with appropriate format to be invoked by LAMMPS input files.

7. These metals are not ready for simulation and a certain procedure needs to be applied to relax at least the mis-coordinated GB atoms. Thus each material is simulated with NVE thermodynamic ensemble with temperature rescaling from 0 to 298K for 50ps to relax the boundary atoms.

8. The atomic coordinates after the MD simulation are collected and new data files of the final state are produced. The two files with the coordinates are merged into one that contains both Cu and Ag blocks making a simulation domain of (410,320,330) Å.

.

The average volume of each grain equates to the volume of a sphere, the ”voronoise” utility generates a total of fifty two grains for the entire simulation domain with average grain size of 14.9 and 15.1 nm for Cu and Ag respectively. The grain thickness was then calculated using Equation 6.4.2. The volume of each grain was calculated and averaged over the total number of grains contained in each material. Equation 6.4.2 is used with the assumption that each grain has approximately the shape of a sphere, thus solving to evaluate the radius and diameter which gives an indication of the approximate GB thickness.

$$V_g = \frac{4}{3} \cdot \pi \cdot r_g^3 \Rightarrow d = 2 \cdot \left(\frac{3}{4 \cdot \pi} \cdot V_{grain} \right)^{\frac{1}{3}} \tag{6.4.2}$$

where V_g, r_g, and d are the volume, radius and diameter of the grain. The relative orientation of two grains was also evaluated by the rotation angle $\theta = \cos^{-1}[(\alpha_{11} + \alpha_{22} + \alpha_{33} - 1)/2]$, which gives the rotation angle θ. The α_{11}, α_{11} and α_{11} are elements of the rotation matrix $\mathcal{R}_m$ given by Equation 6.4.3, hence θ was calculated to be approximately 90 degrees. For HAGBs the misorientation is approximately greater than 11 degrees. To identify the defects within the materials the centro-symmetric parameters were calculated as shown in Equation 4.5.1.

$$\mathcal{R}_m = \begin{bmatrix} \alpha_{11} & \alpha_{12} & \alpha_{13} \\ \alpha_{21} & \alpha_{22} & \alpha_{23} \\ \alpha_{31} & \alpha_{32} & \alpha_{33} \end{bmatrix} \tag{6.4.3}$$

6.4.3 Equilibrium of the grain boundaries of Cu/Ag tribopair

Nanostructured block of Cu and Ag have been successfully generated using the methodology and techniques mentioned in previous section. Prior to sliding conditions pressure equilibration forced the two materials to compress at a pressure of 5.1 GPa for simulation time of 140 ps. Figures 6.15(a) and 6.15(b) show a visualisation snapshot of the compressed Cu (upper slab) and Ag (lower slab). Upon the initiation of sliding friction, structural changes are dominating and a large number of stacking faults are produced as seen in Figures 6.16(a) and 6.16(b) at simulation time of 52 and 135 ps respectively. These stacking faults are primarily caused by partial dislocations (Shockley partials), which nucleate at the grain boundaries and tend to move through the grains.

As sliding progresses the grains are plastically deformed almost instantly. In chapter 5 in the case of the perfect crystal sliding dislocations nucleate starting from the interface growing up to the reservoirs. The sliding of nanostructured Cu/Ag tribopair showed that although the interface is heavily deformed partial dislocations not only travel through the grains, but dislocations are generated because of grain boundary sliding. It has been observed that grain boundaries and atomic rotation within the grains contribute to plastic deformation. At relative sliding speed of 200 m/s the Figures 6.17(a), 6.17(b), 6.18(a) and 6.18(b) illustrate how grains are deformed at times of 0 , 2.7 , 8.1 , 24.3 ps. The perpendicular red line going through the lower and upper blocks are layers of atoms coloured to observe the slip planes.

It was observed that at relative sliding speed of 25 m/s the Ag block being the weaker shows no stacking faults nucleation at simulations times of 2.7 and 81 ps as shown in Figures 6.19(a) and 6.19(b) respectively. As the sliding progresses at later times stacking faults appear on the Ag block, as shown in Figures 6.20(a) and 6.20(b) for times of 162 and 270 ps respectively. At this speed Cu is the block that plastically deforms instantly.

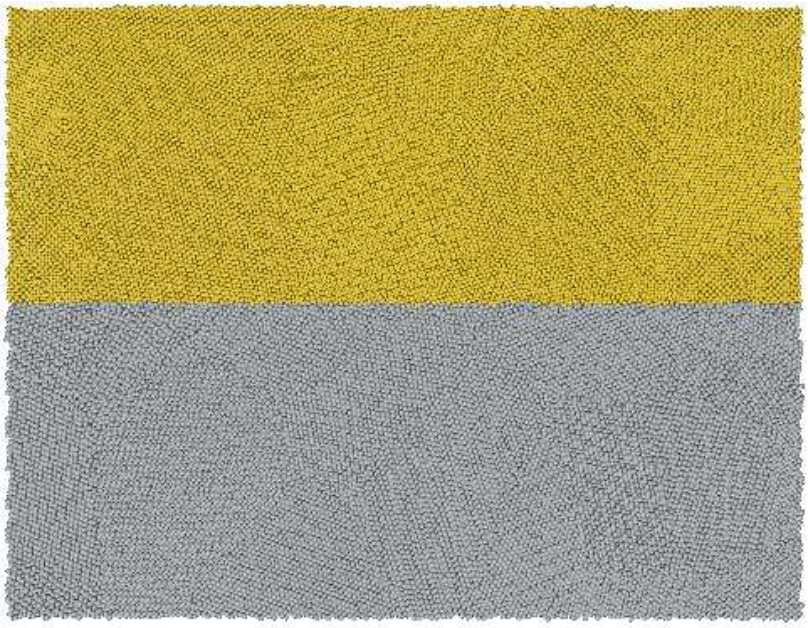

(a) Cu and Ag nanocrystalline block: figure after pressure equilibration

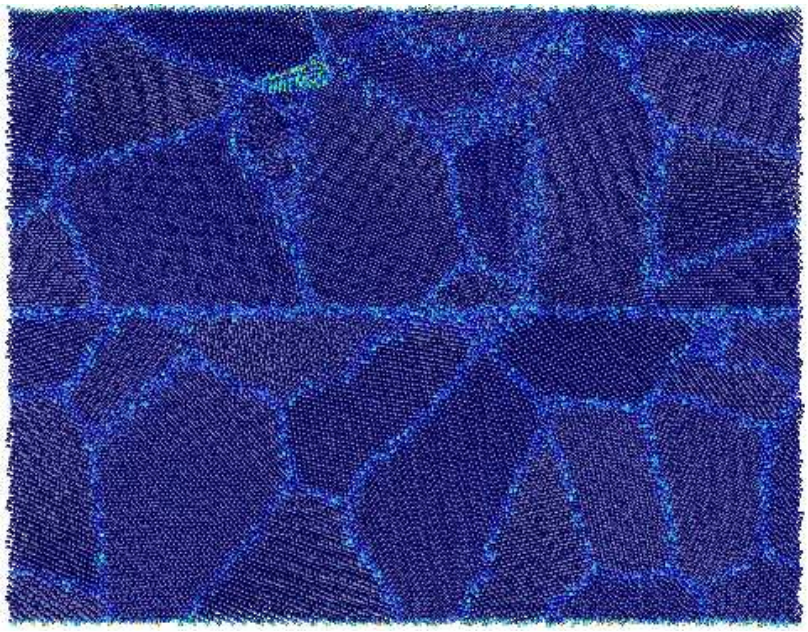

(b) Cu and Ag nanocrystalline block: Figure showing the centro-symmetric parameter

Figure 6.15: Pressure of nanocrystalline Cu and Ag at the equilibration point.

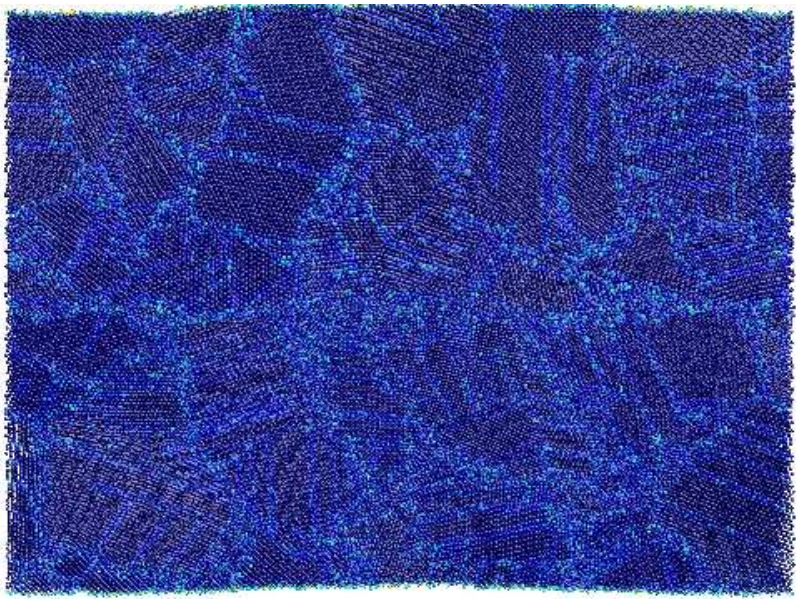

(a) Cu and Ag nanocrystalline sliding, snapshot at time of 52ps

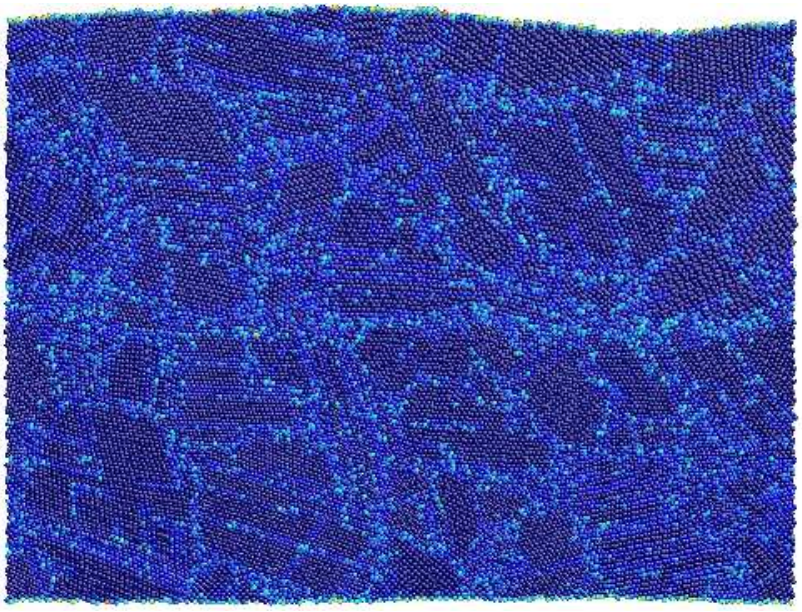

(b) Cu and Ag nanocrystalline sliding, snapshot at time of 135ps

Figure 6.16: Nanocrystalline sliding of Cu/Ag slabs at relative velocity of 200m/s.

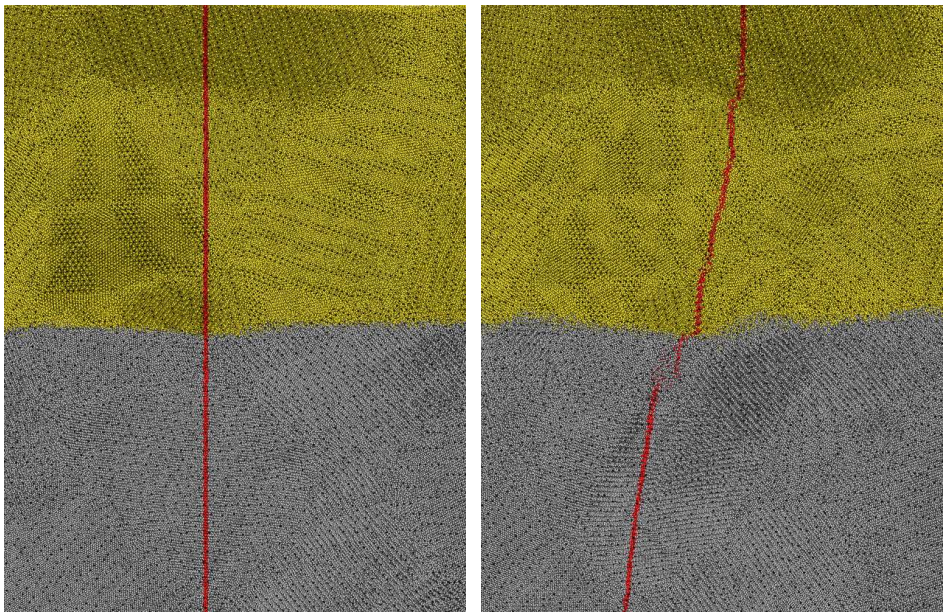

(a) Cu and Ag nanocrystalline sliding, snapshot prior to sliding

(b) Cu and Ag nanocrystalline sliding, snapshot at time of 2.7ps

Figure 6.17: Nanocrystalline sliding of Cu/Ag slabs at relative velocity of 200m/s, vmd snapshots.

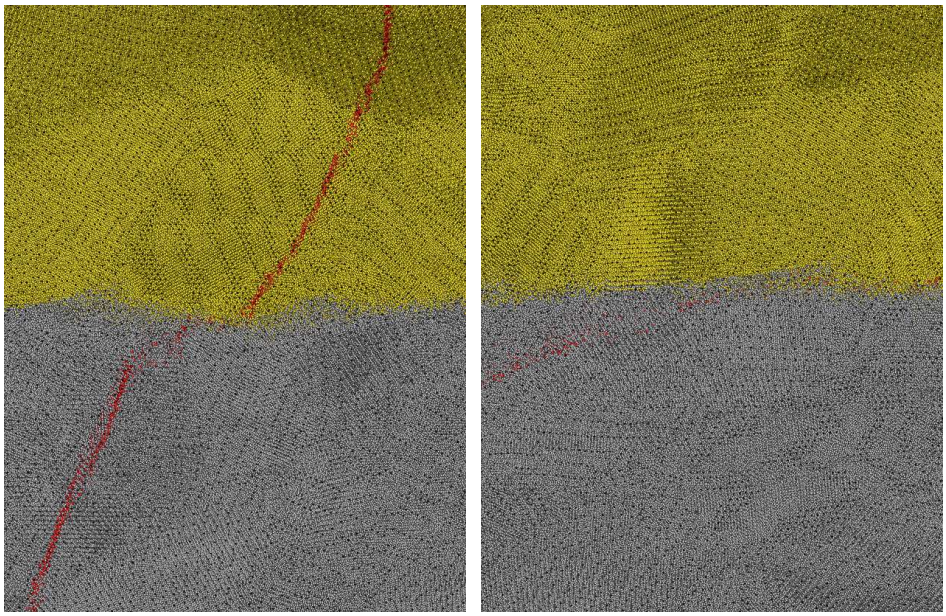

(a) Cu and Ag nanocrystalline sliding, snapshot at time 8.1ps

(b) Cu and Ag nanocrystalline sliding, snapshot at time of 24.3ps

Figure 6.18: Nanocrystalline sliding of Cu/Ag slabs at relative velocity of 200m/s, vmd snapshots.

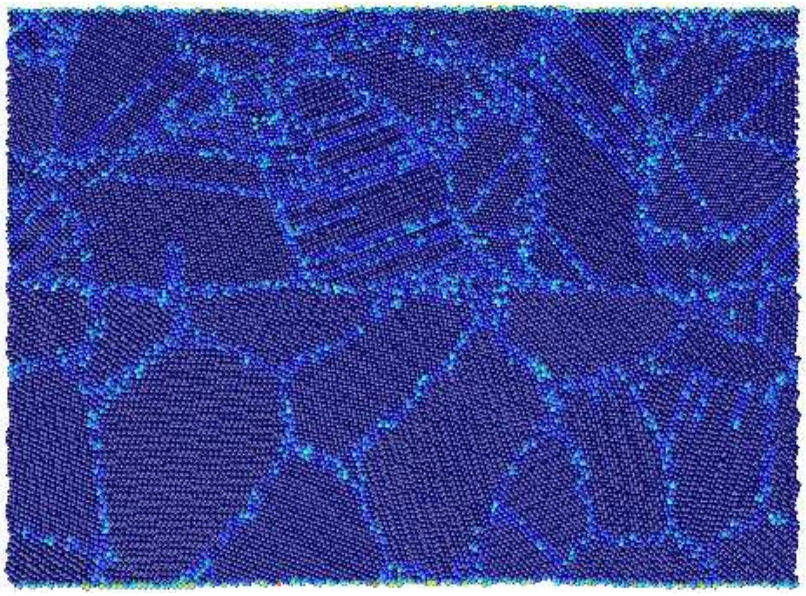

(a) Snapshot at 2.7ps

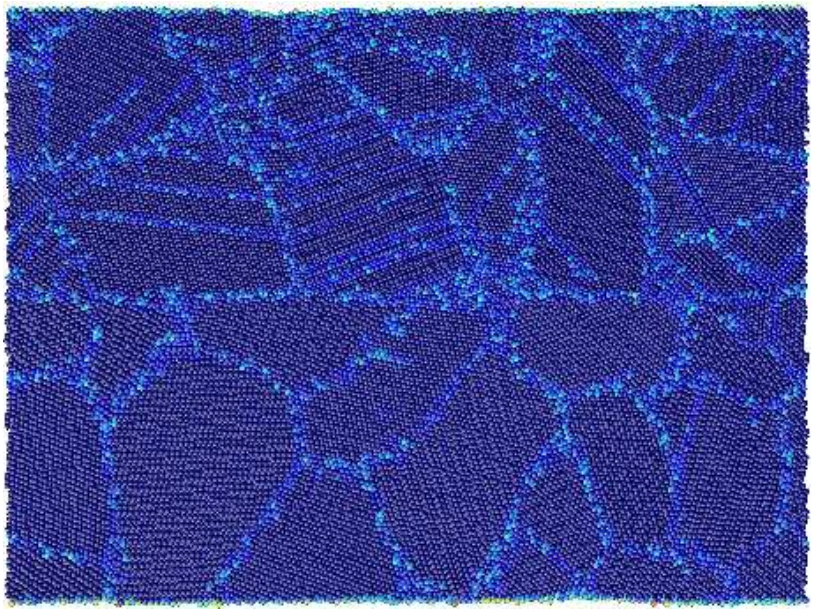

(b) Snapshot at 81ps

Figure 6.19: Sliding of Cu/Ag tribopair at relative speed of 25m/s.

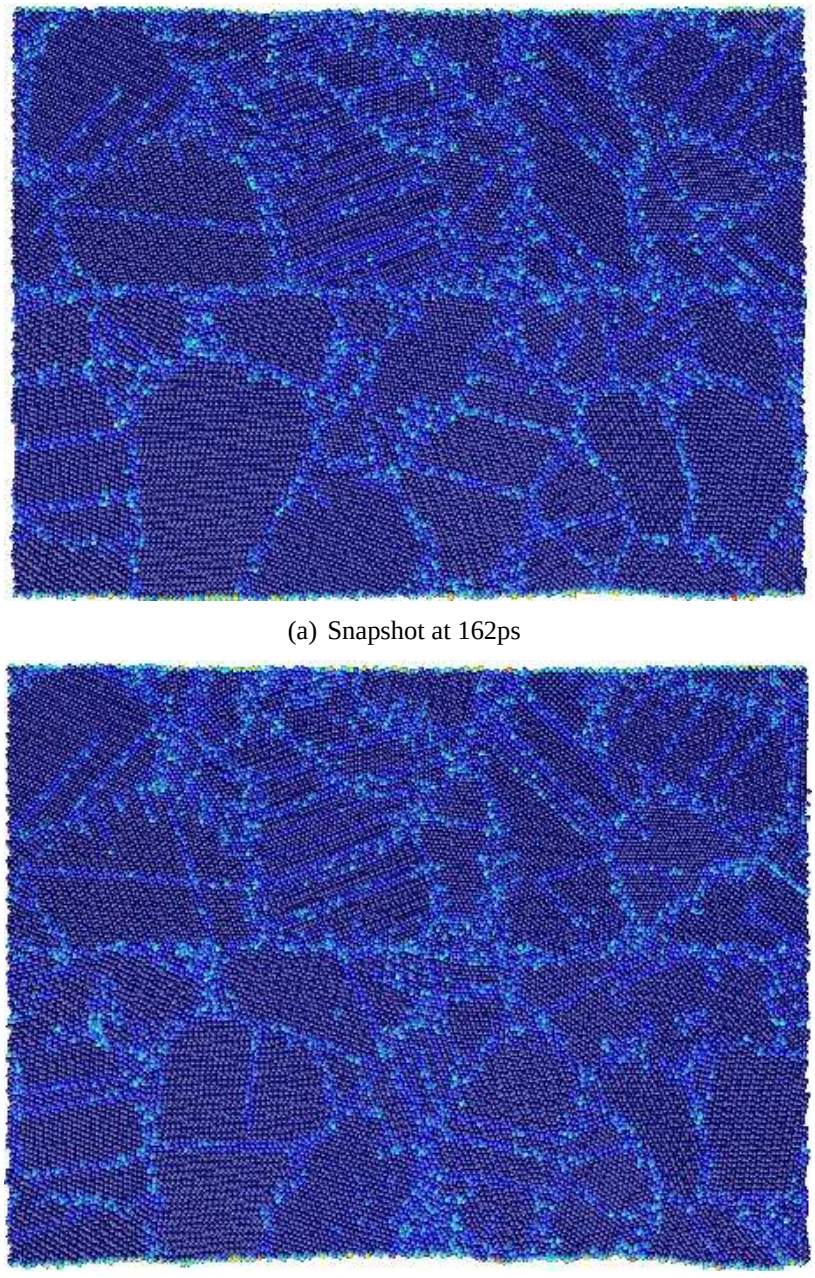

(a) Snapshot at 162ps

(b) Snapshot at 270ps

Figure 6.20: Sliding of Cu/Ag tribopair at relative speed of 25m/s.

6.4.4 Mechanical response of nanocrystalline Cu/Ag tribopair under sliding

The velocity dependence of the frictional force for single (perfect) crystal sliding of Cu/Ag tribopair is discussed in chapter 5.2, the mechanical response under the conditions of sliding was also highlighted in section 6.2. This section presents the novel stress-stain results obtained from molecular dynamics simulations against nanostructured Cu/Ag tribopair. The frictional force, F_t, over time is shown in Figure 6.21 in which a comparison between the perfect crystals is attained. As described in the previous section, the frictional force, F_t, approaches a plateau value during the simulation around which it fluctuates. The level of the plateau can be obtained by averaging F_t over time, once the simulation has reached a steady state. The perfect crystals of Cu and Ag sliding at 200 m/s showing by the in Figure 6.21 indicate large fluctuation due to the shear waves travelling through the medium. However, smoother response is shown during sliding between the nanocrystalline tribopair (Figure 6.21).

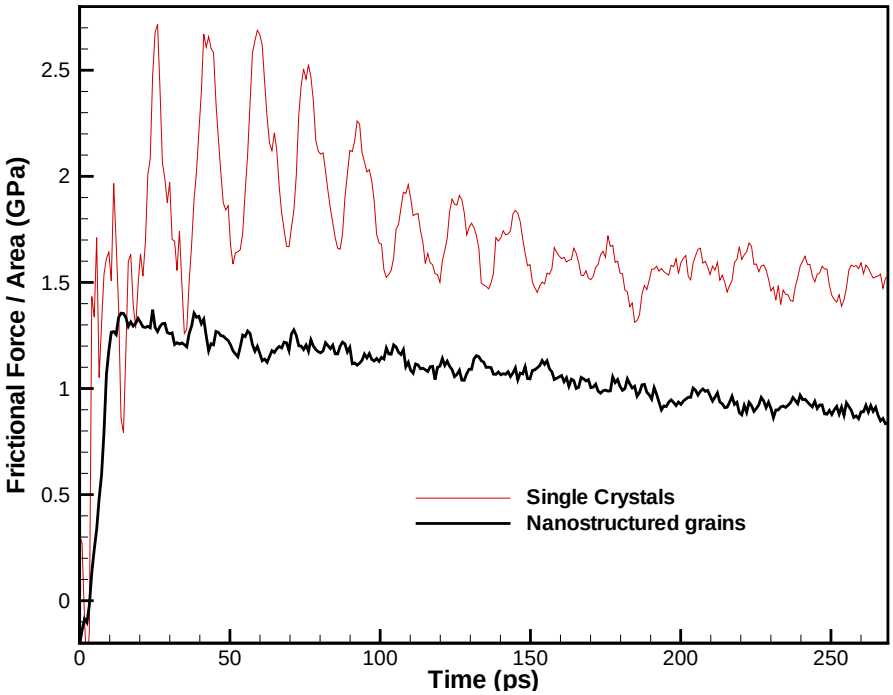

Figure 6.21: Frictional force per unit area of perfect crystal and nanostructured sliding; comparison at sliding speed of 200 m/s.

The velocity weakening of the frictional force is also shown for the nanocrystalline sliding of Cu/Ag in Figure 6.22, which is also compared against the results from perfect crystal sliding. The frictional force per unit area for nanocrystalline tribopairs follows

the same trend in which at low speeds (u_s < 100); the frictional force is low increasing linearly as velocity increases. In this case the frictional force per unit area at sliding speed is between 100 and 200 m/s; however, beyond this point there is a dramatic reduction as velocity increases approaching a plateau at speeds greater than 800 m/s.

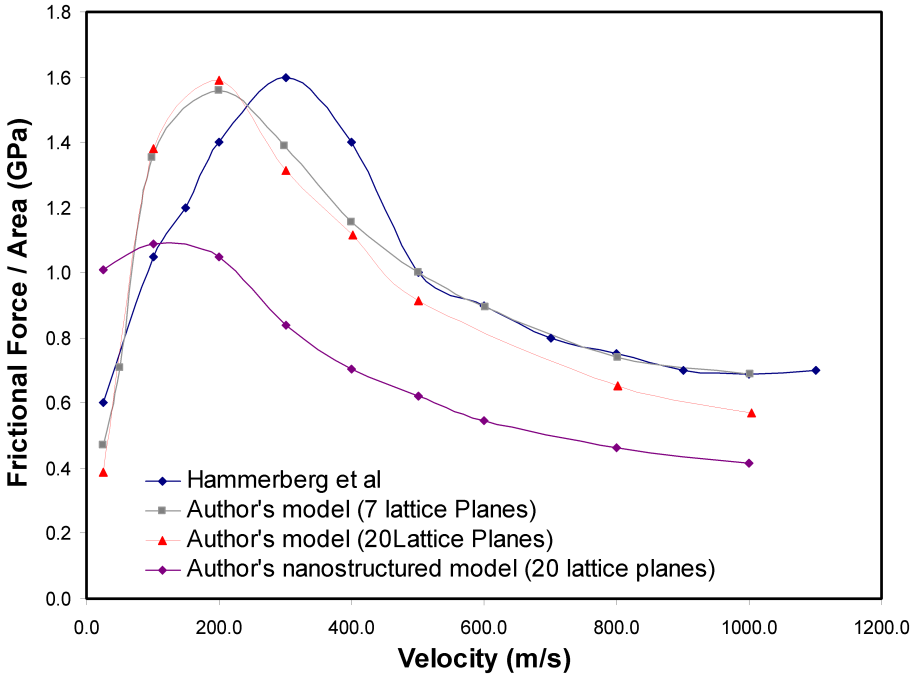

Figure 6.22: Frictional force per unit area results on domain size containing approximately 3 million atoms. The value within the parenthesis indicates the number of lattice planes within the reservoirs.

An interesting observation in these simulations is the fact that the interfacial temperature on the nanocrystalline test cases is lower due to the lower frictional force. As seen in Figure 6.23 the temperature variation for total simulation time of 220 ps reaches 770 K, as compared to 950 K for perfect crystal sliding at the same speed, as seen in Figure 5.13. As the relative sliding speed increases the interfacial temperature builds up to u_s=1000 m/s, reaching values of approximately 1920 K as opposed to perfect crystal sliding which exceeds values of 2000 K.

The procedure for evaluating the strain and stresses is illustrated in sections 6.1 and 6.2 in which values are derived only from the plastic deformation regions. Thus, Figure 6.25(b) at relative speed of 200 m/s presents the stress-strain in each region, and as can be seen the variation between the layers is minor as observed in the perfect crystal sliding. An average plot was generated to capture the stress transformations as shown in Figure 6.25(b). Imposing the same procedure the final state of the stress-strain response is obtained

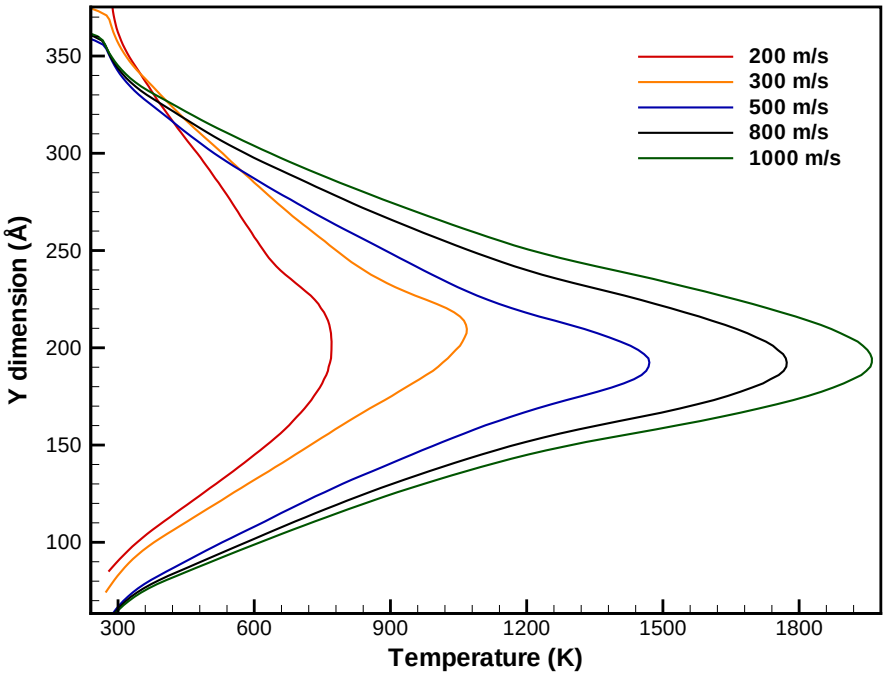

Figure 6.23: Temperature variation across the interface for time of 220 ps at various speeds.

in Figures 6.24(a) and 6.24(b) for relative speeds of 25, 100, ... 1000 m/s. At relative speed of 200 m/s as shown in Figure 6.24(a) there is a dramatic reduction in the yield point of the Cu block which has a value of $\sigma_y = 400MPa$ compared to single crystal sliding of value $\sigma_y = 1.5GPa$ in section 6.6. Additionally, the maximum stress for nanocrystalline Cu occurs at $\sigma_{max} = 1.2GPa$ as opposed to $\sigma_y = 2.1GPa$ in perfect crystal sliding. As observed in section 6.2 the yield point of the material and the maximum stress increases reaching a plateau at sliding speeds of 800 m/s in which the values are approximately $\sigma_y = 1.1GPa$ and $\sigma_{max} = 1.6GPa$. Materials with grains formed into the metal matrix are generally weaker compared to perfect crystals therefore, reduction in the σ_{max} and σ_y as mentioned above is expected.

Considering the stress-strain Figures 6.7, 6.24(a) and 6.24(b), for single crystals and nanocrystalline sliding, it is observed that the yield point of the Cu block consistently increases with sliding speed. Additionally, results from Figure 6.23 and from Chapter 5.2.3 show that interfacial temperature also increases with sliding speed. In general the mechanical strength of metals decreases with increasing temperature, hence the properties are becoming time dependent. The outcome of this study shows that at this size and timescale the increasing interfacial temperature has no effect on the yield point, thus work hardening is not affected by change in temperature.

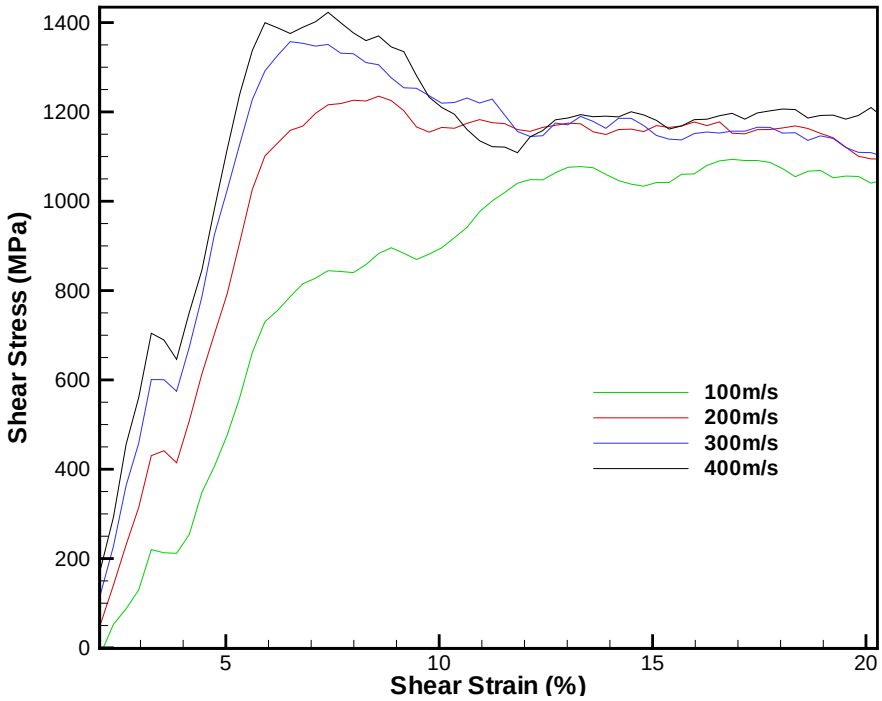

(a) Average stress-strain response at relative sliding speeds ranging from 100-400m/s.

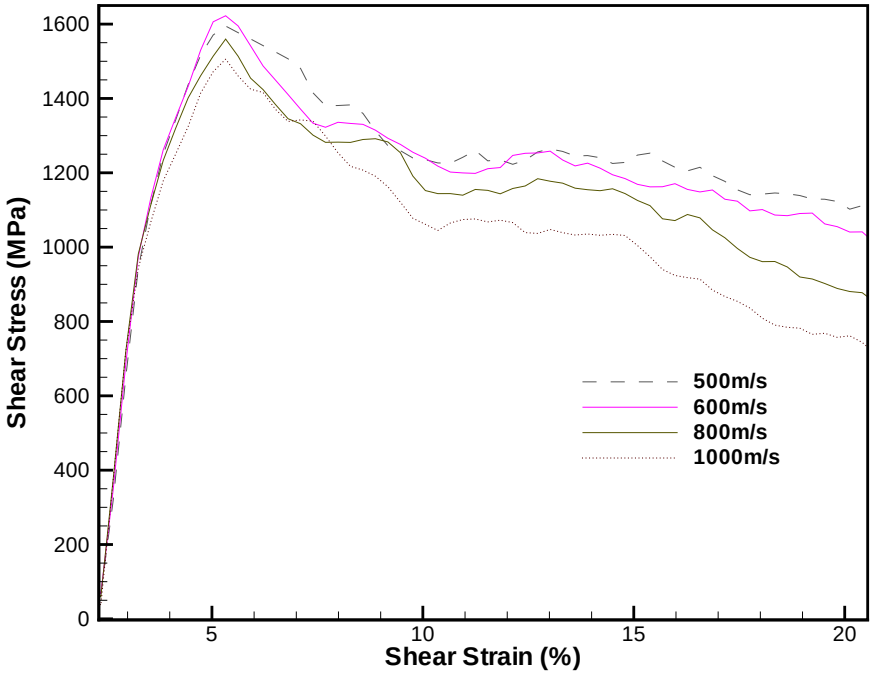

(b) Average stress-strain response at speeds of 500-1000m/s

Figure 6.24: Stress strain response of nanocrystalline Cu/Ag materials.

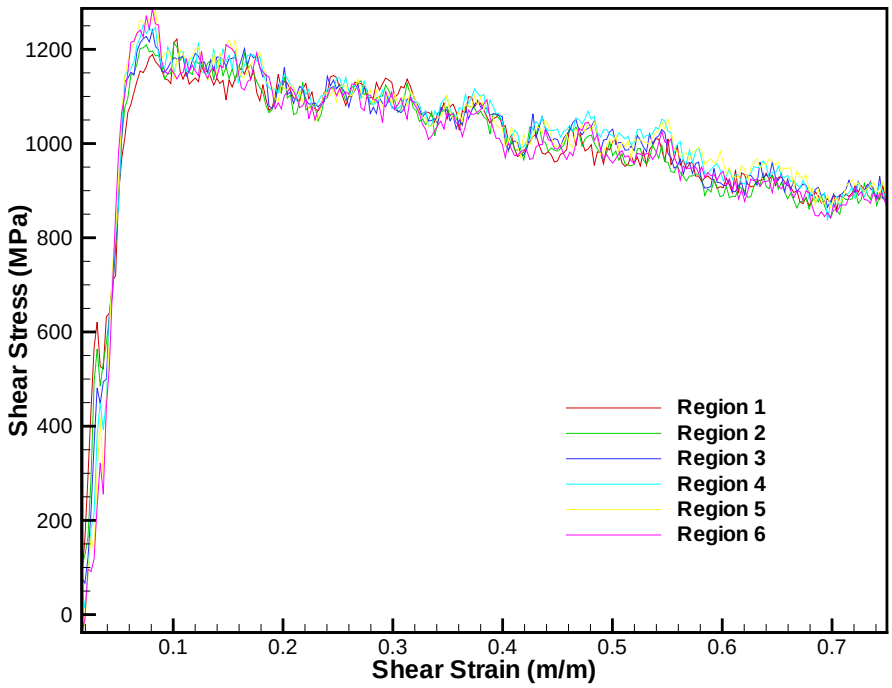

(a) Stress-strain response of Cu/Ag tribopair for all regions at 200m/s

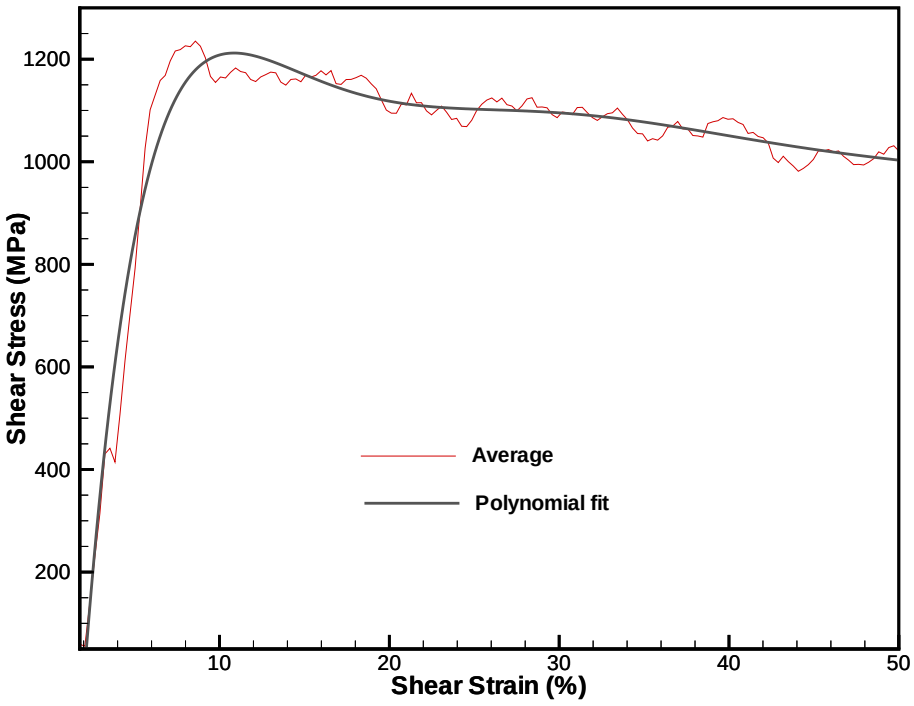

(b) Average stress-strain response of Cu/Ag tribopair at 200m/s

Figure 6.25: Stress strain response of nanocrystalline Cu/Ag materials.

CHAPTER 7

Conclusion and future work

7.1 Conclusion

The structural transformation and changes in non-equilibrium systems were investigated using a simple embedded atom model potential by means of molecular dynamics simulations. This work has focused on the relationship between intermediate structural changes, mechanical response of the system and material transfer at model metal interfaces under the initiation of high speed sliding. The velocity dependence of the frictional force is associated with the plastic deformation of nanocrystalline materials. Additionally the temperature profiles across the interface show that at sliding speeds greater than 200 m/s the softer material is first reaching a temperature close to the melting point. Modelling issues regarding the thermal conductivity are addressed and a way to overcome this was developed via continuum models coupled with MD. Finally, this thesis also sheds light on the yield point of the materials and how they plastically deform during sliding friction, gaining knowledge on how the constitutive models for shear stresses could be developed at high strain rates. The following sections give the concluding remarks for this PhD thesis.

Interatomic potential validations

The EAM potentials used throughout this PhD thesis have been extensively tested to validate and verify the MD code against experimental and computational studies. Thermodynamic macroscopic variables such as melting point heat capacity, thermal expansion and thermal conductivities have been tested for Ag and Cu materials. Although most of these variables show good agreement with experimental results, the thermal conductivity is

greatly underestimated. The MD methods only account for the phonon contribution to the thermal conductivity and not for the free electrons or electron-phonon interaction, which is vital in friction related phenomena.

A thorough investigation was carried out to verify that the TTM method could resolve the underestimation of the thermal conductivity as discussed in Chapter 3.2.2. In theory this method is the state-of-the-art approach to take into account the electron contribution to the thermal conductivity, however, the results are still not consistent with experimental values. This will require further development of the TTM algorithm that will be part of the future work. The need to correct the underestimation of the thermal conductivity leads to the development of a new algorithm as discussed in Chapter 3.2.3, in which the heat conduction equation is solved by taking into account the experimental conductivity of the metal of interest. The algorithm was validated successfully resulting in values of k consistent with experiments.

Finally, mechanical properties such Young's modulus, shear modulus, and yield stress of FCC copper were investigated and results show good agreement with experimental results. Verification of LAMMPS against other MD codes for the mechanical properties was also proved successful.

Boundary conditions for sliding friction

The sliding friction simulations required the development of boundary conditions for imposing desired velocity and external pressure on the system. Several test cases have been successfully performed for the algorithm's verification so that these schemes could be used efficiently for large scale dynamic friction simulations. The first attempt of the boundary conditions was used for test cases to calculate the coefficient of friction for a variety of system sizes. Results show that friction coefficient is independent of the selection of the domain sizes.

Sliding frictions on single crystals

Plastic deformation in metal structures is a complex phenomenon due to the non-linearity of dynamical processes related to the macroscopic defects. The dislocations patterns, which tend to be chaotic and self-organised at the nanoscale as shown in chapter 5, form heterogeneous field of deformation unlike the homogeneous field observed in the macroscopic scale. The sliding friction of single crystals obtained in this PhD confirmed

that the frictional force depends on the frictional velocity imposed. The results show a direct link between the frictional force reduction at high strain rates and the plastic deformation nucleated in the interfacial region. It was observed that deformation is initiated at relative speeds greater than 50 m/s starting from the weaker material. Plastic deformation is associated with temperature rise of the system and hence gradual melting of the interfacial region that results in frictional force reduction. The liquid layer formed in the proximity of the interfacial region constantly increases during sliding and the higher the sliding velocity the thicker the mixed interface. As discussed in chapter 5 for relative velocities of 25 m/s the interfacial region reaches a plateau unlike, at speeds of 400 and 1000 m/s in which the interfacial thickness progressed linearly over time.

The material deformation depends on the rate at which deformation takes place, the temperature and crystallographic structure of the material. This thesis deals with high deformation loading rates, which are isothermal in nature meaning that the energy produced in the system is flowing fast leading to an increase in temperature at the atomic scale. At the macroscale the process is approximately adiabatic since the energy produced cannot flow out of the system due to the short period of time; this ultimately leading to an increase in temperature locally and resulting in a strong interaction between the temperature and deformation rate.

The investigation presented in this thesis provides insight into the mechanisms of dynamic friction and the author identifies the sources of systematic error, which include the under-prediction of the thermal conductivity and the artefacts arising from the reservoir boundary conditions. This was obtained by the continuum simulations using a 1-D hydrocode. Conducting the continuum simulations using phonon-only thermal conductivities derived from MD simulations generate temperature profiles comparable with MD at relative sliding speed of 200 m/s. Furthermore, the reservoir boundary conditions rescaling the temperature used in MD simulations are also imposed in the hydrocode simulations and the results showed that shear waves travelling across both materials are constantly reflected by their presence. The shear wave reverberations are present when continuum simulations are conducted without the reservoir boundary conditions but they are significantly smoother, meaning that slip velocity fluctuates less. The shear stress is also reflected by the reservoir boundary conditions causing plastic deformation and ultimately work hardening resulting in an increase in the shear stress of both blocks. The stress predicted by MD predicts the frictional stress indirectly using velocity contribution part of which is the shear wave reflections. Calculating the stress during a simulation by excluding the kinetic contribu-

tions results to a negligible variation in the stress-strain response as shown in Chapter 6.2. Finally, this work shows how molecular dynamics can provide information about the mechanical behaviour of sliding materials. This is achieved by investigating the material's yield point and its variation with different strain rates. It was found that the yield point and the maximum stress increases as the strain rate increases up to a critical strain rate; beyond this point the yield point hits a plateau.

Sliding friction on nanocrystalline simulations

This PhD thesis also presents for the first time simulations of nanostructured sliding and the results were compared against single crystal's behaviour. The frictional force over time at 200 m/s shows significantly less fluctuations compared with a single crystal plot; this indicates that shear wave reverberation does not greatly affect the frictional force since this occurs within each grain. The frictional force per unit area for nanostructured/nanocrystalline holds lower values for each speed but follows the same trend compared to single crystal sliding. Interestingly at low speeds (25 m/s) the values of frictional force per unit area approaches values close to speeds of 100 and 200 m/s. Producing temperature profiles for these simulations showed that the interfacial temperature is lower than in single crystals and this is because of the presence of the grain boundaries within the structure. Specifically, a temperature reduction of around 20 % is observed at sliding speeds of 200 m/s.

Material with a number of grains formed within the metal matrix is weaker compare to single crystals, thus the values of σ_y decreases. The stress-strain data on nanostructured blocks show a significant reduction in the yield point and the maximum stress of around 73 % and 42 % compared to the single crystals for sliding speed of 200 m/s. As in the study of single crystals the yield point of the stronger material was evaluated as the strain rate is increasing and the plateau is reached at 800 m/s.

7.2 Future work

Following an extensive literature review there are several useful areas that could be considered for a future work as highlighted below:

1. Thermal conductivity correction:

Modification/debugging of the TTM model to correct the thermal conductivity underestimation. Application of this scheme to frictional models to investigate temperature profiles and mechanical response.

The thermal conductivity underestimation of the MD method was successfully corrected by developing the TKC scheme; however, additional work is required to resolve issues for the sliding friction model of Cu/Ag tribopair.

The constant heat algorithm correction studied in Chapter 6.3 is artificially imposed on the interfacial region to subtract heat. The scheme needs to be implemented in the grid analysis module as done in Chapter 3.2.3 for the TKC scheme.

2. Incorporating nanomaterials on sliding metallic surfaces:

   The limited understanding of nanotribology is a significant barrier to the design of many products and processes where there are moving parts. New experimental methods have expanded measuring friction in systems to molecular level is gained, however the results are often specific to a set of experiments and therefore difficult to scale up to macroscopic systems and risky if applied to a wider range of industrial applications. There are dark areas in understanding the molecular processes underpinning marcoscopic tribology that limit the benefits of these emerging methods. This is particularly true regarding the anti-wear properties of nanoparticles, where the mechanism of boundary additives as a main substance included into lubricants has not been researched extensively. These additives aim is to bind lubricants strongly into the surface of the metal, therefore higher stresses can be employed with reduction in wear. Little is known regarding this; however, computer simulations can play an increasingly important role in investigating this phenomenon and improve the knowledge and therefore application of nanotribology (friction, lubrication and wear).

   Simulations may be especially useful when determining how to ensure that nanoparticles enter and remain in the contact area to understand their behaviour. The use of solid/liquid lubricants is increasing in several fields of engineering involving various types of vehicles, heavy industrial equipment and machines, biological devices, and metalworking processes and supercomputers. The European consumption of lubricants reaches approximately 5 million tonnes per annum, and the worldwide consumption is around 40 million. The automotive industry uses the largest lubricant volumes for applications such as internal combustion engines, which uses the most demanding combinations of physical and chemical conditions. The demand for emission minimisation of harmful chemicals such as SO_2 and CO_2 requires highly complex formulation and combination of crankcase and the lubricant interaction. The

types of lubrication condition governing engines are varied, ranging from hydrodynamic to elastohydrodynamic.

The frictional properties of inorganic fullerenes (IF), Tungsten sulfide (WS_2) and its structural analogue Molybdenum sulfide (MoS_2) have been the centre of attention for the last decade. This great interest is due to their amazing mechanical and frictional properties whilst used as additives to lubricants; they have undergone extensive tribological testing using experimental techniques by Tenne [234] and mechanical behaviour using molecular dynamics methods according to Kaplan-Ashiri et al. [135]. Experiments have shown that these spherical nanoparticles demonstrate rolling friction under mild loads typically less than 0.5GPa in the hydrodynamic lubrication regime. Studies show that there is no degradation of the spherical nanoparticles at high-pressure loads ranging from 25 to 30 GPa. Extensive literature shows these nanoparticles can reduce the coefficient of friction (μ) and provide good wear properties. These nanoparticles are the strongest known today, and confined under extreme conditions (high pressure and sliding velocities) between metallic surfaces they could potentially plastically deform these surfaces affecting both μ and wear. Molecular dynamics (MD) capabilities provide excellent opportunities for performing simulations to study the mechanical and frictional properties of WS_2 and MoS_2. Molecular dynamics techniques can be used to obtain the dynamic friction of confined lubricant (including the nanoparticles evenly dispersed) between metals, thus the following points can be investigated in the future as a continuation of this work:

- Generation of the structure of nanoparticles (IF, WS_2, MoS_2, carbon nanotubes and others) and mechanical testing to validate experimental and/or DFT data.
- Possibilities of simulating lubricants used in engines such as polyalfaolefine oil (PAO) and measurements of viscocity and other thermodynamic properties to compare against experimental data.
- Merge the MD models of the nanoparticles with the liquids and observe the dispersion of the nanoparticles within the liquid. Develop a method of mixing both materials to get a uniform liquid.
- The generated liquid will be confined between two metallic interfaces of known metals and sliding friction simulations will be conducted. Molecular dynamics can reveal the physics and structural transformations under dynamic friction and high-pressure conditions of these nanoparticles.
- The evolution of the coefficient of friction μ and the efficiency of these nanoparticles under high pressures ranging from 0.83 to 1.72 GPa will be validated

using the MD friction model.

- Experimental evidence have shown that the IF under friction conditions are subjected to structural changes resulting in their exfoliation in sheets directly into the contact area. If this phenomenon happens within few picoseconds after the initiation of high-speed sliding then the MD will reveal the mechanism of this phenomenon.
- Study of materials mixing, diffusion, and heat dissipation across the interfacial region will be studied.

3. Friction work on silicon and MEMS:

   Silicon (Si) is important for MEMs, especially where there is contact between components. Satyanarayana et al. [211] showed dramatic reduction of the coefficient of friction by at least a factor of 6 and increase of the wear resistance of Si by at least by a factor of 1000 times have been experimentally verified by a combination of dual layer of high molecular weight Polyethylene (UHMWDE) and perfluoropolyether (PFPE). Quantitative and qualitative validation of these simulations using molecular dynamics could lead to a breakthrough in understanding and ultimately improving wear on other applications.

4. Lubrication, MEMS and molecular dynamics:

   The concept of mixed molecular films is when a fluid contains more than a single component which might not be evenly distributed between the bulk and the wall region. In other words, when different molecules assembled together could potentially give greater opportunities for more effective thin films. Therefore, what we have is a combination of two molecular films of different structures, chain lengths, functional groups. Molecular compatibility and solubility between molecules is an unexplored area. This concept is considered a general case for many engineering fluids. MD studies can shed light on how molecules of different structures bond together in order to create a molecule which reduces the friction and wear which is important for MEMs as claimed by Hsu [111].

Bibliography

[1] J. B. Adams, A. Rockett, J. Kieffer, W. Xu, M. Nomura, K. A. Kilian, D. F. Richards, and R. Ramprasad. Atomic-level computer simulation. *J. Nucl. Mater.*, 216:265–274, 1994.

[2] M. P Allen and D. J. Tildesley. *Computer simulation of liquids*. Clarendon Press, Great Britain, 1990.

[3] O. E. Arregui, M. Caro, and A. Caro. Numerical evaluation of the exact phase diagram of an empirical hamiltonian: Embedded atom model for the Au-Ni system. *Phys. Rev. B*, 66(5):054201, 2002.

[4] S. Aubry, D. J. Bammann, J. J. Hoyt, R. E. Jones, C. J. Kimmer, P. A. Klein, G. J. Wagner, E. B. Webb, and J. A. Zimmerman. A robust, coupled approach for atomistic-continuum simulation. *Sandia Report*, pages 1–153, 2004.

[5] J. Barrigaa, B. Fernandez-Diaz, A. Juarros, S. I. U. Ahmedb, and J. L. Arana. Microtribological analysis of gold and copper contacts. *Tribol. Int.*, 40:1526–1530, 2007.

[6] P. T. Barton, M. Kalweit, and D Drikakis. Coupled molecular dynamics and continuum mechanics method for simulating dynamic friction experiments. *In preparation*, 2009.

[7] P. T. Barton, D. Drikakis, and E. I. Romenski. An eulerian finite-volume scheme for large elastoplastic deformations in solids. *International Journal for Numerical Methods in Engineering*, 81(4):453–484, 209.

[8] W. J. Bartz. History of tribologythe bridge between classical antiquity and the 21st century. *Proceedings of the second world tribology congress*, pages 3–12, 2001.

[9] M. I. Baskes. Modified embedded-atom potentials for cubic materials and impurities. *Phy. Rev. B*, 46:2727–2742, 1992.

[10] M. I. Baskes. Atomistic model of plutonium. *Phys. Rev. B*, 62(23):15532–15537, 2000.

[11] A. A. Batista and J. M. Carlson. Bifurcations from steady sliding to stick slip in boundary lubrication. *Phys. Rev. E*, 57(5):4986–4996, 1998.

[12] D. M. Beazley and P. S. Lomdahl. Controlling the data glut in large-scale molecular-dynamics simulations. *Comput. Phys.*, 11(3):230–238, 1997.

[13] A Bejan and A. D. Kraus. *Heat Transfer Handbook*. John Wiley and Sons, 2003.

[14] A. B. Belonoshko, R. Ahuja, O. Eriksson, and B. Johansson. Quasi ab initio molecular dynamic study of Cu melting. *Phys. Rev. B*, 61(6):3838–3844, 2000.

[15] F.R. Berry and J.R. Barber. The division of fictional heat-a guide to the nature of sliding contact. *J. Tribol. ASME*, 106:405–415, 1984.

[16] B. Bhushan. *Boundary Lubrication Studies Using Atomic Force/Friction Force Microscopy*. CRC Press LLC., 1999. B. Bhushan, Handbook of Micro/Nanotribology.

[17] B. H. Billings. *American Institute of Physics Handbook*. McGraw-Hill, New York, 1982.

[18] R. Birringer. Nanocrystalline materials. *Mater. Sci. Eng., A*, 117:33–43, 1989.

[19] E. Bitzek, P. M. Derlet, P. M. Anderson, and H. V. Swygenhoven. The stress-strain response of nanocrystalline metals: A statistical analysis of atomistic simulations. *Acta Mater.*, 56(17):4846–4857, 2008.

[20] P. Blaha, K. Schwarz, P. Sorantin, and S. B. Trickey. Full-potential linearised augmented plane wave programs for crystalline systems. *Comput. Phys. Commun.*, 59: 339–415, 1990.

[21] F. P. Bowden and E. H. Freitag. The friction of solids at very high speeds. I. Metal on metal; II. Metal on diamond. *Proc. R. Soc. Lond. A, Mathematical and Physical Sciences*, 248:350–367, 1958.

[22] F. P. Bowden and P. A. Persson. *Proc. Roy. Soc. 260A*, 433, 1960.

[23] F. P. Bowden and K. E. W. Ridler. Physical properties of surfaces. III. the surface temperature of sliding metals the temperature of lubricated surfaces. *Proc. R. Soc. Lond. A, Mathematical and Physical Sciences*, 154:640–656, 1936.

[24] F. P. Bowden and D. Tabor. *Friction and lubrication of solids*. Clarendon press, 1986.

[25] F. P. Bowden and P. H. Thomas. The surface temperature of sliding solids. *Proc. R. Soc. Lond. A, Mathematical and Physical Sciences*, 223:29–40, 1954.

[26] P. S. Branício and J. P. Rino. Large deformation and amorphization of ni nanowires under uniaxial strain: A molecular dynamics study. *Phys. Rev. B*, 62(24):16950–16955, 2000.

[27] G. Buffa, J. Hua, R. Shivpuri, and L. Fratini. Design of the friction stir welding tool using the continuum based FEM model. *Mater. Sci. Eng., A*, 419:381–388, 2006.

[28] W. D. Callister. *Materials Science and Engineering an Introduction*. John Willey and Sons, Inc, USA, 2007. 7th Edition.

[29] R. Car and M. Parrinello. Unified approach for molecular dynamics and density-functional theory. *Phys. Rev. Lett.*, 55(22):2471–2474, 1985.

[30] A. Caro and M. Victoria. Ion-electron interaction in molecular-dynamics cascades. *Phys. Rev. A*, 40(5):2287–2291, 1989.

[31] R. Catlow and E. Kotomin. *Computational Materials Science*, volume 187. IOS Press, USA, 2003.

[32] W. J. Chang. Molecular-dynamics study of mechanical properties of nanoscale copper with vacancies under static and cyclic loading. *Microelectron. Eng.*, 65:239–246, 2003.

[33] W.-J. Chang and T.-H. Fang. Influence of temperature on tensile and fatigue behavior of nanoscale copper using molecular dynamics simulation. *J. Phys. Chem. Solids*, 64:1279–1283, 2003.

[34] S. Chen, F. Ke, M. Zhou, and Y. Bai. Atomistic investigation of the effects of temperature and surface roughness on diffusion bonding between Cu and Al. *Scr. Mater.*, 55:3169–3175, 2007.

[35] S. D. Chen, A. K. Soh, and F. J. Ke. Molecular dynamics modeling of diffusion bonding. *Scr. Mater.*, 52:1135–1140, 2005.

[36] S. Cheng, J. A. Spencer, and W. W. Milligan. Strength and tension/compression asymmetry in nanostructured and ultrafine-grain metals. *Acta Mater.*, 51(15):4505–4518, 2003.

[37] K. S. Cheung and S. Yip. Atomic-level stress in an inhomogeneous system. *J. Appl. Phys.*, 70(10):5688–5690, 1991.

[38] B. H. Christensen, K. Vestentoft, and P. Balling. Short-pulse ablation rates and the two-temperature model. *Appl. Surf. Sci.*, 253(15):6347–6352, 2007. Proceedings of the Fifth International Conference on Photo-Excited Processes and Applications (5-ICPEPA).

[39] G Ciccotti and W. G. Hoover. *Molecular-Dynamics Simulation of Statistical-Mechanical Systems*. North-Holland, Amsterdam, 1986.

[40] R. J. E. Clausius. On a mechanical theorem applicable to heat. *Philos. Mag.*, 40: 122–127, 1870.

[41] J. Cormier, J. M. Rickman, and T. J. Delph. Stress calculation in atomistic simulations of perfect and imperfect solids. *J. Appl. Phys.*, 89(1):99–104, 2001.

[42] M. Dao, L. Lu, R.J. Asaro, J. T. M. De Hosson, and E. Ma. Toward a quantitative understanding of mechanical behavior of nanocrystalline metals. *Acta Mater.*, 55 (12):4041–4065, 2007.

[43] M. S. Daw and M. I. Baskes. Semiempirical, quantum mechanical calculation of hydrogen embrittlement in metals. *Phys. Rev. Lett.*, 50(17):1285–1288, 1983.

[44] M. S. Daw and M. I. Baskes. Embedded-atom method: Derivation and application to impurities, surfaces, and other defects in metals. *Phys. Rev. B*, 29(12):6443–6453, 1984.

[45] M. S. Daw, S. M. Foiles, and M. I. Baskes. The embedded atom method: a review of theory and applications, materials science reports. *Materials Science Reports*, 9 (7,8):251–310, 1993.

[46] P. M. Derlet and H. V. Swygenhoven. Length scale effects in the simulation of deformation properties of nanocrystalline metals. *Scr. Mater.*, 47(11):719–724, 2002.

[47] P. M. Derlet and V. H. Swygenhoven. Atomic positional disorder in fcc metal nanocrystalline grain boundaries. *Phys. Rev. B*, 67(1):014202, 2003.

[48] P. M. Derlet, A. Hasnaoui, and H. V. Swygenhoven. Atomistic simulations as guidance to experiments. *Scr. Mater.*, 49(7):629–635, 2003. Viewpoint Set No. 31. Mechanical Properties of Fully Dense Nanocrystalline Metals.

[49] C S. Desai. *Mechanics of Materials and Interfaces: The Disturbed State Concept*. CRC Press, USA, 2000.

[50] J. K. Diao, K. Gall, and M. L. Dunn. Surface-stress-induced phase transformation in metal nanowires. *Nat. Mater.*, 2(10):656–660, 2003.

[51] J. K. Diao, K. Gall, and M. L. Dunn. Yield strength asymmetry in metal nanowires. *Nano Lett.*, 4(10):1863–1867, 2004.

[52] Duncan Dowson. *History of Tribology*. Wiley Blackwell, 1998.

[53] D. Drikakis and M. Kalweit. Computational modelling of flow and mass transport processes in nano-technology. In *Handbook of Computational Nanotechnology*. American Scientific Publishers, Stevenson Ranch, CA, USA, 2006.

[54] R. Dronskowski. *Computational Chemistry of Solid State Materials: A Guide for Materials Scientists, Chemists, Physicists and others.* Willey-VCH, USA, 2005.

[55] D. M. Duffy and A. M. Rutherford. Including the effects of electronic stopping and electron-ion interactions in radiation damage simulations. *J. Phys. Condens. Matter*, 19(1):016207, 2007.

[56] F. Ercolessi and J. B. Adams. Interatomic Potentials from first-principles calculations: the force-matching method. *J. Phys. Condens. Matter*, 1993.

[57] Horstemeyer. M. F., M. I. Baskes, A. Godfrey, and D. A. Hughes. A large deformation atomistic study examining crystal orientation effects on the stress-strain relationship. *Int. J. Plast.*, 18:203–229, 2002.

[58] H. Fang, M. F. Horstemeyer, and M. K. Baskes, Solanki. Atomistic simulations of bauschinger effects of metals with high angle and low angle grain boundaries. *Comput. Methods Appl. Mech. Engrg.*, 193:1789–1802, 2004.

[59] R. P. Feynman. Theres plenty of room at the bottom. *Engineering and Science*, 123: 22–36, 1960.

[60] M. Finnis. *Interatomic Forces in Condenced Matter*. Oxford University Press, USA, 2003.

[61] M. W. Finnis and J. E. Sinclair. A simple empirical n-body potential for transition metals. *Philos. Mag. A*, 50:45–55, 1984.

[62] M. W. Finnis, P. Agnew, and A. J. E. Foreman. Thermal excitation of electrons in energetic displacement cascades. *Phys. Rev. B*, 44(2):567–574, 1991.

[63] C. P. Flynn and R. S. Averback. Electron-phonon interactions in energetic displacement cascades. *Phys. Rev. B*, 38(10):7118–7120, 1988.

[64] S. M. Foiles and J. B. Adams. Thermodynamic properties of FCC transition metals as calculated with the embedded-atom method. *Phys. Rev. B*, 40(9):5909–5915, 1989.

[65] S. M. Foiles and M. S. Daw. Calculation of the thermal expansion of metals using the embedded-atom method. *Phys. Rev. B*, 38(17):12643–12644, 1988.

[66] S. M. Foiles, M. I. Baskes, and M. S. Daw. Embedded-atom-method functions for the fcc metals Cu, Ag, Au, Ni, Pd, Pt, and their alloys. *Phys. Rev. B*, 33(12):7983–7991, 1986.

[67] A. Franks. Nanotechnology. *J. Phys. E: Sci. Instrum.*, 20(12):1442–1451, 1987.

[68] D Frenkel and B Smit. *Understanding Molecular Dynamics Simulations: From Alcorithms to Applications*. Elsevier, 2002.

[69] X.-Y. Fu, M. L. Falk, and D. A. Rigney. Sliding behaviour of metallic glass part I: Experimental investigation. *Wear*, Vol 250:409–419, 2001.

[70] X.-Y. Fu, T. Kasai, M. L. Falk, and D. A. Rigney. Sliding behaviour of metallic glass part II: Computer simulation. *Wear*, 250:pp 420–430, 2001.

[71] J Gao, W. D. Luedtke, and U. Landman. Friction control in thin-film lubrication. *J. Phys. Chem. B*, 102:5033–5037, 1998.

[72] J Gao, W. D. Luedtke, and U. Landman. Structures, solvation forces and shear of molecular films in a rough nano-confinement. *Tribol. Lett.*, 9:3–13, 2000.

[73] C. W. Gear. Prentice-Hall, Englewood Cliffs, NJ, 1971.

[74] Totten E. George. *Surface Modification and Mechanisms: Friction, Stress, and Reaction Engineering.*, chapter Simulation Methods for Interfacial Friction in Solids by James E.Hammerberg and Brad Lee Holian. Taylor and Francis, 2004.

[75] T. C. Germann, K. Kadau, and P. S. Lomdahl. 25 tflop/s multibillion-atom molecular dynamics simulations and visualization/analysis on bluegene/l. *Association for Computing Machinery*, 2005.

[76] N. M. Ghoniem, E. P. Busso, N. Kioussis, and H. Huang. Multiscale modelling of nanomechanics and micromechanics: an overview. *Philos. Mag.*, 83:3475–3528, 2003.

[77] H. Gleiter. Nanocrystalline materials. *Prog. Mater Sci.*, 33(4):223–315, 1989.

[78] H. Gleiter. Materials with ultrafine microstructures: Retrospectives and perspectives. *Nanostruct. Mater.*, 1(1):1–19, 1992.

[79] H. Gleiter. Nanostructured materials: basic concepts and microstructure. *Acta Mater.*, 48(1):1–29, 2000.

[80] J. Hafner. Atomic scale materials science. *Acta Mater.*, 48:71–92, 2000.

[81] T. A. Hahn. Thermal expansion of copper from 20 to 800K-standard reference material 736. *J. Appl. Phys.*, 41:5096, 1970.

[82] J. M Haile. *Molecular Dynamics Simulation: Elementary Methods*. Jonh Wiley and Sons, Inc., USA, 1992.

[83] H Hakkinen and M Manninen. The effective-medium theory beyond the nearest-neighbour interaction. *J. Phys.: Condens. Matter*, 1(48):9765–9777, 1989.

[84] J. E. Hammerberg and B. L. Holian. *Simulation methods for interfacial friction in solids.* Marcel Dekker, USA, 2004. G. T. Totten and L. Hong in Surface Modification and Mechanisms, Friction, Stress, and Reaction Engineering.

[85] J. E. Hammerberg and D. A. Rigney. Unlubricated sliding behavior of metals. *MRS Bulletin*, 23(6):32–36, 1998.

[86] J. E. Hammerberg, B. L. Holian, and T. C. Germann. Modeling high friction at ductile metal interfaces. .

[87] J. E. Hammerberg, B. L. Holian, R. Mikulla, and J. Roder. Friction at high rates. *Los Alomas National Laboratory*, .

[88] J. E. Hammerberg, B. L. Holian, J. Roder, A. R. Bishop, and S. J. Zhou. Nonlinear dynamics and the problem of slip at material interfaces. *Physica D*, 123:330–340, 1998.

[89] J. E. Hammerberg, T. C. Germann, B. L. Holian, and R. Ravelo. Nanoscale structure and high velocity sliding at Cu-Ag interfaces. *Materials Research Society Symposium Proceedings*, 821:103–108, 2004.

[90] J. E. Hammerberg, T. C. Germann, B. L. Holian, and R. Ravelo. Nanoscale structure and high velocity sliding at Cu-Ag interfaces. *Materials Research Society Symposium Proceedings*, 821:103–108, 2004.

[91] J. E. Hammerberg, B. L. Holian, T. C. Germann, and R. Ravelo. Nonequilibrium molecular dynamics simulation of metallic friction at Ta/Al and Cu/Ag interfaces. *Metall. Mater. Trans. A*, 35A:2741–2745, 2004.

[92] J. E. Hammerberg, R. Ravelo, T. C. Germann, J. D. Kress, and B. L. Holian. Sliding friction at compressed Ta/Al interfaces. *Shock compression of condensed matter-2003: Proceedings of the Conference of the American Physical Society Topical Group on Shock Compression of Condensed Matter*, 706(1):565–568, 2004.

[93] X. J. Han, M. Chen, and Z. Y. Guo. Thermophysical properties of undercooled liquid Au-Cu from molecular dynamics simulations. *J. Phys. Condens. Matter*, 16: 705–714, 2004.

[94] R. J. Hardy, S Root, and D. R. Swanson. Continuum properties from molecular simulations. *Shock Compression of Condensed Matter - 2001: 12th APS Topical Conference*, 620(1):363–366, 2002.

[95] N. M. Harison. *An introduction to Density Functional Theory*, volume 187. IOS Press, USA, 2003. R. Catlow and E. Kotomin in Computational Materials Science.

[96] J. A. Harrison, C. T. White, R. J. Colton, and D. W. Brenner. Molecular-dynamics simulations of atomic-scale friction of diamond surfaces. *Phys. Rev. B*, 46(15):9700–9708, 1992.

[97] J. W. Harrison. The use of divergent beam interferometry in the measurement of small displacements: an application to the measurement of the thermal expansion of copper up to 1200K. *J. Phys. E: Sci. Instrum.*, 9:545, 1976.

[98] P. J. Hegedus and A. R. Abramson. A molecular dynamics study of interfacial thermal transport in heterogeneous systems. *Int. J. Heat Mass Transfer*, 49:4921–4931, 2006.

[99] P. Heino and E. Ristolainen. Molecular dynamics study of thermally induced shear strain in nanoscale copper. *IEEE Trans. Adv. Packag.*, 22(3):510–514, 1999.

[100] P. Heino and E. Ristolainen. Thermal conduction at the nanoscale in some metals by MD. *Microelectron. J.*, 34:773–777, 2003.

[101] W. Hergert, A. Ernst, and M. Dane. *Computational Materials Science: From Basic Principles to Materials Properties (Lecture Notes in Physics)*. Springer-Verlag Berlin, New York, 2004.

[102] M. Hirano and K. Shinjo. Atomistic locking and friction. *Phys. Rev. B*, 41(17): 11837–11851, Jun 1990.

[103] M. Hirano and K. Shinjo. Superlubricity and frictional anisotropy. *Wear*, 168(1-2): 121 – 125, 1993. ISSN 0043-1648.

[104] B. L. Holian and P. S. Lomdahl. Plasticity induced by shock waves in nonequilibrium molecular-dynamics simulations. *Science*, 280:2085–2088, 1998.

[105] B. L. Holian, A. F. Voter, N. J. Wagner, R. J. Ravelo, S. P. Chen, W. G. Hoover, C. G. Hoover, J. E. Hammerberg, and T. D. Dontje. Effects of pairwise versus many-body forces on high-stress plastic deformation. *Phys. Rev. A*, 43(6):2655–2661, 1991.

[106] B. L. Holian, J. E. Hammerberg, and P. S. Lomdahl. The birth of dislocations in shock waves and high-speed friction. *J. Comput. Aided Mater. Des.*, 5:207–224, 1998.

[107] Y. Hong, L. YongJun, C. Min, and G. ZengYuan. A molecular dynamics study on melting point and specific heat of Ni3Al alloy. *Science in China Series G: Physics, Mechanics and Astronomy*, 50(4):407–413, 2007.

[108] M. F. Horstemeyer and M. I. Baskes. Atomistic finite deformation simulations: a discussion on length scale effects in relation to mechanical stresses. *J. Engrg. Matls. Techn. Transactions of the ASIVIE*, 121(24):114–119, 1998.

[109] M. F. Horstemeyer, L. Lim, W. Y. Lu, D. A. Mosher, M. I. Baskes, V. C. Pantil, and S. J. Plimpton. Torsion/simple shear of single crystal copper. *Trans. of the ASME*, 124:322–328, 2002.

[110] M.F Horstemeyer, M.I. Baskes, and S.J. Plimpton. Computational nanoscale plasticity simulations using embedded atom potentials. *Theoretical and Applied Fracture Mechanics*, 37(1):49–98, 2001.

[111] S. M. Hsu. Nano-lubrication: concept and design. *Tribology International*, 37(7): 537–545, 2004. The New Trends and Frontiers in Tribology.

[112] Y.-Z. Hu and S. Granick. Microscopic study of thin film lubrication and its contributions to macroscopic tribology. *Tribol. Lett.*, 5:81–88, 1998.

[113] Y.-Z. Hu, H. Wang, Y. Guo, and L.-Q. Zheng. Simulation of lubricant rheology in thin film lubrication part I: simulation of Poiseuille flow. *Wear*, 196:243–248, 1996.

[114] Y.-Z. Hu, H. Wang, Y. Guo, and L.-Q. Zheng. Simulation of lubricant rheology in thin film lubrication part 2: simulation of Couette flow. *Wear*, 196:249–253, 1996.

[115] Z.-X. Huang and Z. Tang. Evaluation of momentum conservation influence in non-equilibrium molecular dynamics methods to compute thermal conductivity. *Physica B*, 373:291–296, 2006.

[116] W. Humphrey, A. Dalke, and K. Schulten. VMD – Visual Molecular Dynamics. *J. Mol. Graphics*, 14:33–38, 1996.

[117] S. Ichikawa, K. Miyazawa, H. Ichinose, and K. Ito. The microstructure of deformed nanocrystalline Ag and Ag/Fe alloy. *Nanostruct. Mater.*, 11(8):1301–1311, 1999.

[118] H. Ikeda, Y. Qi, T. Çagin, K. Samwer, W. L. Johnson, and W. A. Goddard. Strain rate induced amorphization in metallic nanowires. *Phys. Rev. Lett.*, 82(14):2900–2903, 1999.

[119] J. H. Irving and J. G. Kirkwood. The statistical mechanical theory of transport processes. iv. the equations of hydrodynamics. *J. Chem. Phys.*, 18(6):817–829, 1950.

[120] D. S. Ivanov and L. V. Zhigilei. Combined atomistic-continuum modeling of short-pulse laser melting and disintegration of metal films. *Phys. Rev. B*, 68(6):064114, 2003.

[121] D. S. Ivanov and L. V. Zhigilei. Effect of pressure relaxation on the mechanisms of short-pulse laser melting. *Phys. Rev. Lett.*, 91(10):105701, 2003.

[122] A. Jabbarzadeh, J.D. Atkinson, and R.I. Tanner. A parallel algorithm for molecular dynamics simulation of branched molecules. *Computer Physics Communications*, 150:65–84, 2002.

[123] A. Jabbarzadeh, P. Harrowell, and R.I. Tanner. The structural origin of the complex rheology in thin dodecane films: Three routes to low friction. *Tribology International*, 40:100–106, 2007.

[124] K. W. Jacobsen, J. K. Norskov, and M. J. Puska. Interatomic interactions in the effective-medium theory. *Phys. Rev. B*, 35(14):7423–7442, 1987.

[125] C. Jarzynski. Nonequilibrium equality for free energy differences. *Phys. Rev. Lett.*, 78(14):2690–2693, 1997.

[126] J.-W. Jeong and K. J. Chang. Molecular-dynamics simulations for the shock Hugoniot meltings of Cu, Pd and Pt. *J.Phys.:Condens. Matter*, 11:3799–3806, 1999.

[127] J.-W. Jeong, I.-H. Lee, and K. J. Chang. Molecular-dynamics study of melting on the shock Hugoniot of Al. *Phys. Rev. B*, 59(1):329–333, 1999.

[128] Simmons J.H. Structural and dynamic modeling of mechanical behavior of solids. *Journal of Computer-Aided Materials Design*, 4(3):207–213, 1998.

[129] R. A. Johnson. Alloy models with the embedded-atom method. *Phys. Rev. B*, 39 (17):12554–12559, 1989.

[130] L. Ju. The mechanics and physics of defect nucleation. *MRS Bulletin*, 32:151–158, 2007.

[131] P. Jund and R. Jullien. Molecular-dynamics calculation of the thermal conductivity of vitreous silica. *Phys. Rev. B*, 59(21):13707–13711, 1999.

[132] M. Kalweit. Molecular modelling of meso- and nanoscale dynamics. *PhD thesis*, 2008.

[133] J.-W. Kang and H.-J. Hwang. Mechanical deformation study of copper nanowire using atomistic simulation. *Nanotechnology*, 12:295–300, 2001.

[134] J. W. Kang and H. J. Hwang. Molecular dynamics simulations of ultra-thin Cu nanowires. *Computational Materials Science*, 27(3):305–312, 2003.

[135] I. Kaplan-Ashiri, S. R. Cohen, K. Gartsman, V. Ivanovskaya, T. Heine, G. Seifert, I. Wiesel, H. D. Wagner, and R. Tenne. On the mechanical behavior of WS_2 nanotubes under axial tension and compression. *PNAS*, 103(3):523–528, 2006.

[136] T. Kawaguchi and H. Matsukawa. Dynamical frictional phenomena in an incommensurate two-chain model. *Phys. Rev. B*, 56(21):13932–13942, Dec 1997.

[137] A. Kawamoto, J. Jameson, K. Cho, and R. W. Dutton. Challenges for atomic scale modeling in alternative gate stack engineering. *IEEE Transaction on electron devices*, 47(10):1787–1794, 2000.

[138] T. Kawamura, Y. Kangawa, and K. Kakimoto. An investigation of thermal conductivity of nitride-semiconductor nanostructures by molecular dynamics simulation. *J. Cryst. Growth*, 298:251–253, 2007.

[139] M. Ke, S. A. Hackney, W. W. Milligan, and E. C. Aifantis. Observation and measurement of grain rotation and plastic strain in nanostructured metal thin films. *Nanostruct. Mater.*, 5(6):689–697, 1995.

[140] C. L. Kelchner, S. J. Plimpton, and J. C. Hamilton. Dislocation nucleation and defect structure during surface indentation. *Phys. Rev. B*, 58(17):11085–11088, 1998.

[141] D.E. Kim and N.P. Suh. Molecular dynamics investigation of two-dimensional atomic-scale friction. *J. Tribol.*, 116:225–231, 1994.

[142] Y. C. Kong, D. J. Alejandre, and J. Tildesley. The molecular dynamics simulation of boundary-layer lubrication. *Molecular Physics*, 92:7–18, 1997.

[143] K. S. Kumar, H. V. Swygenhoven, and S. Suresh. Mechanical behavior of nanocrystalline metals and alloys. *Acta Mater.*, 51(19):5743–5774, 2003. The Golden Jubilee Issue. Selected topics in Materials Science and Engineering: Past, Present and Future.

[144] S. Kumar, S. K. Kurtz, J. R. Banavar, and M. G. Sharma. Properties of a three-dimensional poisson-voronoi tesselation: A monte carlo study. *Journal of Statistical Physics*, 67(3–4):523–551, 2005.

[145] U. Landman, W. D. Luedtke, R. N. Barnett, C. L. Cleveland, M. W. Ribarsky, E. Arnold, S. Ramesh, H. Baumgart, A. Martinez, and B. Khan. Faceting at the silicon (100) crystal-melt interface: Theory and experiment. *Phys. Rev. Lett.*, 56(2): 155–158, 1986.

[146] Uzi Landman, W. D. Luedtke, and Jianping Gao. Atomic-scale issues in tribology: Interfacial junctions and nano-elastohydrodynamics. *Langmuir*, 12:4514–4528, 1996.

[147] A.B. Lebedev, Yu.A. Burenkov, A.E. Romanov, V.I. Kopylov, V.P. Filonenko, and V.G. Gryaznov. Softening of the elastic modulus in submicrocrystalline copper. *Materials Science and Engineering A*, 203:165–170, 1995.

[148] Y. H. Lee, R. Biswas, C. M. Soukoulis, C. Z. Wang, C. T. Chan, and K. M. Ho. Molecular-dynamics simulation of thermal conductivity in amorphous silicon. *Phys. Rev. B*, 43(8):6573–6580, 1991.

[149] M. Legros, B. R. Elliott, M. N. Rittner, J. R. Weertman, and K. J. Hemker. Microsample tensile testing of nanocrystalline metals. *Philosophical Magazine A*, 80 (4):1017–1026, 2000.

[150] Anael Lemaitre and Jean Carlson. Boundary lubrication with a glassy interface. *Journal of Physics: Condense Matter (online source)*, 1:1–18, 2003.

[151] B. Li, P. C. Clapp, J. A. Rifkin, and X. M. Zhang. Molecular dynamics calculation of heat dissipation during sliding friction. *Int. J. Heat Mass Transfer*, 46:37–43, 2003.

[152] Ju Li. *Atomistic Visualisation.* Springer, Netherlands, 2005. Yip, Sindney in Handbook of Materials Modeling, Part A. Methods.

[153] L. Li. Atomeye: an efficient atomistic configuration viewer. *Modelling Simulation in Materials Science and Engineering*, 11:173–177, 2003.

[154] X. Li and E. Weinan. Variational boundary conditions for molecular dynamics simulation of solids at low temperature. *Comm. Comput. Phys.*, Vol 1, No. 1,:135–175., 2006.

[155] W Liang and M Zhou. Response of copper nanowires in dynamic tensile deformation. *Proc. Inst. Mech. Engrs. Part C: Journal of Mechanical Engineering Science*, 218:599–606, 2004.

[156] J. Lindhard and M. Scharff. Energy dissipation by ions in the Kev region. *Phys. Rev.*, 124(1):128–130, 1961.

[157] E. M. Lopasso, M. Caro, A. Caro, and P. E. A. Turchi. Phase diagram of an empirical potential: The case of Fe-Cu. *Phys. Rev. B*, 68(21):214205, 2003.

[158] Gang Lu and Efthimios Kaxiras. Overview of multiscale simulations of materials. 2005. Rieth, Michael and Schommers, Wolfram.,Handbook of Theoretical and Computational Nanotechnology.

[159] K. Lu. Nanocrystalline metals crystallized from amorphous solids: nanocrystallization, structure, and properties. *Mater. Sci. Eng., R*, 16(4):161–221, 1996.

[160] J. R. Lukes, D. Y. Li, X.-G. Liang, and C.-L. Tien. Molecular dynamics study of solid thin-film thermal conductivity. *Journal of Heat Transfer*, 122(3):536–543, 2000.

[161] S.-N. Luo and T. J. Ahrens. Superheating systematics of crystalline solids. *Appl. Phys. Lett.*, 82(12):1836, 2003.

[162] S. N. Luo, T. J. Ahrens, T. Cagin, A. Strachan, W. A. Goddard, and D. C. Swift. Maximum superheating and undercooling: Systematics, molecular dynamics simulations, and dynamic experiments. *Phys. Rev. B*, 68(13):134206, 2003.

[163] S.-N. Luo, S. Strachan, and D. C. Swift. Nonequilibrium melting and crystallization of a model Lennard-Jones system. *J. Chem. Phys.*, 120(24):11640–11649, 2004.

[164] J. F. Lutsko. Stress and elastic constants in anisotropic solids: Molecular dynamics techniques. *J. Appl. Phys.*, 64(3):1152–1154, 1988.

[165] J. F. Lutsko, D. Wolf, S. Yip, S. R. Phillpot, and T. Nguyen. Molecular-dynamics method for the simulation of bulk-solid interfaces at high temperatures. *Phys. Rev. B*, 38(16):11572–11581, 1988.

[166] J. F. Lutsko, D. Wolf, S. R. Phillpot, and S. Yip. Molecular-dynamics study of lattice-defect-nucleated melting in metals using an embedded-atom-method potential. *Phys. Rev. B*, 40(5):2841–2855, 1989.

[167] J. F. Lutsko, D. Wolf, S. R. Phillpot, and S. Yip. On the relevance of extrinsic defects to melting: A molecular dynamics study using an embedded atom potential. *Scr. Mater.*, 23:333–338, 1989.

[168] S. E. Lyshevski. *Nano- and Micro-Electromechanical Systems: Fundamentals of Nano-and-Micro-Engineering.* CRC Press LLC., 2001.

[169] X. L. Ma and W. Yang. Dislocation-assisted grain growth in nanocrystalline copper under large deformation. *Scr. Mater.*, 59(7):792–795, 2008.

[170] S. P. Marsh. *LASL Shock Hugoniot Data.* Berkeley,University of California Press, USA, 1980.

[171] TB Massalski. *Binary alloy diagrams*, volume 1. Metals Park: ASM, 1986.

[172] J. C. Maxwell. On reciprocal figures, frames and diagrams of forces. *Trans. R. Soc. Edinburgh*, XXVI:1–43, 1870.

[173] J. C. Maxwell. Van der waals on the continuity of the gaseous and liquid states. *Nature*, pages 477–480, 1874.

[174] M. A. Mayers. *Dynamic Behaviour of Materials*. John Wiley and Sons, USA, 1994.

[175] D. A McQuarie. *Statistical Mechanics*. Harper and Row, 1992.

[176] J. Mei and J. W. Davenport. Free-energy calculations and the melting point of Al. *Phys. Rev. B*, 46(1):21–25, 1992.

[177] J. Mei, J. W. Davenport, and G. W. Fernando. Analytic embedded-atom potentials for FCC metals: Application to liquid and solid copper. *Phys. Rev. B*, 43(6):4653–4658, 1991.

[178] E. A. Merritt and D. J. Bacon. Raster3D version 2: photorealistic molecular graphics. *Methods in Enzymology*, 277:505–524, 1997.

[179] M. A. Meyers, A. Mishra, and D. J. Benson. Mechanical properties of nanocrystalline materials. *Progress in Materials Science*, 51(4):427–556, 2006.

[180] Paul T. Mikulski, Guangtu Gao, Ginger M. Chateauneuf, and Judith A. Harrison. Contact forces at the sliding interface: Mixed versus pure model alkane monolayers. *The Journal of chemical physics*, 122:024701.

[181] P. C. Millett, T. Desai, V. Yamakov, and D. Wolf. Atomistic simulations of diffusional creep in a nanocrystalline body-centered cubic material. *Acta Mater.*, 56(14): 3688–3698, 2008.

[182] W. W. Milligan, S. A. Hackney, M. Ke, and E. C. Aifantis. In situ studies of deformation and fracture in nanophase materials. *Nanostruct. Mater.*, 2(3):267–276, 1993. Viewpoint Set of Selected Papers from a Special Symposium on Nanocrystalline Materials.

[183] U. Mizutani, S. Noguchi, and T. B. Massalski. Electronic specific heat of α-phase alloys based on copper and silver. *Phys. Rev. B*, 5(6):2057–2065, 1972.

[184] F. Mller-Plathe and D. Reith. Cause and effect reversed in non-equilibrium molecular dynamics: an easy route to transport coefficients. *Comput. Theor. Polym. Sci.*, 9(3-4): 203–209, 1999.

[185] J. R. Morris and K. M. Ho. Calculating accurate free energies of solids directly from simulations. *Phys. Rev. Lett.*, 74(6):940–943, 1995.

[186] J. R. Morris and X. Song. The melting lines of model systems calculated from coexistence simulations. *J. Chem. Phys.*, 116(21):9352–9358, 2002.

[187] J. R. Morris, C. Z. Wang, K. M. Ho, and C. T. Chan. Melting line of aluminum from simulations of coexisting phases. *Phys. Rev. B*, 49(5):3109–3115, 1994.

[188] P. M. Morse. Diatomic molecules according to the wave mechanics. II. vibrational levels. *Phys. Rev.*, 34(1):57–64, 1929.

[189] R. M. Nieminen. From atomistic simulation towards multiscale modelling of materials. *J. Phys. Condens. Matter*, 14:2859–2876, 2002.

[190] V. V. Ogorodnikov and Y. I. Rogovoi. Buckingham-potential parameters and relations between them for solids. *Powder Metall. Met. Ceram.*, 33(2A):327–333, 1995.

[191] T. Ohzono and M. Fujihira. Molecular dynamics simulations of friction between an ordered organic monolayer and a rigid slider with an atomic-scale protuberance. *Phys. Rev. B*, 62:17055–17071, 2000.

[192] T. Ohzono and M. Fujihira. Simulation of friction anisotropy on ordered organic monolayers. *Tribol. Lett.*, 9:63–61, 2000.

[193] C. Oligschleger and J. C. Schön. Simulation of thermal conductivity and heat transport in solids. *Phys. Rev. B*, 59(6):4125–4133, 1999.

[194] A. V. Olver and H. A. Spikes. Predictions of traction in elastohydrodynamic lubrication. *Proc. Inst. Mech. Eng. Part J J. Eng. Tribol.*, 212(J):321–332, 1998.

[195] Z. Pan, Y. Li, and Q. Wei. Tensile properties of nanocrystalline tantalum from molecular dynamics simulations. *Acta Mater.*, 56(14):3470–3480, 2008.

[196] D. L. Patrick, J. F. Flanagan, P. Kohl, and R. M. Lynden-Bell. Atomistic molecular dynamics simulations of chemical force microscopy. *J. Am. Chem. Soc.*, 125:6762–6773, 2003.

[197] S. J. Plimpton. Fast parallel algorithms for short-range molecular dynamics. *J. Comput. Phys.*, 117:1–19, 1995.

[198] T. Prevenslik, editor. *Nanoscale Heat Transfer by Quantum Mechanics*, May 2010.

[199] A. Rahman. Correlations in the motion of atoms in liquid argon. *Phys. Rev.*, 136 (2A):A405–A411, 1964.

[200] D. C. Rapaport. *The Art of Molecular Dynamics Simulation*. Cambridge University Press, UK, 2004.

[201] D. T. Read. Tension-tension fatigue of copper thin films. *Int. J. Fatigue*, 20(3): 203–209, 1998.

[202] C. Richard, A. Catlow, R. G. Bell, and J. D. Gale. Computer modelling as a technique in materials chemistry. *J. Mater. Chem.*, 4(6):781–792, 1994.

[203] M Rieth. *Nano-Engineering in Science and Technology: An introduction to the world of Nano-Design*. World Scientific, USA, 2003.

[204] D. A. Rigney and J. P. Hirth. Plastic deformation and sliding friction of metals. *Wear*, 53:345–370, 1979.

[205] D. A. Rigney, M. G. S. Naylor, R. Divakar, and L. K. Ives. Low energy dislocation structures caused by sliding and by particle impact. *Mater. Sci. Eng.*, 81:409, 1986.

[206] D. A. Rigney, X.-Y. Fu, J. E. Hammerberg, and M. L. Falk. Examples of structural evolution during sliding and shear of ductile materials. *Scr. Mater.*, 49:977–983, 2003.

[207] M. O. Robbins and M. H. Muser. *Computer Simulations of Friction, Lubrication and Wear*, volume 2. CRC Press Inc., 2000. B. Bhushan in Modern Tribology Handbook, Two Volume Set (Mechanics and Materials Science).

[208] J. Röder, J. E. Hammerberg, B. L. Holian, and A. R. Bishop. Multichain frenkel-kontorova model for interfacial slip. *Phys. Rev. B*, 57(5):2759–2766, Feb 1998. doi: 10.1103/PhysRevB.57.2759.

[209] J. Röder, J. E. Hammerberg, B. L. Holian, and A. R. Bishop. Multichain Frenkel-Kontorova model for interfacial slip. *Phys. Rev. B*, 57(5):2759–2766, 1998.

[210] A. M. Rutherford and D. M. Duffy. The effect of electron-ion interactions on radiation damage simulations. *J. Phys. Condens. Matter.*, 19(49):496201, 2007.

[211] N. Satyanarayana, S. K. Sinha, and B. H. Ong. Tribology of a novel UHMWPE/PFPE dual-film coated onto Si surface. *Sens. Actuators, A*, 128(1):98–108, 2006.

[212] R. Sayle and E. J. Milner-White. Rasmol: Biomolecular graphics for all. *Trends Biochem. Sci.*, 20:374, 1995.

[213] C. Schafer, H. M. Urbassek, and L. V. Zhigilei. Metal ablation by picosecond laser pulses: A hybrid simulation. *Phys. Rev. B*, 66(11):115404, 2002.

[214] P. K. Schelling, S. R. Phillpot, and P. Keblinski. Comparison of atomic-level simulation methods for computing thermal conductivity. *Phys. Rev. B*, 65(14):144306, 2002.

[215] J. Schiotz, T. Vegge, F. D. Di Tolla, and K. W. Jacobsen. Atomic-scale simulations of the mechanical deformation of nanocrystalline metals. *Phys. Rev. B*, 60(17):11971–11983, 1999.

[216] Jakob Schiotz. Atomic-scale modeling of plastic deformation of nanocrystalline copper. *Scr. Mater.*, 51(8):837–841, 2004. Viewpoint set no. 35. Metals and alloys with a structural scale from the micrometer to the atomic dimensions.

[217] J. Schneider, R. Beshears, and A.C. Nunes. Interfacial sticking and slipping in the friction stir welding process. *Mater. Sci. Eng., A*, 435-436:297–304, 2006.

[218] W. Schommers. Pair potentials in disordered many-particle systems: A study for liquid gallium. *Phys. Rev. A*, 28(6):3599–3605, 1983.

[219] A. Sharma, R. V. Kalia, A. Nakano, and P. Vashishta. Large multidimensional data visualization for materials science. *Computing in Science and Engineering*, 5 (2): 26–33, 2003.

[220] T. D. Shen, C. C. Koch, T. Y. Tsui, and G. M. Pharr. On the elastic moduli of nanocrystalline Fe, Cu, Ni, and Cu-Ni alloys prepared by mechanical milling/alloying. *J. Mater. Res.*, 10:2892, 1995.

[221] J. A. Sprague, F. Montalenti, B. P. Uberuaga, J. D. Kress, and A. F. Voter. Simulation of growth of Cu on Ag(001) at experimental deposition rates. *Phys. Rev. B*, 66(20): 205415, 2002.

[222] D. J. Steinberg, S. G. Cochran, and M. W. Guinan. A constitutive model for metals applicable at high-strain rate. *Journal of Applied Physics*, 51(3):1498–1504, 1980.

[223] D. Stewart and K.-S. Cheong. Molecular dynamics simulations of dislocations and nanocrystals. *Curr. Appl Phys.*, 8(3-4):494–497, 2008. AMN-3 (Third International Conference on Advanced Materials and Nanotechnology), Third International Conference on Advanced Materials and Nanotechnology.

[224] F. H. Stillinger and T. A. Weber. Computer simulation of local order in condensed phases of silicon. *Phys. Rev. B*, 31(8):5262–5271, 1985.

[225] A. M. Stoneham. Energy transfer between electrons and ions in collision cascades in solids. *Nucl. Instrum. Methods Phys. Res., Sect. B*, 48(1-4):389–398, 1990.

[226] F. H. Streitz, J. N. Glosli, M. V. Patel, B. Chan, R. K. Yates, B. R. Supinski, J. Sexton, and J. A. Gunnels. 100+ tflop solidification simulations on bluegene/l. 2005.

[227] A. P. Sutton and J. Chen. Long-range finnis sinclair potentials. *Philos. Mag. Lett*, 61:139–146, 1990.

[228] W. C. Swope, H. C. Andersen, P. H. Berens, and K. R. Wilson. A computer simulation method for the calculation of equilibrium constants for the formation of physical clusters of molecules: Application to small water clusters. *J. Chem. Phys.*, 76(1): 637–649, 1982.

[229] H. V. Swygenhoven and A. Caro. Molecular dynamics computer simulation of nanophase ni: structure and mechanical properties. *Nanostruct. Mater.*, 9(1-8):669–672, 1997.

[230] H. V. Swygenhoven, M. Spaczer, and A. Caro. Microscopic description of plasticity in computer generated metallic nanophase samples: a comparison between cu and ni. *Acta Mater.*, 47(10):3117–3126, 1999.

[231] H. V. Swygenhoven, M. Spaczr, D. Farkas, and A. Caro. The role of grain size and the presence of low and high angle grain boundaries in the deformation mechanism of nanophase ni: A molecular dynamics computer simulation. *Nanostruct. Mater.*, 12(1-4):323–326, 1999.

[232] H. Van Swygenhoven, M. Spaczr, and A. Caro. Role of low and high angle grain boundaries in the deformation mechanism of nanophase ni: A molecular dynamics simulation study. *Nanostruct. Mater.*, 10(5):819–828, 1998. Selected Papers from the Conference on Microstructure and its Effects on Amorphous, Nanophase and Nanocrystalline Materials TMS Annual Meeting and Exposition.

[233] D. Tabor. Tribology - the last 25 years a personal view. *Tribology International*, 28 (1):7–10, 1995.

[234] R. Tenne. Inorganic nanotubes and fullerene-like nanoparticles. *Nat. Nanotechnol.*, 1:103–111, 2006.

[235] J. Tersoff. Empirical interatomic potential for carbon, with applications to amorphous carbon. *Phys. Rev. Lett.*, 61(25):2879–2882, 1988.

[236] P. A. Thompson and M. O. Robbins. The shear flow near solids: Epitaxial order and flow boundary conditions. *Phys. Rev. A*, 41(2):6830–6837, 1990.

[237] P. A. Thompson, G. S. Crest, and M. O. Robbins. Phase transition and universal dynamics in confined films. *Phys. Rev. Lett.*, 68(23):3448–3451, 1992.

[238] G. A. Tomlinson. A molecular theory of friction. *Philosophical Magazine, Series 7*, 7(46):905–939, June 1929.

[239] G. A. Tomlinson. A molecular theory of friction. *Philos. Mag., Series 7*, 7(46): 905–939, 1929.

[240] K. V. Tretiakov and S. Scandolo. Thermal conductivity of solid argon from molecular dynamics simulations. *J. Chem. Phys.*, 120(8):3765–3769, 2004.

[241] T. Tsuji, N. Yanagi, M. Makino, and N. Noda. Some challenges for molecular dynamics techniques with considaration of the movement of free electrons in order to simulate thermodynamics by electronic current. *Advances in Electronic Packaging, EEP*, 2(26-2):1565–1568, 1999.

[242] R. Z. Valiev, R. K. Islamgaliev, and I. V. Alexandrov. Bulk nanostructured materials from severe plastic deformation. *Prog. Mater Sci.*, 45(2):103–189, 2000.

[243] T. S. Van Erp, A. Fasolino, O. Radulescu, and T. Janssen. Pinning and phonon localization in frenkel-kontorova models on quasiperiodic substrates. *Phys. Rev. B*, 60(9):6522–6528, Sep 1999.

[244] H. Van Swygenhoven and P. M. Derlet. Grain-boundary sliding in nanocrystalline FCC metals. *Phys. Rev. B*, 64(22):224105, 2001.

[245] H. Van Swygenhoven, M. Spaczer, A. Caro, and D. Farkas. Competing plastic deformation mechanisms in nanophase metals. *Phys. Rev. B*, 60(1):22–25, 1999.

[246] H. Van Swygenhoven, P. M. Derlet, and A. Hasnaoui. Atomic mechanism for dislocation emission from nanosized grain boundaries. *Phys. Rev. B*, 66(2):024101, 2002.

[247] P. Vashishta, R. K. Kalia, and A. Nakano. *Multimillion Atom Molecular-Dynamics Simulations of Nanostructured Materials and Processeson Parallel Computers*, volume Part A. Springer, Netherlands, 2005. S. Yip in Handbook of Materials Modeling.

[248] S. Veprek, M. G. J. Veprek-Heijman, P. Karvankova, and J. Prochazka. Different approaches to superhard coatings and nanocomposites. *Thin Solid Films*, 476(1): 1–29, 2005.

[249] L. Verlet. Computer experiments on classical fluids. I. thermodynamical properties of Lennard-Jones molecules. *Phys. Rev.*, 159(1):98, 1967.

[250] Z. G. Wang, C. Dufour, E. Paumier, and M. Toulemoude. The Se sensitivity of metals under swift-heavy-ion irradiation: a transient thermal process. *J. Phys.: Condens. Matter*, 6:6733–6750, 1992.

[251] M. S. Warren, T. C. Germann, P. S. Lomdahl, D. M. Beaszley, and J. K. Salmon. Avalon: An alpha/linux cluster achieves 10GFlops for 150K. 1998.

[252] R. J Weertman. *Mechanical Behaviour of Nanocrystalline Metals*. William Andrew, 2007. C. C. Koch in Nanostructured Materials: Processing, Properties and Applications.

[253] M. Weiss and F. J. Elmer. Dry friction in the frenkel-kontorova-tomlinson model: Static properties. *Phys. Rev. B*, 53(11):7539–7549, Mar 1996.

[254] E. Wimmer. Computational materials design: A perspective of atomistic approaches. *J. Comp. Aid. Des.*, 1:215–242, 1993.

[255] R. E. Winter, G. J. Ball, and P. T. Keightkey. Mechanisms of shock-induced dynamic friction. *J. Phys. D: Appl. Phys.*, 39:5043–5053, 2006.

[256] D. Wolf. *Atomic-Level Geometry of Crystalline Interfaces*. Chapman and Hall, London, UK, 1992. D. Wolf and D. Yip in Materials Interfaces: Atomic-Level Structure and Properties.

[257] D. Wolf, V. Yamakov, S.R. Phillpot, A. Mukherjee, and H. Gleiter. Deformation of nanocrystalline materials by molecular-dynamics simulation: relationship to experiments? *Acta Mater.*, 53(1):1 – 40, 2005.

[258] H. A. Wu. Molecular dynamics study of the mechanism of metal nanowires at finite temperature. *European Journal of Mechanics of Solids: A*, 25:370–377, 2006.

[259] P. Xu and P. Huang. Study on the energy dissipation mechanism of atomic-scale friction with composite oscillator model. *Wear*, 262(7-8):972 – 977, 2007.

[260] W. Xueyuan and R. K. Asok. A Full Potential Linearized Augmented Plane Wave electronic structure study of delta-plutonium and the (001) surface. pages 1–27, 2004.

[261] S. Yim, N. Sonwalkar, and N. Saka. Molecular dynamics simulation of boundary lubricated interfaces. *J. Comput. Aided Mater. Des.*, 6:69–80, 1999.

[262] S Yip. Nanocrystals: The strongest size. *Nature*, 391(4):532–533, 1998.

[263] K. Yoshida, Y. Goto, and M. Yamatoto. Yielding of copper whiskers. *J. Phys. Soc. Jpn.*, 21(4):825–826, 1966.

[264] S. You, X. C. Zeng, and J. Morris. The melting lines of model silicon calculated from existing solid-liquid phases. *J. Chem. Phys.*, 120(3):1654–1656, 2004.

[265] M. H. Yu, G. W. Ma, H. F. Qiang, and Y. Q. Zhang. *Basic Characteristics of Yield of Materials under Complex Stress*. Springer Berlin Heidelberg, 2006.

[266] W. Zenghui and L. Zhixin. Lattice dynamics analysis of thermal conductivity in silicon nanoscale film. *Appl. Therm. Eng.*, 26:2063–2066, 2006.

[267] Y. W. Zhang, P. Liu, and C. Lu. Molecular dynamics simulations of the preparation and deformation of nanocrystalline copper. *Acta Mater.*, 52(17):5105–5114, 2004.

[268] C. Zheng and Y.W. Zhang. Atomistic simulations of mechanical deformation of high-angle and low-angle nanocrystalline copper at room temperature. *Materials Science and Engineering: A*, 423(1-2):97–101, 2006. Mechanical Behaviour of Micro- and Nano-scale Systems.

[269] M. Zhou. A new look at the atomic level virial stress: on continuum-molecular system equivalence. *Proc. R. Soc. London, Ser. A: Mathematical, Physical and Engineering Sciences*, 459(2037):2347–2392, 2003.

[270] J. F. Ziegler, J. P. Biersack, and U. Littmark. *The Stopping and Range of Ions in Solids*. Pergamon Press., 1985.

[271] J. A. Zimmerman, E. B. Webb, J. J. Hoyt, R. E. Jones, P. A. Klein, and D. J. Bammann. Calculation of stress in atomistic simulation. *Modell. Simul. Mater. Sci. Eng.*, 12(4):S319–S332, 2004.

APPENDIX **A**

Voronorised Cu/Ag: Velocity variation

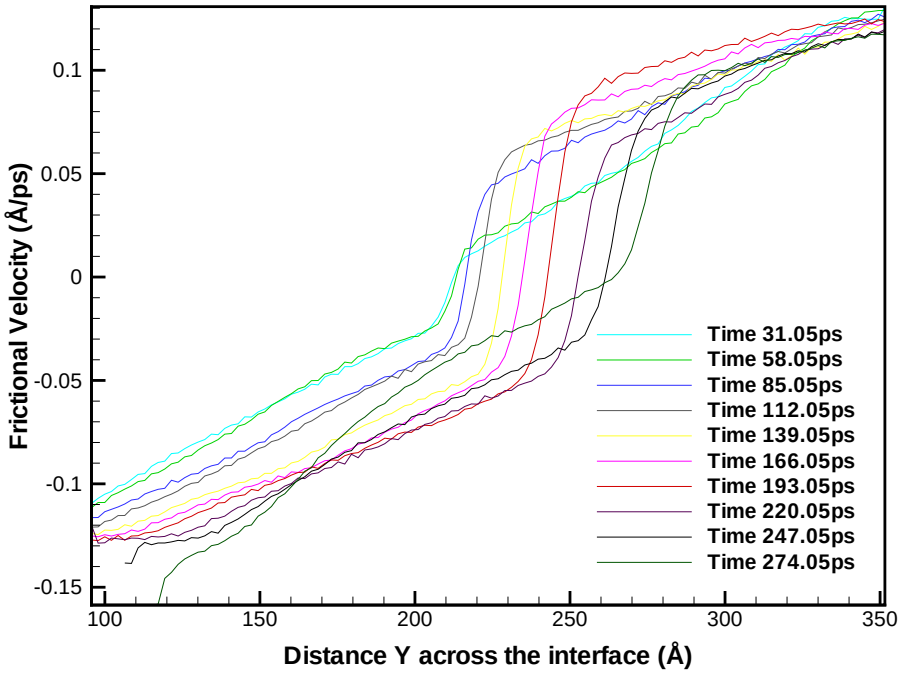

Figure A.1: Velocity variation of nanocrystalline Cu/Ag tribopair. Sliding speed of 25 m/s

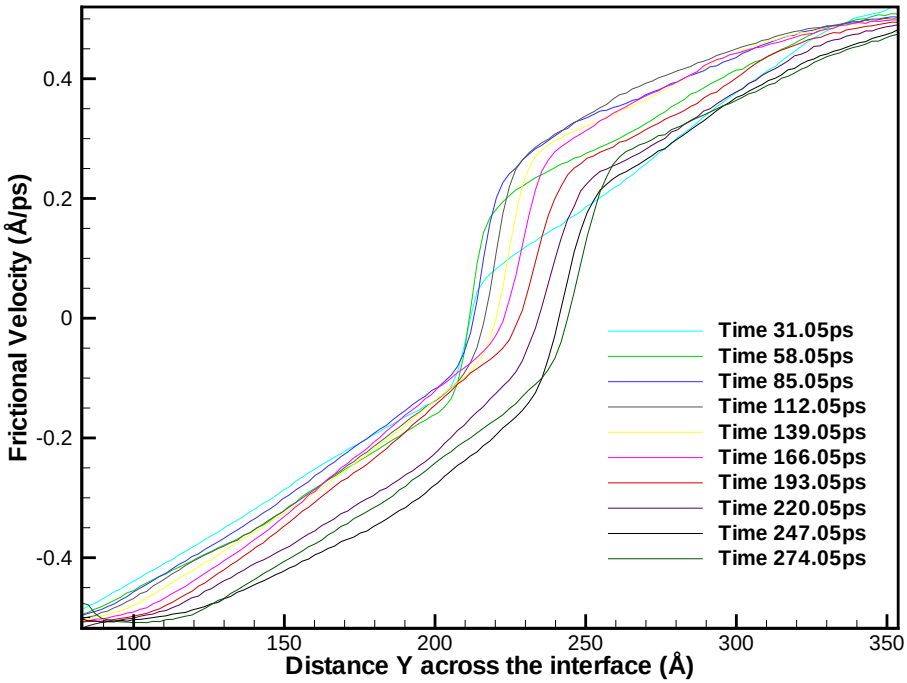

Figure A.2: Velocity variation of nanocrystalline Cu/Ag tribopair. Sliding speed of 100 m/s

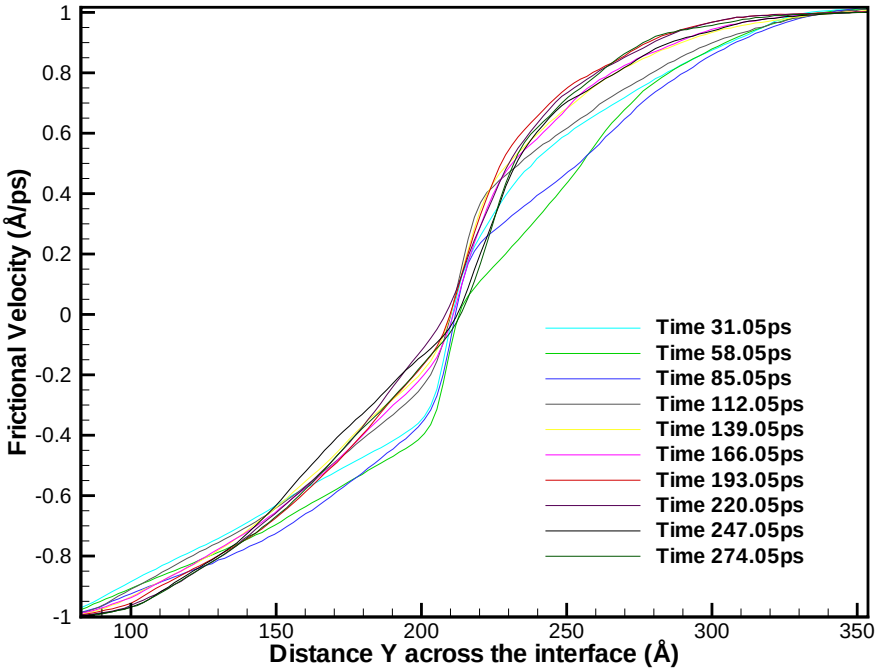

Figure A.3: Velocity variation of nanocrystalline Cu/Ag tribopair. Sliding speed of 200 m/s

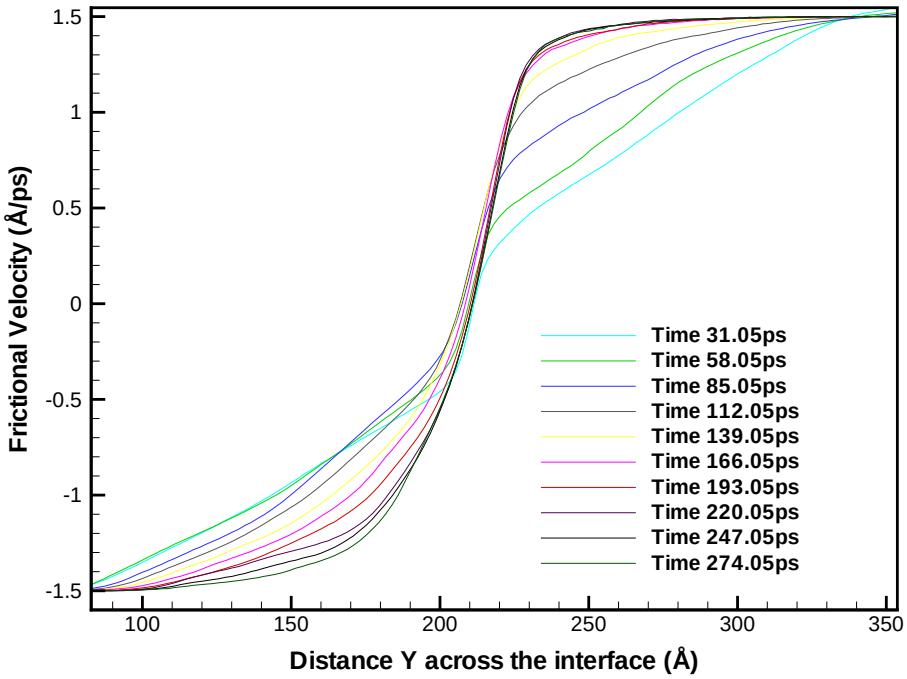

Figure A.4: Velocity variation of nanocrystalline Cu/Ag tribopair. Sliding speed of 300 m/s

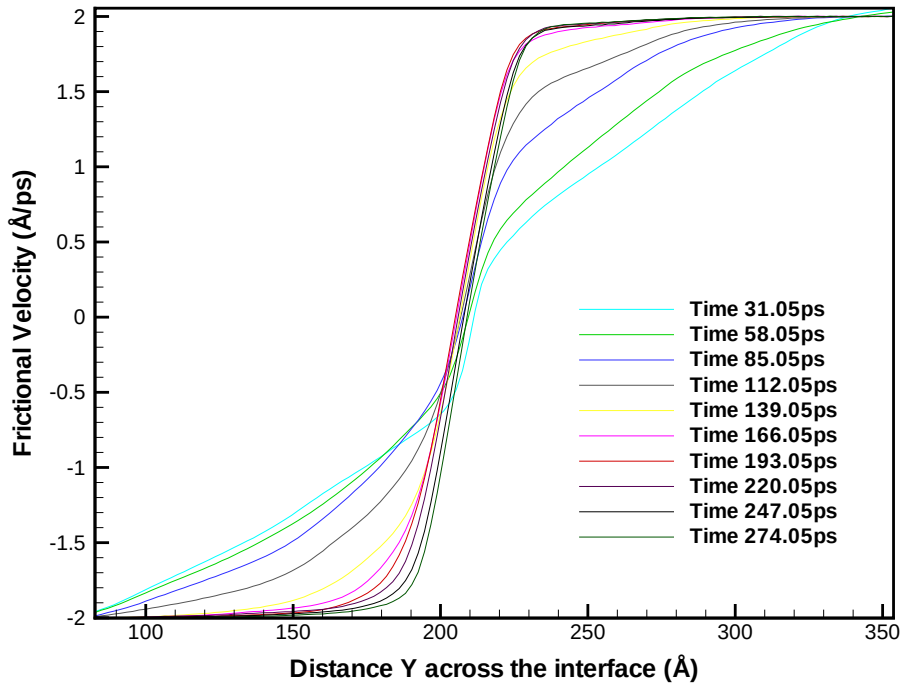

Figure A.5: Velocity variation of nanocrystalline Cu/Ag tribopair. Sliding speed of 400 m/s

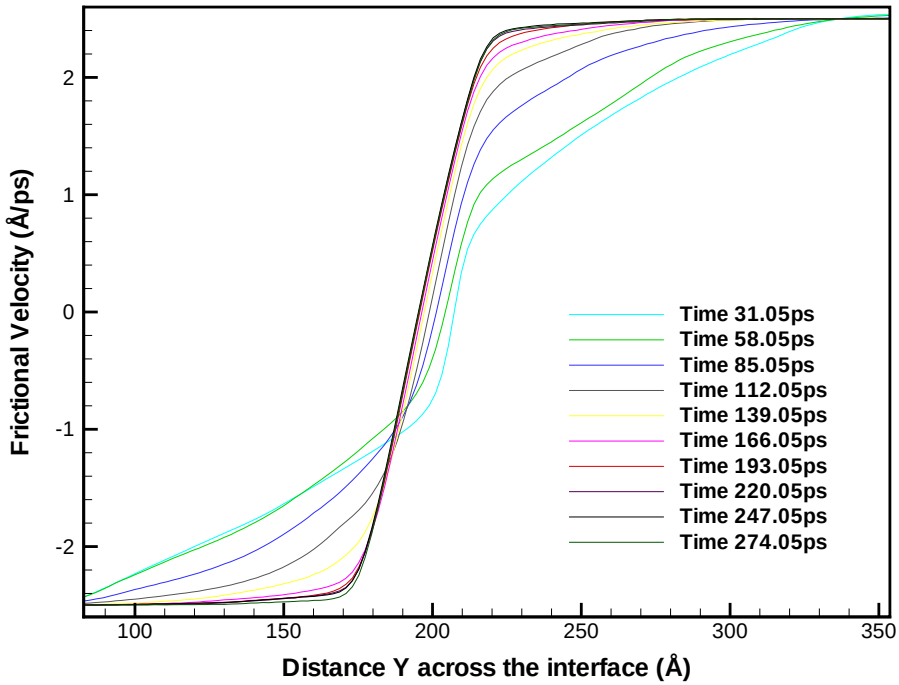

Figure A.6: Velocity variation of nanocrystalline Cu/Ag tribopair. Sliding speed of 500 m/s

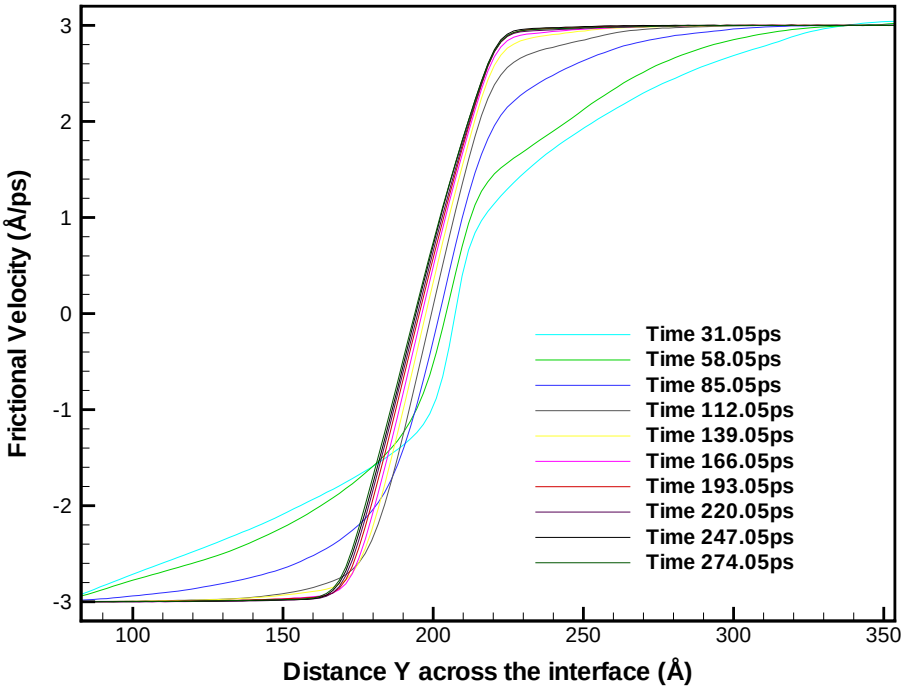

Figure A.7: Velocity variation of nanocrystalline Cu/Ag tribopair. Sliding speed of 600 m/s

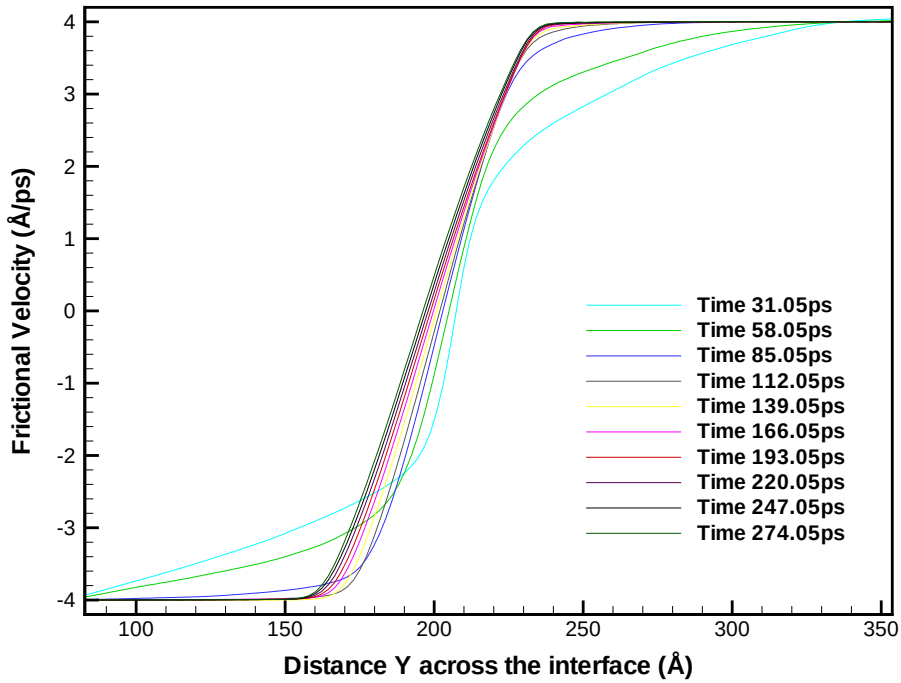

Figure A.8: Velocity variation of nanocrystalline Cu/Ag tribopair. Sliding speed of 800 m/s

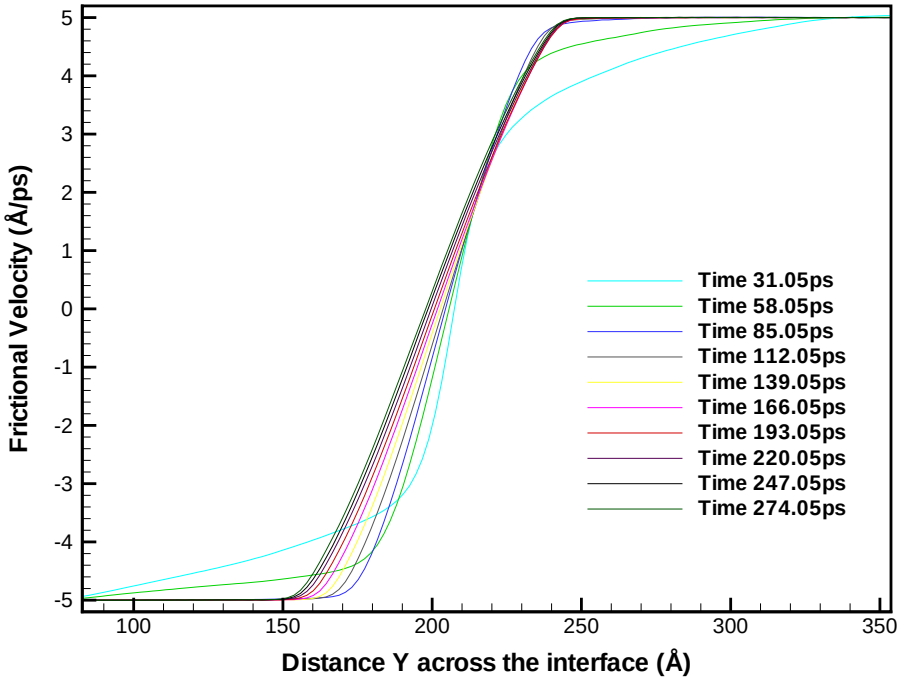

Figure A.9: Velocity variation of nanocrystalline Cu/Ag tribopair. Sliding speed of 1000 m/s

APPENDIX B

Voronorised Cu/Ag: Stress-strain curves

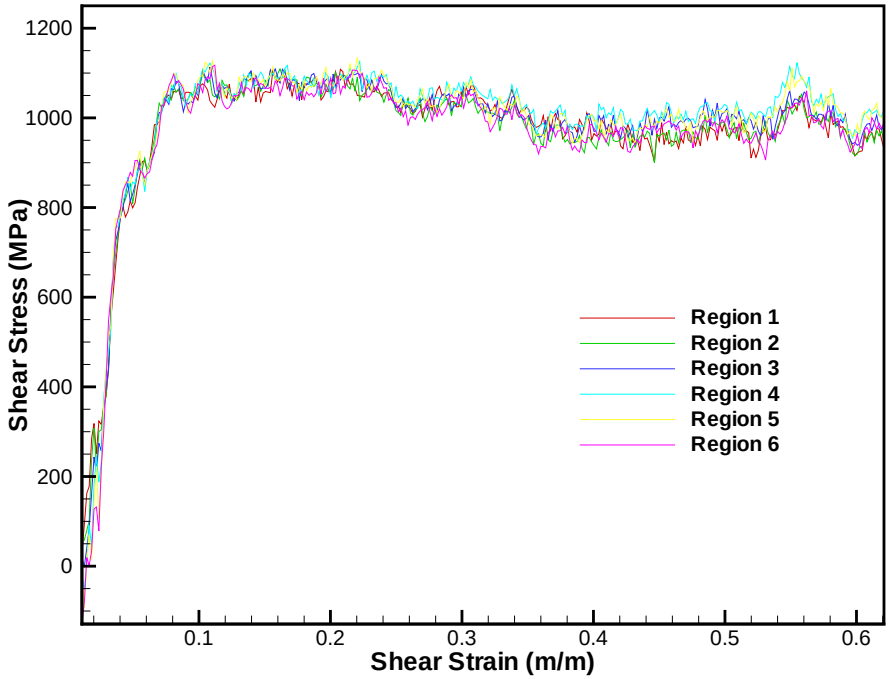

Figure B.1: Stress strain response of voronorised Cu sliding on Ag. Sliding speed of 100 m/s

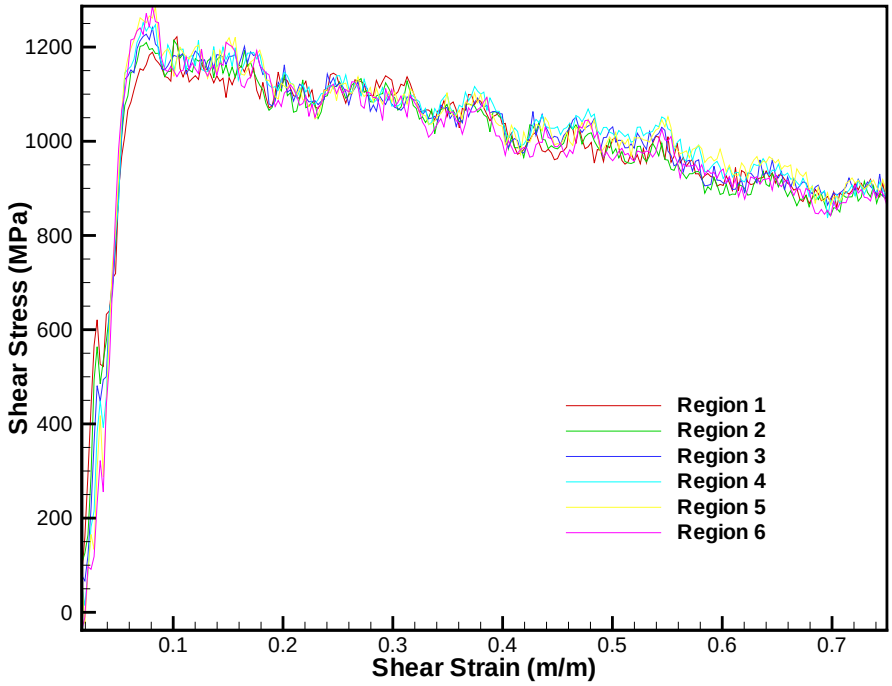

Figure B.2: Stress strain response of voronorised Cu sliding on Ag. Sliding speed of 200 m/s

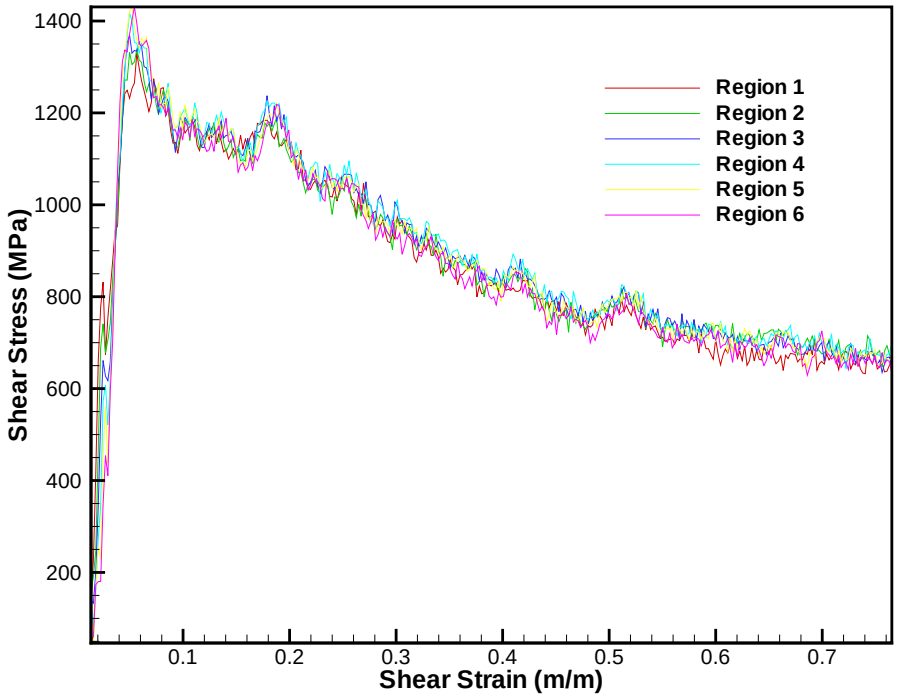

Figure B.3: Stress strain response of voronorised Cu sliding on Ag. Sliding speed of 300 m/s

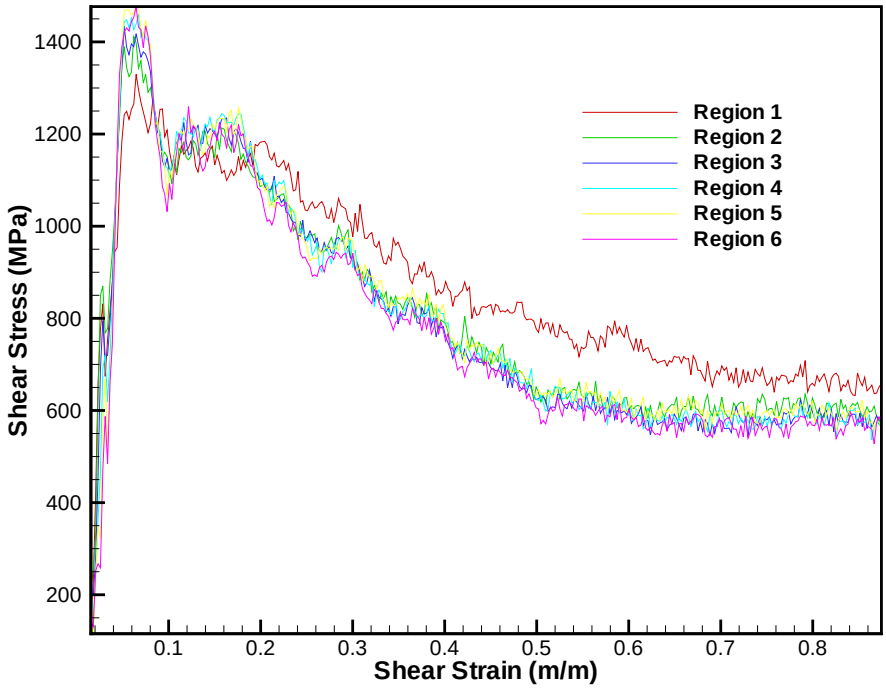

Figure B.4: Stress strain response of voronorised Cu sliding on Ag. Sliding speed of 400 m/s

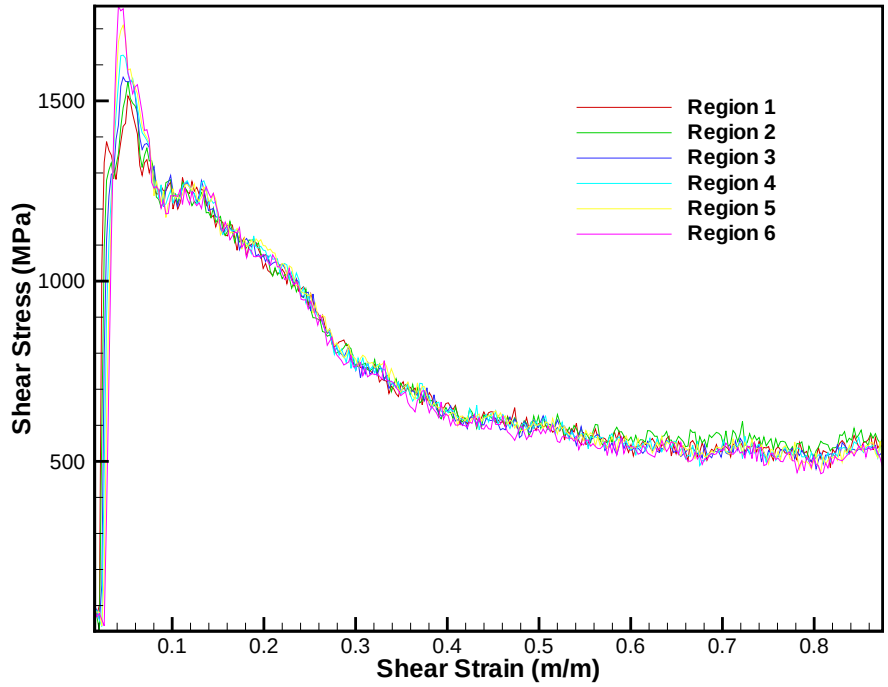

Figure B.5: Stress strain response of voronorised Cu sliding on Ag. Sliding speed of 500 m/s

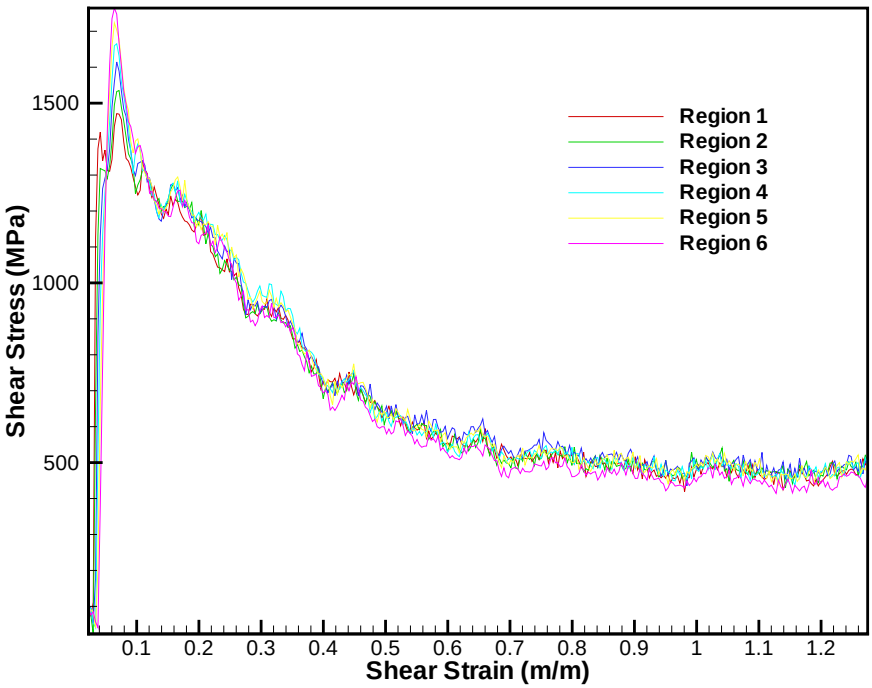

Figure B.6: Stress strain response of voronorised Cu sliding on Ag. Sliding speed of 600 m/s

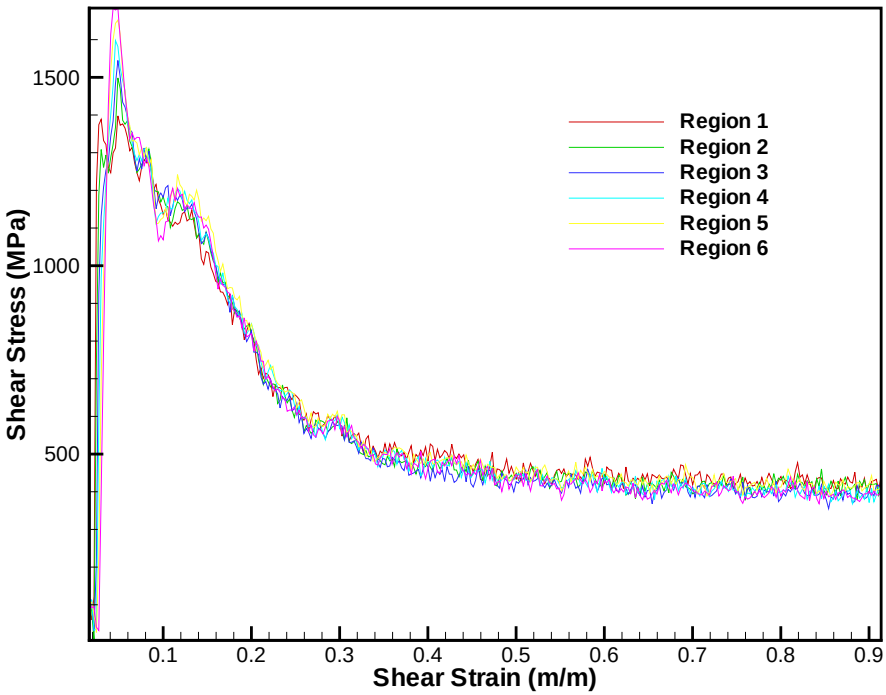

Figure B.7: Stress strain response of voronorised Cu sliding on Ag. Sliding speed of 800 m/s

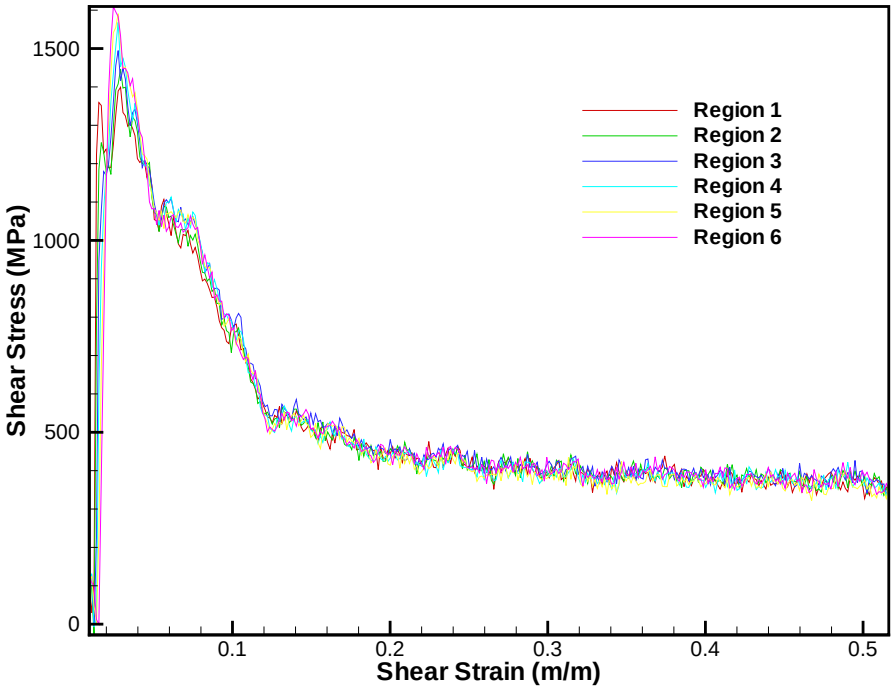

Figure B.8: Stress strain response of voronorised Cu sliding on Ag. Sliding speed of 1000 m/s